UC Berkeley
UC Berkeley Electronic Theses and Dissertations

Title
Defect-Structure-Property Relations in Complex-Oxide Ferroelectric Thin Films

Permalink
https://escholarship.org/uc/item/9q259355

Author
Sareminaeini, Sahar

Publication Date
2019

Peer reviewed|Thesis/dissertation

eScholarship.org Powered by the California Digital Library
University of California

Defect-Structure-Property Relations in Complex-Oxide Ferroelectric Thin Films

By

Sahar Sareminaeini

A thesis submitted in partial satisfaction of the

requirements for the degree of

Doctor of Philosophy

in

Engineering - Materials Science and Engineering

in the

Graduate Division

of the

University of California, Berkeley

Committee in charge:

Professor Lane W. Martin, Chair
Professor Ramamoorthy Ramesh
Professor Peter Hosemann

Summer 2019

Defect-Structure-Property Relations in Complex-Oxide Ferroelectric Thin Films

Copyright 2019

by

Sahar Sareminaeini

Abstract

Defect-Structure-Property Relations in Complex-Oxide Ferroelectric Thin Films

by

Sahar Sareminaeini

Doctor of Philosophy in Materials Science and Engineering

University of California, Berkeley

Professor Lane W. Martin, Chair

One role for modern materials science is to provide a foundation upon which scientists and engineers in diverse fields can address the needs of current and future societal challenges through the realization of next-generation technologies. Key to such advances is not only the development of advanced materials with novel or enhanced properties and performance, but also the know-how to synthesize and process such materials in a deterministic manner so that their properties can be effectively and efficiently utilized. Materials science is founded upon the concept that structure, processing, properties, and, ultimately, performance of materials are intimately interconnected. And, as the field has evolved, materials scientists and engineers have increasingly realized that even our best efforts to control these tenets can be remarkably hampered if we do not account for and address the role of material imperfections. Underlying all this is the fact that defects are unavoidable. Even in the most "perfect" materials, there are always finite concentrations of various structural and compositional defects. Although in some material systems defects have been extensively studied and used to engineer and improve properties, the general opinion of defects in ferroelectric community is not a good one – defects are regarded as "bad guys" and thought to be (uniformly) deleterious to material performance. But, armed with advances in our ability to synthesize, characterize, and model these materials, this negative connotation stands poised to be redefined. So can defects really be "good guys" in the ferroelectric world? In this Thesis I aim to view defects in a new light – a positive one – that casts them as another tool to design better ferroelectric materials with emergent properties and functionalities.

In the present work, I demonstrate strong defect-structure-property couplings in thin film versions of various complex-oxide ferroelectrics (including $BaTiO_3$, $BiFeO_3$, $PbTiO_3$, $PbZr_xTi_{1-x}O_3$) and relaxor ferroelectrics (such as $0.68PbMg_{1/3}Nb_{2/3}O_3$-$0.32PbTiO_3$) grown via pulsed-laser deposition, and show that such defect-structure-property interplays can be manipulated with deliberate introduction of certain defect types at controlled concentrations and locations which can provide new pathways to enhanced properties and novel functions. Among all defect types that can be present, this work only focuses on point defects as they are the most abundant defects in ionically-bonded solids such as complex-oxide ferroelectrics and play a particularly important role in impacting the properties of these materials. Nevertheless, in surprisingly few cases does one have a detailed understanding of point defects and their impact on the properties due to difficulties in their control and characterization. In the present work, I introduce various *in situ* and *ex situ* approaches for on-demand defect creation. The *in situ* approach relies on the variations of growth parameters (such as laser fluence, laser-repetition rate,

target composition, and growth pressure) in order to control defects during the synthesis process of the thin films, while the *ex situ* approach focuses on the use of energetic ion beams (both defocused high-energy, and focused low-energy ion beams) to introduce defects in already-grown films. This controlled defect production is then used to perform systematic experimental studies on the evolution of various material properties (including transport, dielectric, and ferroelectric properties) as a function of defect type and across many orders of magnitude of defect concentration, which provides valuable understanding regarding the physics of defects in these complex systems. The nature of the induced defects and their impact on the properties are studied using a combination of conventional and advanced characterization techniques including X-ray diffraction, Rutherford backscattering spectrometry, scanning transmission electron microscopy, scanning probe microscopy, and electrical measurements such as traditional dielectric, ferroelectric, and transport measurements, switching kinetics studies, first-order reversal curve analysis, impedance spectroscopy, and deep-level transient spectroscopy. Ultimately, I show that establishing routes to achieve such control and understanding over defects is the key if we desire to use defects as “good guys” and as tools to our advantage for material control and design rather than being limited by them.

To Payam

ACKNOLEDGEMENTS

Today, I feel truly lucky and thankful for having a great number of people in my academic and personal life who continuously helped and supported me in completing my doctoral degree; this journey would not have been possible without them.

First, my deepest appreciation goes out to my Ph.D. advisor, Professor Lane W. Martin, for his continued guidance, support, and encouragements throughout the years. I do not think I can ever thank you enough for what you have done for me. What I have achieved in your lab is more than just a Ph.D. degree; you taught me how to work with discipline, ethics, professionalism, and optimism; to be organized and efficient; to think outside the box and be creative; to have a good judgment, and to handle criticism while staying respectful of myself and others. Such values not only helped me progress in my scientific research but also made me more confident and successful in my personal life. You have been a great teacher and mentor to me, challenged me every day, pushed my boundaries, and helped me grow both professionally and personally. So thank you for helping me become a better version of myself.

I would also like to acknowledge my master's thesis advisors Professor Dragan Damjanovic (Ecole Polytechnique Fédérale de Lausanne) and Professor Gustau Catalan (Catalan Institute of Nanoscience and Nanotechnology) for introducing me to the world of complex-oxide ferroelectrics, and for motivating me to start my Ph.D. in this area. You have been always tremendous mentors and support to me.

I am greatly thankful to Professor Ramamoorthy Ramesh and everyone in his group. I have learnt a lot from all of you and always enjoyed our collaborations.

My sincere thanks go out to Professor Peter Hosemann for providing me with valuable suggestions and recommendations that greatly improved my research, and for facilitating my access to the focused helium-ion microscope located in the QB3 Biomolecular Nanotechnology Center at the University of California, Berkeley.

I would like to thank Andre Anders and Joseph G. Wallig from the Ion Beam Analysis lab at the Lawrence Berkeley National Laboratory for their continued help and support with the use of pelletron tandem accelerator for both Rutherford backscattering spectrometry and defocused helium-ion bombardment experiments.

I would like to express my sincere gratitude to Frances I. Allen from Lawrence Berkeley National Laboratory for her valuable help in conducting focused helium-ion bombardment experiments.

I would like to acknowledge Scott P. Chapman and Joseph T. Evans from Radiant Technologies, Inc., for guiding me through building a deep-level transient spectroscopy set-up in our lab which greatly helped me in my research.

I would like to extend my special appreciation and thanks to all my colleagues and fellow labmates for their contribution to my research, and also for their friendship which made this journey more enjoyable for me. Here, I would like to specially acknowledge those who have contributed to specific aspects of my research: I acknowledge Ruijuan Xu for her contributions in scanning probe microscopy, ferroelectric switching, and first-order reversal curve measurements and analyses. I acknowledge Liv R. Dedon for growth of $BiFeO_3$ thin films, and for conducting the experimental studies of growth-induced defects in $BiFeO_3$. I acknowledge Arvind Dasgupta

for growth of $BaTiO_3$ thin films, and for conducting the experimental studies of growth-induced defects in $BaTiO_3$. I acknowledge Jieun Kim for growth of $(1\text{-}x)PbMg_{1/3}Nb_{2/3}O_3\text{-}(x)PbTiO_3$ thin films, and for providing useful insights regarding relaxor ferroelectrics. I acknowledge Julia A. Mundy for conducting scanning transmission electron microscopy experiments. I acknowledge Joshua C. Agar for conducting band excitation piezoresponse spectroscopy experiments and analyses. I am also grateful to all my other colleagues with whom I have closely collaborated over the years including: Anoop R. Damodaran, Ran Gao, Lei Zhang, Eduardo Lupi, Gabriel Velarde, Josh Maher, David Garcia, Zuhuang Chen, Anirban Ghosh, and Derek Meyers.

I would like to gratefully acknowledge various funding sources which supported the research presented in this Thesis including Lam Research Graduate Fellowship (2016-2017 academic year) and funding from National Science Foundation, Department of Energy, Army Research Office, and Gordon and Betty Moore Foundation's EPiQS Initiative.

A very special gratitude also goes out to my parents who have always encouraged me to follow my dreams, and always supported me along my way to this point with everything I have been passionate about, despite all difficult circumstances. I owe it all to you. Hearing your encouraging voice from distance has been the brightest light in my darkest days during the last few years. You have been dearly missed and I am truly sorry for not being there for you when you needed me.

And finally, last but by no means least, I will be forever indebted to Payam, my husband, who has always been by my side throughout this Ph.D., living every single minute of it. Words cannot express how grateful I am to you. Without you, I would not have had the courage to embark on this journey in the first place and would not be able to complete what I started. You never stopped believing in me and always pushed me forward and kept me going when I was ready to quit. Thank you for always being there for me and thank you for bringing happiness and balance into my life.

TABLE OF CONTENTS

LIST OF FIGURES vii

LIST OF TABLES xv

LIST OF ABBREVIATIONS xvi

LIST OF SYMBOLS xvii

CHAPTER 1 Motivation and Outline 1

1.1 Motivation 2
1.2 Central Questions and Organization of the Dissertation 4

CHAPTER 2 Introduction to Ferroelectricity: Definitions, Properties, and Materials 7

2.1 Basic Definitions 8
2.2 The Origins of Ferroelectricity 8
2.3 Domains in Ferroelectrics 9
2.4 Properties of Ferroelectric Materials 10
2.4.1 Ferroelectric Switching 10
2.4.2 Dielectric, Piezoelectric, and Pyroelectric Susceptibilities 12
2.5 Complex-Oxide Ferroelectric Materials 13
2.5.1 $BaTiO_3$ 13
2.5.2 $PbTiO_3$ 13
2.5.3 $PbZr_xTi_{1-x}O_3$ 13
2.5.4 $BiFeO_3$ 14
2.5.5 $(1-x)PbMg_{1/3}Nb_{2/3}O_3-(x)PbTiO_3$ 14
2.6 Epitaxial Ferroelectric Thin Films 15
2.7 Applications of Ferroelectrics 16
2.8 Ferroelectric Device Reliability Issues 16
2.8.1 Leakage 17
2.8.2 Imprint 19
2.8.3 Retention 19

CHAPTER 3 Point Defects in Complex-Oxide Ferroelectrics 21

3.1 Types of Point Defects 22
3.2 Kröger-Vink Notation 22
3.3 Equilibrium Point Defects 23
3.4 Non-Equilibrium Point-Defects 24
3.5 Impact of Point Defects on the Properties of Ferroelectric Thin Films 26

CHAPTER 4 Synthesis, Processing, and Characterization of Ferroelectric Thin-Film Heterostructures 28

4.1 Synthesis of Ferroelectric Thin Film Heterostructures 29
4.1.1 Pulsed-Laser Deposition 29
4.2 Processing of Ferroelectric Thin-Film Heterostructures 31
4.2.1 Device Fabrication 31
4.2.2 Defect Production 32
4.2.3 Stopping and Range of Ions in Matter (SRIM) Simulations 33
4.3 Characterization of Ferroelectric Thin Film Heterostructures 34
4.3.1 Structural and Chemical Analyses 34
4.3.2 Surface Topography and Domain-Structure Analyses 37

4.3.3 Electrical Characterization 38

CHAPTER 5 Growth-Induced Control of Off-Stoichiometric Defects and Their Impact on the Structure and Properties of $BaTiO_3$ and $BiFeO_3$ Thin Films 47

5.1 Introduction 48
5.2 *In Situ* Creation of Off-Stoichiometric Defects in $BaTiO_3$ Thin Films via Variations of Laser Fluence 48
5.3 Effect of Growth-Induced Off-Stoichiometric Defects on Transport, Dielectric, and Ferroelectric Properties of $BaTiO_3$ Thin Films 50
5.4 *In Situ* Creation of Off-Stoichiometric Defects in $BiFeO_3$ Thin Films via Variations of Laser-Repetition Rate and Target Composition 55
5.5 Effect of Growth-Induced Off-Stoichiometric Defects on Transport, Dielectric, and Ferroelectric Properties of $BiFeO_3$ Thin Films 57
5.6 Conclusions 62

CHAPTER 6 *In Situ* and *Ex Situ* Control of Bombardment-Induced Defects and Their Impact on Electrical Resistivity of $PbTiO_3$ Thin Films 64

6.1 Introduction 65
6.2 *In Situ* Creation of Defects via Variations of Growth Pressure and Their Impact on Leakage Properties of $PbTiO_3$ Thin Films 65
6.3 *Ex Situ* Creation of Defects via High-Energy Helium-Ion Bombardment and Their Impact on Leakage Properties of $PbTiO_3$ Thin Films 68
6.4 Characterization of Bombardment-Induced Defects in $PbTiO_3$ Thin Films 72
6.5 Conclusions 76

CHAPTER 7 *Ex Situ* Control of Bombardment-Induced Defects and Their Impact on Transport and Ferroelectric Switching Properties of $BiFeO_3$ Thin Films 77

7.1 Introduction 78
7.2 *Ex Situ* Creation of Defects in $BiFeO_3$ Thin Films via High-Energy Helium-Ion Bombardment 79
7.3 Effect of Bombardment-Induced Defects on Transport Properties of $BiFeO_3$ Thin Films 81
7.4 Effect of Bombardment-Induced Defects on Ferroelectric Switching Properties of $BiFeO_3$ Thin Films 86
7.5 Conclusions 90

CHAPTER 8 Local Control of Defects and Switching Properties in $PbZr_{0.2}Ti_{0.8}O_3$ Thin Films via Focused-Helium-Ion Bombardment 91

8.1 Introduction 92
8.2 *Ex Situ* Creation of Bombardment-Induced Defects via Focused-Helium-Ion Bombardment and Study of Their Impact on Ferroelectric Switching Properties of $PbZr_{0.2}Ti_{0.8}O_3$ Thin Films 93
8.3 Designing New Functionalities in $PbZr_{0.2}Ti_{0.8}O_3$ Thin Films via Control of the Location of Bombardment-Induced Defects 98
8.4 Conclusions 103

CHAPTER 9 *Ex Situ* Control of Bombardment-Induced Defects and Study of Defect-Induced (Dis)Order in Relaxor Ferroelectric Thin Films 104

9.1 Introduction 105
9.2 *Ex Situ* Creation of Bombardment-Induced Defects in $0.68PbMg_{1/3}Nb_{2/3}O_3$-$0.32PbTiO_3$ Thin Films via High-Energy Helium-Ion Bombardment 105

9.3 Effect of Bombardment-Induced Defects on Relaxor Properties of $0.68PbMg_{1/3}Nb_{2/3}O_3$-$0.32PbTiO_3$ Thin Films ... 107
9.4 Conclusions ... 112

CHAPTER 10 Summary of Findings and Suggestions for Future Work ... 113

10.1 Summary of Findings ... 113
10.2 Suggestions for Future Work ... 116

APPENDIX A Pulsed-Laser Deposition of Ferroelectric Thin Film Heterostructures ... 121

A.1 Growth of $BaTiO_3$ Heterostructures ... 121
A.2 Growth of $PbTiO_3$ Heterostructures ... 122
A.3 Growth of $PbZr_{0.2}Ti_{0.8}O_3$ Heterostructures ... 122
A.4 Growth of $BiFeO_3$ Heterostructures ... 122
A.5 Growth of $0.68PbMg_{1/3}Nb_{2/3}O_3$-$0.32PbTiO_3$ Heterostructures ... 123

APPENDIX B Band Excitation Piezoresponse Spectroscopy – Loop Fitting ... 124

REFERENCES ... 126

LIST OF FIGURES

Figure 2.1. The schematic representation of atomic structure in an ABO_3 perovskite oxide.

Figure 2.2. The schematics of (a) ferroelectric domains with 180° domain walls, and (b) ferroelastic domains with 90° domain walls.

Figure 2.3. The schematic of a ferroelectric polarization-electric field hysteresis loop.

Figure 2.4. A Heckmann diagram describing the coupling between thermal, electrical, and mechanical properties of ferroelectric materials. S in this diagram represents the entropy.

Figure 2.5. Classification of conduction mechanisms.

Figure 2.6. Schematic representation of electrical imprint giving rise to a shift of ferroelectric hysteresis loop on the electric field axis.

Figure 2.7. Schematic representation of time-dependent drop of remanent polarization due to retention.

Figure 4.1. Schematic illustration of the pulsed-laser deposition setup used in this work.

Figure 4.2. Schematic illustration of the parallel-plate capacitor structure used in this work for electrical measurements.

Figure 4.3. Geometry of the X-ray diffractometer used in this work.

Figure 4.4. Schematic illustration of basic principles of Rutherford backscattering spectrometry.

Figure 4.5. The voltage profile used in this work for ferroelectric hysteresis-loop measurements.

Figure 4.6. Sequence of voltage pulses used in this work for switching kinetics measurements.

Figure 4.7. The modified PUND pulse sequence used in this work.

Figure 4.8. The pulse sequence used in this work for retention measurements.

Figure 4.9. The unswitched triangular voltage profile used in this work for current-voltage measurements.

Figure 4.10. Schematic representation of a Nyquist complex-impedance plane.

Figure 4.11. Basic principles of deep-level transient spectroscopy.

Figure 5.1. (a) $\omega - 2\theta$ X-ray diffraction scans for heterostructures grown at laser fluences of 1.25 J cm^{-2} (top, red), 1.45 J cm^{-2} (middle, orange), and 1.65 J cm^{-2} (bottom, blue). Off-axis reciprocal space mapping studies about the $\bar{1}03$- and $33\bar{2}$-diffraction conditions of the film and substrate, respectively, for heterostructures grown at laser fluences of (b) 1.25 J cm^{-2}, (c) 1.45 J cm^{-2}, and (d) 1.65 J cm^{-2}. Rutherford backscattering spectrometry data with a zoom-in image of the oxygen resonance peak (inset) for heterostructures grown at laser fluences of (e) 1.25 J cm^{-2}, (f) 1.45 J cm^{-2}, and (g) 1.65 J cm^{-2}.

Figure 5.2. X-ray rocking curve studies about the 002-diffraction condition of the film and 220-diffraction condition of the substrate for heterostructures grown at laser fluences of (a) 1.25 J cm^{-2}, (b) 1.45 J cm^{-2}, and (c) 1.65 J cm^{-2}. The numbers in the upper right-hand corner are the FWHM values for the substrate (top) and film (bottom).

Figure 5.3. Room temperature current-voltage measurements, (b) room-temperature, low-field dielectric permittivity (left axis) and loss tangent (right axis), (c) temperature dependence of dielectric permittivity, and (d) polarization-electric field hysteresis loops measured at 1 kHz for $Ba_{1.00}TiO_{3.00}$, $Ba_{0.96}TiO_{2.92}$, and $Ba_{0.93}TiO_{2.87}$ heterostructures.

Figure 5.4. Calculated first-order reversal curve distributions for (a) $Ba_{1.00}TiO_{3.00}$, (b) $Ba_{0.96}TiO_{2.92}$, and (c) $Ba_{0.93}TiO_{2.87}$ heterostructures.

Figure 5.5. (a) Derivatives of J *vs.* E. Neither of the heterostructures exhibits ohmic conduction $(d(\ln(J))/d(\ln(E)) = 1)$ or space-charge limited conduction $(d(\ln(J))/d(\ln(E)) = 2)$. Positive bias room temperature current-voltage data represented on the standard (b) Schottky and (c) Poole-Frenkel plots. Schottky emission fits reveal a poor match with the expected optical dielectric constant of $BaTiO_3$, while modified Poole-Frenkel emission reveals a good fit to the experimental data.

Figure 5.6. Deep-level transient spectroscopy data and the extracted intragap trap energies for (a) $Ba_{1.00}TiO_{3.00}$, (b) $Ba_{0.96}TiO_{2.92}$, and (c) $Ba_{0.93}TiO_{2.87}$ heterostructures.

Figure 5.7. Deep-level transient spectroscopy fits used to extract trap energies in the (a) $Ba_{0.96}TiO_{2.92}$, (b) $Ba_{0.93}TiO_{2.87}$, and (c) vacuum-annealed $Ba_{0.93}TiO_{2.87}$ heterostructures.

Figure 5.8. Deep-level transient spectroscopy data for (a) an as-grown $Ba_{0.93}TiO_{2.87}$ heterostructure, (b) the same film after vacuum annealing at 500°C, and (f) the same film after barium addition via a chemical vapor deposition-like process. (c) Rutherford backscattering spectrometry data, (d) $\omega - 2\theta$ X-ray diffraction scans, and (e) polarization-electric field hysteresis loops for the $Ba_{0.93}TiO_{2.87}$ heterostructure in the as-grown state and followed by barium addition. (g) Schematic of the defect state energies present within the $Ba_{1-x}TiO_y$ films wherein E_G is the band gap.

Figure 5.9. (a) $\omega - 2\theta$ X-ray diffraction patterns about the 001- and 002-diffraction conditions of the $BiFeO_3$ and $SrRuO_3$ films and 110- and 220-diffraction conditions of the $DyScO_3$ substrate. (b) Zoom-in about the 002- and 220-diffraction conditions showing minimal variation in the out-of-plane lattice parameter of the $BiFeO_3$ with changing growth conditions.

Figure 5.10. X-ray rocking curve studies about the 002-diffraction condition of the film and 220-diffraction condition of the substrate for heterostructures grown at various growth conditions. The numbers in the upper right-hand corner are the FWHM values from the substrate (top, red) and film (bottom, black) curves.

Figure 5.11. Enlarged view of Rutherford backscattering spectrometry data showing the (a-e) top of the bismuth peak, and (f-j) the oxygen resonance peak for the (a, f) $Bi_{0.90}Fe_{0.98}O_{2.49}$, (b, g) $Bi_{0.92}Fe_{0.98}O_{2.67}$, (c, h) $Bi_{0.92}Fe_{0.98}O_{2.70}$, (d, i) $Bi_{1.01}Fe_{0.98}O_{2.97}$, and (e, j) $Bi_{1.04}Fe_{0.98}O_{3.00}$ heterostructures, respectively.

Figure 5.12. (a) Leakage response of, for example, a stoichiometric $Bi_{0.92}Fe_{0.98}O_{2.77}$ heterostructure with 6% ∇[Bi] and 5% ∇[O] grown on 0.5% Nb:$SrTiO_3$ which exhibits ohmic conduction

$(d(\ln(J))/d(\ln(V)) = 1$, inset) in the negative bias regime, indicating *n*-type conduction as per (b) the predicted band diagram for this system.

Figure 5.13. Current-voltage characteristics for heterostructures of (a) varying average [Bi] but little to no ∇[Bi], and (b) little to no change in average [Bi] but varying ∇[Bi]. (c) Schottky emission and (d) Poole-Frenkel ($r = 1$, solid lines) and modified Poole-Frenkel ($r = 2$, dashed lines) emission fits for heterostructures with varying average [Bi] but little to no ∇[Bi] as shown in part (a). (e) Schottky emission and (f) Poole-Frenkel ($r = 1$, solid lines) and modified Poole-Frenkel ($r = 2$, dashed lines) emission fits for heterostructures with little to no change in average [Bi] but varying ∇[Bi] as shown in part (b). In all cases, the lines show the slope required to produce a $\varepsilon_{opt} = 6.25$.

Figure 5.14. Derivatives of J *vs.* E for (a) $Bi_{0.90}Fe_{0.98}O_{2.49}$, $Bi_{1.01}Fe_{0.98}O_{2.97}$ and $Bi_{1.04}Fe_{0.98}O_{3.00}$, and (b) $Bi_{0.90}Fe_{0.98}O_{2.49}$, $Bi_{0.92}Fe_{0.98}O_{2.67}$, and $Bi_{0.92}Fe_{0.98}O_{2.70}$ heterostructures. Neither set of variants exhibits ohmic conduction $(d(ln(J))/d(ln(E)) = 1)$ or space-charge limited conduction $(d(ln(J))/d(ln(E)) = 2)$.

Figure 5.15. Ferroelectric hysteresis loops measured at 0.1, 1, and 10 kHz for (a) $Bi_{0.90}Fe_{0.98}O_{2.49}$, (b) $Bi_{0.92}Fe_{0.98}O_{2.67}$, (c) $Bi_{0.92}Fe_{0.98}O_{2.70}$, (d) $Bi_{1.01}Fe_{0.98}O_{2.97}$, and (e) $Bi_{1.04}Fe_{0.98}O_{3.00}$ heterostructures. (f) Frequency-dependence of dielectric permittivity (left axis) and loss tangent (right axis) for all heterostructures (colors match other data).

Figure 6.1. Rutherford backscattering spectrometry studies for (a) high-pressure O_2, (b) high-pressure O_2/Ar, and (c) low-pressure O_2 heterostructures with the corresponding best fit chemistry as obtained from the software package SIMNRA.

Figure 6.2. (a) $\omega - 2\theta$ X-ray diffraction scans of high-pressure O_2 (top), high-pressure O_2/Ar (middle), and low-pressure O_2 (bottom) heterostructures. (b) Rocking curves about the 002-diffraction conditions of film (left) and substrate (right) for high-pressure O_2 (FWHM=0.038°), high-pressure O_2/Ar (FWHM=0.045°), and low-pressure O_2 (FWHM=0.368°) heterostructures; substrate rocking curves are also shown for comparison (FWHM = 0.023-0.026°). (c) Leakage current density as a function of DC electric field, and (d) ferroelectric polarization-electric field hysteresis loops measured at 10 kHz for high-pressure O_2, high-pressure O_2/Ar, and low-pressure O_2 heterostructures.

Figure 6.3. (a) $\omega - 2\theta$ X-ray diffraction scans, (b) ω-scans (rocking curves) about the 002-diffraction conditions of film and substrate, (c) current density *vs.* DC electric field, and (d) ferroelectric polarization-electric field hysteresis loops measured at 10 kHz for a low-pressure O_2 heterostructure before (in the as-grown state) and after annealing in an oxygen pressure of 760 Torr for 3 hours at 600°C.

Figure 6.4. (a) SRIM simulation of He^{2+} concentration as a function of depth, suggesting that essentially no He^{2+} ions are implanted into the film, but instead the vast majority of the ions are stopped at a depth of ≈ 13.5 μm into the $SrTiO_3$ substrate, due to high incident energy of the ions (3.04 MeV). (b) SRIM simulation of induced defect concentrations as a function of depth in $PbTiO_3$ layer.

Figure 6.5. Rutherford backscattering spectrometry data for a heterostructure grown in high-pressure O_2 (a) before and (b) after He^{2+} ion bombardment with a dose of 10^{16} ions cm^{-2}. No overall change of chemistry is detected as a result of ion bombardment.

Figure 6.6. (a) Rocking curves of a high-pressure O_2 heterostructure as a function of He^{2+} bombardment dose obtained about the 002-diffraction condition; the bottom rocking curve is for a low-pressure O_2 heterostructure for comparison. LAADF-STEM and HAADF-STEM images of (b), (c) high-pressure O_2, (d), (e) He^{2+} bombarded, high-pressure O_2 (dose of 10^{16} ions cm^{-2}), and (f), (g) low-pressure O_2 heterostructures, respectively.

Figure 6.7. $\omega - 2\theta$ X-ray diffraction scans of high-pressure O_2, high-pressure O_2-bombarded (dose of 3.33×10^{15} ions cm^{-2}), and low-pressure O_2 heterostructures. Both *in situ* and *ex situ* bombardment of the heterostructures result in slight expansion of the out-of-plane lattice parameter.

Figure 6.8. (a) Leakage current density as a function of DC electric field for a high-pressure O_2 heterostructure which is progressively He^{2+} bombarded with the noted doses. (b) Ferroelectric polarization-electric field hysteresis loops measured at 10 kHz for the same high-pressure O_2 heterostructures after various He^{2+} bombardment doses. (c) Nyquist plots of Z_{Img} *vs.* Z_{Real} for high-pressure O_2, He^{2+} bombarded, high-pressure O_2 (dose of 10^{16} ions cm^{-2}), and low-pressure O_2 heterostructures. The presence of one semicircle in all heterostructures reveals a single transport mechanism while the magnitude of resistance (extracted from the intercept of the semicircles on the real axis) varies as noted.

Figure 6.9. Deep-level transient spectroscopy signal measured at five different time windows for (a) high-pressure O_2, (b) low-pressure O_2, and (c) He^{2+} bombarded, high-pressure O_2 (dose of 10^{16} ions cm^{-2}) heterostructures. Arrhenius plots of $ln(J)$ *vs.* $1000/T$ at different voltages for (d) high-pressure O_2, (e) low-pressure O_2, and (f) He^{2+} bombarded, high-pressure O_2 (dose of 10^{16} ions cm^{-2}) heterostructures. The activation energies (noted) are extracted from the slope of the linear fits.

Figure 6.10. Arrhenius plot of $\ln(\frac{T_m^2}{e(T_m)})$ *vs.* $\frac{1000}{T_m}$. The activation energy of each trap state is extracted from the slope of the linear fits.

Figure 6.11. Forward bias room temperature current-voltage data represented on the standard Schottky and Poole-Frenkel plots for (a) high-pressure O_2, (b) low-pressure O_2, and (c) He^{2+} bombarded, high-pressure O_2 (dose of 10^{16} ions cm^{-2}) heterostructures. The data shows good linear fit (red lines) to both mechanisms at high electric fields, but only Poole-Frenkel fits give reasonable values of optical dielectric constant (extracted from the slope of linear fits). Temperature dependence of the current-voltage characteristics in a Poole-Frenkel plot for (d) high-pressure O_2, (e) low-pressure O_2, and (f) He^{2+} bombarded, high-pressure O_2 (dose of 10^{16} ions cm^{-2}) heterostructures.

Figure 7.1. (a) Wide angle $\omega - 2\theta$ X-ray diffraction scans and (b) zoom-in about the 002- and 220-diffraction conditions for heterostructures ion bombarded with various He^{2+} doses. (c) Rocking curves for heterostructures ion bombarded with various He^{2+} doses obtained about the 002-diffraction conditions of film and substrate. (d) Leakage current density as a function of DC

electric field, and (e) ferroelectric polarization-electric field hysteresis loops measured at 1 kHz after ion bombardment with various He^{2+} doses.

Figure 7.2. Rutherford backscattering spectrometry studies before and after He^{2+} ion bombardment with a dose of 10^{16} ions cm^{-2}. The corresponding best fit chemistries are obtained from SIMNRA.

Figure 7.3. (a) SRIM simulation of He^{2+} concentration as a function of depth, suggesting that essentially no He^{2+} ions are implanted into the film, but instead the vast majority of ions are stopped at a depth of ≈ 15 µm into the $DyScO_3$ substrate, due to high incident energy of the ions (3.04 MeV). (b) SRIM simulation of induced defect concentrations as a function of depth in $BiFeO_3$ layer.

Figure 7.4. (a) Nyquist plots of Z_{Img} *vs.* Z_{Real} for heterostructures ion bombarded with various He^{2+} doses suggesting a single transport mechanism dominated by the bulk of the film with increasing resistance (extracted from the intercept of the semicircles on the real axis) with increasing dose. Arrhenius plots of $\ln(J)$ *vs.* $1000/T$ at different voltages for (b) as-grown (no bombardment), (c) 10^{15} ions cm^{-2}, and (d) 10^{16} ions cm^{-2} heterostructures. The activation energies (noted) are extracted from the slope of the linear fits. The range of activation energies corresponds to small variation in the slope of the linear fits at different voltages. (e) Deep-level transient spectroscopy signal measured at the same rate window (80-160 ms) for heterostructures bombarded with various He^{2+} doses. Inset shows the Arrhenius plot of $\ln(\frac{T_m^2}{e(T_m)})$ *vs.* $\frac{1000}{T_m}$. The activation energy of each trap state is extracted from the slope of the linear fits.

Figure 7.5. Nyquist plots of Z_{Img} *vs.* Z_{Real} for heterostructures bombarded with (a) zero (as-grown), (b) 10^{15} ions cm^{-2}, and (c) 10^{16} ions cm^{-2} He^{2+} doses. The scattered points correspond to the experimental data, and the bold lines to the fittings.

Figure 7.6. (a) Derivatives of J *vs.* E for heterostructures bombarded with various He^{2+} doses. Neither of the heterostructures exhibits ohmic conduction ($d(\ln(J))/d(\ln(E)) = 1$) or space-charge limited conduction ($d(\ln(J))/d(\ln(E)) = 2$). Positive bias room temperature current-voltage data represented on the standard (b) Schottky and (c) Poole-Frenkel plots for heterostructures bombarded with various He^{2+} doses. Dashed lines show the fits using the reported values of optical dielectric constant for $BiFeO_3$ ($\varepsilon_{opt} = 6.25$).

Figure 7.7. Temperature dependence of the current-voltage characteristics (in positive bias) measured in the temperature range of 25-175°C for (a) as-grow (no bombardment), (b) 10^{15} ions cm^{-2}, and c) 10^{16} ions cm^{-2} He^{2+} dose heterostructures.

Figure 7.8. Deep-level transient spectroscopy signal measured at five different time windows, for heterostructures bombarded with He^{2+} doses of (a) zero (as-grown), (b) 10^{15} ions cm^{-2}, and (c) 10^{16} ions cm^{-2}.

Figure 7.9. Current density *vs.* applied electric field for an as-bombarded (10^{16} ions cm^{-2}) $BiFeO_3$ heterostructure which is cumulatively annealed for 15 minutes at various progressively increasing temperatures. Conduction is seen to increase after annealing at above 400°C.

Figure 7.10. (a) Ferroelectric polarization-electric field hysteresis loops measured at 10 kHz after ion bombardment with various He^{2+} doses. (b) Switching speed as a function of electric field for heterostructures ion bombarded with various He^{2+} doses. Inset shows the plot of $\ln(\vartheta)$ *vs.* $1/E$.

The activation energies are extracted from the linear fits. The minor loops measured between the negative saturation field and various reversal fields for (c) as-grown (no bombardment) and (d) 10^{16} ions cm^{-2} heterostructures. (e) The first-order reversal curve distributions for the as-grown (no bombardment) and 10^{16} ions cm^{-2} heterostructures.

Figure 7.11. Vertical (left) and lateral (right) piezoresponse force microscopy amplitude for the heterostructures bombarded with He^{2+} doses of zero (top) and 10^{16} ions cm^{-2} (bottom).

Figure 7.12. Switching polarization as a function of pulse width, under various voltages, measured at room temperature for (a) as grown heterostructures, and heterostructures bombarded with doses of (b) 10^{15} ions cm^{-2}, and (c) 10^{16} ions cm^{-2}. The solid lines show the fitting results using the Kolmogorov-Avrami-Ishibashi model (the fitting parameters are presented in Table 7.1).

Figure 8.1. (a) Wide angle $\omega - 2\theta$ X-ray diffraction scans on as-grown heterostructures. (b) Rutherford backscattering spectrometry studies on the as-grown heterostructures. The corresponding fits are obtained from SIMNRA.

Figure 8.2. (a) SRIM simulations of the induced defect concentrations as a function of depth in the ferroelectric layer. (b) SRIM simulations of He^{+} concentration as a function of depth, suggesting that He^{+} ions are implanted into the ferroelectric layer. Range of ions is calculated to be around 240 nm. (c) SRIM simulations of the total concentration of the implanted helium ions in the ferroelectric layer in comparison to the total initial concentration of *intrinsic* point defect.

Figure 8.3. Atomic force microscopy images for (a) as-grown, and (b) bombarded (dose of 10^{15} ions cm^{-2}) regions.

Figure 8.4. A polarization-electric field hysteresis loop measured on an as-grown capacitor.

Figure 8.5. (a) Polarization-electric field hysteresis loops for capacitors exposed to bombardment doses in the range of 10^{12}-10^{15} ions cm^{-2}. (b) Evolution of the ferroelectric switching characteristics including the saturation polarization, coercive field, and imprint with ion dose. (c) Evolution of the extracted defect-pinning energy as a function of ion dose; inset shows the evolution of the switching speed as a function of inverse electric field with ion dose. The pinning energy is extracted from the slope of the linear fits. (d) Evolution of the coercive field as a function of defect concentration; inset shows mathematical relationship between defect concentration and coercive field.

Figure 8.6. Switching polarization as a function of pulse width and under various voltages, measured at room temperature for heterostructures bombarded (a-f) in the low-dose regime (zero-2.2×10^{13} ions cm^{-2}–data in shades of gray), (g-i) in the intermediate-dose regime (2.2×10^{13}-2.2×10^{14} ions cm^{-2}–data in shades of blue), and (j-l) in the high-dose regime (2.2×10^{14}-10^{15} ions cm^{-2}–data in shades of red). The symbols show the measured values, while the solid lines show the fitting results using the Kolmogorov-Avrami-Ishibashi model (the fitting parameters can be found in Table 8.1).

Figure 8.7. Polarization-electric field hysteresis loops for capacitors exposed to various ion-bombardment procedures including (a) as-grown (grey region) and 2.2×10^{14} ions cm^{-2} (blue region) resulting in symmetric two-step switching, (b) 2.2×10^{14} ions cm^{-2} (blue region) and 4.6×10^{14} ions cm^{-2} (red region) resulting in asymmetric two-step switching, and (c) as-grown (no bombardment, grey region), 2.2×10^{14} ions cm^{-2} (blue region), and 4.6×10^{14} ions cm^{-2} (red region)

resulting in three-step switching. Focusing on the capacitors in (c), subsequent (d) PUND studies reveal the pathway to the different polarization states at a constant pulse width of 0.1 ms, (e) the ability to deterministically switch between the different polarization states, and (f) the long-term retention and stability of the multiple polarization states.

Figure 8.8. Polarization-electric field hysteresis loops taken between a negative saturation field and various positive reversal fields for (a) as-grown and (b) 4.6×10^{14} and 7.0×10^{14} ions cm^{-2} two-region ion-bombarded capacitors. Analysis of the first-order reversal curve data reveals the distribution of elementary switchable units over their coercive and bias fields for the (c) as-grown and (d) 4.6×10^{14} and 7.0×10^{14} ions cm^{-2} two-region ion-bombarded capacitors.

Figure 8.9. (a) Schematic of the probing waveform used for band excitation piezoresponse spectroscopy measurements. The piezoresponse was measured at remanence. (b) Schematic of the entire region studied herein (Top) including the doses used in each area, as well as the phase response at different voltages (V_0, V_1, V_2, and V_3) showing the step-by-step nature of the switching. (c) Average piezoresponse loops extracted from each region in (b). (d) The extracted work of switching (defined as the area within the piezoelectric loops) for each region. Piezoresponse force microscopy phase images of a given area in (e) as-poled ($-V_3$), (f) partially switched ($+V_1$), and (g) fully switched states showing the ability to determinisitically write defects to produce arbitrary 180° ferroelectric domain structures.

Figure 8.10. (a) Piezoresponse amplitude as extracted from piezoresponse force microscopy studies and (b) dielectric permittivity (constant) as a function of applied bias for as-grown capacitors. (c) Piezoresponse amplitude as extracted from piezoresponse force microscopy studies and (d) dielectric permittivity (constant) as a function of applied bias for 10^{15} ions cm^{-2} ion-bombarded capacitors.

Figure 9.1. (a) SRIM simulation of induced defects concentration as a function of depth in $0.68PbMg_{1/3}Nb_{2/3}O_3$-$0.32PbTiO_3$ layer. (b) SRIM simulation of He^{2+} concentration as a function of depth, suggesting that essentially no He^{2+} ions are implanted into the film, but instead the vast majority of ions are stopped at a depth of $\approx$ 14.5 μm into the $NdScO_3$ substrate, due to high incident energy (3.04 MeV) of the ions.

Figure 9.2. (a) Wide angle $\omega - 2\theta$ X-ray diffraction scans for heterostructures bombarded with various ion doses. (b) Zoom-in of $\omega - 2\theta$ scans about the 002- and 220-diffraction conditions. (c) Rocking curves for heterostructures bombarded with various doses obtained about the 002- and 220-diffraction conditions of film and substrate.

Figure 9.3. (a) Room-temperature dielectric permittivity (filled squares) and loss (open squares) as a function of frequency for heterostructures bombarded with various ion doses. (b) Dielectric permittivity as a function of ion dose extracted at various frequencies (0.1-1000 kHz). (c) Dielectric permittivity as a function of temperature and frequency (0.3-300 kHz) for heterostructures bombarded with various ion doses. (d) Extracted values of T_{max} as a function of ion dose at various frequencies (0.3-300 kHz).

Figure 9.4. (a-e) Two-dimensional reciprocal space mapping studies and KL-cuts about the 002-diffraction conditions of $0.68PbMg_{1/3}Nb_{2/3}O_3$-$0.32PbTiO_3$ for heterostructures bombarded with various ion doses. (f) Diffuse-scattering intensity profiles extracted along [011] direction for various ion doses.

Figure 9.5. (a-f) Polarization-electric field hysteresis loops measured at a frequency of 10 kHz at 77 K and 293 K for heterostructures bombarded with various ion doses. (g) Width of the hysteresis loops extracted as a function of temperature for heterostructures bombarded with various ion doses. (h) Width of the hysteresis loops as a function of ion dose extracted at 77 K and 293 K. (i) Horizontal shift of the hysteresis loops as a function of ion dose extracted at 77 K and 293 K.

Figure 9.6. (a) Plot of modified Curie-Weiss law ($log\,(\frac{1}{\varepsilon}-\frac{1}{\varepsilon_{max}})$ *vs.* $log\,(T-T_{max})$) for heterostructures bombarded with various ion doses. The critical exponent γ is extracted from the slope of the linear fits (inset). (b) Vogel-Fulcher plot ($\ln(f)$ *vs.* T_{max}) for heterostructures bombarded with various ion doses. Solid squares and lines correspond to experimental data and fittings, respectively. (c) Vogel-Fulcher parameters extracted from fits of the experimental data for various ion doses.

Figure 10.1. Polarization-electric field hysteresis loops obtained from a $PbZr_{0.2}Ti_{0.8}O_3$ thin film in the (a) as-grow state, and (b) after high-energy helium-ion bombardment to a dose of 3.3×10^{15} ions cm^{-2}.

Figure 10.2. A schematic of a pyroelectric Olsen cycle showing various isothermal and isoelectric processes.

Figure 10.3. Ferroelectric polarization-electric field hysteresis loops as a function of temperatures, and (b) saturation polarization as a function of temperature for a $PbZr_{0.2}Ti_{0.8}O_3$ thin film.

Figure B.1. Schematic illustration of work flow for band excitation piezoresponse spectroscopy. (a) Schematic of the sampling, and fast and slow scan direction used for imaging. (b) Example of band excitation chirp waveform in time domain used to excite the tip at a range of frequencies. (c) Triangular switching waveform used to locally switch the film. (d) Schematic drawing of a cantilever in contact with surface. (e) Typical cantilever resonance response shown in frequency domain. Red dashed line shows the fit, based on Equations B.1 and B.2. (f) Typical piezoelectric hysteresis loop obtained from band excitation piezoresponse spectroscopy.

LIST OF TABLES

Table 5.1. Summary of data including growth conditions, final chemical formula of heterostructure, [Bi]/[Fe] ratio, ∇[Bi], [O]/[Fe] ratio, and ∇[O].

Table 7.1. The Kolmogorov-Avrami-Ishibashi fitting parameters t_s (characteristic switching time), and n_s (effective geometric dimension) used in fitting of the switching data in Figure 7.12, as a function of electric field for heterostructures bombarded with varying He^{2+} ion doses.

Table 8.1. Kolmogorov-Avrami-Ishibashi fitting parameters t_s (characteristic switching time) and n_s (effective geometric dimension) used in fitting of the switching data in Figure 8.6, as a function of electric field for heterostructures bombarded with varying He^{+} ion doses.

Table A.1. Summary of optimized growth conditions for various materials used in this work.

LIST OF ABBREVIATIONS

AC	Alternating current
DC	Direct current
FWHM	Full-width at half-maximum
HAADF-STEM	High-angle annular dark-field scanning transmission electron microscopy
LAADF-STEM	Low-angle annular dark-field scanning transmission electron microscopy
PUND	Positive-up-negative-down
SRIM	Stopping and range of ions in matter
STEM	Scanning transmission electron microscopy
TRIM	Transport of ions in matter

LIST OF SYMBOLS

A	Capacitor area
A	Amplitude of response – Band excitation piezoresponse spectroscopy
A_0	Resonance amplitude – Band excitation piezoresponse spectroscopy
A^*	Effective Richardson's constant
a_{1-2}	Saturation amplitude – Band excitation piezoresponse spectroscopy
a_3	Linear contribution – Band excitation piezoresponse spectroscopy
b_{1-4}	Loop sharpness – Band excitation piezoresponse spectroscopy
b_{5-6}	Loop transition parameter – Band excitation piezoresponse spectroscopy
b_{7-8}	Transition midpoint – Band excitation piezoresponse spectroscopy
C	Capacitance
c	Curie constant – Curie-Weiss law
c	Constant – Modified Curie-Weiss law
D	Electric displacement
d	Film thickness
d_{ijk}	Piezoelectric coefficient
d_z	Out-of-plane spacing between crystal planes – X-ray diffraction
E	Electric field
E_a	Activation energy for cooperative transition between different polarization configurations in a relaxor – Vogel-Fulcher relation
E_C	Coercive field
E_C^+	Positive coercive field
E_C^-	Negative coercive field
$\bar{E}_C$	Average coercive field
E_{C0}	Threshold electric field at 0 K above which pinning-depinning transition occurs – Switching kinetics
E_{dis}	Displacement energy of a lattice atom
E_d	Activation energy of a trap state
E_G	Band gap
E_i	Electrical imprint
E_{ion}	Energy of an ion beam
E_n	Energy loss of a particle in primary and secondary nuclear collisions
E_r	Reversal field – First-order reversal curve analysis
e	Emission rate of a trap state

F Pinning strength of a defect
F_D Domain wall area
f Frequency
f_0 Limiting response frequency of dipoles – Vogel-Fulcher relation
G Gibbs free energy
g_0 Geometrical factor depending on the angle between the electric field and polarization
H Enthalpy of defect formation
h Planck's constant
I Electric current
I^e Experimental data – Rutherford backscattering spectrometry
I^f Fitted data – Rutherford backscattering spectrometry
J Current density
k Constant – Scattering cross section relation for electronic stopping
k_B Boltzmann's constant
L_0 Average distance between points of zero force encountered by a domain wall
L_3 Average distance between domain walls
M Atomic mass
m^* Effective electron mass
m_0 Free-electron mass
N Atomic density
N_C Density of states in the conduction band
N_{dis} Density of displaced ions
n Optical refractive index
n Free carrier concentration – Transport
n Order of reflection – X-ray diffraction
n_d Density of defects
n_s Geometric dimension – Switching kinetics
P Polarization
P_r^+ Positive remanent polarization
P_r^- Negative remanent polarization
$\bar{P}_r$ Average remanent Polarization
P_s Spontaneous polarization
P_{sat}^+ Positive saturation polarization
P_{sat}^- Negative saturation polarization
$\bar{P}_{Sat}$ Average saturation polarization
P_{sw} Switched polarization – Switching kinetics

P_{ns}	Unswitched polarization – Switching kinetics
Q	Quality factor – Band excitation piezoresponse spectroscopy
q	Electronic charge
$q\phi_T$	Trap energy level – Poole-Frenkel conduction
R	Resistance
R^2	Accuracy of fits extracted from least-squares method – Rutherford backscattering spectrometry
R_{ion}	Average range of ions
r	Exponential scaling constant – Poole-Frenkel conduction
r_A	Radius of *A*-site cations in an ABO_3 perovskite oxide
r_B	Radius of *B*-site cations in an ABO_3 perovskite oxide
r_O	Radius of oxygen ions in an ABO_3 perovskite oxide
S	Entropy
S_{config}	Configurational entropy
S_e	Scattering cross section for electronic stopping
S_n	Scattering cross section for nuclear stopping
S_{vib}	Vibrational entropy
T	Temperature
T_0	Curie-Weiss temperature – Curie-Weiss law
T_b	Burns temperature – relaxor ferroelectrics
T_C	Curie temperature
T_F	Freezing temperature – relaxor ferroelectrics
T_m	Temperature of peak maximum – Deep-level transient spectroscopy
T_{max}	Temperature of the maximum dielectric permittivity – relaxor ferroelectrics
t	Time
t_G	Goldschmidt's tolerance factor
t_R	Retention time
t_s	Characteristic switching time – Switching kinetics
U	Energy barrier for switching in creep motion – Switching kinetics
V	Voltage
V_{DC}	DC Voltage
W	Thermodynamic probability
X	Mechanical stress
X_{ion}	Path length of ions
x	Mechanical strain
Z	Atomic number

Z Impedance – Impedance spectroscopy

Z_{Img} Imaginary part of total impedance – Impedance spectroscopy

Z_{Real} Real part of the total impedance – Impedance spectroscopy

ΔT_{disp} Frequency dispersion of dielectric maximum temperature – relaxor ferroelectrics

γ Pre-exponential factor – Deep-level transient spectroscopy

γ Critical exponent related to diffuseness of phase transitions – Modified Curie-Weiss law

δ Dielectric loss

ε Dielectric permittivity

ε_0 Dielectric permittivity of free space

ε_{max} Maximum dielectric permittivity – relaxor ferroelectrics

ε_{opt} Optical dielectric constant

ε_r Dielectric constant or relative dielectric permittivity

θ Phase of response – Band excitation piezoresponse spectroscopy

θ Angle between incident beam and normal to the lattice planes – X-ray diffraction

θ_B Bragg angle – X-ray diffraction

θ_s Velocity exponent – Switching kinetics

λ Wavelength of X-rays – X-ray diffraction

μ Free-carrier mobility

μ_s Dynamical exponent for switching in creep motion – Switching kinetics

π Pyroelectric coefficient

ρ Intensity of contour plots – First-order reversal curve analysis

σ Electrical conductivity

σ_{1-2} Loop fitting parameter – Band excitation piezoresponse spectroscopy

σ_c Capture cross section of a deep trap state – Deep-level transient spectroscopy

τ Time constant – Impedance spectroscopy

φ Phase difference between current and voltage – Impedance spectroscopy

φ Rotation angle – Band excitation piezoresponse spectroscopy

ω Angle between X-ray source and sample – X-ray diffraction

ω Angular frequency – Impedance spectroscopy

ω Angular frequency – Band excitation piezoresponse spectroscopy

ω_0 Resonance frequency – Band excitation piezoresponse spectroscopy

ω_{max} Angular frequency at maximum of a semicircle in complex-impedance plane – Impedance spectroscopy

ϑ Switching speed – Switching kinetics

ϕ_B Schottky barrier height

Γ_{1-2} Top and bottom loop branches – Band excitation piezoresponse spectroscopy

CHAPTER 1

Motivation and Outline

This Chapter introduces the motivation, overall goals, and organization of this Thesis. It briefly summarizes the scientific and technological opportunities which can be brought about by establishing defect-engineering techniques in complex-oxide ferroelectric thin films and aims to motivate the need for systematic studies of defect-structure-property relations in these systems. The central questions and overall outline of the Thesis are provided at the end of this Chapter.

1.1 Motivation

Next-generation technologies will increasingly call upon advanced, non-traditional materials with novel properties and geometries to satisfy the desire for multi-functionality. Among the many systems considered, complex-oxide ferroelectric thin films have been extensively pursued due to their unique properties, structures, and functionalities which are not available in traditional systems [1]. The existence of a spontaneous switchable polarization and strong coupling between thermal, mechanical, electrical, and optical responses in complex-oxide ferroelectric thin films provide a rich spectrum of properties and functionalities which can be harnessed for a diverse range of applications and have driven considerable research in materials science and condensed matter physics over the past decades [2-5]. Engineering the response of these systems, however, is a challenging task due to the presence of such highly-coupled susceptibilities and their complex structural and chemical nature. Achieving exacting control of these exotic and complex systems, therefore, requires a deep understanding of their physics and all factors that impact their properties, and development of the know-how to synthesize and process such materials in a deterministic manner. Such understanding and control, in turn, can pave the way to, at a minimum, marked improvements in device reliability and consistency and, in the future, to enhanced properties, new modes of response, and emergent functions in these materials that will, in turn, expand their application in modern technologies.

The properties of complex-oxide ferroelectric thin films are sensitive to perturbations from chemistry, mechanical strain, structural defects, and more. This sensitivity to external factors, in turn, provides a number of routes by which to engineer new functionalities, and provides an enormous phase space for materials design [2-8]. Conventionally, two main approaches have been undertaken for property control in complex-oxide ferroelectrics including chemical modification and strain engineering. Chemical alloying has been extensively used as an effective means for tailoring the structure and properties of ferroelectrics [9-12]. By exploiting the flexibility of chemical modifications in perovskite oxides, for example, a large number of ferroelectric compounds have been developed. Chemical alloying and substitution with elements of different valences and/or sizes have been used to control the crystal structure, nature of phase transitions, and phase competitions (*e.g.*, $PbZr_xTi_{1-x}O_3$, $Ba_{1-x}Sr_xTiO_3$), to control the degree of ordering and relaxor behavior (*e.g.*, $PbMg_{1/3}Nb_{2/3}O_3$, $PbSc_{1/2}Nb_{1/2}O_3$), and in turn, to achieve a wide variety of physical properties (*i.e.*, ferroelectric, dielectric, piezoelectric, pyroelectric, *etc.*) [9-12]. Ferroelectric ceramics and thin films are also often doped with the goal of tailoring their properties for specific applications [9-12]. The $PbZr_xTi_{1-x}O_3$ system, for example, is rarely used in its chemically pure form and acceptor- and donor-doping give rise to the so-called hard and soft compositions, with largely modified ferroelectric, piezoelectric, dielectric, and electrical conduction properties.

The other commonly-used approach for controlling the properties and phase evolution in complex-oxide ferroelectrics focuses on the application of a pressure in bulk materials or an epitaxial strain (tensile or compressive) in thin films [2-4,13-15]. Crystal structure and symmetry, stability of phases, the nature, sequence, and diffuseness of phase transitions, critical temperatures, ferroelectric order, polarization values and domain structures, as well as functional properties such as dielectric permittivity and piezoelectric response can be largely tuned via strain engineering [16-21]. Epitaxial thin films, compared to bulk ferroelectrics, provide for the ability to apply considerably larger strains. In thin-film epitaxy, the thin-film-strain state can be tuned through the use of a range of available single-crystal substrates [3]. The biaxial strain imposed by the lattice

misfit between the film and the single-crystalline substrate onto which the films is epitaxially grown provides extra degrees of freedom to tune the behavior of ferroelectrics. Recent advances in thin-film growth have paved the way for the synthesis of high-quality ferroelectric thin-film heterostructures and superlattices with atomically-sharp interfaces and unit-cell-level thickness control and, in turn, have resulted in rapid advances in strain engineering [3,4,14,15].

Despite such spectacular advances in chemical modification and strain engineering of ferroelectrics, the search for additional knobs for property control remains an ongoing effort. This continued effort stems from the limitations in controlling the strain and chemistry. For example, the degree of freedom in tailoring the properties of ferroelectrics by chemical alloying is limited by the solid solubility of the chemical elements, as well as by the simultaneous changes in the ferroelectric properties (*e.g.*, reduction in polarization) [11]. The ability to engineer ferroelectrics using thin-film epitaxy, on the other hand, is limited by the availability of the lattice matched commercial substrates, and strain relaxational processes which arise at high magnitudes of strain. This work, therefore, focuses on defect engineering as an additional and novel route to understanding and tailoring the properties of ferroelectric thin films with an aim to satisfy the ever-increasing need for finely-controlled materials with enhanced responses and novel functions.

Similar to any material system, imperfections or defects (including point and extended defects) are known to strongly impact the structural, chemical, electronic, dielectric, thermal, and other properties of ferroelectrics [12,22,23]. This interplay between defects and properties, however, has been long regarded as deleterious to the performance of ferroelectric materials and related devices. The presence of defects, for example, is regularly blamed for the degradation of performance by increasing leakage, reducing polarization, increasing switching voltages, inducing fatigue, exacerbating aging, and prompting imprint [12]. As a result of this negative connotation, defects are generally considered to be "bad guys" to avoid in the ferroelectric world, and immense efforts have attempted to either minimize their concentration or to counterbalance their detrimental impact through brute-force approaches such as chemical alloying [9,11,12,23].

What has not been undertaken, however, is an approach akin to that applied in other material systems wherein the properties of a material are deterministically altered by controlled introduction of specific defects. In the semiconductor industry, for example, "defects" – lovingly called dopants in a successful rebranding effort – underpin the modern electronic materials we all rely upon. There, years of development have gone into the production of large-scale, high-purity crystals with extremely low concentrations of defects. These high-quality crystals, however, have limited utility in their pristine state. Instead, once wiped clean of defects, engineers rely on their ability to deliberately "dope" defects back, often with subpart-per-million level of control, to precisely control properties such as conductivity [24-26]. Such an approach in ferroelectrics has not yet been thoroughly embraced. This is not to say that there are not researchers and engineers (in both research laboratories and industry) that do not understand, control, and utilize defects in some shape or form, but that this approach to deterministically use defects to improve material function and performance is not pervasive in the ferroelectrics community.

Defect engineering in ferroelectric world has remained underdeveloped mainly due to the complex nature of the structure and chemistry and the resulting difficulties in the characterization and control of defects in these materials [23]. Complex-oxide ferroelectrics, for example, have many constituent elements and possess more diversified crystal structures compared to elemental/binary semiconductors. In turn, they can accommodate a wider variety of defects, including *intrinsic* (*i.e.*, related to the constituent elements) and *extrinsic* (*i.e.*, related to the

impurities and/or dopants) point defects, point-defect complexes and clusters, line defects, and planar and volume defects. Also, complex-oxide ferroelectrics have a strong penchant for defects because of relatively low energy barrier of formation and because they are readily formed to maintain charge neutrality (to compensate for impurities that are often present in the source materials and/or off-stoichiometry) due to the ionic nature of these systems [27,28]. Finally, there has not been a need or strong driving force to accomplish the same exacting chemical control in these materials, and even the source materials are generally many orders of magnitude less pure than semiconductor sources. As a result, state-of-the-art defect and composition control has been limited to ≈ 1 atomic percent in many complex-oxide thin films – far from the parts-per-billion control in semiconductors.

This is exacerbated by the fact that there are few characterization methods that reliably probe these complex defect structures, and those that do exist are not (generally) widely applied within the ferroelectric community. Researchers have used theoretical, modeling, and computational approaches to study defects in these materials, but they require considerable computational resources and have been limited to a few model systems where the approaches, potentials, and parameters are fairly well-known. As a result, a detailed description of defect structures and predictions of their impact on materials behavior remains a challenging and time-consuming task [23].

All told, these challenges have limited the advance of defect engineering in ferroelectrics. Defects are often created in an uncontrolled fashion giving rise to unwanted and detrimental effects. Establishing routes for intentional and purposeful introduction of defects, therefore, is crucial for advancing defect engineering in ferroelectrics and presents an opportunity to make use of defects rather than being limited by them. In this Thesis, I show that the existence of strong defect-structure-property relations in complex-oxide ferroelectric thin films can provide a powerful tool for materials engineering and introduces new routes to novel or enhanced properties and function, provided that pathways are identified for the type, concentration, and location of defects to be closely controlled [29- 34]. This Thesis, therefor, aims to redefine the role of defects in ferroelectrics from "bad guys" to "good guys." In this new role, defects are viewed as a tool for tailoring and enhancing the properties, designing better materials, and even enabling new and emergent functionalities.

1.2 Central Questions and Organization of the Dissertation

This Thesis focuses, primarily, on the study of *intrinsic* point defects (*i.e.*, vacancies, interstitial, and substitutional defects related to the constituent elements, and their complexes and clusters) in pulsed-laser deposited complex-oxide ferroelectric thin films. This Thesis aims to achieve the following goals:

1- To establish novel synthesis, processing, and characterization routes for the deterministic control of type, concentration, and location of point defects. Two main approaches are used in this work for on-demand control of such defects:

   a) *In situ* approaches: to control the defects during the synthesis process using energetics of the growth; and

   b) *Ex situ* approaches: to control the defects after the synthesis process using energetic ion beams.

2- To use the on-demand and controlled introduction of point defects in order to enable systematic studies of defect-structure-property relations. The physics of the interplay between various types of *intrinsic* point defects and materials response, including transport properties, ferroelectric switching, and dielectric response are studied as a function of defect concentration and type (including off-stoichiometric defects and stoichiometric displacement defects (*i.e.*, bombardment-induced defects) in the form of isolated point defects, defect complexes, and clusters).

3- To take advantage of this understanding and control to establish defect-engineering approaches which enable the use of defects as tools for tailoring the properties of these materials, enhancing their performance, and even engineering new and emergent functionalities.

The remainder of this Thesis will consist of the following Chapters:

Chapter 2 provides a general review of the basic concepts relevant to the ferroelectricity, related properties, materials, and devices.

Chapter 3 briefly introduces various types of point defects, and their impact on functional properties of complex-oxide ferroelectric materials.

Chapter 4 provides details of the growth and processing of ferroelectric thin-film heterostructures studied in this work and introduces basic principles of the techniques and methodologies used for control, production, and characterization of *intrinsic* point defects in those systems.

Chapter 5 focuses on the study of off-stoichiometric point defects and their impact on the chemistry, structure, electrical leakage, conduction mechanisms, and dielectric and ferroelectric response of $BaTiO_3$ and $BiFeO_3$ thin films. This Chapter focuses on an *in situ* approach for control of the type and concentration of defects, and provides examples of how various parameters such as laser fluence, laser-repetition rate, and target composition can be used for growth-induced defect creation and control. Ultimately, this Chapter provides roadmaps to achieve better control over the properties and to manipulate functionalities of these complex materials via growth-induced control of off-stoichiometric point defects.

Chapter 6 focuses on the study of stoichiometric displacement point defects and their impact on the structure, electrical leakage, and ferroelectric device performance of $PbTiO_3$ thin films. This Chapter focuses on both *in situ* and *ex situ* approaches for control of the type and concentration of defects. In this Chapter, I show that variations in growth parameters which directly impact the energetics of the growth (*e.g.*, growth pressure) can give rise to knock-on damage, and can be used for *in situ*, growth-induced creation and control of stoichiometric displacement defects. I also introduce high-energy ion bombardment as a practical technique for *ex situ* creation and control of such defects, and show that using this technique, dramatic enhancements in electrical resistivity and ferroelectric device performance can be achieved. Ultimately, this Chapter introduces new avenues for the study of defect-structure-property relations and novel opportunities for defect-induced property control and enhancement in complex-oxide ferroelectric thin films.

Chapter 7 focuses on the study of stoichiometric displacement point defects and their impact on the electrical leakage and ferroelectric switching properties of $BiFeO_3$ thin films. This Chapter focuses on *ex situ* control of the type and concentration of defects via high-energy ion bombardment. In this Chapter, I present the potential of this ion-bombardment technique for

enhancing the properties and performance of complex-oxide ferroelectric thin films by demonstrating some of the most resistive $BiFeO_3$ thin films reported to date. I also discuss the complex role of point defects in material control and design by focusing on simultaneous defect-induced changes in various properties (*e.g.*, electronic leakage and switching properties), and show that successful use of such defect-engineering routes to enhance ferroelectric device performance requires careful optimization of type and concentration of defects to maximize the positive impact of defects on some properties while minimizing their negative impact on others.

Chapter 8 introduces focused ion beams as practical *ex situ* tools for controlling the position of bombardment-induced stoichiometric point defects, in addition to control over their type and concentration. This Chapter focuses on $PbZr_{0.2}Ti_{0.8}O_3$ thin films and studies the impact of displacement point defects on the ferroelectric-polarization switching properties. In this Chapter, I show that such defect-polarization coupling can be carefully confined to select regions of the material defined by a focused-ion beam, and use this local control of ferroelectric switching as a route to elicit novel functions, namely tunable multiple polarization states, rewritable pre-determined 180° ferroelectric domain patterns, and multiple, zero-field piezoresponse and permittivity states.

Chapter 9 focuses on the study of stoichiometric displacement point defects and their impact on the properties of relaxor ferroelectric materials. This Chapter focuses on $0.68PbMg_{1/3}Nb_{2/3}O_3\text{-}0.32PbTiO_3$ relaxor thin films and demonstrates *ex situ* control of the type and concentration of point defects via high-energy ion bombardment. In this Chapter, I provide systematic experimental evidence of the defect-polarization coupling and complex effect of point defects on the evolution of local (dis)order in relaxor ferroelectrics.

Chapter 10 summarizes the findings of this Thesis and outlines the opportunities for future work.

The main text is supplemented by two Appendices that include additional and supporting details of the main text. Appendix A provides details of the growth-optimization process for various materials used in this thesis. Appendix B provides details of the band excitation piezoresponse spectroscopy and data-fitting procedure.

CHAPTER 2

Introduction to Ferroelectricity: Definitions, Properties, and Materials

This Chapter provides a general overview of the ferroelectrics and related materials. After providing a review of the basic definitions related to ferroelectricity, the origin of the effect is discussed in relation to the crystal symmetry and the nature of chemical bonding, and in terms of the stability of crystal-lattice dynamics and the concept of soft modes. This is followed by a brief discussion of the general properties of ferroelectric materials. A number of prototypical perovskite ferroelectric material systems and thin films (which will later be used in this Thesis) are then introduced, and advantages of fabricating these materials in the form of thin films are discussed. Finally, an overview of the practical applications of these materials is given, followed by a discussion of the technological challenges related to the use of ferroelectrics in electronic devices.

2.1 Basic Definitions

Ferroelectric materials are defined as insulating systems that exhibit a spontaneous electric polarization in two or more energetically-degenerate equilibrium directions in the absence of an external electric field. The direction of the spontaneous polarization in ferroelectrics can be switched between equilibrium states by application of an external electric field [35-38]. Most ferroelectrics undergo a structural phase transition from a high-temperature, high-symmetry non-polar (*i.e.,* paraelectric) phase into a low-temperature, low-symmetry ferroelectric phase via small structural distortions [35-38]. The phase transition from paraelectric to ferroelectric phase occurs at a critical temperature called the Curie temperature (T_C), and is accompanied by changes in the dimensions of the unit cell and a resulting spontaneous strain, emergence of the spontaneous polarization, which usually increases with decreasing temperature below T_C, as well as strong anomalies in the dielectric, elastic, and thermal properties [35-39].

For ferroelectricity to exist the material must belong to a polar crystal class of materials which are characterized by the simultaneous presence of non-centrosymmetry (*i.e.*, lack of an inversion center) and a polar axis. Of the 32 crystallographic point groups, only 21 are non-centrosymmetric. Of these, 20 exhibit a polarization upon application of an applied stress and are known as piezoelectrics. Point group 432, while non-centrosymmetric, is non-piezoelectric due to other symmetry considerations. Of the 20 piezoelectric point groups, 10 groups (1, 2, m, $2mm$, 4, $4mm$, 3, $3m$, 6, and $6mm$) possess a unique polar axis in the absence of strain and electric field, and a temperature-dependent spontaneous polarization. The materials that belong to these 10 polar groups are called pyroelectrics [37,40]. Ferroelectrics are a subgroup of the pyroelectric polar crystals in which the direction of the spontaneous polarization can be switched by an external electric field. Therefore, all ferroelectrics are also pyroelectrics and piezoelectrics simultaneously.

2.2 The Origins of Ferroelectricity

Ferroelectricity can be understood from a structural point of view. Most widely used ferroelectrics have a perovskite structure with the chemical formula ABO_3 including simple compounds such as $BaTiO_3$, $PbTiO_3$, and $BiFeO_3$, as well as solid solutions such as $PbZr_xTi_{1-x}O_3$, $PbMg_{1/3}Nb_{2/3}O_3$, (1-x)$PbMg_{1/3}Nb_{2/3}O_3$-(x)$PbTiO_3$, *etc.* [11,41,42]. The cation sites in ternary perovskite oxides can accommodate a wide range of rare-earth and transition metal species with a variety of ionic radii and valence states [43], providing a rich spectrum of chemistries and properties. Perovskite ferroelectrics often exhibit a high-symmetry, cubic structure ($Pm\bar{3}m$) in the high-temperature, paraelectric phase, described by a corner-linked network of oxygen octahedra (oxygen ions sitting at the cube faces) with large A-site cations located on the corners of the cube and small B-site cations occupying the center of the octahedral cages (Figure 2.1) [11,39,41]. From the structural point of view, the onset of ferroelectricity in simple perovskite ferroelectrics (like $BaTiO_3$) can be described by shifts of the B-site and oxygen ions relative to the A-site cations upon transitioning through T_C. Due to this structural distortion the centers of negative and positive charges no longer coincide, giving rise to a spontaneous polarization [11,39,41].

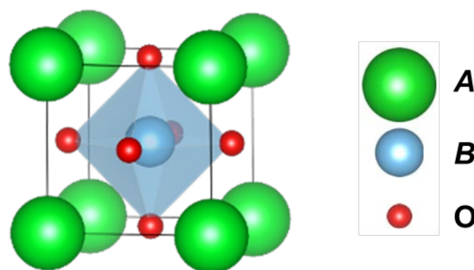

Figure 2.1. The schematic representation of atomic structure in an ABO_3 perovskite oxide.

From the atomic level, ferroelectricity results from the competition between short-range repulsive forces which favor a centrosymmetric non-ferroelectric structure and long-range attractive Coulomb forces which favor an ionically off-centered ferroelectric structure [44-46]. As described by the *second-order Jahn-Teller* effect [47-49], the distorted ferroelectric structure can be stabilized through changes in the chemical bonding via two different mechanisms. In ABO_3 perovskites which have a transition-metal cation with a nonmagnetic d^0 electronic structure on the B site, weakening of the short-range repulsive forces and formation of covalent bonds between empty transition metal d orbitals and filled oxygen $2p$ orbitals [44-46] are known to be responsible for the onset of ferroelectricity. $BaTiO_3$, is a prototypical example of such a B-site driven ferroelectricity, where the hybridization of titanium $3d$ with oxygen $2p$ results in the displacement of the titanium ions towards oxygen ions and formation of a spontaneous polarization, while the barium $5p$ remains stereochemically inactive [45]. In $PbTiO_3$, on the other hand, in addition to the B-site driven ferroelectricity, the *second-order Jahn-Teller* effect can also be driven by the stereochemical activity of A-site $6s$ electron "lone pairs" and their hybridization with oxygen $2p$, giving rise to loss of the center of symmetry (or A-site-driven ferroelectric distortions) [44-46]. In perovskite materials such as $BiFeO_3$ with non-d^0 B-site cations, ferroelectric distortion is solely driven by the stereochemical activity of lone pair electrons on A-site cations [50].

Polar distortions in perovskite oxides can be also predicted using the semi-empirical *Goldschmidt's tolerance factor* (t_G):

$$t_G = \frac{r_O + r_A}{\sqrt{2}(r_O + r_B)} \tag{2.1}$$

where r_A, r_B, and r_O are the radii of the A, B, and oxygen ions, respectively [51]. When $t_G > 1$, the B-site cations are too small for the oxygen octahedra and the structure is imposed by the distance between A-site cations and oxygen ions. In turn, the structure will develop a small polar distortion (*e.g.*, in $BaTiO_3$ and $PbTiO_3$). On the other hand, when $t_G < 1$, the A-site cations are small in comparison to the hole between the oxygen octahedra and cannot effectively bond with all neighboring oxygen ions. In this case, rotation and tilting of the oxygen octahedra will be favored while the polar distortion is suppressed (*e.g.*, in $SrTiO_3$ and $CaTiO_3$). For large deviations of t_G from unity the perovskite structure becomes unstable [38].

Lastly, the origin of ferroelectricity can be qualitatively studied in terms of the stability of crystal-lattice dynamics and the concept of soft modes [37,52,53]. A structural phase transition is accompanied by instabilities in the order parameter (*i.e.*, polarization in ferroelectrics) which is associated with the condensation of a lattice vibrational mode. Phonon modes in non-primitive lattices of perovskite-oxide ferroelectrics include acoustic and optical phonons, referring to the coherent and out-of-phase movement of the atoms, respectively. Upon cooling a ferroelectric material from its high-temperature phase, the frequency of the transverse optical phonon goes down (*i.e.*, the phonon "softens") and becomes zero at T_C. This freezing of the lattice vibrations at T_C gives rise to a new structure with lower symmetry and a finite dipole moment.

2.3 Domains in Ferroelectrics

When a perovskite ferroelectric is cooled from its high-temperature cubic phase, a ferroelectric distortion may arise in all crystallographically equivalent directions, which can, in turn, split the crystal into multiple regions of different polarization directions. The regions of the crystal with

uniformly oriented spontaneous polarization are called domains, and neighboring domains are separated from one another by domain walls which are on the order of 1-10 nm across [37,39,54].

Domains in ferroelectrics are formed to minimize the electrostatic and elastic energies due to formation of spontaneous polarization and strain [37,39,54]. Abrupt fall-off of polarization at the surface of a ferroelectric, for example, increases the electrostatic energy by giving rise to a surface charge density and a corresponding electric field (*i.e.*, depolarization field) in the opposite direction to the spontaneous polarization [37,38,55]. In order to minimize the electrostatic energy, the system can compensate the depolarization field by available charges in the material's surrounding, by electrical conduction through the crystal, or by splitting itself into domains with oppositely oriented polarization. The walls separating the anti-parallel domains are called 180° domain walls (Figure 2.2a). Since the origin of these domain is purely electrostatic in nature, 180° domain walls are called ferroelectric domain walls. In addition to reducing the electrostatic energy, domains can also form in order to minimize the elastic energy of the ferroelectric phase (*e.g.*, in mechanically constrained crystals or thin film ferroelectrics) [54]. The non-180° walls separating the domains with different strain states are called ferroelastic domains (Figure 2.2b). The non-180° walls with head-to-tail polarization vectors can also reduce the electrostatic energy of the system. Non-180° domain walls are, therefore, both ferroelectric and ferroelastic in nature. A combination of electric and elastic boundary conditions can lead to very complex domain structures with many 180° and non-180° domain walls. The presence of domain walls, however, introduces extra domain-wall energy by itself. Ultimately, the domains form in a manner to minimize the sum of electrostatic, elastic, and domain-wall energies [38], and the domain structure is dependent upon any factor which affects this balance.

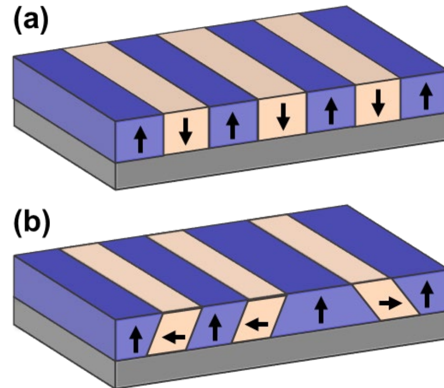

Figure 2.2. The schematics of (a) ferroelectric domains with 180° domain walls, and (b) ferroelastic domains with 90° domain walls.

The types of domain walls that can form depend on the symmetry of both the ferroelectric and paraelectric phases of the crystal [56]. For a tetragonal perovskite ferroelectric, the ferroelectric distortion may occur along the *a* axis of the paraelectric cubic cell (*i.e.*, <100>). This gives rise to six possible directions for the spontaneous polarization (including positive and negative orientations) with 180° and 90° domain walls separating regions of those polarizations. For a rhombohedral ferroelectric the spontaneous polarization may develop along the body diagonals of the paraelectric cubic unit cell (*i.e.*, <111>). This gives eight possible directions of the spontaneous polarization with 180°, 71°, and 109° domain walls.

2.4 Properties of Ferroelectric Materials

2.4.1 Ferroelectric Switching

As mentioned in Section 2.1, switching of spontaneous polarization between crystallographically equivalent directions by application of an external electric field is a requirement for ferroelectricity. This polarization switching gives rise to a polarization-electric field hysteresis loop (Figure 2.3). A ferroelectric hysteresis loop is a plot of the integrated switching current as a function of applied electric field and is direct experimental proof of ferroelectricity [38]. As

mentioned in Section 2.3, ferroelectrics may split into domains with differently oriented polarization directions depending on their electrostatic and mechanical boundary conditions. If equal fractions of oppositely polarized domains exist in the system, it gives rise to a zero net macroscopic polarization (point A, Figure 2.3). In this case application of a small positive electric field, linearly increases the polarization value according to the following relation [12]:

$$D = \varepsilon E \tag{2.2}$$

where D is the electric displacement, ε is the dielectric permittivity, and E is the external electric field (segment AB, Figure 2.3). Larger values of applied electric fields, however, can energetically favor the domains with a spontaneous polarization parallel to the direction of the electric field. In response to larger electric fields, therefore, the system maximizes the volume fraction of the domains with energetically favorable polarization direction through movement and redistribution of the domain walls, rapidly increasing the measured charge density (segment BC, Figure 2.3). The total polarization response in this region consists of the macroscopic spontaneous polarization (P_s) and the polarization due to the external electric field and is strongly nonlinear [12]:

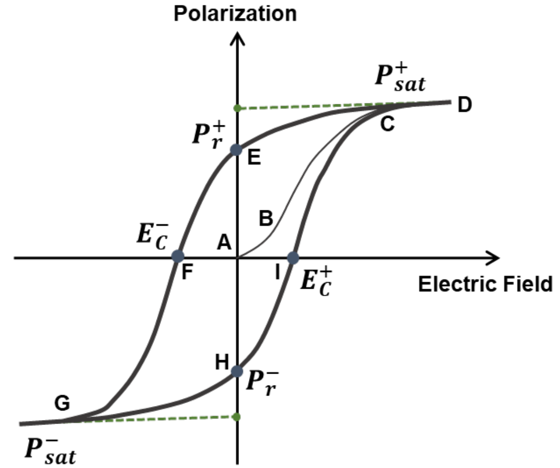

Figure 2.3. The schematic of a ferroelectric polarization-electric field hysteresis loop.

$$D = \varepsilon E + P_s. \tag{2.3}$$

Once the movement and redistribution of the domain walls is complete the macroscopic spontaneous polarization reaches a saturation value, P_{sat}^{+} (point C, Figure 2.3), and the ferroelectricity again behaves linearly (segment CD, Figure 2.3) with electric field. If now the field starts to decrease most of the domains do not have a driving force for switching back to their original directions, and a non-zero macroscopic polarization is achieved at zero external electric field (point E, Figure 2.3). The polarization at zero external electric field is known as the remanent polarization, P_r^{+}. Remanent polarization is often smaller than the saturation polarization due to the back-switching of some domains to their original direction (*e.g.*, due to the presence of defects) after the electric field is removed. A negative electric field in then required to bring the polarization to zero (point F, Figure 2.3), and is called the negative coercive field, E_C^{-}. Further increase of the field in the negative direction gives rise to a new alignment of domains and saturation in the negative direction, P_{sat}^{-} (point G, Figure 2.3). Upon reducing the external field to zero a negative remanent polarization, P_r^{-}, is achieved (point H, Figure 2.3). Reversal of the field to and above the positive coercive field, E_C^{+}, brings the polarization to zero (point I, Figure 2.3) and its positive saturation value, P_{sat}^{+}, respectively, and completes the cycle. The polarization reversal takes place by the growth of existing antiparallel domains, by domain-wall motion, and by nucleation and growth of new reversed domains. Growth of existing and nucleated domains involves the forward growth as well as sideway propagation of the domains [57,58]. An ideal hysteresis loop is symmetrical such that the positive and negative values of P_{sat}, P_r, and E_C are identical. The shape of the loop, however, may be affected by variety of factors including the presence of charged defects, mechanical stresses, preparation conditions, and thermal treatment.

2.4.2 Dielectric, Piezoelectric, and Pyroelectric Susceptibilities

In addition to hysteretic polarization-switching response of ferroelectrics under high electric fields, these materials also exhibit strong thermo-electro-mechanical coupling as described by Heckmann diagram (Figure 2.4) [40,59]. The most interesting and technologically important properties of ferroelectrics result from their linear, small-signal susceptibilities to electric fields, mechanical stresses, and temperature which give rise to strong dielectric, piezoelectric, and pyroelectric effects, respectively [35,37,60]. These materials are often used near a structural or polar instabilities (such as near T_C) where their susceptibilities are typically maximized [11,36,37].

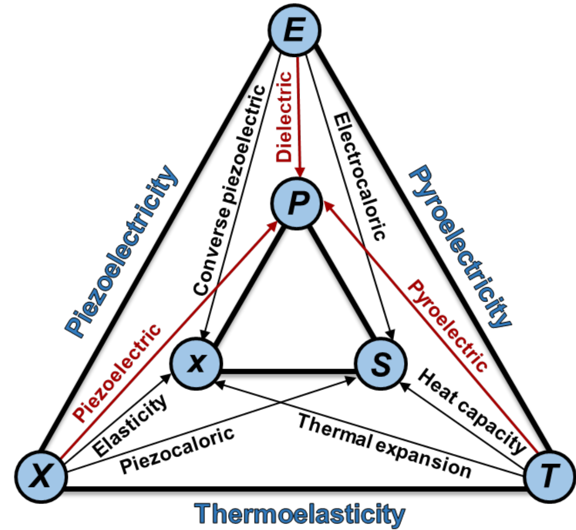

Figure 2.4. A Heckmann diagram describing the coupling between thermal, electrical, and mechanical properties of ferroelectric materials. S in this diagram represents the entropy.

Dielectric permittivity (ε) describes how the polarization (P) is perturbed by an applied electric field as [12]:

$$P_i = \varepsilon_{ij} E_j. \quad (2.4)$$

This relation is only valid in the linear limit (*i.e.*, at low fields) of nonlinear dielectrics such as ferroelectrics. Outside of this linear regime, polarization depends on higher-order terms of the field. Perovskite ferroelectrics have some of the highest dielectric permittivity values of any materials. Dielectric permittivity changes as a function of temperature and reaches a maximum near T_C, accompanied by a peak in the dielectric loss. Above T_C, the temperature dependence of dielectric permittivity is known to follow the Curie-Weiss law [12]:

$$\varepsilon \approx \frac{c}{T - T_0} \quad (2.5)$$

where c is the Curie constant, T is the temperature, and T_0 is the Curie-Weiss temperature. Dielectric permittivity in ferroelectrics is also strongly frequency-dependent. This frequency dependence originates from the presence of various mechanisms contributing to the dielectric response including intrinsic electronic and ionic contributions, as well as extrinsic space charge and dipolar contributions [53,61]. Strong dielectric-loss peaks also occur near the relaxation frequency of each dielectric contribution.

In addition to a strong dielectric susceptibility, ferroelectrics also exhibit strong piezoelectric and pyroelectric responses. Piezoelectric susceptibility of ferroelectrics leads to the formation of polarization charges as a result of the application of a mechanical stress (X), which can be described by direct piezoelectric effect [12]:

$$P_i = d_{ijk} X_{jk} \quad (2.6)$$

where d_{ijk} is the piezoelectric coefficient. Moreover, application of an electric field to piezoelectric materials gives rise to a strain (x) through converse piezoelectric effect (with a converse piezoelectric coefficient that is thermodynamically identical to the direct piezoelectric coefficient) [12]:

$$x_{ij} = d_{ijk} E_k. \quad (2.7)$$

Finally, pyroelectric susceptibility leads to a change in the vector of spontaneous polarization with temperature. The pyroelectric coefficient (π) is defined as [12]:

$$\pi_i = \frac{\partial P_i}{\partial T}. \quad (2.8)$$

2.5 Complex-Oxide Ferroelectric Materials

2.5.1 $BaTiO_3$

$BaTiO_3$ was the first perovskite ferroelectric to be discovered [10]. It undergoes successive phase transitions from cubic to tetragonal to orthorhombic and to rhombohedral symmetry upon cooling from high temperature. The cubic phase is non-polar and paraelectric. In bulk, $BaTiO_3$ undergoes a first-order phase transition from a paraelectric cubic to a ferroelectric tetragonal phase (*P*4*mm* symmetry) at a T_C of ≈ 120°C [12,62]. This transition gives rise to the formation of a spontaneous polarization of ≈ 30 μC cm^{-2} along the [001] of the cubic unit cell. The additional ferroelectric-to-ferroelectric phase transitions from tetragonal to orthorhombic (*mm*2 symmetry) to rhombohedral (*R*3*m* symmetry) phases occur at ≈ 0°C and ≈ -70°C, respectively [12,62]. The ferroelectric distortion in the orthorhombic phase occurs in the [110] of the original cubic cell (*i.e.*, parallel to a face diagonal). In the rhombohedral phase, the spontaneous polarization forms in the [111] of the original cubic cell (*i.e.*, along the body diagonal).

2.5.2 $PbTiO_3$

$PbTiO_3$ is another classical perovskite ferroelectric which undergoes a first-order phase transition from a paraelectric cubic to a ferroelectric tetragonal phase at ≈ 490°C in bulk [63]. The spontaneous polarization in tetragonal $PbTiO_3$ lies along the [001] of the original cubic cell (*i.e.*, along the *c* axis of the tetragonal unit cell). This polarization is ≈ 75 μC cm^{-2} at room temperature, one of the largest spontaneous polarizations of all known ferroelectrics. Despite this large polarization, pure $PbTiO_3$ is not widely used in commercial applications, due to the presence of high defect- and impurity-induced conduction which limits their functionality. Doped $PbTiO_3$ and $PbTiO_3$-based solid solutions are, instead, often utilized [12].

2.5.3 $PbZr_xTi_{1-x}O_3$

$PbZr_xTi_{1-x}O_3$ is one of the most common solid solutions based on $PbTiO_3$ (with ferroelectric $PbTiO_3$ and antiferroelectric $PbZrO_3$ as its end members), and one of the most widely used ferroelectric and piezoelectric materials. The presence of zirconium in $PbZr_xTi_{1-x}O_3$ largely reduces the leakage current which is often present in pure $PbTiO_3$, and therefore, expands the applicability of this material. $PbZr_xTi_{1-x}O_3$ exhibits a rich phase diagram with a variety of structural phases as a function of composition [64]. The structure of the high-temperature paraelectric phase is cubic, but at lower temperatures, the structure adopts many distorted versions of the parent phase depending on the composition and temperature. The ferroelectric phase adopts a tetragonal structure (with polarization along the [001] of the original cubic cell) for titanium-rich compositions, and a rhombohedral structure (with the polarization along the [111] of the original cubic cell) for zirconium-rich compositions. At high zirconium content ($x > 95\%$) the structure adopts an orthorhombic antiferroelectric phase. Near 52% zirconium composition, the rhombohedral and tetragonal phases are separated by an almost temperature-independent phase boundary, which is referred to as a so-called morphotropic phase boundary. Near the morphotropic phase boundary a mixture of tetragonal, rhombohedral, and even monoclinic structures can be present in the ferroelectric phase [65,66]. Large enhancement in susceptibilities can be achieved

by tuning the composition to be in the proximity of the morphotropic phase boundary due to the presence of structural phase competitions. For applications which require large polarization, however, titanium-rich compositions are usually preferred due to their larger spontaneous polarization and square ferroelectric hysteresis response. This Thesis only focuses on one member of $PbZr_xTi_{1-x}O_3$ family with composition $PbZr_{0.2}Ti_{0.8}O_3$ and a tetragonal ferroelectric phase.

2.5.4 $BiFeO_3$

A critical drawback of the $PbZr_xTi_{1-x}O_3$ family of materials is their toxicity due to the presence of lead ions, which is a matter of environmental concern. Recently, lead-free $BiFeO_3$ has attracted a great deal of attention due to its non-toxicity. In addition, $BiFeO_3$ is known to be a single-phase multiferroic material that exhibits a co-existence of ferroelectricity and G-type antiferromagnetism at ambient conditions, and the potential for magnetoelectric coupling between the electric and magnetic order parameters [4,67-69]. $BiFeO_3$ has a high ferroelectric Curie temperature ≈ 830°C, and a high antiferromagnetic Néel temperature ≈ 370°C [68-72]. The non-polar, paraelectric phase has a cubic crystal structure. The ferroelectric phase possesses a rhombohedral structure which is characterized by two distorted perovskite unit cells connected along their body diagonal (*i.e.*, along the [111] of the original cubic unit cell) [73]. The spontaneous polarization, therefore, may have directions along the four cube diagonals, giving rise to the presence of ferroelectric 180° as well as ferroelastic 71° and 109° domain walls [74]. Despite low reported values of polarization around 2.5-40 μC cm^{-2} in bulk ceramics, spontaneous polarization values as high as 50-100 μC cm^{-2} have been predicted and measured in epitaxial thin films [75-77], comparable to those of the tetragonal titanium-rich $PbZr_xTi_{1-x}O_3$ system. Despite these promising characteristics, $BiFeO_3$ thin films suffer from a high leakage current which limits their applicability in devices.

2.5.5 (1-x)$PbMg_{1/3}Nb_{2/3}O_3$-(x)$PbTiO_3$

(1-x)$PbMg_{1/3}Nb_{2/3}O_3$-(x)$PbTiO_3$ is a solid solution of ferroelectric $PbTiO_3$ and relaxor $PbMg_{1/3}Nb_{2/3}O_3$ and is a relaxor ferroelectric with a perovskite structure. Relaxors are a special class of ferroelectric materials which are characterized by chemical heterogeneity on the nanometer scale [11]. In relaxors, unlike-valence cations belonging to a given site (A or B) are present in the correct ratio for charge balance, but are situated randomly on the cation sites [78]. These randomly different cation charges give rise to random fields, which tend to make the phase transitions "diffuse" instead of sharp as in normal ferroelectrics [79]. As a result, a well-defined Curie temperature does not exist in relaxors. Relaxors exhibit a broad and diffuse phase transition from the paraelectric to the ferroelectric state with a broad maximum in the temperature-dependent dielectric permittivity and strong frequency dispersion of the dielectric response below the temperature of the maximum permittivity (T_{max}). Relaxors also exhibit high dielectric permittivity over a broad temperature range, large electromechanical response (*i.e.*, ultrahigh piezoelectric coefficients), negligible hysteresis, and a weak remanent polarization. Above the temperature of the maximum permittivity, relaxors do not obey the Curie-Weiss behavior [80-82]. In addition, it is known that, due to the presence of dipolar correlations, the frequency dependence of T_{max} in relaxors deviates from the Arrhenius dependence expected for normal dielectrics [83,84].

In (1-x)$PbMg_{1/3}Nb_{2/3}O_3$-(x)$PbTiO_3$ solid solutions, similar to other solid solutions such as $PbZr_xTi_{1-x}O_3$, a morphotropic phase boundary can be observed by tuning the composition in the range of $0.28 < x < 0.36$ [85]. Near their morphotropic phase boundary, these materials are found to be among the most promising candidates for a wide range of applications due to their superior dielectric and electromechanical responses. Therefore, in the present work, I focus on thin films of $0.68PbMg_{1/3}Nb_{2/3}O_3$-$0.32PbTiO_3$, well within the morphotropic phase boundary composition

range. As temperature decreases at the morphotropic phase boundary composition, successive phase transitions from cubic-paraelectric, to tetragonal-ferroelectric and, finally, to rhombohedral-ferroelectric phases occur. The coexistence of tetragonal, rhombohedral, and even monoclinic or orthorhombic phases near the morphotropic phase boundary is thought to be responsible for the high susceptibilities observed for those compositions [86].

The existence of polar nanoclusters or nanoregions in a non-polar matrix is believed to be responsible for the unique physical properties of relaxor ferroelectrics [81]. A few critical temperatures are defined to explain the properties of relaxors in the context of polar nanoregions, including the Burns temperature (T_b) [87], dielectric maximum temperature (T_{max}), and freezing temperature (T_F), which correspond to the formation of polar nanoregions, onset of the slowing-down of the dynamics of the polar nanoregions, and freezing of the thermal fluctuations of polar nanoregions, respectively [81,87]. More recent studies, however, have shown that the polar-nanoregion model is not fully consistent with recent experimental observations [88-92]. To better explain the relaxor behavior, the concept of polar nanodomains are instead introduced which describes the relaxors as exhibiting a multi-domain state with small domain sizes ($\approx$ 6 nm) and a high density of low-angle domain walls, with no requirement for existence of a non-polar matrix [88,91-94].

2.6 Epitaxial Ferroelectric Thin Films

For years ferroelectric materials have been used in the form of bulk polycrystalline ceramics in a wide range of applications. More recently, however, there has been a growing interest in the use of these materials as thin films. This increased interest is the result of several advantages these materials bring about in reduced dimensions [1-4, 95-98]:

1. Ferroelectric materials exhibit unique properties very different from and often superior to those of their bulk counterparts.
2. Ferroelectric materials with reduced dimensions are promising candidates for modern technologies based on miniaturized, slim, and light-weight devices.
3. Ferroelectric thin films can be readily integrated as active elements into modern oxide nanoelectronic devices, micro-fabricated architectures, micro-electro-mechanical systems, and integrated circuits.
4. Due to their reduced dimensions, ferroelectric thin films require much smaller voltages for switching, and, in turn, are promising candidates for applications that require low-power operations.
5. Ferroelectric thin films provide a large degree of freedom and enormous flexibilities for property control and materials design. For example, crystalline phases, nature and sequence of the phase transitions, Curie temperature, domain structure, ferroelectric properties and other susceptibilities of ferroelectric thin films in response to the electric field or temperature can be carefully engineered via strain, film thickness, film chemistry, electrodes, interfaces, *etc*.
6. Fabrication of ferroelectrics in the form of thin films eliminates the challenges associated with bulk polycrystalline ferroelectrics. For example, the properties of polycrystalline ferroelectric materials are largely affected by so-called extrinsic contributions resulting from domain-wall displacements, grain boundaries, *etc*. Such extrinsic contributions give rise to strong frequency-

and field-dependence of properties and make the theoretical treatment of bulk ferroelectric systems very challenging.

When a ferroelectric thin film is grown on a single-crystalline substrate it adjusts its in-plane lattice parameters to adopt the crystalline structure and dimensions of the substrate. Epitaxy refers to the mutual orientation of film and substrate with two-dimensional lattice control. Coherency refers to atom-by-atom matching across the film-substrate interface and matching of lattice parameters [99]. The epitaxial growth of high-quality and stoichiometric complex-oxide ferroelectric thin films with unit-cell-level control of thickness has been vastly developed in recent years as a result of advances in thin-film growth techniques, development of complex-oxide metals which can be used as electrodes, and the availability of commercial single-crystalline substrates with various miscut angles and lattice constants [3,4]. Such versatility in the fabrication of ferroelectric thin-film heterostructures has enabled marked control over the structure and properties of ferroelectrics and provided an enormous phase space for engineering of these materials.

2.7 Applications of Ferroelectrics

Ferroelectric materials and thin films have been implemented in variety of functional devices and are promising candidates for next-generation technologies, due to the unique properties and wide-range of functionalities accessible in these systems including the existence of switchable spontaneous polarization, high dielectric constant, piezoelectricity and pyroelectricity, as discussed in Section 2.4. Due to the existence of a switchable spontaneous polarization, ferroelectric materials can be used as active elements of non-volatile ferroelectric random-access memories, low-power logics, and radio-frequency identification tags [57,100-103]. The high dielectric constant of ferroelectrics makes these materials useful for highly tunable high-dielectric-constant capacitors [11,36,37,104]. The strong piezoelectric effect in ferroelectrics, makes them ideal in situations where conversion between electrical and mechanical energy is required including sensing, actuation, energy harvesting, sound and ultrasound production and detection, electronic frequency generation, and ultra-fine positioning [105-109]. Also, owing to their pyroelectric response, ferroelectric materials are used in thermal detectors, temperature sensing elements, infrared imaging devices, pyroelectric energy and waste heat harvesting, and more [11,36,37,110-112].

2.8 Ferroelectric Device Reliability Issues

Despite the unique properties and wide range of potential applications for ferroelectric materials and thin films, there are several challenges associated with the lifetime and reliable operations of ferroelectric capacitors in electronic devices including high leakage currents, imprint, retention, aging, and fatigue [2,10,12]. These reliability issues often degrade the performance of the electronic devices with ferroelectric active elements, especially devices that rely on the switching of the spontaneous polarization (*e.g.*, memories). These issues are known to be directly related to the presence of defects, and therefore, are relevant to the scope of this Thesis. In the following, the concepts of leakage, imprint, and retention and the mechanisms responsible for such effects will be introduced.

2.8.1 Leakage

Ferroelectrics are rarely perfectly resistive, especially when they are grown in the form of thin films, such that an applied electric field results in a leakage-current that flows through the material. Leakage currents result from the movement of free electrons/holes (*i.e.*, electronic conduction), and/or the movement of mobile ions (*i.e.*, ionic conduction) under a given temperature and applied electric field [113]. The leakage current through a ferroelectric must be lower than a certain level to meet the specific reliability criteria under normal operation of the devices which have ferroelectrics as their active elements. Additionally, the presence of leakage current makes it challenging to study the electrical properties of ferroelectrics by giving rise to high losses and screening the measured electrical signals. In ferroelectric switching studies, for example, high leakage in the ferroelectric can lead to rounding and distortion of the hysteresis loops and an overestimate of the value of the polarization [38]. Similar leakage-related problems can be also observed in measuring other susceptibilities such as dielectric permittivity, pyroelectricity, *etc*. Consequently, understanding the mechanisms responsible for high leakage, and developing routes to control and minimize the leakage currents in ferroelectrics are of utmost technological and scientific importance.

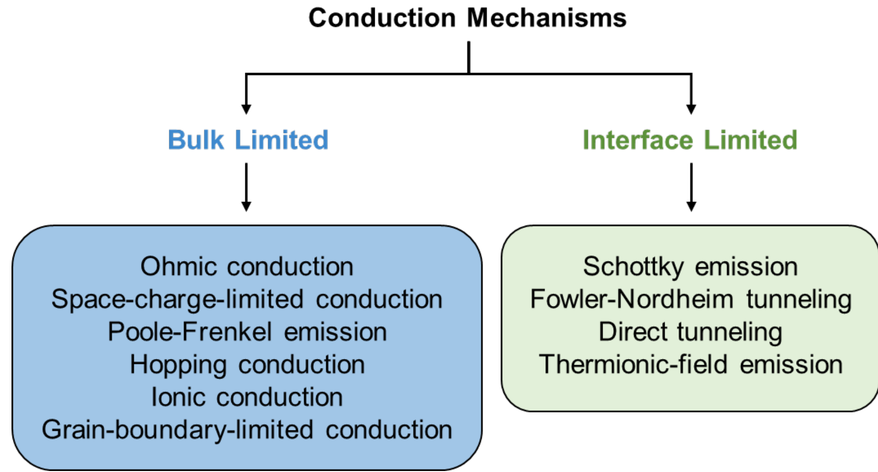

Figure 2.5. Classification of conduction mechanisms.

Conduction in ferroelectric thin films can be governed by variety of mechanisms depending on the film chemistry (*i.e.*, off-stoichiometry, doping, impurities), nature of the film-electrode interface, magnitude of the applied electric field, and temperature. All possible conduction mechanisms fall into two general categories. They can be limited by the interface between the film and electrodes (*i.e.*, interface-limited conduction), or by the bulk of the material (*i.e.*, bulk-limited conduction) (Figure 2.5) [113]. This Section only introduces the mechanisms which are most relevant to the study of conduction in ferroelectric thin films.

2.8.1.1 Ohmic Conduction. Ohmic conduction is a bulk-limited conduction which is caused by the movement of mobile electrons in the conduction band and holes in the valence band. Under ohmic conduction the current density (J) varies linearly with applied electric field [113]:

$$J = \sigma E = nq\mu E \tag{2.9}$$

where σ is the electrical conductivity, q is the electronic charge, n is the free carrier concentration, and μ is the free carrier mobility. Therefore, if ohmic conduction is the dominant mechanism, the derivative of J with respect to E must be equal to 1:

$$\frac{d(\ln(J))}{d(\ln(E))} = 1. \tag{2.10}$$

2.8.1.2 Space-Charge Limited Conduction. Space-charge limited conduction is another type of bulk-limited conduction. The mechanism involves the bulk-limited conduction of injected

space charges where the rate of charge injection into the film outpaces the bulk charge transport such that a limiting space charge is formed and governs the overall behavior [114,115]. The current density in space-charge limited conduction is defined as:

$$J = \frac{9\mu\varepsilon_0\varepsilon_{opt}}{8}\frac{E^2}{d} \tag{2.11}$$

where ε_0 is the permittivity of free space, ε_{opt} is the optical/dynamic dielectric constant (close to the square of the optical refractive index, *i.e.*, $\varepsilon_{opt} = n^2$), and d is the thickness of the film. Therefore, the space-charge limited conduction can be characterized by [113]:

$$\frac{d(\ln(J))}{d(\ln(E))} = 2. \tag{2.12}$$

2.8.1.3 Poole-Frenkel Emission. Poole-Frenkel emission is yet another bulk-limited conduction mechanism governed by field-assisted emission of charge carriers from internal trap centers [116]. The emission of carriers from internal trap centers can be both thermally activated and/or field assisted [113]. Application of an electric field may reduce the Coulomb potential energy of electrons or holes which occupy the trap centers. This reduction in potential energy may increase the probability of electrons or holes being thermally excited out of the trap centers into the conduction band or valence band, respectively. The current density due to the Poole-Frenkel emission is defined as [113]:

$$J = q\mu N_C E\ exp[\frac{-q(\ \phi_T - \sqrt{qE/\pi\varepsilon_{opt}\varepsilon_0}\ )}{k_B T}] \tag{2.13}$$

where $q\mu N_C$ is the zero-field conductivity (N_C is the density of states in the conduction band), $q\phi_T$ is the trap energy level, and k_B is the Boltzmann's constant. In situations where there are large concentrations of donor and/or acceptor trap states, Poole-Frenkel emission is modified by adding an exponential scaling constant r ($1 \leq r \leq 2$) in order to fit the experimental data [117,118]. The modified Poole-Frenkel model is defined as:

$$J = q\mu N_C E\ exp[\frac{-q(\ \phi_T - \sqrt{qE/\pi\varepsilon_{opt}\varepsilon_0}\ )}{k_B T}]. \tag{2.14}$$

The value of $r = 1$ refers to the traditional Poole-Frenkel model. For Poole-Frenkel emission to be the dominant conduction mechanism, the plot of $\ln(J/E)$ *vs.* $E^{1/2}$ should be linear, and physically reasonable values of optical dielectric constant must be extracted from the linear fits. The values of optical dielectric constant and the trap energy level can be extracted from the slope and from the intercept of Poole-Frenkel plots, respectively. The activation energies of dominant trap states are often extracted from the slope of the linear fits to the Arrhenius plots of $\ln(J)$ *vs.* $1000/T$ at different values of electric field.

2.8.1.4 Schottky or Thermionic Emission. Schottky emission is an interface-limited transport mechanism which is governed by the potential barrier height at the film-electrode interface [119]. This potential barrier arises from a difference in the Fermi energy levels of the electrode and the film. If the electrons/holes obtain enough energy through thermal activation to overcome the energy barrier at the electrode-film interface they can move to the film under an electric field and contribute to the conduction. The current density due to Schottky emission is defined as [113]:

$$J = A^{*}T^{2}exp[\frac{-q(\phi_B - \sqrt{qE/4\pi\varepsilon_{opt}\varepsilon_0})}{k_B T}], \tag{2.15}$$

$$A^{*} = \frac{4\pi q k^{2} m^{*}}{h^{3}} = \frac{120 m^{*}}{m_0} \tag{2.16}$$

where A^{*} is the effective Richardson's constant, m_0 is the free-electron mass, m^{*} is the effective electron mass in the dielectric, ϕ_B is the Schottky barrier height (*i.e.*, conduction band offset), and h is the Planck's constant. For Schottky emission to be dominant, the plot of $\ln(J/T^{2})$ *vs.* $E^{1/2}$ must be linear, and physically reasonable values of optical dielectric constant must be extracted from the linear fits. The values of optical dielectric constant and the barrier height can be extracted from the slope and from the intercept of the Schottky plots, respectively.

2.8.2 Imprint

Electrical imprint can be described as the preference of one polarization state over the other in ferroelectric bistable states, which gives rise to an asymmetry in a ferroelectric hysteresis loop (*i.e.*, a horizontal shift along the electric-field axis), and leads to a loss of remanent polarization at least in one polarity (Figure 2.6) [53,120]. Electrical imprint, in turn, can deteriorate the nonvolatility of polarization and lead to failure of stored ferroelectric information. The electrical imprint (E_i) is often quantified by the magnitude of the horizontal shift of a hysteresis loop as:

$$E_i = \frac{|E_C^{+}| - |E_C^{-}|}{2}. \tag{2.17}$$

As mentioned in Section 2.4.1, in an ideal ferroelectric equal electric fields are required to switch the polarization in the two opposite directions (*i.e.*, $E_C^{+} = E_C^{-}$). The positive and negative coercive fields, however, may not be equal due to a host of factors which disturb the degeneracy of polarization states, giving rise to an imprint. Electrical imprint can be developed intrinsically during the fabrication process due to the formation of ferroelectric dead layers, trapped charges, and defects. It may also arise from extrinsic factors related to the capacitor structure such as the presence of ferroelectric-electrode rectifying contacts, or asymmetric bottom and top electrodes. An imprint may also develop during the operation of the devices at various read/write operating conditions such as high temperature and a large number of unipolar pulses [12,121-123].

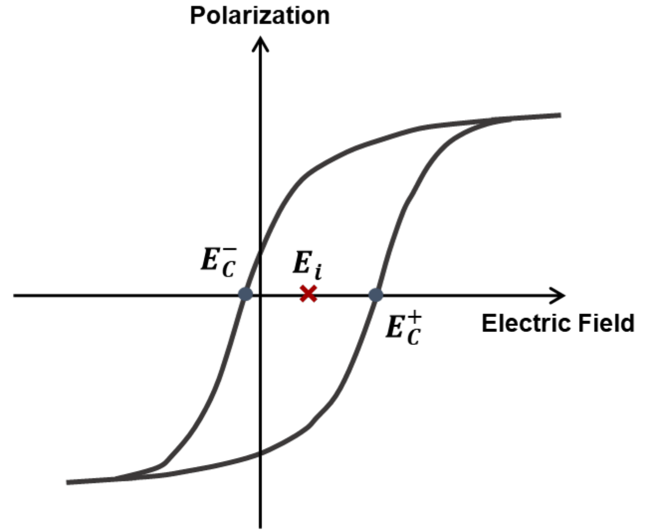

Figure 2.6. Schematic representation of electrical imprint giving rise to a shift of ferroelectric hysteresis loop on the electric field axis.

2.8.3 Retention

Retention (or aging) describes the drop of the remanent polarization of a ferroelectric material with time (Figure 2.7) and is exacerbated by temperature changes or by application of strong external fields [9,124]. From a device perspective, retention may be defined as the ability of the device to

retain a given level of electric signal after a given time from the write operation. The loss of remanent polarization is often described over several decades of time (t) as [124]:

$$P_r(t) = P_r(t_0) + Alog(\frac{t}{t_0}) \qquad (2.18)$$

where t_0 is an arbitrary point in time when the measurement is started and A is a constant. Retention can lead to a failure of memory cells if polarization decreases and drops below a limit which can be distinguished by the sense amplifier during the read operation. Retention is often attributed to a gradual change in the domain configuration with time, due to internal stresses and/or the presence of space charges or defects in the material [125-127].

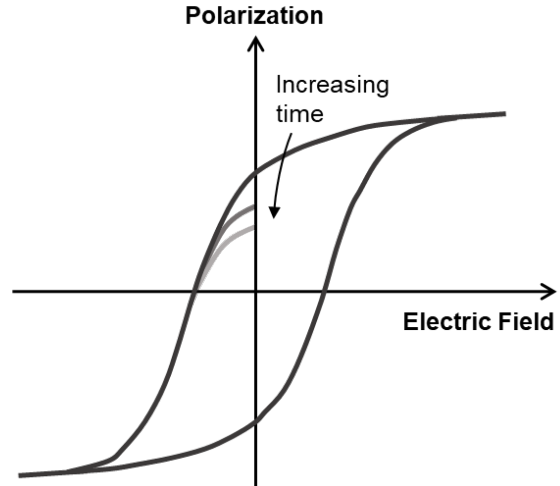

Figure 2.7. Schematic representation of time-dependent drop of remanent polarization due to retention.

CHAPTER 3

Point Defects in Complex-Oxide Ferroelectrics

This Chapter provides a brief review of point defects in complex-oxide ferroelectric materials. Various types of point defects which can be present in these materials are introduced. Equilibrium and non-equilibrium formation of point defects are discussed. And finally, the impact of different types of point defects on various functional properties of ferroelectric materials are briefly summarized.

3.1 Types of Point Defects

Defects are unavoidable in crystalline materials, and even in the most "perfect" materials there are always finite concentrations of various structural and compositional defects [128]. Therefore, even our best efforts to control these materials can be remarkably hampered if we do not account for and address the role of defects on the evolution of properties. Defects can form in many dimensionalities, including point defects (zero dimensional), line defects (one dimensional), planar defects (two dimensional), and volume defects (three dimensional). In ionic solids, point defects are the most abundant defects and play the most important role in affecting electrical, thermal, mechanical, optical, and other properties.

Complex-oxide ferroelectric, in particular, have a strong penchant for point defects due to their relatively low formation energies [27,28]. Moreover, the structure of these materials can accommodate large concentrations of point defects related to impurities and/or off-stoichiometry without formation of secondary phases [129]. In addition, a stoichiometric transfer from target to substrate during the thin-film growth processes is rarely achieved, and the loss of volatile elements (which often exist in these materials) during the high-temperature growth and fabrication processes can also give rise to large degrees of off-stoichiometry. Due to their ionic nature, the presence of off-stoichiometry in complex-oxide ferroelectrics disturbs the charge neutrality. The electronic charges resulting from off-stoichiometry need to be compensated either by formation of defects of opposite charge or by adding electron/holes to the lattice. In addition to off-stoichiometry, the regular presence of impurities in source materials, which also disturb the charge neutrality of the system, can give rise to the formation of compensating point defects and/or free charge carriers.

Complex-oxide ferroelectric thin films, therefore, essentially always contain a variety of point defects that are formed during the growth processes. The key types of point defects include vacancies (*i.e.*, missing ions from lattice sites), interstitials (*i.e.*, ions occupying interstitial crystallographic sites), antisites (*i.e.*, ions occupying the lattice sites which belong to another element), and substitutional defects (*i.e.*, dopants and/or impurities on the lattice sites). Impurities and dopants can also sit on interstitial sites. These singular point defects are referred to as isolated point defects. Point defects can also cluster together in order to maintain stoichiometry and/or reduce the electrostatic or elastic energy of the system [130,131]. These complex defects include Schottky pairs (consisting of a cation and anion vacancy), Frenkel pairs (consisting of a vacancy and an interstitial), di-vacancies, tri-vacancies, and larger defect clusters [132-135]. Such defects are referred to as defect complexes. Pairs of oppositely-charges point defects are called defect dipoles or dipolar defects. Defect dipoles in perovskite ferroelectrics are often formed as a complex between oxygen vacancies and either *B*-site acceptor dopants [136,137] or *A*-site vacancies [138]. Point defects can be also classified as *intrinsic* or *extrinsic*. *Intrinsic* point defects are related to the constituent elements of a materials, while *extrinsic* point defects are related to the foreign species such as impurities or dopants.

3.2 Kröger-Vink Notation

Point defects – and their equilibrium – are commonly described in Kröger-Vink notation [139]. In this notation, the first letter denotes either an atom or a vacancy, the subscript specifies the lattice site, and the superscript describes the electronic charge. In the superscript, a cross symbol (×) stands for neutral, a prime symbol (′) for negative, and a dot symbol (•) for positive charges relative to the charge of the host ion. In an $A^{2+}B^{4+}O_3$ perovskite compound, for example, $A_A^{\times}$ is an A^{2+}

ion located on an A^{2+} site which has a neutral charge with respect to the crystal lattice. A $B_i^{\bullet\bullet\bullet\bullet}$ defect, on the other hand, is a B^{4+} ion located on a normally neutral interstitial site giving rise to a net charge of +4. Vacancies on the A, B, and oxygen sites are represented as V_A'', V_B'''', and $V_O^{\bullet\bullet}$, respectively. In this notation, free electrons and holes are represented as e' and $h^{\bullet}$, respectively.

3.3 Equilibrium Point Defects

Equilibrium point defects are thermodynamically generated in order to reduce the free energy of the system and are characterized by an equilibrium concentration. Spontaneous defect generation, therefore, requires a negative change in the free energy (ΔG) [140]:

$$\Delta G = n_d(\Delta H - T\Delta S_{vib}) - T\Delta S_{config} < 0 \tag{3.1}$$

where ΔH is the enthalpy of formation, ΔS_{vib} is the change in vibrational entropy that arises from the change in frequency of vibrating atoms adjacent to the defect compared with those in undisturbed regions of the lattice, ΔS_{config} is the configurational entropy change induced by the formation of n_d defects in a lattice of N atoms. Because the formation of a defect always requires external energy, the reduction in the free energy must come from a negative contribution from the entropic terms. Since the contribution of vibrational entropy to the free energy is small, the equilibrium defects are mainly formed as a result of an increase in configurational entropy [140]:

$$\Delta S_{config} = k_B \, lnW \tag{3.2}$$

where W is the thermodynamic probability representing the number of ways defects can be distributed over the lattice sites. The concentration of defects of a given type (# m^{-3}) under equilibrium conditions, at a given temperature and pressure, can be found by minimizing Equation 3.1 with respect to n_d [140]:

$$n_d \approx Nexp(\Delta S_{vib})exp\left(-\frac{\Delta H}{k_B T}\right). \tag{3.3}$$

Therefore, while the formation of equilibrium defects has an energy cost (*e.g.*, energy required for breaking the bonds in order to form a vacancy), the availability of new ways in which the atoms can arrange themselves leads to an increase in configurational entropy and correspondingly to an overall reduction in free energy. The concentration of such defects increases exponentially with temperature and decreases exponentially with the magnitude of the enthalpy needed to form the defect. At a given temperature and pressure, the probability of observing a specific point defect, therefore, depends on its formation energy. For example, vacancies and substitutional impurities are more common, while interstitial and antisite defects are less likely to form due to the extra energy needed for squeezing an ion into an interstitial site or a lattice site which belongs to an ion of a different size. Chemical driving forces can be also responsible for the formation of such defects. The presence of off-stoichiometry, for example, drives the formation of accommodating defects such as vacancies or more complex defect structures [141]. The concentration and type of equilibrium point defects in ferroelectric thin films, therefore, are strongly dependent on the nature of the synthesis process, growth conditions, and post-growth treatments which can directly affect the thermodynamic parameters and the chemistry of the material.

The defect equilibrium equations and reactions (ionic and electronic defect formations and equilibration of the solid with the gas phase) in ionic oxides need to satisfy the requirements of charge neutrality. The main reactions for an $A^{2+}B^{4+}O_3$ perovskite compound, for example, are:

$$nil \Leftrightarrow e' + h^{\bullet}, \quad (3.4)$$

$$nil \Leftrightarrow V_A'' + V_O^{\bullet\bullet}, \quad (3.5)$$

$$nil \Leftrightarrow V_B'''' + 2V_O^{\bullet\bullet}, \quad (3.6)$$

$$nil \Leftrightarrow V_A'' + V_B'''' + 3V_O^{\bullet\bullet}, \quad (3.7)$$

$$O_O^{\times} \Leftrightarrow O_i'' + V_O^{\bullet\bullet}, \quad (3.8)$$

$$O_O^{\times} \Leftrightarrow {}^1\!/_2\, O_2 + V_O^{\bullet\bullet} + 2e', \quad (3.9)$$

$$A_A^{\times} + {}^1\!/_2\, O_2 \Leftrightarrow V_A'' + 2h^{\bullet} + AO, \quad (3.10)$$

$$A_A^{\times} + O_O^{\times} \Leftrightarrow V_A'' + V_O^{\bullet\bullet} + AO, \quad (3.11)$$

$$B_B^{\times} + O_2 \Leftrightarrow V_B'''' + 4h^{\bullet} + BO_2, \quad (3.12)$$

$$B_B^{\times} + 2O_O^{\times} \Leftrightarrow V_B'''' + 2V_O^{\bullet\bullet} + BO_2. \quad (3.13)$$

In some cases, changes in the valence of cations may occur which also need to be accounted for:

$$3({A^{2+}}_{A^{2+}})^{\times} + {}^1\!/_2\, O_2 \Leftrightarrow 2({A^{3+}}_{A^{2+}})^{\bullet} + V_A'' + AO, \quad (3.14)$$

$$2({B^{4+}}_{B^{4+}})^{\times} + O_O^{\times} \Leftrightarrow 2({B^{2+}}_{B^{4+}})' + V_O^{\bullet\bullet} + {}^1\!/_2\, O_2. \quad (3.15)$$

Donor and acceptor dopants and impurities may also induce the formation of charged ionic defects or free electrons/holes and must be accounted for in similar electroneutrality expressions.

3.4 Non-Equilibrium Point-Defects

In addition to the equilibrium defects that are always present, non-equilibrium defects can be also introduced through energetic processes. For example, in highly-energetic thin-film growth processes such as pulsed-laser deposition, the high kinetic energy of incoming adatoms can provide additional energy for defect formation and change the nature and density of defects [142]. In pulsed-laser deposition, the kinetic energy of the species in the laser-induced plume is approximated to be in the range of 45-1000 eV [143,144]. The velocity of the laser-induced species is around 6×10^5-5×10^6 cm s^{-1} as they emerge from the target, but decreases rapidly as they travel from source material to the substrate due to the frequent collision with the ambient gas molecules inside the deposition chamber [143,145]. The energy of the incident species during growth, therefore, is mainly dependent on the gas pressure and the energy parameters characterizing the laser impact (*i.e.*, the laser energy and the impact surface of the laser on the source material) [146]. The energetic species transfer their energy to the lattice atoms upon impact with the previously deposited material, displace the atoms from their equilibrium positions, and create bombardment-induced point defects [30,31,147]. The presence of heavier species in the plume results in higher concentration of such non-equilibrium point defects. Non-equilibrium defects, therefore, can be formed *in situ* during energetic growth processes.

Non-equilibrium defects can be also induced *ex situ* by exposing a deposited thin film to an energetic ion beam [30,32-34,148- 156]. The incident ions, again, transfer a part of their kinetic energy to the lattice atoms during the collision events and give rise to the creation of bombardment-induced non-equilibrium defects. The displaced atoms may also have enough energy to displace other atoms, leading to collision cascades until the energy given up per collision becomes too small and the cascade ends. Isolated point defects, defect pairs, and more complex defects, such as di-vacancies, tri-vacancies, and larger clusters are known to form as a result of atomic

displacements. In such *ex situ* approaches the nature and the energy of the incoming ions can be easily tuned providing a larger degree of freedom in controlling the type and concentration of non-equilibrium defects as compared to the *in situ* approaches.

Two main energy-loss processes are in effect upon exposure of a crystalline solid to energetic ions [157]: (1) Electronic stopping which involves inelastic collisions between the ions and bound electrons in the solid. The energy transferred from the incident ions to the electrons of the target material gives rise to excitation or ionization of the target atoms and is eventually dissipated as heat. Electronic stopping does not create displacement damage. (2) Nuclear stopping which involves elastic collisions of the ions with nuclei of the solid, in which a part of the kinetic energy of the incoming ion is transferred to the nuclei. Nuclear stopping is responsible for formation of displacement damage.

The relative importance of electronic and nuclear stopping processes depends on the initial energy and mass of the incoming ions, and the mass and atomic density of the solid. A scattering cross section ($S_{e,n}$) can be defined for both electronic and nuclear stopping, and the total energy loss per unit path length of the ions ($\frac{dE_{ion}}{dX_{ion}}$) can be calculated as [157]:

$$-\frac{dE_{ion}}{dX_{ion}} = N[S_n(E_{ion}) + S_e(E_{ion})]. \quad (3.16)$$

The average range (R_{ion}) or the total path length of the ions in the target before coming to rest is defined as [157]:

$$R_{ion} = \frac{1}{N}\int_0^{E_{ion}} \frac{dE_{ion}}{S_n(E_{ion})+S_e(E_{ion})}. \quad (3.17)$$

For a Gaussian distribution of the ions, R_{ion} corresponds to the point of maximum concentration of the distribution. S_n can be approximated as [157]:

$$S_n = 2.8 \times 10^{-15} \frac{Z_1 Z_2}{{Z_1}^{2/3}+{Z_2}^{2/3}} \frac{M_1}{M_1+M_2} \quad (3.18)$$

where M_1 and M_2 are the masses, and Z_1 and Z_2 are the atomic numbers of the target and incident ions, giving rise to an energy loss rate between 10 and 100 eV Å^{-1} for the ion-target combinations of interest. S_e, on the other hand, is proportional to the velocity of the implanted ions, and therefore, to the square root of their energy [157]:

$$S_e = k{E_{ion}}^{1/2} \quad (3.19)$$

where k is a function of N, Z_1, Z_2, M_1, and M_2.

Only the nuclear interactions result in displacement of the target atoms. The total number of atoms displaced by an incoming ion (N_{dis}) can be approximated as [158]:

$$N_{dis} \approx \frac{E_n}{2E_{dis}} \quad (3.20)$$

where E_n is the total energy loss of a particle in primary and secondary nuclear collisions, and E_{dis} is the displacement energy of a lattice atom. Light ions tend to leave tracks characterized by relatively small amounts of damage. They slow down initially mainly by electronic stopping processes with tittle displacement damage, while nuclear stopping becomes dominant at the end of their range. Heavy ions, on the other hand, undergo a relatively higher degree of nuclear stopping, displacing target atoms right from the surface inward. With increasing ion dose, damaged areas begin to overlap leading to amorphization [157]. The critical dose for formation of an amorphous layer strongly depends on the temperature of the sample during ion bombardment and

the dose rate. The probability of recombination of vacancies and interstitials increases at higher temperatures and lower dose rates, leading to a higher critical dose for amorphization. For higher dose rates the sample may heat up, leading to a dynamic self-annealing, in which case an amorphous layer may never form [157]. Furthermore, self-annealing and defect recombination that occur during room-temperature ion bombardment are shown to increase the probability of formation of point-defect complexes [157].

3.5 Impact of Point Defects on the Properties of Ferroelectric Thin Films

The presence of point defects in complex-oxide ferroelectrics has a strong impact on the properties and applicability of these materials. Point defects affect various materials properties in many ways, including the structure, phase transitions, and the ferroelectric, dielectric, electrical, thermal, mechanical, and optical responses. Point defects, for example, can induce mechanical strain fields and structural changes associated with the lattice distortions, give rise to lattice expansion, and impact the electromechanical couplings which are present in ferroelectric materials. Dipolar defects can also shift the ferroelectric-to-paraelectric phase transition temperature [159].

Point defects also have a large impact on the transport properties of complex-oxide ferroelectrics. In general, defect-free complex-oxide ferroelectrics are good insulators. The presence of point defects in such ionic solids, however, can give rise to enhanced conduction through doping the lattice with free electrons/holes (*i.e.*, enhanced electronic conduction), or by introducing mobile charged defects (*i.e.*, enhanced ionic conduction). Oxygen vacancies, for example, often make ferroelectric materials semiconducting because the hopping energy barrier between adjacent oxygen sites is rather low giving rise to ionic conduction which quickly increases at elevated temperatures. Oxygen vacancies can also dope the lattice with free electrons and contribute to electronic leakage. The conduction mechanism and its magnitude, therefore, are closely controlled by point defects [159].

Dielectric properties are also closely related to the presence of point defects. The magnitude of dielectric permittivity and dielectric losses can be altered by the introduction of point defects [159]. In addition, point defects can change the phase-transition temperature of ferroelectrics which in turn can have a large impact on the magnitude of dielectric permittivity which peaks at the transition temperature [159]. Point defects can also change the broadness of the dielectric peak at the phase transition. Relaxor ferroelectrics, for example, exhibit a defuse phase transition and broad dielectric peak near the dielectric maximum due to the presence of point defects [159].

Point defects also play an important role in controlling ferroelectric properties. Ferroelectricity arises from a competition between short-range covalent and long-range Coulombic interactions. The appearance of point defects perturbs such interactions by breaking the long-range periodicity of the crystal structure. Moreover, point defects in ferroelectric oxides are charged and, therefore, can interact with the lattice polarization and domain walls. This defect-polarization coupling, in turn, strongly impacts the ferroelectric properties. Both isolated point defects and defects dipoles, for example, are known to be energetically more stable at domain walls [130,131]. The driving force for this defect displacement may be neutralization of stresses or compensation of electric charges in the domain-wall region. Given enough energy and time, therefore, defects diffuse into the domain-wall regions, and consequently, stabilize the position of the domain walls. This effect is referred to as a “domain-wall effect” and such defects are known to behave as “random-bond” defects [131]. In addition, dipolar defects, are known to have a tendency to reorient

themselves by diffusional processes through the course of time, into new and more energetically-favorable directions (*i.e.*, parallel to the direction of the spontaneous polarization or strain tensor). This alignment, which can be due to both electrostatic and elastic reasons, breaks the degeneracy of polarization states to prefer a certain orientation. This effect is referred to as a "volume effect" and such defects are known to behave as "random-field" defects [131]. Defects, therefore, act as pinning centers for domain-wall motion and make the subsequent field-driven reorientation of the polarization and displacement of domain walls very difficult. This pinning effect of defects is a result of both domain-wall and volume effects, and the pinning strength is directly related to the nature of the point defects [131]. Such defect-polarization interactions result in suppression of remanent polarization, an increase of the energy required for polarization reversal, an increase of the coercive field, a decrease in the speed of polarization reversal, and give rise to internal bias and electrical imprint that shifts and deforms the ferroelectric hysteresis loops and can exacerbate aging and fatigue [12,125,127,131,136-138,147,160-162]. In addition to restricting the domain-wall motion and growth of domains, point defects can also act as nucleation sites for domain formation and polarization reversal [58]. The role of defects in polarization reversal, therefore, is rather complex.

In addition to processes associated with polarization reversal, ferroelectric domain walls may move under weak (sub-switching) fields, strongly impacting the dielectric, mechanical and piezoelectric properties. Domain-wall motion at sub-switching fields occurs either by vibration or bending around an equilibrium position or by small jumps into new equilibrium states. The domain-wall contributions to the properties and losses associated with domain-wall displacements can be strongly impacted by the presence of point defects [12].

CHAPTER 4

Synthesis, Processing, and Characterization of Ferroelectric Thin-Film Heterostructures

This Chapter introduces the techniques and methodologies used for the growth, processing and characterization of ferroelectric thin-film heterostructures studied in this work. Details of pulsed-laser deposition (which is the primary growth method used in this work) including the experimental setup and the optimized growth conditions for epitaxial ferroelectric thin-film systems reported upon herein are described. Details of the device fabrication processes which enable the electrical measurements of the heterostructures are then provided. This is followed by an introduction to the procedures used in this work for *in situ* and *ex situ* control and production of *intrinsic* point defects. The Chapter concludes by introducing the principles of a variety of conventional and advanced techniques used in this work to characterize the induced point defects by probing their impact on the structure, chemistry, topography, as well as ferroelectric, dielectric, and electrical properties of the ferroelectric thin films.

4.1 Synthesis of Ferroelectric Thin Film Heterostructures

4.1.1 Pulsed-Laser Deposition

In this work, pulsed-laser deposition was used for the growth of epitaxial complex-oxide ferroelectric thin-film heterostructures. The widespread use of pulsed-laser deposition for the growth of complex oxides is due to several advantages this technique has over other thin-film growth techniques. Pulsed-laser deposition has attracted considerable interest due to its relatively simple and inexpensive setup, its high throughput, the high quality of the resulting thin films, and the versatility it offers to synthesize a wide range of oxide material systems [142,163,164]. The targets used in pulsed-laser deposition are typically sintered ceramics or single crystals of the desired materials, which are relatively inexpensive and easy to replace. A number of targets can be placed in a single chamber allowing for integration of ferroelectric thin films with dielectrics, metals, superconductors, *etc*. Pulsed-laser deposition also allows for the integration of *in situ* growth monitoring capabilities such as reflection high-energy electron diffraction which enables the surface structure and thickness of the films to be monitored during the growth. Such capabilities, combined with the development of a wider variety of single-crystal substrates and surface treatments has enabled the growth of high-quality epitaxial thin films with unit-cell-level control over thickness, and synthesis of artificial nanostructures and superlattices with atomically sharp interfaces. Finally, pulsed-laser deposition is known (a reputation that is, perhaps, unjustified) as a technique which enables stoichiometric transfer of materials from target to substrate. In reality, a stoichiometric transfer can be only achieved through careful optimization of growth conditions.

Pulsed-laser deposition is a physical vapor deposition technique which deposits a vaporized form of the material onto a substrate. The growth process involves very short and rapid depositions with every laser pulse, followed by annealing in the time intervals between the laser pulses. A high-power pulsed laser is focused on a target of the desired composition. The energy of the incident laser is absorbed by the target which creates a molten layer (*i.e.*, Knudsen layer) and consequently vaporizes the material on the target surface. The high energy density (*i.e.*, fluence) of the laser beam on the target surface (usually 1-5 J cm^{-2}) leads to the formation of a plasma plume [142,163,164]. The plasma plume which contains highly-energetic neutral atoms, ions, electrons, molecules, particulates, and molten globules, rapidly expands away from the target and transfers the material from target to a heated substrate held in the path of the plume with temperatures in the range of 400-800°C. The material transfer involves various mechanisms including thermal, electronic, and macroscopic sputtering. The relative importance of these mechanisms is highly material- and laser-dependent [142,163,164]. The pulsed-laser deposition process typically takes place in a conventional vacuum chamber in the presence of a background gas. The growth of oxides is often done in a reactive oxygen ambient with pressures in the range of 1-500 mTorr.

There are many interactions involved in the pulsed-laser deposition process including interactions between laser and target, laser and plasma plume, species within the plasma, and the plasma plume with the background gas. These interactions have a large impact on the composition and energy of the species in the plume [142,163,164]. There are a large number of "controllable" parameters involved in the pulsed-laser deposition process, such as substrate temperature, laser fluence, laser-pulse repetition rate, nature of the background gas, pressure, target-substrate distance, deposition angle, *etc.*, which affect such interactions, and in turn, have a marked impact on the growth mode, growth rate, chemistry and structure of the synthesized thin films. Growth of

high-quality ferroelectric thin films, therefore, requires a careful optimization of all these parameters.

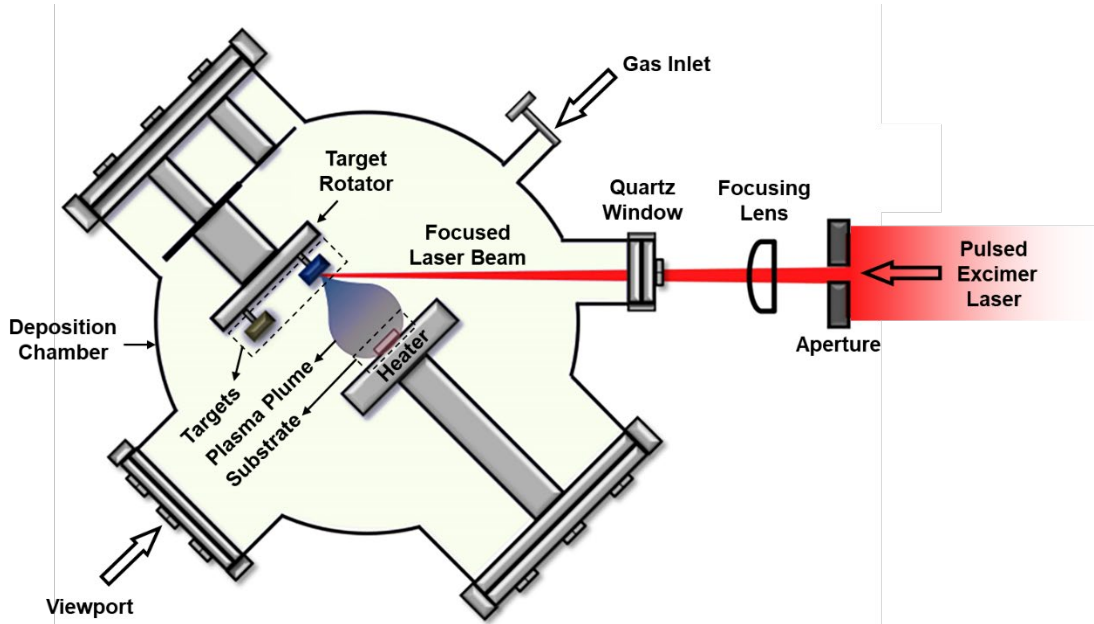

Figure 4.1. Schematic illustration of the pulsed-laser deposition setup used in this work.

In this work, a KrF excimer laser with a wavelength of 248 nm (Compex, Coherent) was used with a pulse width of 10-50 ns and an energy of 50-100 mJ resulting in a power of $\approx 10^7$ W. All depositions were performed using an on-axis geometry with a target-substrate distance of ≈ 6 cm. A schematic of the pulsed-laser deposition setup used in this work is provided (Figure 4.1). The vacuum chamber was equipped with a target holder and a substrate heater. Targets were sanded before being mounted on the target holder and were set to rotate and raster during the growth. The substrates were ultrasonicated for five minutes each in acetone and isopropanol, and then mounted on the heater. All substrates were adhered to the heater using silver paint (Leitsilber 200 silver paint, Ted Pella, Inc.), and cured for fifteen minutes at 60°C. Single-crystalline substrates (Crystec, GmbH), and ceramic targets (Praxair, Inc.) were used for deposition of all films in this work. After mounting targets and substrates, the chamber was pumped down to a base pressure of less than 5×10^{-6} Torr. A variable leak valve was then used to fill the chamber with oxygen gas (99.995% pure) to the desired dynamic growth pressure. The substrates were heated to the growth temperature at a ramp rate of 20°C min^{-1}. Prior to deposition, the targets were pre-ablated to assure that the target surface reached a steady state. Following growth, the chamber was filled with oxygen to promote complete oxidation of the thin films. The substrates were then cooled down to room temperature at a rate of 5-10°C min^{-1} in a static oxygen pressure of ≈ 700 Torr. Growth pressure, temperature, laser-repetition rate, and laser fluence were optimized for every ferroelectric material system used in this work in order to achieve desired composition, phases, and morphologies. The optimized parameters for each material system are provided in Appendix A. Every growth was started with the deposition of a conductive oxide (in this work $SrRuO_3$ or $Ba_{0.5}Sr_{0.5}RuO_3$) to be used as a bottom electrode for subsequent electrical studies, followed by deposition of the ferroelectric film. A top electrode was also deposited after the growth of the ferroelectric layer and patterned in the form of circular capacitors using established *in situ* or *ex situ* techniques which will be discussed in Section 4.2.1. The top electrodes in all cases were grown

at a reduced temperature of 550°C to minimize the loss of volatile elements, while all other growth parameters were the same as for the growth of the bottom electrodes.

4.2 Processing of Ferroelectric Thin-Film Heterostructures

4.2.1 Device Fabrication

All electrical measurements in this study were performed on circular, parallel-plate capacitor structures (*i.e.*, a ferroelectric slab with electrodes on both sides) with diameters varying in the range of 12.5-100 μm (Figure 4.2). Epitaxial conductive perovskite oxides such as $SrRuO_3$ and $Ba_{0.5}Sr_{0.5}RuO_3$ were used as the bottom and top electrodes, due to their excellent chemical and structural compatibility with perovskite-oxide ferroelectrics. The same material was chosen for both the bottom and top electrodes in order to obtain symmetric capacitor structures. These compatible and symmetric electrodes are known to mitigate problems such as delamination from surfaces, formation of dead layers, low thermal stability, high and asymmetric leakage, and electrode-induced fatigue, retention, and imprint [165- 169], which often occur in the presence of elemental metal and asymmetric electrodes. The chemical and structural compatibility of the oxide electrodes also allow for the entire all-oxide heterostructures to be grown epitaxially.

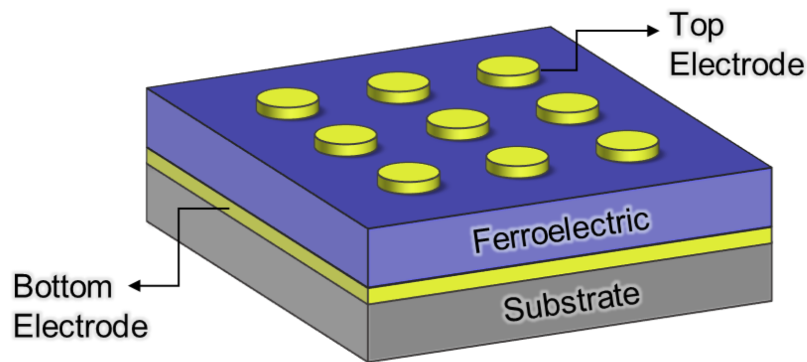

Figure 4.2. Schematic illustration of the parallel-plate capacitor structure used in this work for electrical measurements.

Two approaches were used for fabrication of devices in this study. The first approach was a bottom-up approach [170]. A blanket bottom electrode was first deposited on the substrate followed by the growth of the ferroelectric layer. The stack was then taken out of the pulsed-laser deposition chamber and a layer of photoresist was spin-coated on the surface. Photolithography was then used to create the inverse of the desired final device pattern. The photoresist, therefore, only covered the circular electrode regions. A 200 nm layer of amorphous MgO, to be used as a hard mask for subsequent deposition of the top electrode, was then deposited at room temperature using pulsed-laser deposition. The use of MgO hard-mask enabled growth of epitaxial top electrodes at elevated temperatures. The unwanted MgO (sitting on top of the photoresist) was then lifted off in acetone, and circular device regions became exposed. The exposed surface of the ferroelectric film was oxygen-plasma cleaned to remove any photoresist residue prior to the high-temperature deposition of the top metal oxide. The top electrode was then deposited using pulsed-laser deposition. After growth, the unwanted metal oxide (sitting on top of MgO) was lifted off by etching the MgO in a 15% phosphoric acid solution.

The second approach was a top-down approach where a tri-layer stack consisting of blanket bottom and top electrodes and the ferroelectric layer were grown *in situ* using pulsed-laser deposition. Top contacts were then defined using photolithography and ion-milling. Since the ferroelectric surface is never exposed, this *in situ* approach gives a cleaner interface between the film and the top electrode, but at the same time eliminates the possibility of surface topography and domain structure studies of the ferroelectric film. This approach, therefore, was only used in cases where such studies were not required.

In the present work, the capacitor structures on $BaTiO_3$, $PbTiO_3$, $PbZr_xTi_{1-x}O_3$, and $BiFeO_3$ thin films were fabricated using the *ex situ* bottom-up approach [29-33], while the *in situ* top-down approach was used for processing of $0.68PbMg_{1/3}Nb_{2/3}O_3$-$0.32PbTiO_3$ thin films [34]. The chemistry, geometry, and growth conditions of the electrodes used for each material system are provided in Section 4.1.1 and Appendix A.

4.2.2 Defect Production

4.2.2.1 In Situ Approach. In situ control and introduction of point defects was achieved through variation of the pulsed-laser deposition parameters (*i.e.*, growth pressure, laser fluence, laser-repetition rate, and target composition). Target composition, for example, directly impacts the chemistry of the resulting films, and was used as a knob to control the concentration of *intrinsic* off-stoichiometric point defects [29]. Laser-repetition rate defines the annealing time between subsequent laser pulses at the growth temperature. Lowering the laser-repetition rate increases the annealing time and allows for vaporization and loss of volatile elements from the surface of the growing films. This parameter, therefore, was used in order to control the chemistry of the volatile elements such as lead and bismuth [29,30].

Laser fluence impacts both the chemistry as well as the energy of the adatoms in the plasma plume. Studies focusing on the relationship between laser fluence and film stoichiometry of ABO_3 (wherein A has a higher atomic mass than B) perovskite-oxide thin films have shown that small deviations in laser fluence result in deviations of cation stoichiometry as large as a few atomic percent [171- 177]. These studies suggest that at higher laser fluences preferential ablation of B-site cations occur leading to an A-site cation deficiency. At lower laser fluences, on the other hand, ablation from the target occurs more evenly but leads to a B-site cation deficiency since the lighter B-site cations scatter more readily in the growth gas. Therefore, variations of laser fluence can give rise to the formation of *intrinsic* off-stoichiometric point defects. Laser fluence also impacts the energy of the adatoms in the plume. At higher laser fluences adatoms reach the surface of the growing film with a higher kinetic energy, leading to the displacement of the ions from their lattice sites and formation of *intrinsic* knock-on-damage-induced point defects [31,147]. At the same time, increasing the laser fluence increases the growth rate.

Laser fluence (defined as the laser energy divided by the area of the laser spot on the target), can be controlled by changing the external focusing optics (which changes the laser spot size) or by changing the laser energy. In this work, the laser fluence was controlled via laser energy while maintaining the same spot size [31]. To calculate the fluence values, both laser energy and spot size need to be measured. The laser energy was measured from within the chamber using an energy monitor. To measure the spot size, a single laser shot was fired on a target, and a high-resolution scan of the resulting laser spot on the target was acquired. The scanned images were then processed to find the spot area.

The last parameter used in this work for controlling the type and concentration of *intrinsic* point defects was the growth pressure [30]. The oxidative potential of the growth can be controlled

by changing the nature of the background gas, which in turn, can impact the stoichiometry of the resulting films. Increasing the magnitude of the growth pressure, on the other hand, spatially confines, focuses and sharpens the plume, changes the chemistry of the plume, changes the growth rate, and slows down the adatoms. Such changes are the result of the scattering and diffusion of the species within the plume as the plume expands outward from the target and interacts with the growth gas [178,179]. As a result, changes in the growth pressure can give rise to the formation of both off-stoichiometric and knock-on-damage-induced *intrinsic* point defects [30].

4.2.2.2 Ex Situ Approach. *Ex situ* control and introduction of point defects was achieved via post-synthesis high-energy ion bombardment of the heterostructures. As mentioned in Section 3.4, exposing a ferroelectric thin film to an energetic ion beam results in transfer of energy from the incident ions to the lattice atoms upon collision, giving rise to creation of bombardment-induced *intrinsic* point defects. Two ion bombardment schemes were used in this work which will be discussed in the following.

Bombardment via Defocused Ion Beams. Ion bombardment was carried out in a National Electrostatics Corp. Model 5SDH pelletron tandem accelerator located at Lawrence Berkeley National Laboratory, using He^{2+} ions with an energy of 3.04 MeV and incident angle of 0° (*i.e.*, normal incidence). A large aperture size (comparable to the size of the sample) was used in order to achieve a uniform irradiation across the entire surface of the heterostructures. All ion bombardment experiments were performed at room temperature. The concentration and type of point defects were controlled by varying the ion dose in the range of 10^{14}-10^{16} ions cm^{-2} through controlling the exposure time. The small size and inert nature of the incident ions combined with the high energy of the ion beam allowed for the generation of *intrinsic* point defects without changing the overall chemistry of the thin films and without ion implantation in the heterostructures [30,32,34].

Bombardment via Focused Ion Beams. Ion bombardment was also carried out using a Zeiss ORION NanoFab helium-ion microscope located in the QB3 Biomolecular Nanotechnology Center at the University of California, Berkeley [33]. All ion bombardment experiments were performed at room temperature using a $\approx$ 25 keV, $\approx$ 2 pA ion beam with a nominal probe size of 0.5 nm (10 μm aperture, spot 4, working distance 9 mm) and incident angle of 0° (*i.e.*, normal incidence). It should be noted that the energy of the ions in this case could not be increased above $\approx$ 25 keV. This low ion energy resulted in helium ion implantation in the ferroelectric heterostructures in addition to the formation of *intrinsic* point defects. The small probe size allowed for the position of the induced defects to be controlled with nm-scale precision, while the concentration and type of point defects were controlled by varying the bombardment dose in the range of 10^{12}-10^{15} ions cm^{-2}. Regions of interest for ion bombardment were located under low-dose imaging conditions (10^9 ions cm^{-2}, at least three orders of magnitude lower than the lowest dose used in this study) in order to assure minimal defect formation during imaging. The patterning (in order to expose select regions of the samples to the ion beam) was performed using NPVE software (Fibics, Inc.) selecting a pixel dwell time of 1 μs and a pixel spacing of typically 0.25 nm [33].

4.2.3 Stopping and Range of Ions in Matter (SRIM) Simulations

SRIM simulations were used to predict the implantation and damage profiles at different experimental conditions. SRIM is a group of programs which calculate the stopping and range of ions in matter using a Monte Carlo method [180]. The damage profiles are also obtained from Monte Carlo calculations of the energy given up in atomic stopping processes, or equivalently, of

vacancy production per incoming ion. Transport of ions in matter (TRIM) is the most comprehensive program included in SRIM, which accepts complex targets made of compound materials with up to eight layers, and calculates final 3D distribution of the ions, target damage, defect concentration, sputtering, ionization, and phonon production. In this work, SRIM simulations were performed using SRIM 2013 (srim.org) in the Kinchin-Pease mode [158].

4.3 Characterization of Ferroelectric Thin Film Heterostructures

4.3.1 Structural and Chemical Analyses

4.3.1.1 X-Ray Diffraction Studies. After the synthesis of the ferroelectric thin films, structural characterization was carried out using X-ray diffraction studies. X-ray diffraction was also used after the introduction of point defects in order to probe the effect of the induced defects on the crystalline structure and quality of the films. X-ray studies were performed using a Panalytical X'Pert[3] MRD 4-circle diffractometer with Cu Kα radiation with a wavelength of 1.54 Å. Peak fittings were done in the *X'Pert[3] Data Viewer* software.

X-ray diffraction is a non-destructive characterization technique which relies on the elastic scattering of X-ray photons by the electrons of the atoms in a periodic lattice (*i.e.*, Thompson scattering). During the measurements an incident beam of monochromatic X-rays is focused on a crystalline material. The diffraction process involves the constructive and destructive interference of X-rays scattered from the crystal planes. The scattered X-rays that are in phase give rise to a constructive interference according to Bragg's law [181]:

$$2d_z \sin\theta = n\lambda \tag{4.1}$$

where n is an integer called the order of reflection, λ is the wavelength of X-rays, d_z is the out-of-plane spacing between the crystal planes, and θ is the angle between the incident beam and the normal to the reflecting lattice planes. The θ angle of possible diffraction peaks depends on the size and shape of the unit cell of the material. The intensities of the diffracted waves depend on the kind and arrangement of atoms in the crystal structure [182].

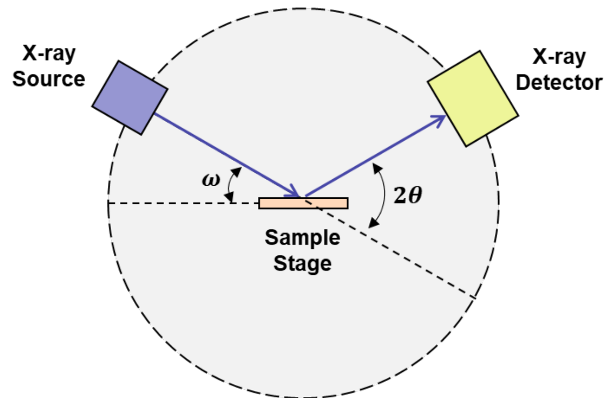

Figure 4.3. Geometry of the X-ray diffractometer used in this work.

The first diffraction method used in this work is $\omega - 2\theta$ scan which measures the Bragg diffraction angles under which the constructively interfering X-rays leave the crystal [182]. The incident angle, ω, is defined between the X-ray source and the sample, while the diffracted angle, 2θ, is defined between the incident beam and detector (Figure 4.3). $\omega - 2\theta$ is a coupled scan in which both angles ω and θ vary continuously but remain linked such that:

$$\omega = \frac{1}{2} \times 2\theta. \tag{4.2}$$

An $\omega - 2\theta$ scan gives a plot of the scattered X-ray intensities as a function of angle 2θ. X-ray peaks occur whenever θ satisfies the Bragg's law. When a film is epitaxially grown on a lattice-matched substrate, $\omega - 2\theta$ scans near the diffraction condition of the substrate also capture the diffraction peaks related to the film. The position, intensity, and shape of the film and substrate

peaks provide information regarding the epitaxial relations, phase, and macroscale crystalline structure of the films, the presence of secondary/impurity phases, the out-of-plane interplanar spacing of every crystallographic phase, the crystalline quality, and film thickness. For example, if a thin film is highly crystalline and homogeneous with pristine surfaces and interfaces, so-called Laue fringes can occur in $\omega - 2\theta$ scans [183]. The thickness of the film can be also approximated from the periodicity of the Laue fringes [184]. Moreover, the strain condition of the film and lattice mismatch between the film and substrate can be estimated from these measurements wherein the in-plane misfit strain can impact the out-of-plane lattice spacing through Poisson's ratio, and thus, cause a shift in the peak position.

The next X-ray diffraction technique used in this work is ω scan or so-called rocking-curve measurement. In this measurement, the 2θ angle of the detector is fixed to the Bragg's angle (θ_B), while ω is changed in the vicinity of θ_B [182]. A rocking curve, therefore, is a plot of X-ray intensity as a function of ω angle. Rocking curves were used in this work in order to determine the crystalline quality of the thin films since the presence of imperfections and crystal mosaicity can lead to the broadening of the rocking-curve peaks. The full-width at half-maximum (FWHM) of the peaks are known to be a direct measure of the crystalline quality.

The last X-ray diffraction technique used in this work is reciprocal space mapping, which probes the Bragg diffraction in a confined area of reciprocal space [182]. A reciprocal space map is collected by performing $\omega - 2\theta$ coupled scans at different ω-offsets such that:

$$\omega = \frac{1}{2} \times 2\theta + offset. \tag{4.3}$$

Reciprocal space mapping was used in order to analyze the crystal structure, lattice parameters, and strain condition of the ferroelectric thin films studied in this work. Two-dimensional reciprocal space mapping was also applied to relaxor $0.68PbMg_{1/3}Nb_{2/3}O_3$-$0.32PbTiO_3$ thin films in order to probe the impact of point defects on the morphology of polar nanodomains in these materials.

4.3.1.2 Rutherford Backscattering Spectrometry. Rutherford backscattering spectrometry studies were used to analyze the chemistry of the thin-film heterostructures in order to assure that nearly stoichiometric compositions were achieved, and after introduction of *intrinsic* point defects in order to probe the effect of such defects on the overall chemistry of the films. Rutherford backscattering spectrometry is an ion-scattering technique used for compositional thin film analysis [185]. This technique allows for quantification of the film chemistry with 1-2% error without the need for reference standards. During a Rutherford backscattering spectrometry measurement, a beam of high-energy ions is directed onto

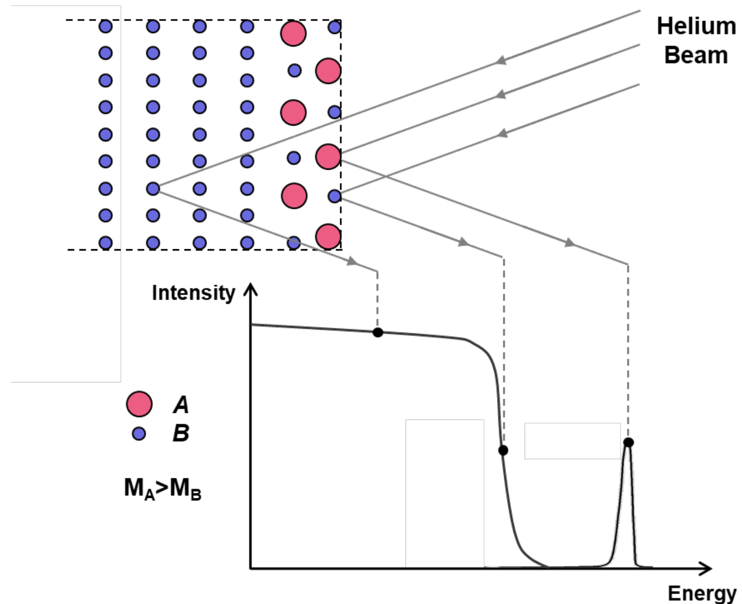

Figure 4.4. Schematic illustration of basic principles of Rutherford backscattering spectrometry.

the sample, and the energy and intensity of the backscattered ions are measured at a given angle. Some ions are elastically scattered from the surface of the film while others penetrate into the film and lose some energy and become backscattered at various depths. Rutherford backscattering spectrometry measurements provide a quantitative compositional depth profile by plotting the number of backscattered ions as a function of their energy and provides information on the nature of the various elements present in the target, their relative ratios, and their depth distribution [Figure 4.4]. The energy of the backscattered ions is dependent on the atomic masses of the elements present in the film and is higher for heavier elements. This mass separation allows for identification of the elements present in the film. The energy of the backscattered ions is also dependent on the penetration depth of the ions. The energy is higher for ions backscattered from a shallower depth compared to those backscattered from larger depths. Therefore, depth distribution of elements and thickness of the thin films can be obtained from Rutherford backscattering spectrometry measurements. The relative intensity of the peaks related to each element provides information about the stoichiometry of the films.

In this work, Rutherford backscattering spectrometry was mostly used for identifying the cation chemistry with an accuracy of 1-2% (that is a change of $A_1B_1O_3$ cation chemistry by 0.01 out of 1). Operating the measurements at an incident ion-beam energy of 3.040 MeV, which corresponds to the oxygen-resonance energy [186], also allows for the simultaneous extraction of anion chemistry. Oxygen exhibits an increased scattering cross-section at this resonance energy, and thus, high scattering intensities. The reaction $^{16}O(\alpha,\alpha)^{16}O$ can be modelled by non-Rutherfordian cross sections which are larger than conventional cross sections, allowing for quantification of the anion concentrations. For this purpose, scattering cross-section parameters for the exact geometry of the instrument and the energy range of ions used in the experiments must be found from previously reported values in the literature [187]. However, due to the errors associated with the cross-section parameters and scattering angles, as well as sensitivity of the fits of the resonance peaks to a wide variety of input parameters [188], and difficulties associated with fitting the low-energy tail of the resonant peaks, the estimations of oxygen chemistries with better than $\approx$ 3% accuracy (that is a change of $A_1B_1O_3$ anion chemistry of 0.1 out of 3) is difficult. In this work, therefore, studies of anion chemistry were focused on the trends of oxygen content rather than the exact numbers themselves. Finally, in order to limit the influence of non-resonance scattering from the oxygen present in the substrate the energy loss of the incident He^{2+} ions as they transit through the heterostructure thickness was calculated using SRIM simulations [180] and compared to the 0.01 MeV FWHM of the oxygen scattering cross-section. The He^{2+} ions were found to lose 0.01 MeV upon transiting through the first 45 nm of the heterostructures from the surface. Thus, 45 nm was considered to be the depth limit for resonant peak fitting and only information pertaining to the top 45 nm of all heterostructures was used to quantify the oxygen chemistry.

Rutherford backscattering spectrometry measurements in this work were performed using a National Electrostatics Corp. Model 5SDH pelletron tandem accelerator located at Lawrence Berkeley National Laboratory. The accelerator provides a He^{2+} ion beam (*i.e.*, alpha particles) with an energy of 3.04 MeV. A Cornell geometry with an incident angle of 22.5°, an exit angle of 25.35°, and a scattering angle of 168° was used. Following the measurements, fits to the experimental data were completed using the built-in fitting program in the Rutherford backscattering spectrometry analysis software SIMNRA (simnra.com), which uses a Simplex algorithm for the fitting [189]. The quality of the fits was evaluated using a least-squares method in which the so-called R^2 values are defined as:

$$R^2 = 1 - \frac{\sum(I_i^e - I_i^f)^2}{\sum(I_i^e - \bar{I}^e)^2} \quad (4.4)$$

where I^e and I^f correspond to experimental and simulated data, respectively. R^2 values were calculated about the peaks of interest to avoid artificially increasing the R^2 value by the inclusion of substrate peaks.

4.3.1.3 Scanning Transmission Electron Microscopy (STEM). High-resolution STEM analysis was attempted to directly image the induced point defects in the ferroelectric thin film heterostructures. Although high-resolution transmission electron microscopy has attained near-atomic resolution in recent years, it still provides limited information regarding point defects, especially in the presence of low defect concentrations. As a result, this technique was not extensively used in this work. Instead, most point defects were characterized by indirect methods.

Cross-sectional TEM specimens were prepared by tripod mechanical polishing at an angle of 1° followed by low-angle argon-ion milling at 4 keV. The samples were glued to a pristine $SrTiO_3$ wafer prior to polishing to confirm that defects were not induced through the sample preparation process. High-angle annular dark-field STEM (HAADF-STEM) and low-angle annular dark-field STEM (LAADF-STEM) images were acquired on a F20 UT Tecnai operated at 200 keV. The HAADF-STEM provides chemical information in the form of *Z*-contrast, while LAADF-STEM is additionally sensitive to structure or anything that dechannels the transiting electrons (*e.g.*, phonons or strain fields from point defects) [190,191].

4.3.2 Surface Topography and Domain-Structure Analyses

4.3.2.1 Scanning Probe Microscopy. Atomic force microscopy and piezoresponse force microscopy, two most-widely used scanning-probe microscopy techniques, were used to probe the microscale surface topography, domain structure, and switching properties of the ferroelectric thin films [192-195]. These techniques were also applied to the films after introduction of point defects in order to study the effect of such defects on the topography, domain structure and microscale ferroelectric switching response. Atomic and piezoresponse force microscopy studies in this work were performed using an MFP-3D microscope (Asylum Research).

In atomic force microscopy a sharp cantilever with a tip radius of 5-10 nm is rastered over the surface (using a piezoelectric actuator) in order to image the surface topography of the films. atomic force microscopy relies on the forces between the cantilever and the sample (*i.e.*, short-range repulsive and long-range attractive forces) which lead to a deflection of the cantilever according to Hooke's law [196]. In order to monitor the deflection and motion of the cantilever, a laser beam is reflected from the back of the cantilever and onto a position-sensitive photo-detector. Atomic force microscopy can be performed in static contact mode or dynamic tapping mode. In contact mode, the tip is in firm contact with the surface and the surface features are probed using the deflection of the cantilever or using a feedback loop which attempts to keep the cantilever at a constant position. In tapping mode, a piezoelectric actuator in the cantilever drives it to oscillate up and down at or near its resonance frequency and the tip is in intermittent contact with the surface of the film. The tip-surface forces change the amplitude of the cantilever's oscillations as the tip gets closer to the surface. The feedback loop adjusts the cantilever height in order to maintain the oscillation amplitude [197]. Atomic force microscopy studies in this work were performed in tapping mode using silicon tips with aluminum reflex coating on the detector side (BudgetSensors, Tap300AL-G). Atomic force microscopy scans were obtained in order to assure that the grown films were smooth, uniform, free from holes, particles, and second phases.

In piezoresponse force microscopy, on the other hand, application of an alternating current (AC) electric field through a conductive cantilever is used to generate oscillations in the sample surface according to a converse piezoelectric effect, which in turn, gives rise to a deflection of the cantilever. The cantilever deflection is often amplified by exciting the cantilever at (or near) its resonance frequency. In this work, a dual-frequency resonance tracking approach was applied which uses two frequencies to excite, measure, and track the resonance [193]. The cantilever deflection is then detected by a photodiode and processed in order to retrieve the amplitude and phase of the surface piezoresponse. Since the magnitude of the piezoresponse depends on the magnitude of polarization and the phase depends on the direction of the polarization, this technique can be used to locally probe the domain structure of ferroelectric thin films [192-194]. Probing both vertical and lateral deflection of the cantilever allows for construction of three-dimensional polarization configuration images. Application of a direct current (DC) electric field to the cantilever also allows for local manipulation of the polarization vector and polarization switching. Piezoresponse force microscopy scans in this work were carried out in dual-frequency resonance tracking mode using platinum/iridium-coated conductive tips (Nanosensor, PPP-EFM, force constant ≈ 2.8 N m^{-1}).

4.3.2.2 Band Excitation Piezoresponse Spectroscopy. Band excitation piezoresponse spectroscopy is a multifrequency piezoresponse force microscopy technique wherein the piezoresponse is measured using a band-excitation waveform at remanence throughout a bipolar triangular switching waveform [198]. Following fitting the cantilever response to a simple harmonic oscillator model using a fast-Fourier transform, the piezoresponse amplitude and phase, as well as cantilever's resonance frequency, loss, and quality factor can be extracted and used to visualize the switching process with a high accuracy in the measured piezoresponse (Appendix B).

Band excitation piezoresponse spectroscopy studies in this work were performed at the Center for Nanophase Materials Sciences at Oak Ridge National Laboratory using a custom Cypher (Asylum Research) atomic force microscope. All measurements were carried out using platinum/iridium-coated conductive tips (NanoSensor PPP-EFM, force constant ≈ 2.8 N m^{-1}). The cantilever response was measured in the time domain at remanence at various voltage steps throughout a bipolar-triangular switching waveform applied in a square-grid as mentioned in Appendix B. The magnitude of the waveform was chosen to be large enough to fully saturate the piezoelectric hysteresis loops. The local piezoresponse was measured at remanence (following a dwell time of 0.5 ms), with a band excitation waveform of sinc character (peak-to-peak voltage of 1 V). The band excitation piezoresponse spectroscopy data was analyzed and piezoelectric loop fits were performed by making custom adjustments (colors, adjusting code to highlight the parameters of interest, *etc.*) to the pycroscopy data analysis python package developed by the Center for Nanophase Materials Sciences at Oak Ridge National Laboratory. Further quantification of the results was achieved by extraction of the average piezoelectric loops and the "work of switching" which is defined as the area within the piezoelectric loops. The average piezoelectric loops were extracted by fitting the amplitude and phase response which were then rotated in order to obtain a flat top and bottom, by adding the opposite sign of the slope of the raw loops to each data point.

4.3.3 Electrical Characterization

All electrical characterizations in this work were performed on circular capacitor structures as described in Section 4.2.1.

4.3.3.1 Dielectric Measurements. In dielectric measurements, the complex dielectric permittivity of ferroelectrics can be probed as a function of frequency, DC electric field, AC excitation field, and temperature, providing a wealth of information about the material. The dielectric susceptibility was measured on parallel plate capacitor structures, where a small AC voltage was applied in the out-of-plane direction to measure both real and imaginary impedance parameters which in turn can generate dielectric capacitance and loss tangent ($tan\,\delta$) values. The out-of-plane component of the dielectric constant or relative permittivity (ε_r) can be calculated from the capacitance value (C):

$$\varepsilon_r = \frac{Cd}{\varepsilon_0 A} \tag{4.5}$$

where A is the capacitor area.

Dielectric measurements in this work were carried out using an impedance analyzer (E4990A, Keysight Technologies) or an LCR meter (E4890, Keysight Technologies) as a function of frequency, DC bias, and temperature. The AC excitation voltage was chosen such that it was safely in the reversible regime and excluded the dielectric non-linearities due to the irreversible extrinsic contributions. Bellow a threshold voltage the dielectric response is independent of the magnitude of the applied electric field and is dominated by the small-signal reversible response of the material. At larger electric fields, due to the irreversible domain-wall motion and switching effects the response is no longer field-independent. The reversible regime was identified through Rayleigh measurements which probe the dielectric constant as a function of AC excitation voltage at a given frequency [199,200].

4.3.3.2 Ferroelectric Hysteresis Measurements. Ferroelectric polarization-electric field hysteresis loops were obtained by application of an external bipolar triangular voltage profile (Figure 4.5) to the capacitor structures at various frequencies in the range of 0.1-100 kHz. All measurements were performed using a Precision Multiferroic Tester (Radiant Technologies, Inc.) which measures the change in the charge of the ferroelectric capacitors in response to the voltage profile. The polarization values were then obtained by dividing the measured change of the charge by the area of the capacitor. Characteristic switching values such as saturation polarization, remanent polarization, and coercive field were extracted from the hysteresis loops. As mentioned in Chapter 2, ferroelectric hysteresis loops are often asymmetric. In such cases, average values were reported:

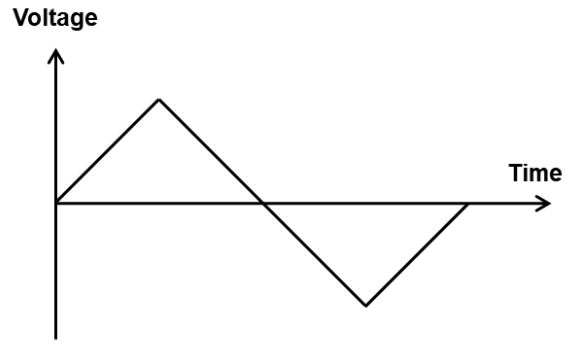

Figure 4.5. The voltage profile used in this work for ferroelectric hysteresis-loop measurements.

$$\bar{E}_C = \frac{|E_C^+|+|E_C^-|}{2} \text{ (average coercive field)}, \tag{4.6}$$

$$\bar{P}_{Sat} = \frac{|P_{sat}^+|+|P_{sat}^-|}{2} \text{ (average saturation polarization)}, \tag{4.7}$$

$$\bar{P}_r = \frac{|P_r^+|+|P_r^-|}{2} \text{ (average remanent polarization)}. \tag{4.8}$$

Such asymmetry also gives rise to an electrical imprint which was extracted according to Equation 2.17.

4.3.3.3 Macroscale Switching Kinetics Measurements. Macroscale switching-kinetics studies provide information on the speed and energy requirements of, and the underlying mechanism for polarization switching. As mentioned in Section 3.5, defects can have a large impact on the switching behavior of ferroelectrics by controlling the local polarization stability, acting as pinning sites for domain-wall motion, and nucleation sites for polarization reversal [12,58,131]. Therefore, it is both scientifically and technologically important to understand the switching behavior of ferroelectric thin films in the presence of defects.

In order to study the switching kinetics, standard pulse measurements were used, in which the change of polarization was probed as a function of pulse width and amplitude according to the established voltage-pulse sequences (Figure 4.6) [201]. The measurements were performed using a Precision Multiferroic Tester (Radiant Technologies, Inc.), by first pre-poling the capacitors in the positive direction using a voltage pulse with a duration of $t_1 = 0.015$ ms. The magnitude of this poling voltage pulse was specifically chosen to assure a full saturation of the polarization in the positive direction. A second positive voltage with the same magnitude and duration as the pre-poling pulse was then applied to allow for calculation of unswitched polarization (P_{ns}). Then a voltage pulse with varying amplitude (V_i) and varying duration (t_i, in the range of 0.0005-0.5 ms) was applied in the negative direction. The next voltage pulse was applied in the positive direction with the same magnitude and duration as the first and second pulses. This pulse allowed for measurement of the switched polarization (P_{sw}). The delay time between all pulses was set to $t_0 = 1$ ms. The total remanent polarization at each voltage V_i was calculated as:

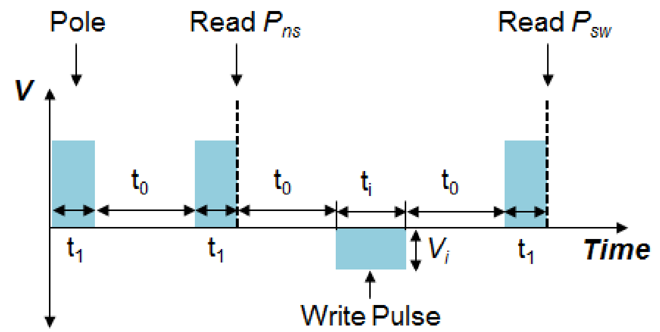

Figure 4.6. Sequence of voltage pulses used in this work for switching kinetics measurements.

$$\Delta P(t) = P_{sw} - P_{ns}. \tag{4.9}$$

The Kolmogorov-Avrami-Ishibashi model is commonly used to fit the experimental switching data [202,203]. According to the classical statistical theory of nucleation and unrestricted domain growth, the polarization for epitaxial ferroelectric thin films varies with time as [204]:

$$\Delta P(t) = 2P_S[1 - \exp(-t/t_s)^{n_s} \tag{4.10}$$

where n_s is the geometric dimension and t_s is the characteristic switching time (*i.e.*, average distance between the nuclei divided by domain-wall speed). The values of $1/t_s$ at each field are assumed to be proportional to the switching speed (ϑ) [204], and are used to find the relation between switching speed and electric field, in order to identify the characteristic switching behavior. As predicted by classical models, domain-wall velocity varies nonlinearly with electric field, and can be classified into creep (*i.e.*, thermally-activated, slow propagation of domain walls between pinning sites (*e.g.*, local disorder such as defects)), depinning (*i.e.*, transition from creep to flow), and flow (*i.e.*, motion of domain walls free from pinning sites) regimes [204]. Under low electric fields (*i.e.*, creep regime), the domain-wall motion is slow and is described by propagation between pinning sites (*e.g.*, defects) due to thermal activation [204]:

$$\vartheta \sim \exp[-(\frac{U}{k_B T})(\frac{E_{C0}}{E})^{\mu_s}] \quad (4.11)$$

where U is an energy barrier, and μ_s is a dynamical exponent reflecting the nature of pinning potential [*i.e.*, long-range-random field ($\mu_s = 1$ regardless of the dimensionality of the domain walls) or short-range-random bond ($\mu_s = 0.25$ for one-dimensional and $\mu_s = 0.5$ for two-dimensional domain walls)] [204]. At very low temperatures (*i.e.*, close to 0 K), the domain wall remains strongly pinned by local disorder until the electric field reaches a threshold value E_{C0}. At higher fields, it experiences a pinning-depinning transition and starts to move with a non-zero velocity [204]:

$$\vartheta \sim (E - E_{C0})^{\theta_s} \quad (4.12)$$

where θ_s is the velocity exponent reflecting the dimension of the growth surface. In the flow regime, when $E \gg E_{C0}$, velocity scales linearly with field [204]:

$$\vartheta \sim E. \quad (4.13)$$

Since at low temperatures, defect-involved creep motion will be deactivated, low-temperature measurements allow one to directly probe the threshold activation field for the transition between defect-driven creep and intrinsic flow motion.

4.3.3.4 Positive-Up-Negative-Down (PUND) Measurements. Another pulse-switching measurement used in this study is the PUND measurement which probes the change of polarization as a function of pulse amplitude at a constant pulse width. This is in contrast to the pulse sequence used in the switching-kinetics measurements which probes the polarization change as a function of pulse width at a constant amplitude.

A modified PUND pulse sequence was used in this study (Figure 4.7). Each measurement cycle consisted of three pulses with equal voltages and widths. The pulse width was kept constant ($t_1 = 0.1\ ms$), while the pulse voltage was varied incrementally for different cycles. The delay time between all pulses was set to $t_0 = 1\ ms$. The positive remanent switched polarization was measured at 0 V after the positive reading pulse was switched off ($+P_i^r$). The measurements were performed using a Precision Multiferroic Tester (Radiant Technologies, Inc.).

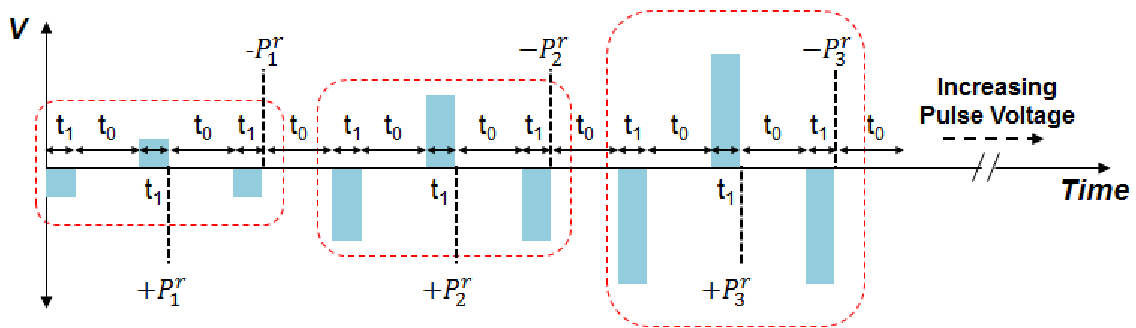

Figure 4.7. The modified PUND pulse sequence used in this work.

4.3.3.5 Retention Measurements. Retention measurements were used to probe the stability of the polarization states and long-term reliability of the ferroelectric devices (Figure 4.8). The retention pulse sequence was used to measure the variation of remanent polarization as a function of time. Each polarization state was first accessed using an appropriate pulse width and voltage, extracted from the PUND measurements. The system was then held at 0 V for various retention

times (t_{Ri}), after which a reading pulse was applied to read the variation in switched polarization ($+P_i^r$). The measurements were performed using a Precision Multiferroic Tester (Radiant Technologies, Inc.).

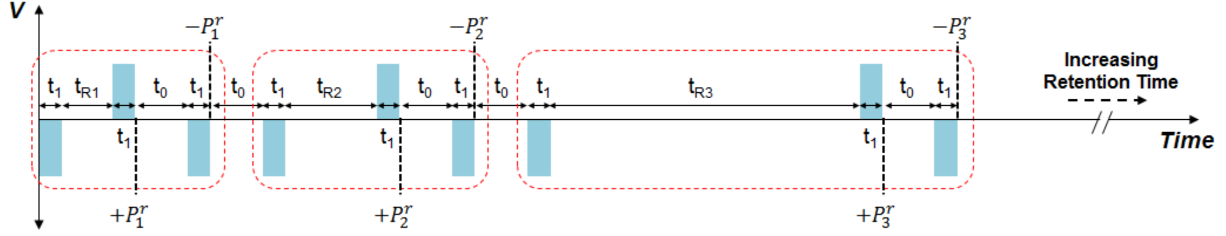

Figure 4.8. The pulse sequence used in this work for retention measurements.

4.3.3.6 First-Order Reversal Curve Analysis. Although switching-kinetics studies provide valuable information about polarization switching dynamics at the macroscale, the switching process can vary locally due to the presence of disorder and randomness in the system [205]. Therefore, macroscopic switching kinetics measurements and single major hysteresis loops measured between saturation fields are insufficient to fully describe the switching process. First-order reversal curve measurements (which involve measurement of multiple minor hysteresis loops), on the other hand, can provide additional information on the characteristic microscopic mechanisms involved in the switching process [206-208]. First-order reversal curve diagrams show a statistical distribution of the bistable elementary switchable units (*i.e.*, hysterons) over their coercive and bias fields, in relation to the Preisach model [209]. In other words, they provide a map of the density of microscopic bistable polarizing units as a function of switching fields (*i.e.*, a population/probability map of the switching fields), offering a graphical method to probe the (in)homogeneity of the switching events.

The experimental first-order reversal curve studies can be performed by measurement of multiple minor hysteresis loops at a given frequency using a monopolar triangular voltage profile and probing the field-dependence of the polarization between a fixed saturation field and various reversal fields (E_r), following either ascending or descending branches of the major hysteresis loop. In this work, first-order reversal curve measurements were carried out between a fixed negative saturation field and a variable reversal field following the ascending branch of the major hysteresis loop using a Precision Multiferroic Tester (Radiant Technologies, Inc.). A first-order reversal curve diagram represents a contour plot of the first-order reversal curve distribution, which is defined as the mixed second derivative of polarization with respect to actual electric field and reversal field [208]:

$$\rho(E_r, E) = \frac{1}{2}\frac{\partial^2 P_{FORC}(E_r,E)}{\partial E_r \partial E}. \tag{4.14}$$

The first-order reversal curve distribution was determined using previously established numerical methods [210,211]. This representation describes the variation of polarization with respect to changes in E_r and E. One can change the coordinates of the first-order reversal curve distribution from E_r and E to E_c (local coercive field) and E_i (local bias/interaction field), where:

$$E_c = \frac{E-E_r}{2}, \tag{4.15}$$

$$E_i = \frac{E+E_r}{2}. \tag{4.16}$$

This coordinate represents the distribution of switchable units over their coercive and bias fields. In this representation of the first-order reversal curve data, the distributions along the bias and coercive-field axes correspond to the reversible and irreversible contributions to the total polarization, respectively [208].

In this work, first-order reversal curve distributions were constructed in order to qualitatively study the effect of point defects on the distribution of the coercive and bias fields of the elementary switchable units. However, if extraction of further quantitative information on the dynamics of the switching process from the first-order reversal curve measurements is desired, the so-called dynamic/moving Preisach models of hysteresis which account for the time-dependent nature of the response via introduction of single or multiple relaxation times into the classical model are required [212].

4.3.3.7 Current-Voltage (Leakage) Measurements. Current-voltage measurements were used to study the transport properties and to identify the dominant conduction mechanisms and trap states. The measurements were carried out using a Keithley 6517B programmable electrometer (Keithley/Tektronix) or a Precision Multiferroic Tester (Radiant Technologies, Inc.) over a temperature range of 300-470 K. The measurements were performed in both positive and negative polarities, using an unswitched triangular voltage profile which uses a pre-poling pulse in order to prevent any contributions from switching currents (Figure 4.9).

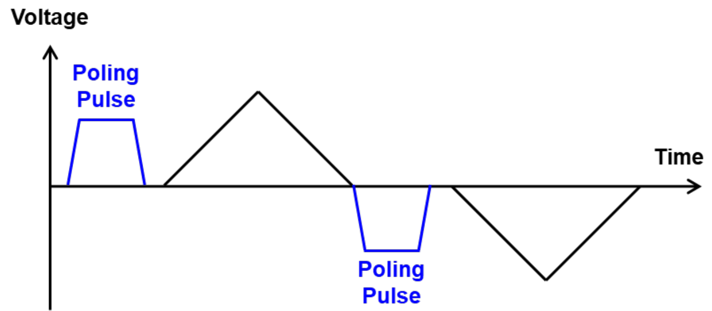

Figure 4.9. The unswitched triangular voltage profile used in this work for current-voltage measurements.

4.3.3.8 Impedance Spectroscopy. Impedance spectroscopy is a powerful technique capable of differentiating between different contributions to the overall resistive response of a material. Nyquist impedance plots (*i.e.*, imaginary *vs.* real) can contain several semicircles wherein each semicircle is characteristic of a single time constant [213,214]. Presence of multiple semicircles in the complex-impedance plane can be attributed to bulk and grain-boundary responses, presence of mixed conduction (*i.e.*, both electronic and ionic), contribution from surface layers, or sample-electrode interfaces. In this work, impedance spectroscopy measurements were used to gain information on whether the changes in the resistivity of the ferroelectric thin films as a result of defect introduction were related to the bulk effects or interfacial effects (*i.e.*, changes at the film-electrode interfaces, or from the formation of surface layers due to the possibility of defect accumulation at the interfaces).

In impedance spectroscopy, the real and imaginary contributions to the impedance are measured as a function of frequency. An alternating sinusoidal electric field is applied to a capacitor:

$$E(t) = E_0 \sin(\omega t) \tag{4.17}$$

and the phase-shifted current response is measured as a function of angular frequency (ω):

$$I(t) = I_0 \sin(\omega t + \varphi) \tag{4.18}$$

where φ is the phase difference between electric field and current [140]. The impedance (Z) can be extracted as:

$$Z = \frac{E(t)}{I(t)}. \tag{4.19}$$

For purely resistive behavior $\varphi = 0$, for purely capacitive behavior $\varphi = -90°$, and for purely inductive behavior $\varphi = +90°$. The response is often presented in a Nyquist complex plane which plots the imaginary part of the total impedance on the y-axis [140]:

$$Z_{Img} = Z \sin \varphi \tag{4.20}$$

and the real part on the x-axis:

$$Z_{Real} = Z \cos \varphi. \tag{4.21}$$

The results form single or multiple semicircles (often only a portion of the semicircles are observed) related to the processes of various time constants. Every semicircle, therefore, is characteristic of a single time constant (Figure 4.10). The semicircles must be modeled using an equivalent circuit in order to differentiate various contributions. A ferroelectric capacitor can be modeled as a resistor with resistance R in parallel with a capacitor with capacitance C. The low-frequency intercept of the semicircle with the x-axis gives the value of resistance, and the inverse of the frequency at the arc maximum gives the time constant of the process [140]:

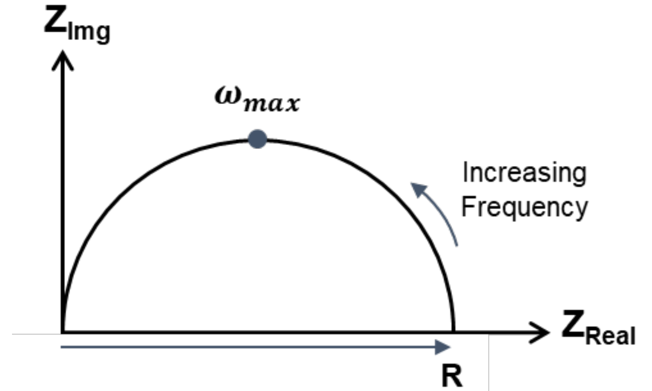

Figure 4.10. Schematic representation of a Nyquist complex-impedance plane.

$$\tau = \frac{1}{\omega_{max}} = RC. \tag{4.22}$$

Impedance spectroscopy measurements in this work were performed using a Gamry Instruments-Reference 600 potentiostat, under an oscillation voltage of 8 mV_{rms}, in a frequency range of 10 mHz-1 MHz. The AC amplitude was chosen to be high enough to avoid noise but low enough for the response to be linear or pseudo-linear.

4.3.3.9 Deep-Level Transient Spectroscopy. Deep-level transient spectroscopy is a powerful experimental technique, which can be used to detect a wide variety of inter-gap charge-carrier trap states (*i.e.*, electrically active defects) in a material. It is a high-frequency capacitance transient thermal scanning method which probes the trap states in the depletion region of a Schottky barrier or p-n junction. Deep-level transient spectroscopy provides a spectrum of traps present in a material as peaks on a flat baseline as a function of temperature [215]. An electron trap is defined as one which tends to be empty of electrons, and thus, capable of capturing them. A hole trap, on the other hand, is one which tends to be full of electrons, and thus, capable of capturing holes through recombination with electrons. Electron traps tend to be in the upper half of the band gap and hole traps in the lower half. The sign of a deep-level transient spectroscopy peak indicates whether the trap is near the conduction or valence band, the height of the peak is proportional to the trap concentration, and temperature of the peak maximum is determined by the thermal emission properties of the trap which can be used to extract the trap activation energy [215].

In deep-level transient spectroscopy measurements, a voltage pulse (*i.e.,* a trap-filling pulse) is applied which introduces charge carriers into the depletion region of a Schottky barrier or p-n junction, and thus, changes the occupation of the electron/hole traps from their equilibrium value [215]. A capacitance change is caused as a result of this change in the traps occupation. After the voltage pulse is removed, the defects start to emit trapped carriers through thermal emission processes, and the capacitance returns to its quiescent value as the trap population returns to its equilibrium. The emission rates are temperature-dependent and proportional to a Boltzmann factor, and thus, depend exponentially on the energy difference between the trap level and the conduction band (electron emission) and the trap level and the valence band (hole emission). Therefore, the activation energy for the traps can be extracted by measuring the time constant of this capacitance transient associated with the return to thermal equilibrium of the occupation of the level as a function of temperature, following an initial nonequilibrium condition.

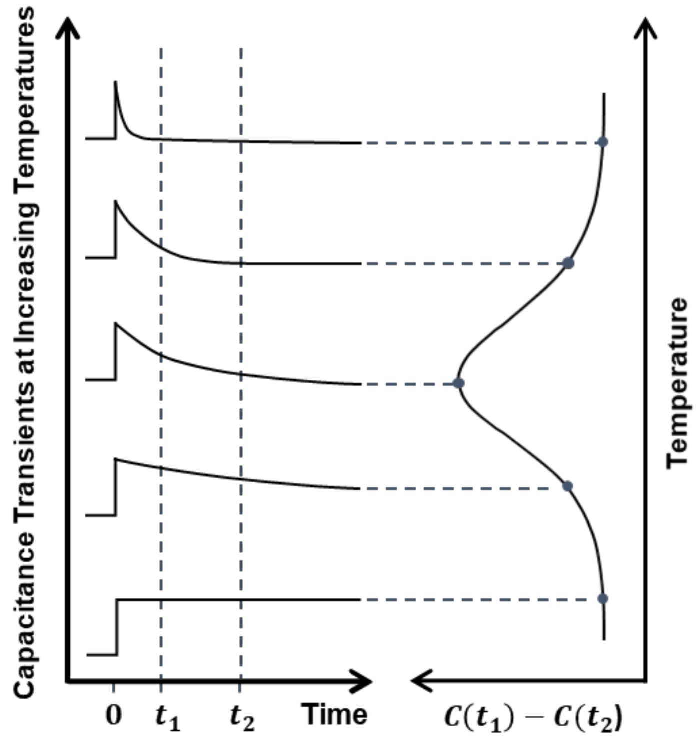

Figure 4.11. Basic principles of deep-level transient spectroscopy.

In order to achieve this, the measurement setup needs to provide the ability to set multiple emission rate windows (set between measurement times t_1 and t_2) such that the sensing apparatus only responds when it sees a transient within this window [215]. Deep-level transient spectroscopy signal is the difference in transient capacitance $C(t_i)$ measured between times t_1 and t_2 after removal of the trap-filling pulse, and as a function of temperature (Figure 4.11). As mentioned previously, the emission rate of trap states is temperature-dependent. It is very small for low temperatures and increases as the temperature is increased. Thus, by varying the temperature, the emission rate of a trap is varied, and a response peak is measured at the temperature where the trap emission rate is within the measurement window. Each peak is related to a single trap state with its characteristic thermal emission properties.

In order to determine the activation energies of the trap states, the deep-level transient spectroscopy signal needs to be measured at different rate windows by varying t_1 and t_2 [215]. This gives rise to a shift of the peaks in temperature. The emission rate of a deep level with a peak maximum located at temperature T_m is defined as:

$$e(T_m) = \frac{t_2 - t_1}{\ln(\frac{t_2}{t_1})} \tag{4.23}$$

and the temperature dependence of the maximum emission rate is given by:

$$e(T_m) = \gamma\sigma_c T_m^2 \exp(-\frac{E_d}{k_B T_m}) \quad (4.24)$$

where E_d is the activation energy, σ_c the capture cross section, and γ is the pre-exponential factor. The activation energy can be extracted from the slope of linear fits to an Arrhenius plot of $\ln(\frac{T_m^2}{e(T_m)})$ *vs.* $\frac{1000}{T_m}$.

The parameters t_1 and t_2 can be varied by: (1) t_1 fixed, t_2 varied, (2) t_1 varied, t_2 fixed, (3) both t_1 and t_2 varied, but $\frac{t_1}{t_2}$ fixed [215]. In this work the fixed ratio scheme was chosen for varying the rate windows, since it shifts the peaks without giving rise to any change in their size and shape. A fixed $\frac{t_1}{t_2}$ ratio also makes the data reduction easier. In methods (1) and (2), on the other hand, the peaks change considerably in both size and shape with the low (high)-temperature side moving as t_2 (t_1) is varied, while the high (low)-temperature side moves very little [215].

Deep-level transient spectroscopy measurements in this work were performed using a Precision Multiferroic Tester (Radiant Technologies, Inc.). The signal was measured in a temperature range of 100-450 K with 5 K intervals, and 3 K min^{-1} ramp rate, using a vacuum-probe station (Lake Shore Cryotronics). The samples were kept for 5 minutes at each temperature before the measurement in order to reach thermal equilibrium. A 5 V pulse of 10 ms duration was then applied to the samples as the trap-filling pulse, and the subsequent transient capacitance decay was measured at the end of the pulse using the rate-window approach described above. The difference in the transient capacitance at two different times t_1 and t_2 after the trap-filling pulse was obtained for five different windows ranging from 5 to 160 ms (with a constant $\frac{t_1}{t_2}$ ratio) and plotted as a function of temperature. The activation energies of trap states were then extracted from the shift of the peaks with temperature. As mentioned previously, deep-level transient spectroscopy probes the defects present in the depletion region of a Schottky barrier. Ohmic contacts, therefore, were avoided in these measurements.

CHAPTER 5

Growth-Induced Control of Off-Stoichiometric Defects and Their Impact on the Structure and Properties of $BaTiO_3$ and $BiFeO_3$ Thin Films

This Chapter focuses on *in situ* control of defects and properties in $BaTiO_3$ and $BiFeO_3$ thin films. Variations in growth conditions (*i.e.*, laser fluence, laser-repetition rate, and target composition) are shown to directly impact both the cation and anion chemistry, and in turn, are used as knobs to modify the type and concentration of *intrinsic* off-stoichiometric point defects. The impact of such growth-induced defects on the chemistry, structure, electrical leakage, conduction mechanisms, and dielectric and ferroelectric response is explored. It is shown that small variations in the laser fluence during pulsed-laser deposition of $BaTiO_3$ thin films can give rise to increased concentrations of *intrinsic* point defects, manifested as large deviations of the films from stoichiometric composition with chemistries ranging from $BaTiO_3$ to $Ba_{0.93}TiO_{2.87}$. Such growth-induced off-stoichiometric defects are shown to impact the crystalline structure by giving rise to large out-of-plane lattice expansions (up to 5.4% beyond the expected value for a perfectly stoichiometric film, reduction in the leakage current density ($\approx 10^3$ times smaller in $Ba_{0.93}TiO_{2.87}$ films), reduction in low-field permittivity and loss tangents, increase in the dielectric maximum temperatures, and large built-in potentials (shifted loops) and hysteresis-loop pinching. The defect states are attributed to $V_{Ba}'' - V_O^{\bullet\bullet}$ defect-dipoles (at $\approx$ 0.4 eV above the valence band) and V_{Ba}'' (at $\approx$ 1.2 eV above the valence band), which grow in concentration with increasing deficiencies of both barium and oxygen, and can be removed via *ex post facto* processing. Similarly, variations in the laser-repetition rate and target composition in pulsed-laser deposition of $BiFeO_3$ thin films are shown to result in films with chemistries ranging from $\approx$ 10% bismuth deficiency to $\approx$ 4% bismuth excess, and films possessing bismuth gradients as large a $\approx$ 6% across the film thickness, with corresponding variations and gradients in the oxygen chemistry. As a result of the varying film chemistry, variations in the dominant conduction mechanism (including Schottky, Poole-Frenkel, and modified Poole-Frenkel emissions), leakage current density, quality of ferroelectric hysteresis loops, and magnitude of dielectric response are observed. Ultimately, slightly bismuth-excess films are found to exhibit the best low-frequency ferroelectric and dielectric response while increasing bismuth deficiency worsens the low-frequency ferroelectric performance and reduces the dielectric permittivity.

5.1 Introduction

$BaTiO_3$ and $BiFeO_3$ are two of the most technologically-important ferroelectric materials. $BaTiO_3$, for example, is widely used as a dielectric material for multilayer ceramic capacitors, piezoelectric actuators and transducers, *etc.* [216-218]. Multiferroic $BiFeO_3$, on the other hand, exhibits large spontaneous polarization (90-100 μC cm^{-2}), G-type antiferromagnetism, and potential for strong magnetoelectric coupling, and in turn, considerable effort has concentrated on the realization of a range of devices that take advantage of the multiferroic nature of this material [43,67-69]. Due to their technological relevance, it is imperative that one can repeatedly produce and control such materials to exhibit the desired properties and functions. In this regard, understanding the defect-structure-property relations is of utmost importance, due to the sensitivity of these materials to defects.

$BaTiO_3$, for example, is almost never used in its pure form; it is often alloyed with a wide variety of dopants (*i.e.*, *extrinsic* point defects) in order to tune and elicit useful and stable responses [219,220]. Similarly, substantial efforts have explored doping/alloying of $BiFeO_3$ in an attempt to reduce its electronic leakage [221- 226]. High leakage in $BiFeO_3$ (arising from electronic conduction in the material under applied bias) results from the fact that, unlike traditional ferroelectrics, $BiFeO_3$ has a partially populated *d* orbital, has a relatively small band gap (≈ 2.67 eV) compared to most ferroelectrics, and is rather susceptible to point defect formation (and, in turn, doping of the lattice with charge) [227- 234]. Thus, despite the need for deep understanding of how chemistry, defects, structure, and properties evolve in these materials, efforts to use defects for controlling the properties have mainly centered on the introduction of *extrinsic* point defects to counterbalance the detrimental impact of the *grown-in* defects present in the material. Considerably less work, however, has been focused on directly probing the role of *intrinsic* defects in determining the structures and properties, and on thoughtful use of such defects to solve materials challenges [235-237].

Advances in materials synthesis – including thin-film deposition approaches – now provide for more exacting control over materials which enables the deterministic creation of *intrinsic*-defect structures in complex materials like the perovskite oxides and, in turn, allows for the study of defect-structure-property couplings, and realization of enhanced properties and emergent functionalities [23,30,147,171,172,174,238-241]. Ultimately, such work to understand the nature of defects, and the ability to probe and control defects in these technologically-important materials can pave the way for development of defect-engineering approaches to shape the properties and functionalities of these complex systems and to expand their application in advanced next-generation technologies [29,31].

5.2 *In Situ* Creation of Off-Stoichiometric Defects in $BaTiO_3$ Thin Films via Variations of Laser Fluence

This work focuses on 100 nm $BaTiO_3$/30 nm $SrRuO_3$/$GdScO_3$(110) heterostructures grown at various laser fluences of 1.25, 1.45, and 1.65 J cm^{-2}, and aims to utilize variations of laser fluence as a means to *in situ* control of off-stoichiometric defects [31]. Most of the experimental studies and analyses in this work were performed by my colleague, Arvind Dasgupta. Wide-angle $\omega - 2\theta$ X-ray line scans suggest that single-phase, 00*l*-oriented, and epitaxial thin films of $BaTiO_3$ are obtained at all laser fluences (Figure 5.1a). The film peaks, however, are found to be shifted towards lower angles, corresponding to an increase in the out-of-plane lattice parameter, as the

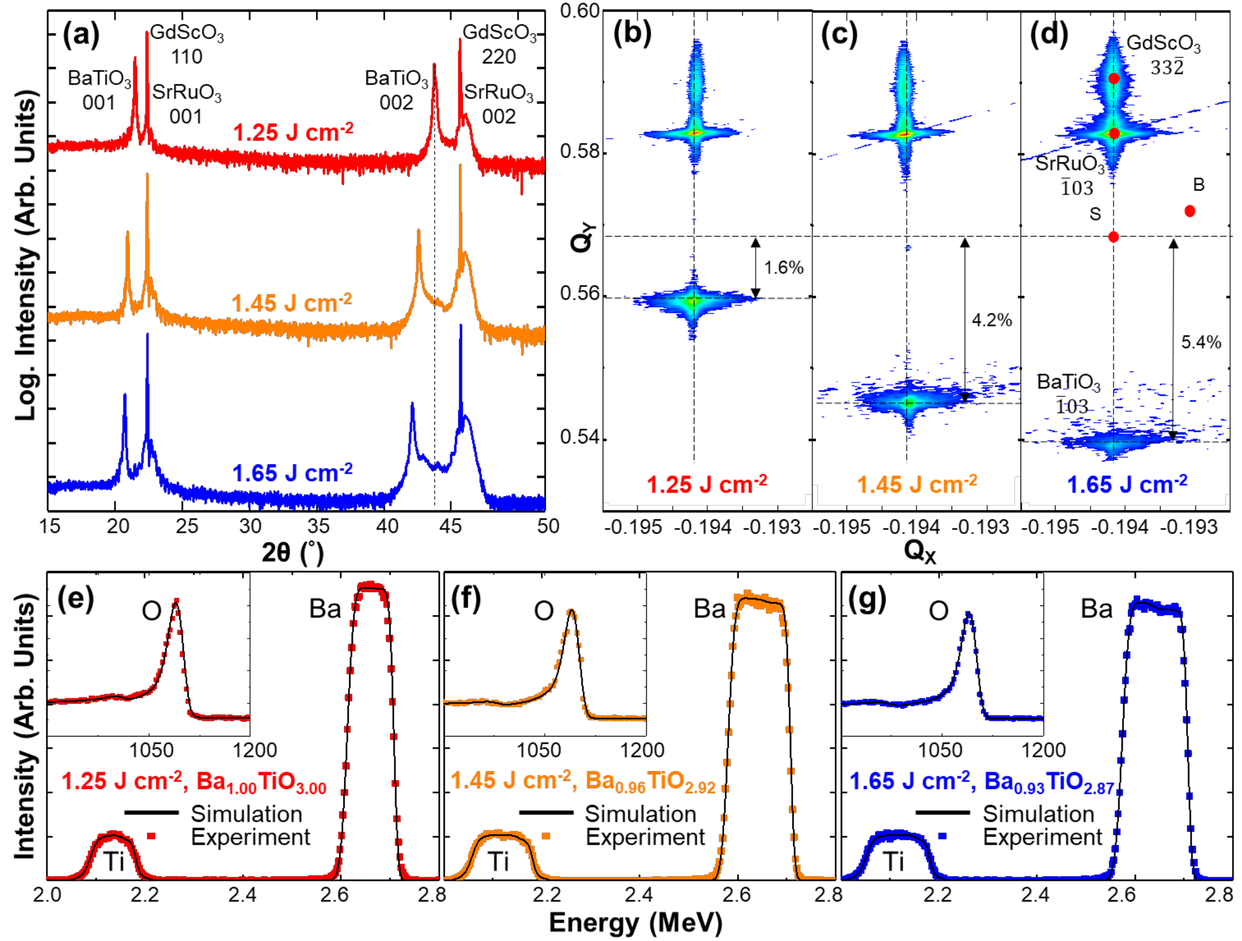

Figure 5.1. (a) $\omega - 2\theta$ X-ray diffraction scans for heterostructures grown at laser fluences of 1.25 J cm^{-2} (top, red), 1.45 J cm^{-2} (middle, orange), and 1.65 J cm^{-2} (bottom, blue). Off-axis reciprocal space mapping studies about the $\bar{1}03$- and $33\bar{2}$-diffraction conditions of the film and substrate, respectively, for heterostructures grown at laser fluences of (b) 1.25 J cm^{-2}, (c) 1.45 J cm^{-2}, and (d) 1.65 J cm^{-2}. Rutherford backscattering spectrometry data with a zoom-in image of the oxygen resonance peak (inset) for heterostructures grown at laser fluences of (e) 1.25 J cm^{-2}, (f) 1.45 J cm^{-2}, and (g) 1.65 J cm^{-2}.

laser fluence is increased. Reciprocal space mapping studies about the $\bar{1}03$- and $33\bar{2}$-diffraction conditions of the film and the substrate, respectively (Figure 5.1b-d), show that the films are coherently strained to the substrate at all laser fluences. A systematic increase in the out-of-plane lattice parameter, however, is observed from 1.6% to 4.2% to 5.4% beyond the theoretically expected strained peak position for $BaTiO_3$ grown on $GdScO_3$ substrates [95], for the films grown at laser fluences of 1.25, 1.45, and 1.65 J cm^{-2}, respectively. This observation indicates that strain alone cannot account for this significant increase in the out-of-plane lattice parameter.

The stoichiometry of the films was probed using Rutherford backscattering spectrometry, and found to vary from $Ba_{1.00}TiO_{3.00}$ to $Ba_{0.96}TiO_{2.92}$ to $Ba_{0.93}TiO_{2.87}$ for the films grown at 1.25, 1.45, and 1.65 J cm^{-2}, respectively, suggesting a systematic decrease in barium and oxygen contents with increasing laser fluence (Figure 5.1e-g). This large difference in the chemistry of the films is somewhat surprising, as a high crystalline quality is maintained even in the face of ≈7% cation off-stoichiometry (*i.e.*, the film peaks remain sharp and the FWHM of their corresponding rocking curves (Figure 5.2a-c) remain essentially the same, in the range of 0.025°-0.037° about

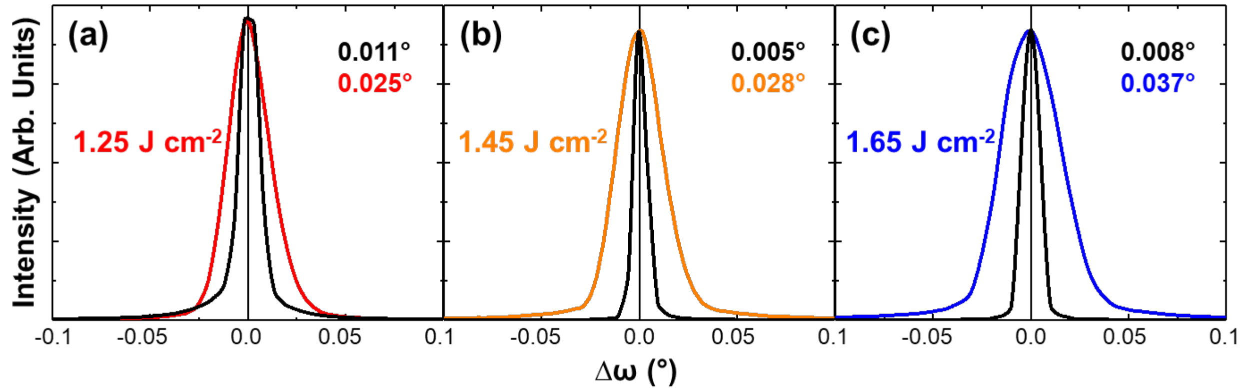

Figure 5.2. X-ray rocking curve studies about the 002-diffraction condition of the film and 220-diffraction condition of the substrate for heterostructures grown at laser fluences of (a) 1.25 J cm^{-2}, (b) 1.45 J cm^{-2}, and (c) 1.65 J cm^{-2}. The numbers in the upper right-hand corner are the FWHM values for the substrate (top) and film (bottom).

the 002-diffraction condition of the films as the laser fluence is increased) – a testament to the tolerance of these perovskite materials to point defects. In turn, the large expansion in the out-of-plane lattice parameter can likely be ascribed to the lattice distortions created by point defects since formation of cation and anion vacancies is often known to drive a lattice expansion [172,242]. Similar lattice expansion with varying laser fluence during pulsed-laser deposition of $BaTiO_3$ thin films has been previously reported [147,173], and attributed to the presence of defects and off-stoichiometry.

5.3 Effect of Growth-Induced Off-Stoichiometric Defects on Transport, Dielectric, and Ferroelectric Properties of $BaTiO_3$ Thin Films

Having established that the growth process (*i.e.*, laser fluence) can be used to vary the cation and anion stoichiometry, and in turn, the concentration of *intrinsic* point defects, the influence of such defects on the leakage, dielectric, and ferroelectric properties was explored [31]. It is shown that increasing the deficiencies of both barium and oxygen give rise to a systematic reduction in the leakage current density by ≈ 3 orders of magnitude for $Ba_{0.93}TiO_{2.87}$ in comparison to $Ba_{1.00}TiO_{3.00}$ films (Figure 5.3a), a reduction in the room-temperature dielectric permittivity from a value of ≈250 for the $Ba_{1.00}TiO_{3.00}$ films to ≈ 175 for the $Ba_{0.93}TiO_{2.87}$ films at 1 kHz (Figure 5.3b), an increase in the maximum of the temperature-dependent dielectric permittivity (and in turn T_C) ranging from ≈ 425°C for $Ba_{1.00}TiO_{3.00}$ films to values higher in temperature than our measurement system can probe (Figure 5.3c), an increase in the shift of the hysteresis loops (Figure 5.3d) and internal bias of first-order reversal curve distributions (Figure 5.4a-c), and emergence of a slight hysteresis-loop pinching (Figure 5.3d) and splitting of the first-order reversal curve distributions (Figure 5.4c) in the most barium- and oxygen-deficient films. As mentioned in Section 3.5, defect dipoles are often responsible for changes in the T_C, have a tendency to align in the polarization direction, stabilize the domain configuration, and pin the domain-wall motion during switching. The changes in the dielectric permittivity, shift and pinching of the hysteresis loops, as well as shift and splitting of the first-order reversal curve distributions, therefore, are signatures of the likely presence of defect dipoles [12,125,131,147,159,160,243,244]. These well-known "fingerprints" of defect dipoles vary systematically with off-stoichiometry, consistent with the fact that more defect dipoles are likely to be formed as the off-stoichiometry increases.

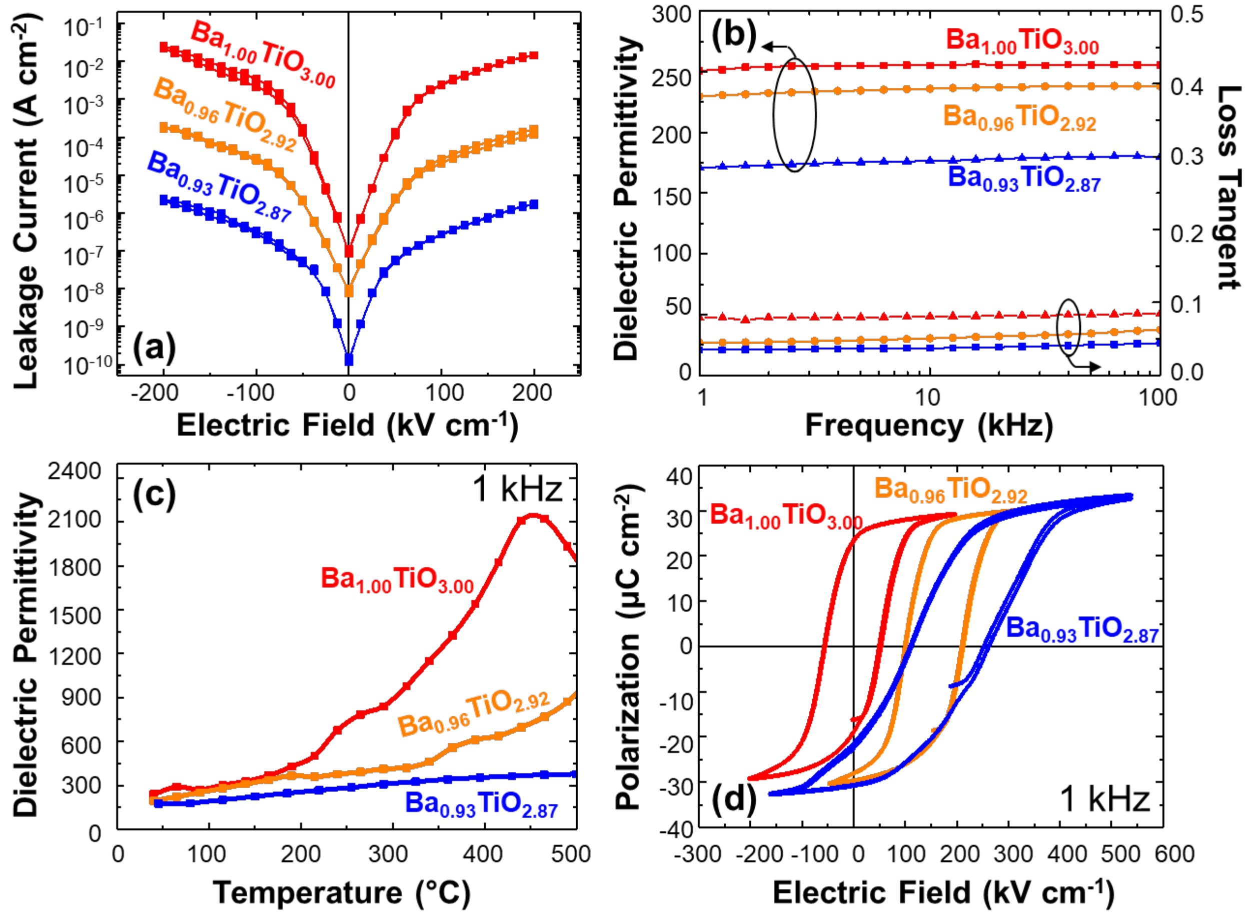

Figure 5.3. (a) Room temperature current-voltage measurements, (b) room-temperature, low-field dielectric permittivity (left axis) and loss tangent (right axis), (c) temperature dependence of dielectric permittivity, and (d) polarization-electric field hysteresis loops measured at 1 kHz for $Ba_{1.00}TiO_{3.00}$, $Ba_{0.96}TiO_{2.92}$, and $Ba_{0.93}TiO_{2.87}$ heterostructures.

A combination of current-voltage measurements, deep-level transient spectroscopy, and annealing experiments were used to gain information on the nature of the growth induced off-stoichiometric defects [31]. First, current-voltage measurements were undertaken to determine the

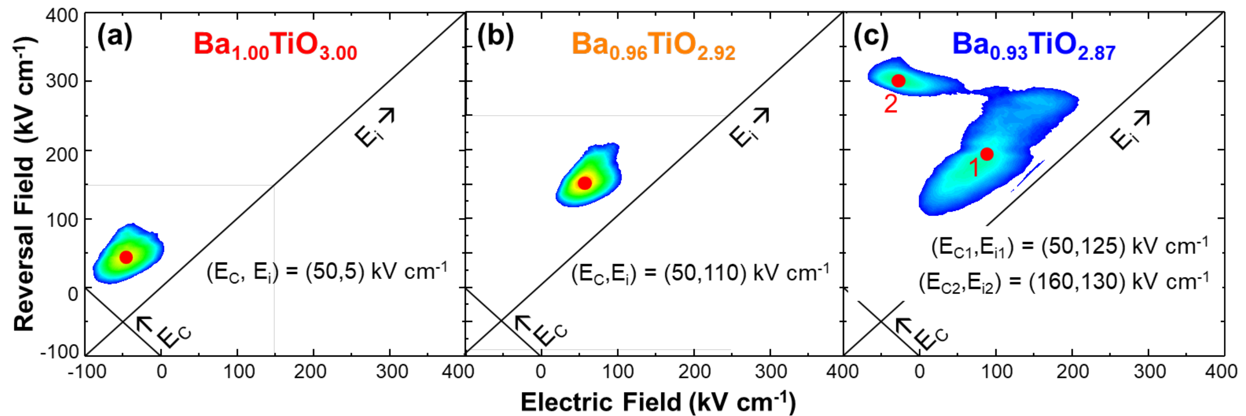

Figure 5.4. Calculated first-order reversal curve distributions for (a) $Ba_{1.00}TiO_{3.00}$, (b) $Ba_{0.96}TiO_{2.92}$, and (c) $Ba_{0.93}TiO_{2.87}$ heterostructures.

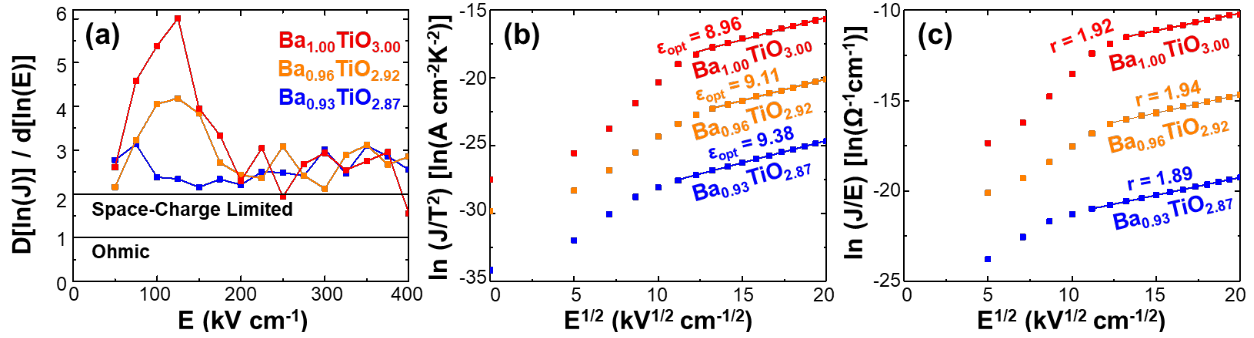

Figure 5.5. (a) Derivatives of J *vs.* E. Neither of the heterostructures exhibits ohmic conduction $(d(\ln(J))/d(\ln(E)) = 1)$ or space-charge limited conduction $(d(\ln(J))/d(\ln(E)) = 2)$. Positive bias room temperature current-voltage data represented on the standard (b) Schottky and (c) Poole-Frenkel plots. Schottky emission fits reveal a poor match with the expected optical dielectric constant of $BaTiO_3$, while modified Poole-Frenkel emission reveals a good fit to the experimental data.

dominant conduction mechanisms (Figure 5.5). Ohmic conduction, space-charge limited conduction, Schottky emission, and Poole-Frenkel emission were considered, as described in Section 2.8.1. Ohmic and space-charge limited conductions are ruled out due to the inability to fit the experimental data (Figure 5.5a). Although the data at high electric fields can be fit using Schottky emission (Figure 5.5b), the extracted values of optical dielectric constant ($\varepsilon_{opt} = 8.96$, 9.11, 9.38 for various heterostructures) are much higher than the value of 5.9 reported in the literature for $BaTiO_3$ [245]. A modified Poole-Frenkel emission, on the other hand, gives rise to reasonable fits to the experimental data at high values of electric fields (Figure 5.5c) for a fixed optical dielectric constant of 5.9 (the value of r is changed in order to obtain the fits). Since this model provides the most reasonable fit to the experimental data, it is hypothesized that the leakage in these heterostructures is dominated by Poole-Frenkel emission which is governed by the emission of charge carriers from internal trap states.

To study the intra-gap states present in the films, deep-level transient spectroscopy measurements were carried out (Figure 5.6a-c) in the temperature range of 100-400 K for five different rate windows in the range of 5-160 ms. For $Ba_{1.00}TiO_{3.00}$ heterostructures (Figure 5.6a), only weak, hard to fit deep-level transient spectroscopy peaks are observed. Two low-intensity peaks are found to extend just above the noise level of our experimental setup and correspond in location to pronounced peaks discussed later. The low intensity of the deep-level transient

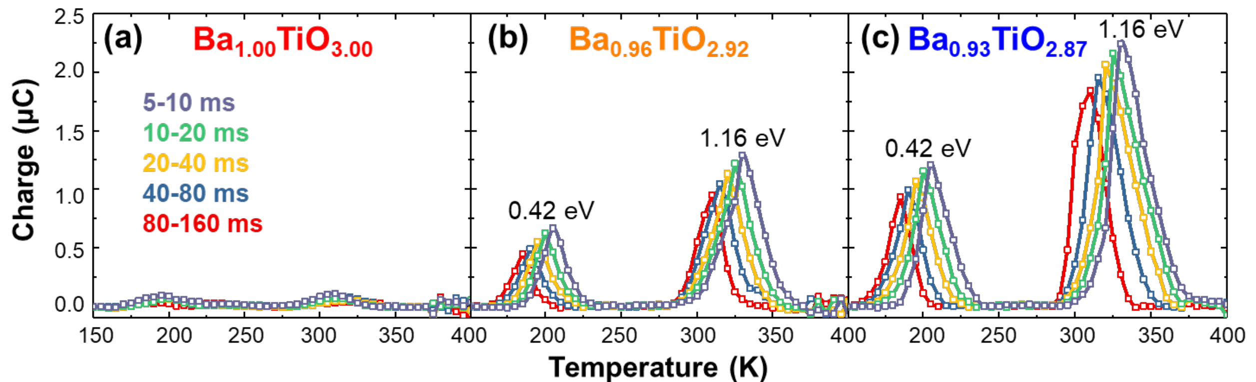

Figure 5.6. Deep-level transient spectroscopy data and the extracted intra-gap trap energies for (a) $Ba_{1.00}TiO_{3.00}$, (b) $Ba_{0.96}TiO_{2.92}$, and (c) $Ba_{0.93}TiO_{2.87}$ heterostructures.

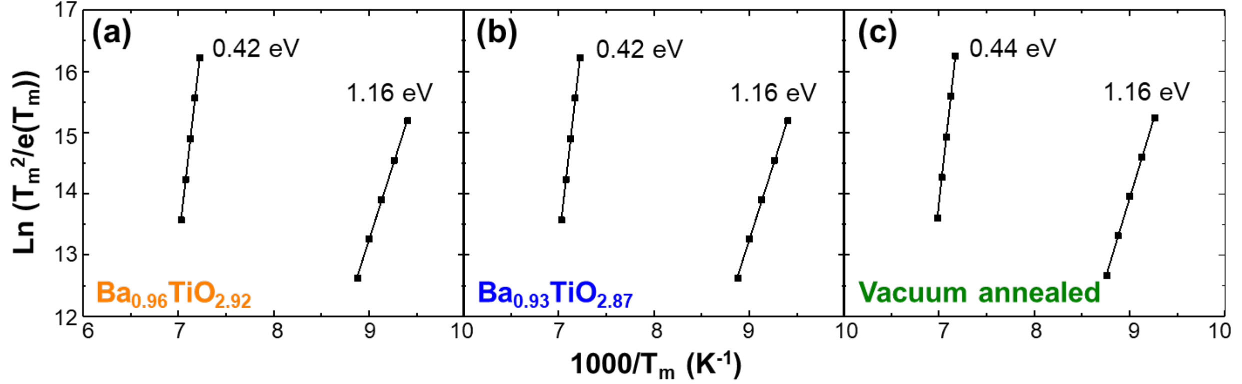

Figure 5.7. Deep-level transient spectroscopy fits used to extract trap energies in the (a) $Ba_{0.96}TiO_{2.92}$, (b) $Ba_{0.93}TiO_{2.87}$, and (c) vacuum-annealed $Ba_{0.93}TiO_{2.87}$ heterostructures.

spectroscopy peaks, therefore, is attributed to likely low concentrations of defects due to nearly stoichiometric composition of these films. As the barium and oxygen deficiency is increased in the $Ba_{0.96}TiO_{2.92}$ (Figure 5.6b) and $Ba_{0.93}TiO_{2.87}$ (Figure 5.6c) heterostructures, two pronounced peaks emerge, corresponding to the energies of ≈ 0.4 eV and ≈ 1.2 eV (fits used for extraction of trap energies are provided, Figure 5.7a,b), and a systematic increase in the intensity of the peaks is observed as barium and oxygen deficiencies are increased.

A series of annealing experiments were carried out on the most defective $Ba_{0.93}TiO_{2.87}$ heterostructures in order to gain further insight on the nature of the observed defect states (Figure 5.8). First, an oxygen annealing was performed at 500°C for 60 minutes at an oxygen pressure of 760 Torr in an attempt to reduce the concentration of oxygen vacancies, but was found to have no detectable effect on the structure, chemistry, and electronic leakage of the heterostructures. This observation suggests that oxygen vacancies are formed in order to compensate for the barium vacancies in Schottky pairs [246], and therefore, must be stable (consistent with variations in the chemistry of the films where increasing barium deficiency also increases the oxygen deficiency).

The second annealing experiment was performed at a low oxygen pressure of 1 mTorr, for 60 minutes at 500°C, in an attempt to introduce additional oxygen vacancies. After this treatment, a stark change in the deep-level transient spectroscopy signal was observed (Figure 5.8b). Although the trap energies corresponding to the two observed peaks remain unchanged (fits used for extraction of trap energies are provided, Figure 5.7c) with respect to the as-grown films (Figure 5.8a), the intensity of the peaks are observed to change (implying a change in the concentration of the trap states). The ≈ 0.4 eV trap state increases in concentration, at the expense of the ≈ 1.2 eV trap.

Conduction in $BaTiO_3$ at ambient pressures is commonly reported to be *p*-type [247] and reinforced by the presence of barium vacancies [248]. The governing defect equations, therefore, can be written as:

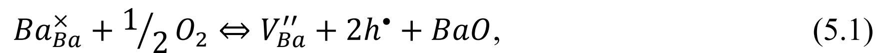

$$Ba_{Ba}^{\times} + {}^{1}\!/_{2}\, O_2 \Leftrightarrow V_{Ba}'' + 2h^{\bullet} + BaO, \quad (5.1)$$

$$nil \Leftrightarrow V_A'' + V_O^{\bullet\bullet}. \quad (5.2)$$

In the former case, the introduction of barium vacancies has the effect of hole doping the lattice in order to maintain charge neutrality, thereby increasing the carrier concentration. In the latter case, the charge neutrality is maintained by formation of a Schottky pair where instead of introducing

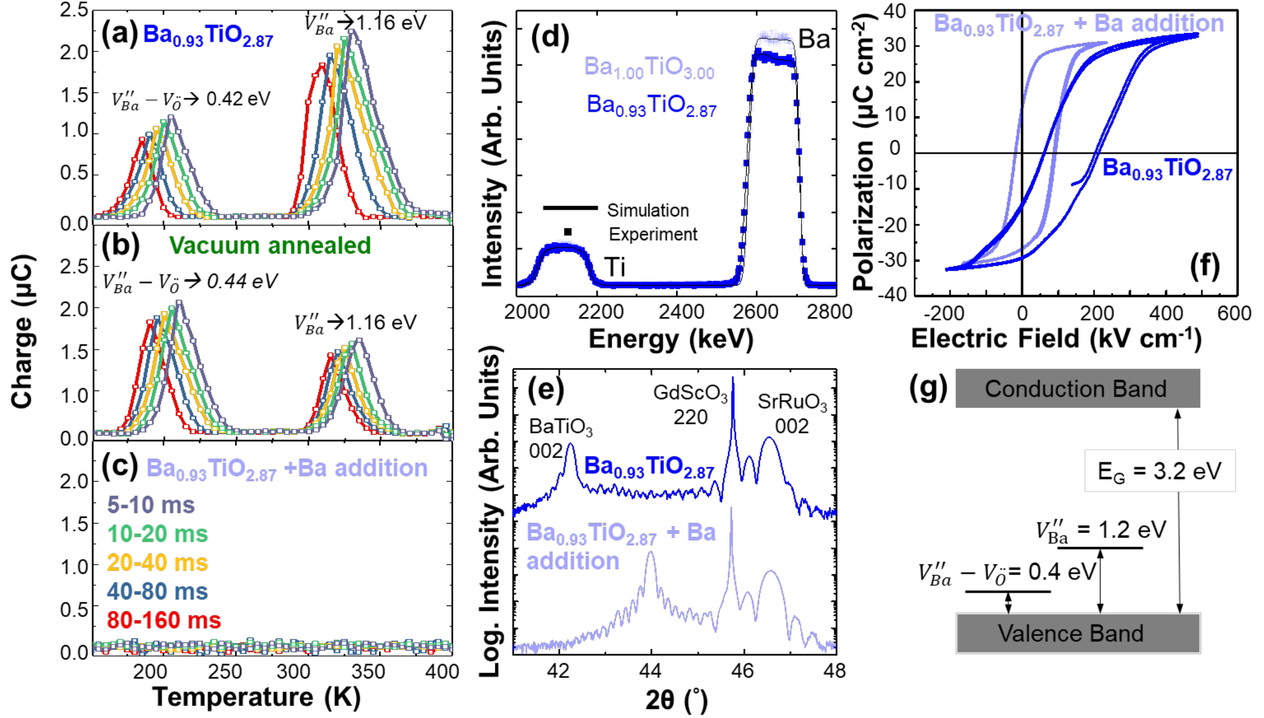

Figure 5.8. Deep-level transient spectroscopy data for (a) an as-grown $Ba_{0.93}TiO_{2.87}$ heterostructure, (b) the same film after vacuum annealing at 500°C, and (c) the same film after barium addition via a chemical vapor deposition-like process. (d) Rutherford backscattering spectrometry data, (e) $\omega - 2\theta$ X-ray diffraction scans, and (f) polarization-electric field hysteresis loops for the $Ba_{0.93}TiO_{2.87}$ heterostructure in the as-grown state and followed by barium addition. (g) Schematic of the defect state energies present within the $Ba_{1-x}TiO_y$ films wherein E_G is the band gap.

charge carriers, a compensatory defect (*i.e.*, an oxygen vacancy) is formed. The trap energy of ≈1.2 eV matches with the reported values in the literature for isolated V''_{Ba} defects [249,250]. The defect state observed at ≈ 1.2 eV, therefore, is attributed to isolated V''_{Ba} defects. Reduction in the concentration of isolated V''_{Ba} as a result of increase in the concentration of oxygen vacancies, in turn, suggests that as more oxygen vacancies are introduced, some of the isolated V''_{Ba} are converted into $V''_{Ba} - V_O^{\bullet\bullet}$ defect-dipoles. The increase in the concentration of the shallower trap state at ≈ 0.4 eV, on the other hand, suggest that this peak is likely related to the $V''_{Ba} - V_O^{\bullet\bullet}$ defect-dipoles, and that such defect dipoles are responsible for the observed defect induced changes in the properties (*i.e.*, reduction of leakage current, reduction of dielectric permittivity, increase in T_C, increase in the shift and pinching of the ferroelectric hysteresis loops, and increase in the internal bias and splitting of the first-order reversal curve distributions). Previous work has shown that V''_{Ba} defects can readily form a defect complex with $V_O^{\bullet\bullet}$ to form a more stable ground state due to electrostatic- and strain-energy considerations [134,135,251,252].

Finally, an annealing in a barium-rich environment at 700°C for 60 minutes was performed in an attempt to reintroduce barium into the lattice. Barium reintroduction was performed using a chemical vapor deposition-style setup in a tube furnace where the films were placed at the end of the hot zone while an alumina boat filled with BaO powder was placed at the beginning of the hot zone. Oxygen was flown into the furnace, over the BaO powder and towards the films, while the temperature was ramped up to 700°C at a rate of 25°C min^{-1}, maintained for 60 minutes at that temperature, and then cooled down to the room temperature at a rate of 5°C min^{-1}. The films were

then cleaned by sonicating in dilute 0.5 M HCl solution for 5 minutes to remove excess BaO from the surface. Similar approaches have been used to overcome the lead loss in sol-gel $PbZr_xTi_{1-x}O_3$ films [253,254]. Subsequent Rutherford backscattering spectrometry studies reveal a new film chemistry of $Ba_{1.00}TiO_{3.00}$ after this annealing experiment, and therefore, confirm the reintroduction of barium into the lattice (Figure 5.8d). After this barium reintroduction, a dramatic change in the structure of the films is observed (Figure 5.8e) wherein the out-of-plane lattice expansion is reduced from ≈ 5.4% (before reintroduction of barium) to ≈ 1.1%, the shift of the ferroelectric hysteresis loops is greatly reduced, and the previously-observed loop pinching is eliminated (Figure 5.8f). Deep-level transient spectroscopy studies of these "healed" films (Figure 5.8c) show the disappearance of the two previously-observed peaks, suggesting that it is possible to almost completely remove the barium vacancies from these films after the fact. This further supports the attribution of both peaks to defects related to the barium vacancies. Ultimately, a band structure for the $Ba_{1-x}TiO_y$ films is proposed to depict the position of the various intra-gap trap states that are formed by barium and oxygen deficiencies (Figure 5.8g).

5.4 *In Situ* Creation of Off-Stoichiometric Defects in $BiFeO_3$ Thin Films via Variations of Laser-Repetition Rate and Target Composition

This work focuses on 100 nm $BiFeO_3$/30 nm $SrRuO_3$/$DyScO_3$ (110) heterostructures, grown at various laser-repetition rates ranging from 8 to 20 Hz from ceramic targets of various compositions including $Bi_{1.1}FeO_3$, $Bi_{1.2}FeO_3$, and $Bi_{1.3}FeO_3$, and aims to utilize variations of laser-repetition rate and target composition as means to *in situ* control of off-stoichiometric defects [29]. Most of the experimental studies and analyses in this work were performed by my colleague, Liv R. Dedon. Wide angle $\omega - 2\theta$ X-ray line scans reveal that all $BiFeO_3$ heterostructures are fully epitaxial, $00l$-oriented, and single-phase (Figure 5.9a). Closer examination of the 002-diffraction condition of $BiFeO_3$ reveals essentially no change in position or shape of the diffraction peaks despite changing growth conditions (Figure 5.9b). It should be noted that the $SrRuO_3$ peak for heterostructures grown at low laser-repetition rates is shifted towards lower 2θ angles, indicating an expansion of the $SrRuO_3$ out-of-plane lattice parameter.

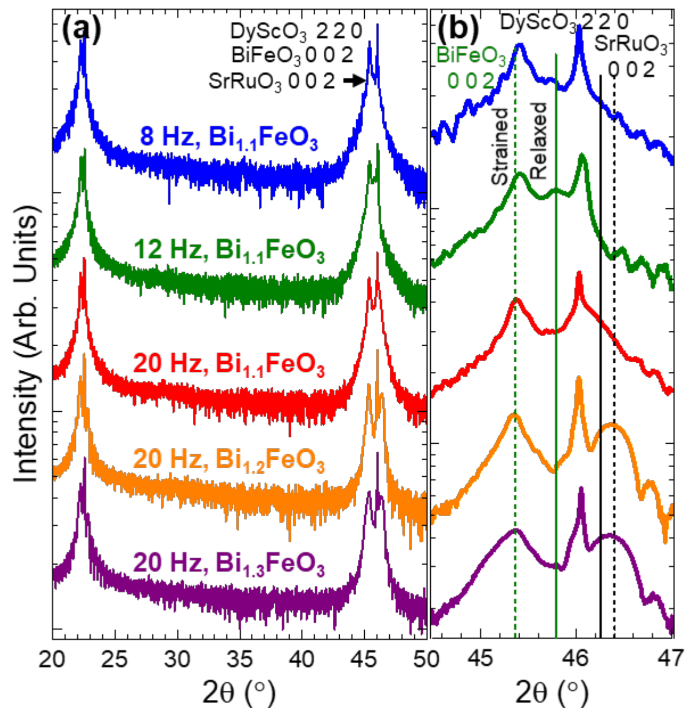

Figure 5.9. (a) $\omega - 2\theta$ X-ray diffraction patterns about the 001- and 002-diffraction conditions of the $BiFeO_3$ and $SrRuO_3$ films and 110- and 220-diffraction conditions of the $DyScO_3$ substrate. (b) Zoom-in about the 002- and 220-diffraction conditions showing minimal variation in the out-of-plane lattice parameter of the $BiFeO_3$ with changing growth conditions.

This is attributed to the presence of a diffuse $BiFeO_3$/$SrRuO_3$ interface due to diffusion of bismuth from $BiFeO_3$ into the underlying $SrRuO_3$ in an attempt to homogenize bismuth concentration in

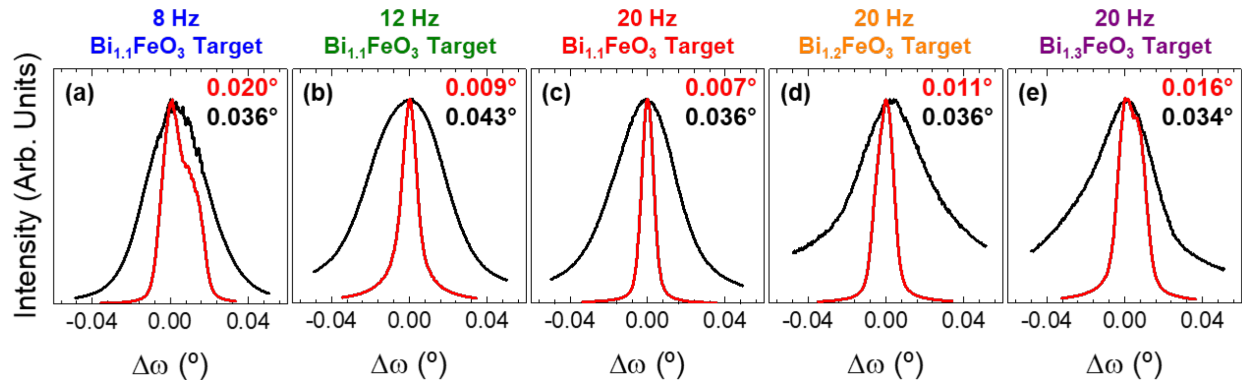

Figure 5.10. X-ray rocking curve studies about the 002-diffraction condition of the film and 220-diffraction condition of the substrate for heterostructures grown at various growth conditions. The numbers in the upper right-hand corner are the FWHM values from the substrate (top, red) and film (bottom, black) curves.

the film. This observation is discussed in more details elsewhere [29]. Rocking curve studies about the 002- and 220-diffraction conditions of the film and substrate suggest that in all cases, the FWHM of the films are between ≈ 2-5 times that of the substrate indicating comparable crystalline qualities (Figure 5.10).

Subsequent studies of heterostructure stoichiometry via Rutherford backscattering spectrometry (Figure 5.11) reveal that both changing the laser-repetition rate while maintaining a constant target composition ($Bi_{1.1}FeO_3$), and changing the target composition while maintaining a constant laser-repetition rate (20 Hz), result in marked changes in the film chemistry. A complete summary of chemical analyses for all growth variants is provided (Table 5.1). The concentration of bismuth, iron, and oxygen are noted as [Bi], [Fe], and [O], respectively, and the reported values represent the fraction of occupation of the ideal chemistry; [Bi]:[Fe] ratio, and [O]:[Fe] ratio. The gradient of chemistry throughout the thickness of the films are also extracted and reported as ∇[Bi]

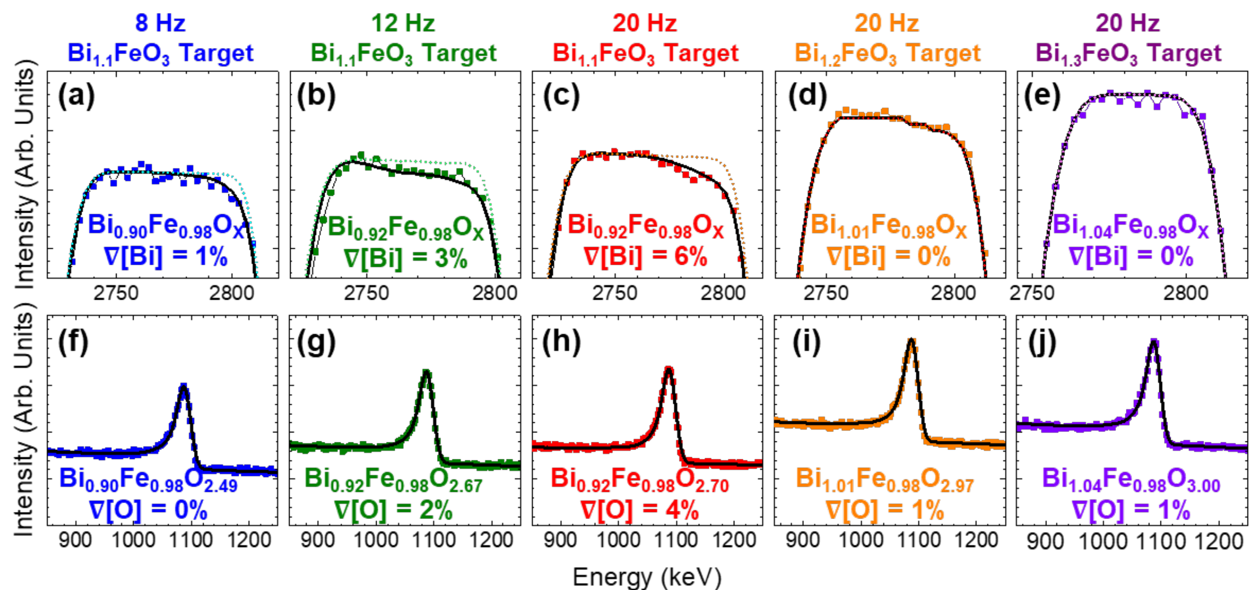

Figure 5.11. Enlarged view of Rutherford backscattering spectrometry data showing the (a-e) top of the bismuth peak, and (f-j) the oxygen resonance peak for the (a, f) $Bi_{0.90}Fe_{0.98}O_{2.49}$, (b, g) $Bi_{0.92}Fe_{0.98}O_{2.67}$, (c, h) $Bi_{0.92}Fe_{0.98}O_{2.70}$, (d, i) $Bi_{1.01}Fe_{0.98}O_{2.97}$, and (e, j) $Bi_{1.04}Fe_{0.98}O_{3.00}$ heterostructures, respectively.

Table 5.1. Summary of data including growth conditions, final chemical formula of heterostructure, [Bi]/[Fe] ratio, ∇[Bi], [O]/[Fe] ratio, and ∇[O].

Growth Conditions	Chemical Formula	[Bi]:[Fe] Ratio			∇[Bi] (%)	[O]:[Fe] Ratio			∇[O] (%)
		Average	Surface	Interface		Average	Surface	Depth Limit	
8 Hz, $Bi_{1.1}FeO_3$ Target	$Bi_{0.90}Fe_{0.98}O_{2.49}$	0.90 : 0.98	0.90 : 0.98	0.91 : 0.98	1	2.49 : 0.98	2.49 : 0.98	2.49 : 0.98	0
12 Hz, $Bi_{1.1}FeO_3$ Target	$Bi_{0.92}Fe_{0.98}O_{2.67}$	0.92 : 0.98	0.91 : 0.98	0.94 : 0.98	3	2.67 : 0.98	2.64 : 0.98	2.70 : 0.88	2
20 Hz, $Bi_{1.1}FeO_3$ Target	$Bi_{0.92}Fe_{0.98}O_{2.70}$	0.92 : 0.98	0.89 : 0.98	0.95 : 0.98	6	2.70 : 0.98	2.67 : 0.98	2.73 : 0.98	4
20 Hz, $Bi_{1.2}FeO_3$ Target	$Bi_{1.01}Fe_{0.98}O_{2.97}$	1.01 : 0.98	1.01 : 0.98	1.01 : 0.98	0	2.97 : 0.98	2.97 : 0.98	3.00 : 0.98	1
20 Hz, $Bi_{1.3}FeO_3$ Target	$Bi_{1.04}Fe_{0.98}O_{3.00}$	1.04 : 0.98	1.04 : 0.98	1.04 : 0.98	0	3.00 : 0.98	2.97 : 0.98	3.00 : 0.98	1

(*i.e.*, gradient of bismuth), and ∇[O] (*i.e.*, gradient of oxygen). Upon increasing the laser-repetition rate, there is an increase in the [Bi], [O], ∇[Bi], and ∇[O]. The average chemistry remains bismuth deficient but becomes slightly richer in bismuth and oxygen as the laser-repetition rate is increased from 8 Hz ($Bi_{0.90}Fe_{0.98}O_{2.49}$, ∇[Bi]=1%, and ∇[O]=0%) to 12 Hz ($Bi_{0.92}Fe_{0.98}O_{2.67}$, ∇[Bi]=3%, and ∇[O]=2%) to 20 HZ ($Bi_{0.92}Fe_{0.98}O_{2.70}$, ∇[Bi]=6%, and ∇[O]=4%). On the other hand, upon increasing the bismuth content in the target, there is an increase in the [Bi], [O], and a reduction in ∇[Bi], and ∇[O]. The average chemistry changes from bismuth deficient ($Bi_{0.92}Fe_{0.98}O_{2.70}$, ∇[Bi]=6%, and ∇[O]=4% for growth from a $Bi_{1.1}FeO_3$ target) to nearly stoichiometric ($Bi_{1.01}Fe_{0.98}O_{2.97}$, ∇[Bi]=0%, and ∇[O]=1% for growth from a $Bi_{1.2}FeO_3$ target) to bismuth excess ($Bi_{1.04}Fe_{0.98}O_{3.00}$, ∇[Bi]=0%, and ∇[O]=1% for growth from a $Bi_{1.3}FeO_3$ target). This analysis suggests that at low laser-repetition rates where the growth rate is slower, more bismuth can desorb from the surface of the growing film due to longer exposure to high temperatures. This bismuth deficiency at the surface, in turn, provides a driving force for diffusion of bismuth from deeper in the film towards the surface. As a result, lowering the laser-repetition rate increases the bismuth deficiency, but also drives a reduction in the ∇[Bi] (Figure 5.11a-c). In contrast, increasing the laser-repetition rate can increase the average [Bi], but at the expense of creating larger ∇[Bi]. This trend can be reduced, however, by growing at high laser-repetition rates from highly-bismuth-excess targets (Figure 5.11c-e) where [Bi] can be maintained close to stoichiometry without formation of any measurable ∇[Bi]; akin to what is achieved in adsorption-controlled growth of $BiFeO_3$ via molecular beam epitaxy [255]. It should be noted that both the average and gradient in anion stoichiometry (Figure 5.11f-j) are coupled to the average and gradient in cation stoichiometry. Such coupled behavior is expected since the oxygen off-stoichiometry can compensate for the cation off-stoichiometry to maintain charge neutrality. Thus, large growth-induced changes in the stoichiometry occurs although the structural studies show little variation in the crystallinity or lattice parameter of the $BiFeO_3$.

5.5 Effect of Growth-Induced Off-Stoichiometric Defects on Transport, Dielectric, and Ferroelectric Properties of $BiFeO_3$ Thin Films

Having established that the growth process (*i.e.*, laser-repetition rate and target composition) can be used to vary the cation and anion stoichiometry, and in turn, the concentration of *intrinsic* point defects, the influence of such defects on the evolution of leakage, dielectric, and ferroelectric properties was explored [29]. Test devices of $BiFeO_3$ were grown on 0.5% Nb:$SrTiO_3$ (001) substrates (CrysTec, GmBH) to confirm the nature of the majority carrier type. Current-voltage measurements (Figure 5.12a) exhibit ohmic conduction in the negative bias regime confirmed by $d(\ln(J))/d(\ln(V)) = 1$ (inset, Figure 5.12a) and Schottky conduction in the positive bias regime.

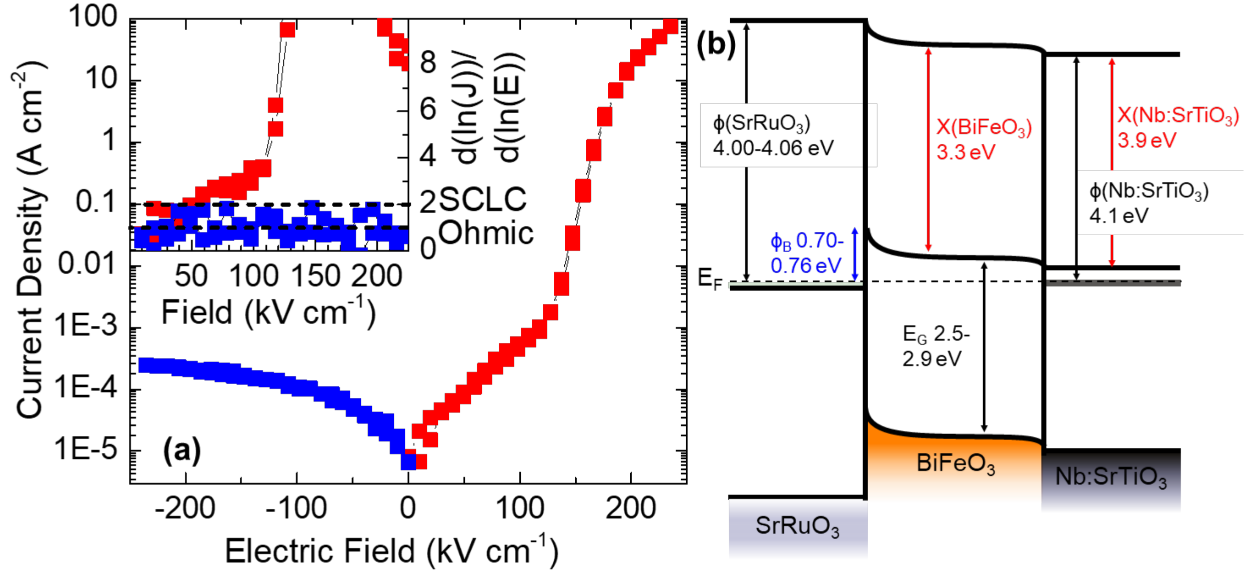

Figure 5.12. (a) Leakage response of, for example, a stoichiometric $Bi_{0.92}Fe_{0.98}O_{2.77}$ heterostructure with 6% ∇[Bi] and 5% ∇[O] grown on 0.5% Nb:$SrTiO_3$ which exhibits ohmic conduction ($d(\ln(J))/d(\ln(V)) = 1$, inset) in the negative bias regime, indicating *n*-type conduction as per (b) the predicted band diagram for this system.

Such a trend in leakage current is expected from *n*-type $BiFeO_3$, where the $BiFeO_3$/Nb:$SrTiO_3$ interface is ohmic in nature due to the small work function of Nb:$SrTiO_3$, and the $BiFeO_3$/$SrRuO_3$ interface is a Schottky junction. Therefore, *n*-type conduction is assumed for all $BiFeO_3$ films. A schematic band diagram is provided (Figure 5.12b).

Current-voltage studies were then performed on $BiFeO_3$/$SrRuO_3$/$DyScO_3$ (110) heterostructures of various chemistries (Figure 5.13a,b). Among the heterostructures with varying average [Bi] but little or no ∇[Bi], the stoichiometric $Bi_{1.01}Fe_{0.98}O_{2.97}$ heterostructures exhibit the highest leakage (Figure 5.13a). This behavior, although perhaps in contrast to what would be desired from the most "ideal" films, is expected due to the low concentration of compensating acceptor states relative to the intrinsic oxygen-vacancy concentration. In turn, by transitioning to either bismuth excess ($Bi_{1.04}Fe_{0.98}O_{3.00}$) or bismuth deficiency ($Bi_{0.90}Fe_{0.98}O_{2.49}$), the leakage is reduced due to the relatively high concentrations of cation vacancies which can compensate the oxygen vacancies, and thus, reduce the free charge carrier densities. The heterostructures exhibiting little or no change in average [Bi] but varying ∇[Bi] (Figure 5.13b) show similar leakage behavior with slightly different leakage current densities.

To better understand the nature of electronic transport in these heterostructures a number of potential transport mechanisms including ohmic conduction, space-charge limited conduction, Schottky emission, classic Poole-Frenkel emission, and modified Poole-Frenkel emission are considered, as described in Section 2.8.1. None of the heterostructure variants exhibit $d(ln(J))/d(ln(E)) = 1$, or $d(ln(J))/d(ln(E)) = 2$, thus ruling out ohmic and space-charge limited conduction as potential mechanisms (Figure 5.14). Despite overall similar leakage current shape and magnitude, the results fall into one of three different classes of behavior. To aid in understanding the relative merits of each fitting procedure (Figure 5.13c-f), the experimental data have been overlaid with lines of slope corresponding to an optical dielectric constant of $\varepsilon_{opt} =$ 6.25 as reported in the literature for $BiFeO_3$ [230,256]. For stoichiometric heterostructures ($Bi_{1.01}Fe_{0.98}O_{2.97}$), the best fit is for Schottky emission (orange data, Figure 5.13c). Comparison

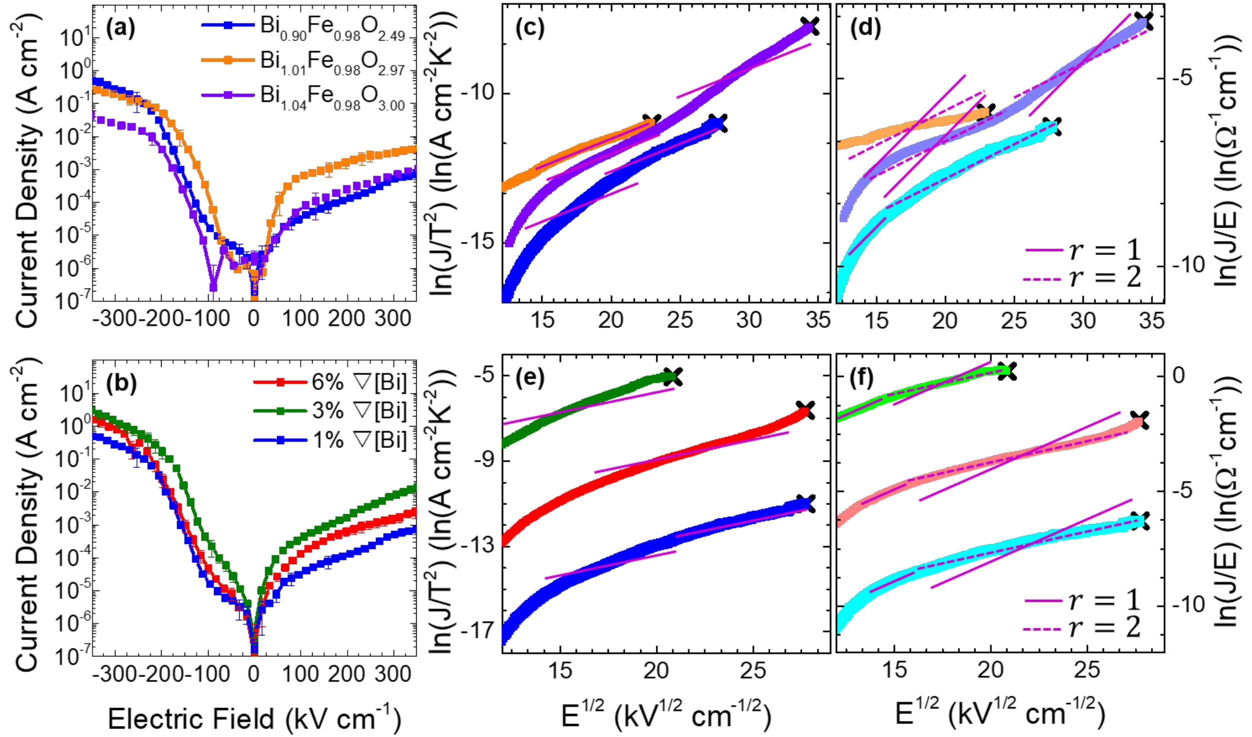

Figure 5.13. Current-voltage characteristics for heterostructures of (a) varying average [Bi] but little to no ∇[Bi], and (b) little to no change in average [Bi] but varying ∇[Bi]. (c) Schottky emission and (d) Poole-Frenkel (r = 1, solid lines) and modified Poole-Frenkel (r = 2, dashed lines) emission fits for heterostructures with varying average [Bi] but little to no ∇[Bi] as shown in part (a). (e) Schottky emission and (f) Poole-Frenkel (r = 1, solid lines) and modified Poole-Frenkel (r = 2, dashed lines) emission fits for heterostructures with little to no change in average [Bi] but varying ∇[Bi] as shown in part (b). In all cases, the lines show the slope required to produce a ε_{opt} = 6.25.

with a Poole-Frenkel or modified Poole-Frenkel emission fit (orange data, Figure 5.13d) shows a poor agreement with the experimental data. For the low ∇[Bi], bismuth-deficient ($Bi_{0.90}Fe_{0.98}O_{2.49}$) and bismuth-excess ($Bi_{1.04}Fe_{0.98}O_{3.00}$) heterostructures, fits to the Schottky emission (blue and purple data, Figure 5.13c) are in poor agreement with the experimental data and, instead, these heterostructures are best fit with something between a classic Poole-Frenkel and modified Poole-Frenkel behavior (blue and purple data, Figure 5.13d). This trend toward the modified Poole-Frenkel behavior is consistent with the fact that these heterostructures have large concentrations of defects from off-stoichiometry and, in turn, should exhibit large concentrations of both acceptor and/or donor states. For the heterostructures exhibiting both overall average bismuth deficiency and varying ∇[Bi], a more complex evolution is observed (Figure 5.13e,f). These heterostructures are not well fit to Schottky emission in any field regime (Figure 5.13e). Investigation of fits to Poole-Frenkel and modified Poole-Frenkel emission reveals that the heterostructures are generally better fit to classic Poole-Frenkel behavior at low fields but the transport is better fit by modified Poole-Frenkel behavior at high field regimes (Figure 5.13f). Such behavior is likely explained by the presence of a gradient in the concentrations of cation and anion defects, and thus, transport through the two interfaces and/or various portions of the film could be different as the defect type and concentration change. Again, the transition from classic Poole-Frenkel to modified Poole-

Frenkel behavior is likely when the concentration of compensating donor states is nontrivial [117,118].

Since growth-induced changes in off-stoichiometric defects are observed to directly impact the evolution of electronic conduction, they are expected to have important implications for the evolution of ferroelectric response as well. Ferroelectric hysteresis loops were measured at a range of frequencies (for brevity data at 0.1, 1, and 10 kHz are provided; Figure 5.15a-e). Similar to the current-voltage response, the data can be grouped into three major categories. First, the stoichiometric heterostructures (Figure 5.15d) show the "worst" ferroelectric hysteresis loops (*i.e.*, largest leakage current contribution to polarization, unclosed and unsaturated loops, *etc.*). This is, in the context of the leakage current data, unsurprising since these heterostructures exhibit the largest leakage response. Again, the low cation vacancy concentration in the stoichiometric heterostructures seems to allow for uncompensated *n*-type carriers (arising from the presence of oxygen vacancies) to dominate the overall leakage behavior. Second, upon transitioning to slightly bismuth-deficient ($Bi_{0.92}Fe_{0.98}O_{2.70}$) and bismuth-excess ($Bi_{1.04}Fe_{0.98}O_{3.00}$) heterostructures, there are marked improvements in the ferroelectric hysteresis loops (Figure 5.15c,e), consistent with the lower overall leakage current densities in these heterostructures compared to the stoichiometric films (Figure 5.13a,b). The third observation, however, is that low leakage current alone is not enough to maintain robust ferroelectric response. Upon transitioning to highly bismuth-deficient heterostructures ($Bi_{0.90}Fe_{0.98}O_{2.49}$ and $Bi_{0.92}Fe_{0.98}O_{2.67}$) the loops again begin to show more signatures of strong leakage components and more difficulty in achieving saturation in both applied field directions (Figure 5.15a,b). In this case, the role of the ∇[Bi] seems to be important in that those heterostructures with lower ∇[Bi] exhibit worse ferroelectric response. For example, comparison of the $Bi_{0.92}Fe_{0.98}O_{2.67}$, ∇[Bi] = 3% (Figure 5.15b) and $Bi_{0.92}Fe_{0.98}O_{2.70}$, ∇[Bi] = 6% (Figure 5.15c) heterostructures reveals that the heterostructure with lower ∇[Bi] has a tendency to show higher leakage. This likely suggests an important role of the chemical gradients in reducing the electronic conduction of the films.

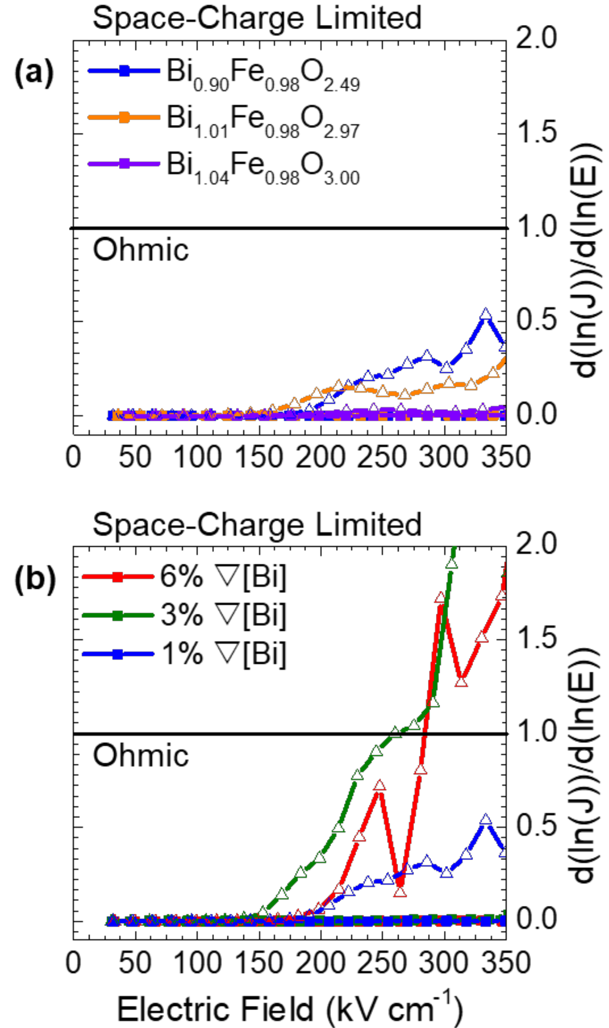

Figure 5.14. Derivatives of J *vs.* E for (a) $Bi_{0.90}Fe_{0.98}O_{2.49}$, $Bi_{1.01}Fe_{0.98}O_{2.97}$ and $Bi_{1.04}Fe_{0.98}O_{3.00}$, and (b) $Bi_{0.90}Fe_{0.98}O_{2.49}$, $Bi_{0.92}Fe_{0.98}O_{2.67}$, and $Bi_{0.92}Fe_{0.98}O_{2.70}$ heterostructures. Neither set of variants exhibits ohmic conduction ($d(ln(J))/d(ln(E)) = 1$) or space-charge limited conduction ($d(ln(J))/d(ln(E)) = 2$).

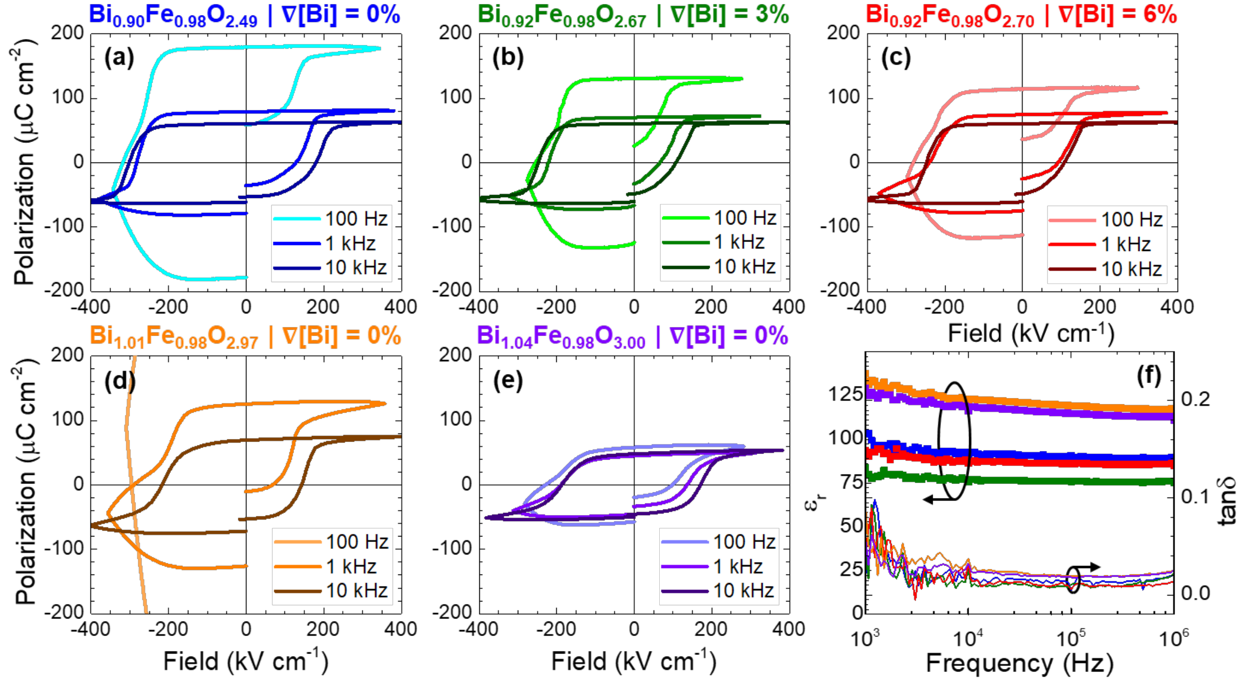

Figure 5.15. Ferroelectric hysteresis loops measured at 0.1, 1, and 10 kHz for (a) $Bi_{0.90}Fe_{0.98}O_{2.49}$, (b) $Bi_{0.92}Fe_{0.98}O_{2.67}$, (c) $Bi_{0.92}Fe_{0.98}O_{2.70}$, (d) $Bi_{1.01}Fe_{0.98}O_{2.97}$, and (e) $Bi_{1.04}Fe_{0.98}O_{3.00}$ heterostructures. (f) Frequency-dependence of dielectric permittivity (left axis) and loss tangent (right axis) for all heterostructures (colors match other data).

Furthermore, there is a trend in the coercive field with stoichiometry in the $BiFeO_3$ heterostructures. The most bismuth-deficient ($Bi_{0.90}Fe_{0.98}O_{2.49}$, ∇[Bi] = 0%) heterostructures exhibit the largest average coercive field (≈ 235 kV cm^{-1}, Figure 5.15a), which is consistent with domain pinning due to the high concentration of point defects. All other heterostructure variants have comparable average coercive fields (≈ 170 kV cm^{-1}, Figure 5.15b-e). The difference, instead, comes in the horizontal shift of the hysteresis loops. A horizontal shift of ≈ 140 kV cm^{-1} is observed in heterostructures exhibiting the largest ∇[Bi] (namely, $Bi_{0.92}Fe_{0.98}O_{2.67}$, ∇[Bi] = 3% (Figure 5.15b) and $Bi_{0.92}Fe_{0.98}O_{2.70}$, ∇[Bi] = 6% (Figure 5.15c)), but horizontal shifts are not observed in the heterostructures with more ideal stoichiometry and minimal ∇[Bi] (namely, $Bi_{1.01}Fe_{0.98}O_{2.97}$, ∇[Bi] = 0% (Figure 5.15d) and $Bi_{1.04}Fe_{0.98}O_{3.00}$, ∇[Bi] = 0% (Figure 5.15e)). There are two possible explanations for these horizontal shifts in the nonhomogeneous heterostructures. First, the Schottky barrier heights at the top and bottom interfaces could be different due to changes in the chemistry at the top and bottom interfaces, thus, producing an asymmetric electrode structure which can induce voltage shifts in ferroelectric hysteresis loops [257,258]. Second, the presence of chemical gradients in the film could result in innate symmetry breaking and formation of higher-order phenomena which can break even-order symmetry in ferroelectrics and can be manifested as built-in potentials (*e.g.*, flexo-chemo-electric effects in compositionally graded ferroelectrics) [259].

Finally, the impact of off-stoichiometric defects on the evolution of dielectric permittivity and loss was examined (Figure 5.15f). Bulk $BiFeO_3$ is expected to exhibit a dielectric permittivity of ≈ 110 (at low frequencies) [260]. Despite showing among the highest leakage currents and the worst ferroelectric response, the stoichiometric ($Bi_{1.01}Fe_{0.98}O_{2.97}$, ∇[Bi] = 0%) heterostructures

(orange data, Figure 5.15f) show essentially bulk-like dielectric behavior and low $\tan\delta$ values. This is consistent with observations for a number of other perovskite phases in recent work wherein only nearly stoichiometric versions of materials show the expected dielectric permittivity [171,176]. The bismuth-excess ($Bi_{1.04}Fe_{0.98}O_{3.00}$, $\nabla[Bi] = 0\%$) heterostructures (purple data, Figure 5.15f) also show nearly ideal dielectric permittivity, consistent with prior work on bismuth-excess (up to 10% excess) ceramics wherein bulk-like dielectric permittivity was observed [237]. Upon moving to bismuth deficiency and/or in the presence of $\nabla[Bi]$, however, the dielectric permittivity falls dramatically. The reduced dielectric permittivity may be explained by the fact that these heterostructures exhibit the most extensive interfacial interdiffusion (discussed elsewhere [29]), and that this interdiffusion can create a region of lower capacitance which dominates the dielectric response of the films.

5.6 Conclusions

This work demonstrates that growth parameters (*e.g.*, laser fluence, laser-repetition rate, and target composition can be used as knobs for *in situ* control of the type and concentration of off-stoichiometric *intrinsic* point defects during pulsed-laser deposition of ferroelectric thin films (*e.g.*, $BaTiO_3$ and $BiFeO_3$). It is shown that the induced defects directly impact the evolution of structure, and properties such as electrical leakage, dielectric response, and ferroelectric behavior of the films. Focusing on $BaTiO_3$ thin films, it is shown that small variations in the laser fluence result in single-phase, coherently strained films with chemistries ranging from $BaTiO_3$ to $Ba_{0.93}TiO_{2.87}$. In turn, as the laser fluence increases, the increased concentrations of point defects give rise to an out-of-plane lattice expansion (as much as 5.4% beyond the expected value), a reduction in leakage current density ($\approx 10^3$ times smaller in $Ba_{0.93}TiO_{2.87}$ films), a reduction in low-field permittivity and loss tangents, and an increase in the dielectric maximum temperatures. Although large polarization values are observed in all cases, hysteresis measurements and first-order reversal curve analysis show an evolution of large built-in potentials (shifted loops) and hysteresis-loop pinching in the barium- and oxygen-deficient films – suggesting the presence of defect dipoles. At least two defect states at ≈ 0.4 eV and ≈ 1.2 eV above the valence band are observed which grow in concentration with increasing deficiencies of barium and oxygen. The defect states are attributed to $V_{Ba}'' - V_O^{\bullet\bullet}$ defect-dipoles, and V_{Ba}'' defect states, respectively. It is also shown that such defects can be removed via *ex post facto* processing, if desired.

Focusing on $BiFeO_3$ thin films, it is shown that variations in laser-repetition rate and target composition have a significant effect on the average chemistry and chemical gradient throughout the thickness of the films. In particular, single-phase, coherently strained films can be produced with chemistries ranging from 10% bismuth deficiency to 4% bismuth excess and possessing bismuth gradients as large a 6% across the film thickness, with corresponding variations and gradients in the oxygen chemistry. Changes in both the overall stoichiometry and gradients are observed to give rise to three different transport mechanisms including Schottky, Poole-Frenkel, and modified Poole-Frenkel emissions with different leakage current densities. This, in turn, results in variations in the quality of ferroelectric hysteresis loops wherein slightly bismuth-deficient and bismuth-excess heterostructures are found to exhibit the best low-frequency ferroelectric response. Study of the dielectric permittivity finds nearly bulk-like response in stoichiometric and bismuth-excess films and permittivity that reduces with bismuth deficiency.

All told, this work provides detailed and systematic studies of the effect of growth-induced *intrinsic* off-stoichiometric point defects on the chemistry, structure, and property evolution in

some of the most technologically-important ferroelectric thin films. With the trends and insights gleaned from this work, it should be possible to prescribe routes to garner better control of such materials in device structures which could, in turn, expand their application in advanced next-generation technologies.

CHAPTER 6

In Situ and *Ex Situ* Control of Bombardment-Induced Defects and Their Impact on Electrical Resistivity of $PbTiO_3$ Thin Films

This Chapter focuses on both *in situ* and *ex situ* control of bombardment-induced defects and their impact on the electrical resistivity of $PbTiO_3$ thin films. Here, enhanced resistivity, and in turn, enhanced ferroelectric properties, are demonstrated in highly defective $PbTiO_3$ thin films. As-grown, highly-crystalline, stoichiometric $PbTiO_3$ thin films are shown to possess some of the least desirable properties; they are shown to suffer from high electrical leakage currents and losses that would preclude utilization of such materials in electronic devices. In turn, structural disorder and defects induced by *in situ* knock-on damage during growth or *ex situ* via ion bombardment are found to systematically reduce electrical leakage currents by up to ≈ 5 orders of magnitude and improve the ferroelectric device performance. A combination of impedance spectroscopy, temperature-dependent current-voltage, and deep-level transient spectroscopy studies reveal no change in the dominant conduction mechanism (*i.e.*, Poole-Frenkel emission), but systematic changes in the dominant trap energy from 0.24-0.27 eV in as-grown, pristine films to 0.93-1.01 eV for the ion-bombarded films which correspond to a complete quenching of the shallow trap states. The improved electrical performance is attributed to the formation of knock-on-damage- or bombardment-induced defect complexes and clusters which produce deeper trap states and reduce the free carrier transport.

6.1 Introduction

As mentioned in Section 1.1, although the word "defect" often carries a negative connotation, the impact of defects on material's properties is not always adverse and often specific characteristics of materials can be engineered through controlled defect introduction [23]. Semiconductor systems are an example in which defect engineering is extensively used to tailor properties. Years of development have gone into the production of large-scale, high-purity crystals with extremely low concentrations of *grown-in* defects [24,25]. These high-quality crystals, however, typically have limited utility in their pristine state and must be further processed to be used in devices. In fact, the wide-spread use of semiconductors in a range of applications is made possible by the finely-controlled and purposeful introduction of *intrinsic* and *extrinsic* defects which is accomplished through a variety of well-established defect-engineering techniques [26]. In ferroelectrics, however, defect-engineering strategies are mainly limited to chemical modifications, which are designed to counteract the detrimental effect of *grown-in* defects [9,11,12]. What has not been undertaken is an approach akin to that applied in semiconductors wherein the properties of materials are deterministically altered by controlled introduction of specific defects in nearly-perfect crystals in order to minimize those defects that detrimentally impact the properties and introduce those that enhance the desired properties.

Deterministic and on-demand control of electronic conduction in ferroelectrics, for example, is critical for a range of modern devices. In semiconductors, considerable effort goes into defining where and when the material will be insulating or conducting. In turn, techniques such as ion bombardment, have been developed to deterministically tune the electrical conduction of semiconductors by controlled defect formation [157]. Ion bombardment enables production of specific regions of high resistivity on a wafer and allows one to isolate neighboring active device regions (hence the name "ion bombardment for isolation"). In such systems, ion bombardment is thought to produce defects which are associated with mid-gap states that act as charge traps and lead to semi-insulating behavior [157]. There has been similar work in complex oxides, wherein ion bombardment has been used to locally disrupt material properties [150,151,154,155]. In this work, I show how such defect-engineering methods widely used in semiconductors can be implemented in classic complex-oxide ferroelectrics (*e.g.*, $PbTiO_3$) resulting in marked improvements of properties (*e.g.*, orders of magnitude enhancements in electrical resistivity) [30]. In turn, this approach shows that, akin to classic semiconductor materials, "pristine" ferroelectric materials are not always better and controlled introduction of specific defect structures can be used to elicit the desired properties.

6.2 *In Situ* Creation of Defects via Variations of Growth Pressure and Their Impact on Leakage Properties of $PbTiO_3$ Thin Films

This work focuses on 140 nm $PbTiO_3$/20 nm/$SrTiO_3$ (001) heterostructures grown at various growth pressures [30]. Three growth variants for the $PbTiO_3$ are explored: 1) low-pressure, low-oxidative potential growth (50 mTorr oxygen; henceforth *low-pressure O_2*), 2) high-pressure, high-oxidative potential growth (200 mTorr oxygen; henceforth *high-pressure O_2*), and 3) high-pressure, low-oxidative potential growth (200 mTorr total pressure, 50 mTorr oxygen, balance argon; henceforth *high-pressure O_2/Ar*). Rutherford backscattering spectrometry studies reveal that it is possible to produce essentially stoichiometric cation ratios within the error of the measurement (1-2%) for all three growth variants (low-pressure O_2, high-pressure O_2, and high-pressure O_2/Ar), simply by adjusting the laser-repetition rate while maintaining the laser fluence

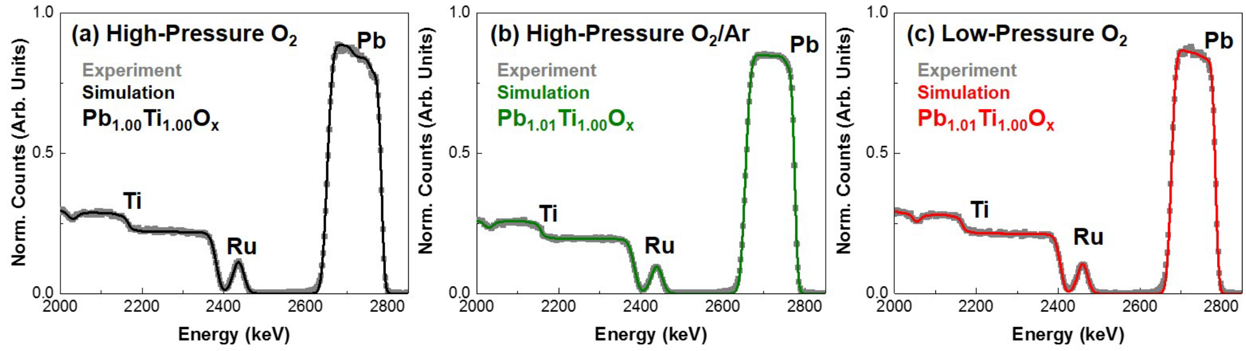

Figure 6.1. Rutherford backscattering spectrometry studies for (a) high-pressure O_2, (b) high-pressure O_2/Ar, and (c) low-pressure O_2 heterostructures with the corresponding best fit chemistry as obtained from the software package SIMNRA.

(Figure 6.1). Rutherford backscattering spectrometry samples were grown on $SrTiO_3$ (001) substrates concurrently with the films studied herein. In particular, films with measured stoichiometries of $Pb_{1.01}Ti_{1.00}O_x$ (low-pressure O_2), $Pb_{1.00}Ti_{1.00}O_x$ (high-pressure O_2), and $Pb_{1.01}Ti_{1.00}O_x$ (high-pressure O_2/Ar) were obtained.

$\omega - 2\theta$ X-ray diffraction studies (Figure 6.2) reveal that all heterostructures are single phase, epitaxial, and 00*l*-oriented, but with marked differences in the crystalline quality of the various heterostructures. It is noted that the substrate and $SrRuO_3$ bottom electrode diffraction peaks are consistent and similar, regardless of the growth conditions of the top $PbTiO_3$. The low-pressure O_2 heterostructures (bottom, Figure 6.2a) exhibit relatively broad, low-intensity diffraction peaks which are slightly shifted to the left of their expected position (indicating a slightly expanded lattice parameter). On the other hand, the high-pressure O_2/Ar (middle, Figure 6.2a) and O_2 (top, Figure 6.2a) heterostructures exhibit high crystallinity as indicated by the presence of sharp, high intensity film peaks and two additional double-diffraction (Umweganregung) reflections (at 24.01° and 45.08°) which are only observed in highly-crystalline heterostructures with coherent interfaces [261,262]. The differences in crystalline quality are further supported by comparison of FWHM of the rocking curves about the 002-diffraction conditions of film and substrate (Figure 6.2b). For all heterostructures, the $SrTiO_3$ substrates are essentially identical (FWHM in the range of 0.023-0.026°). The high-pressure O_2 and O_2/Ar heterostructures exhibit relatively narrow rocking curves of 0.038° and 0.045°, respectively; indicating the excellent structural quality. The same analysis of the low-pressure O_2 heterostructures, however, reveals a full order of magnitude broader rocking curve (0.368°); indicative of considerably lower crystalline quality. Current-voltage measurements also reveal dramatic differences in the leakage characteristics of the heterostructures (Figure 6.2c). The high-pressure O_2 and O_2/Ar heterostructures reveal more than two orders of magnitude higher leakage current densities as compared to the low-pressure O_2 heterostructures. In turn, the high leakage current density of the heterostructures grown in high pressures precludes measurement of closed, saturated ferroelectric hysteresis loops, while nearly-square fully-saturated and closed hysteresis loops can be measured for the low-pressure O_2 heterostructures (Figure 6.2d). The ferroelectric loops were measured at a range of frequencies, but for brevity only data at 10 kHz is shown here.

This dramatic difference in crystalline quality, transport, and ferroelectric properties of the films grown at low- and high- pressures cannot be attributed simply to differences in stoichiometry. According to the Rutherford backscattering spectrometry studies the films are nominally

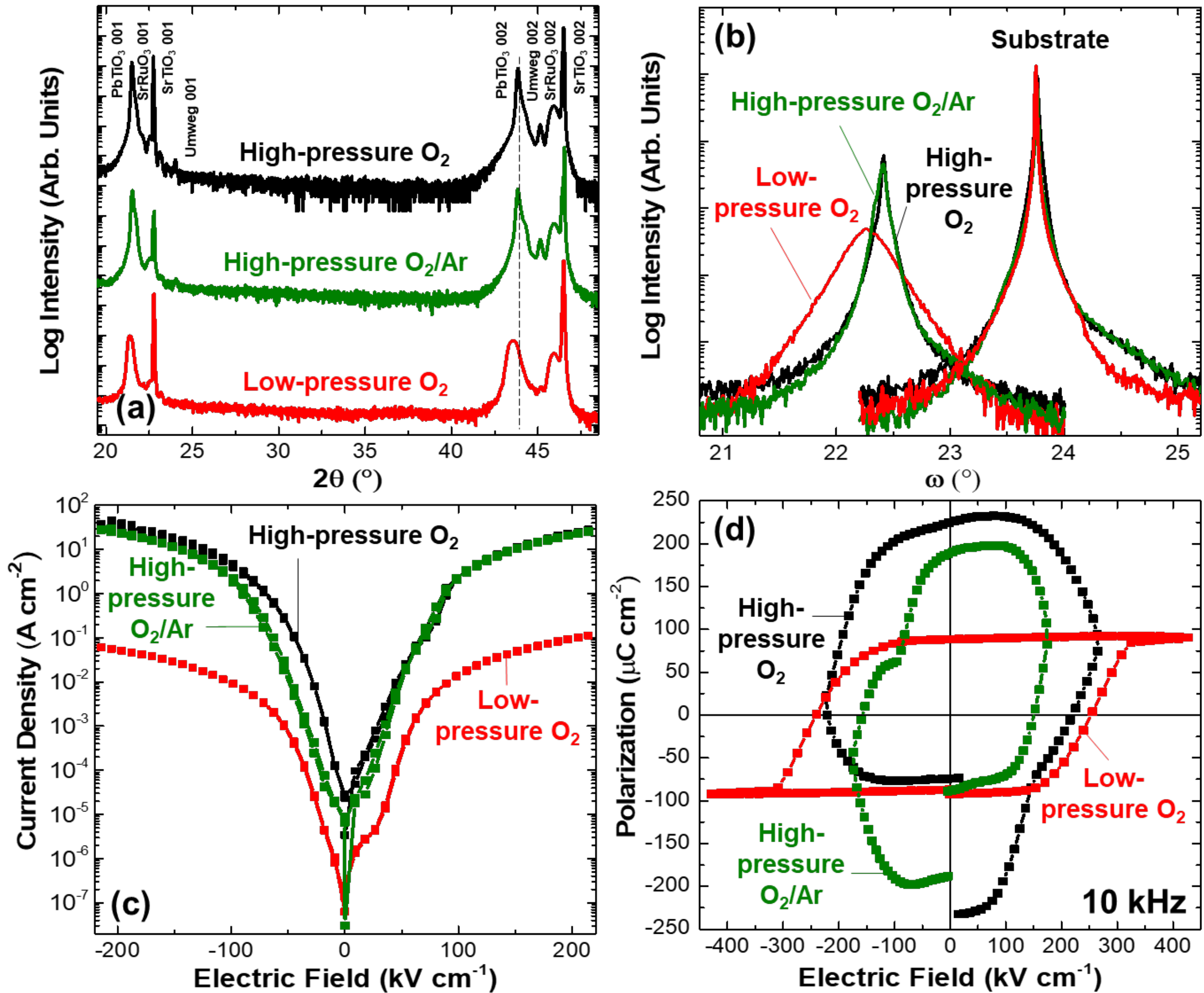

Figure 6.2. (a) $\omega - 2\theta$ X-ray diffraction scans of high-pressure O_2 (top), high-pressure O_2/Ar (middle), and low-pressure O_2 (bottom) heterostructures. (b) Rocking curves about the 002-diffraction conditions of film (left) and substrate (right) for high-pressure O_2 (FWHM=0.038°), high-pressure O_2/Ar (FWHM=0.045°), and low-pressure O_2 (FWHM=0.368°) heterostructures; substrate rocking curves are also shown for comparison (FWHM = 0.023-0.026°). (c) Leakage current density as a function of DC electric field, and (d) ferroelectric polarization-electric field hysteresis loops measured at 10 kHz for high-pressure O_2, high-pressure O_2/Ar, and low-pressure O_2 heterostructures.

stoichiometric with respect to the cations. Furthermore, the high-pressure O_2/Ar heterostructures were produced at the same oxidative potential as the low-pressure O_2 heterostructures but exhibit crystalline quality and properties akin to the high-pressure O_2 heterostructures, thus ruling out oxygen stoichiometry as a potential cause of the variations in crystalline quality and properties. Moreover, a series of *ex situ* oxygen annealing studies were completed in order to probe the role of oxygen off-stoichiometry on the observed differences in the structure and properties of heterostructures grown in different oxygen ambients. In particular, a low-pressure O_2 heterostructure was annealed in an oxygen pressure of 760 Torr for 3 hours at 600°C. This oxygen annealing results in no obvious changes to the crystalline quality, structure, transport, and ferroelectric properties (Figure 6.3). In turn, I propose that the differences between low- and high-pressure heterostructures are independent of the oxidative potential during the growth (within the

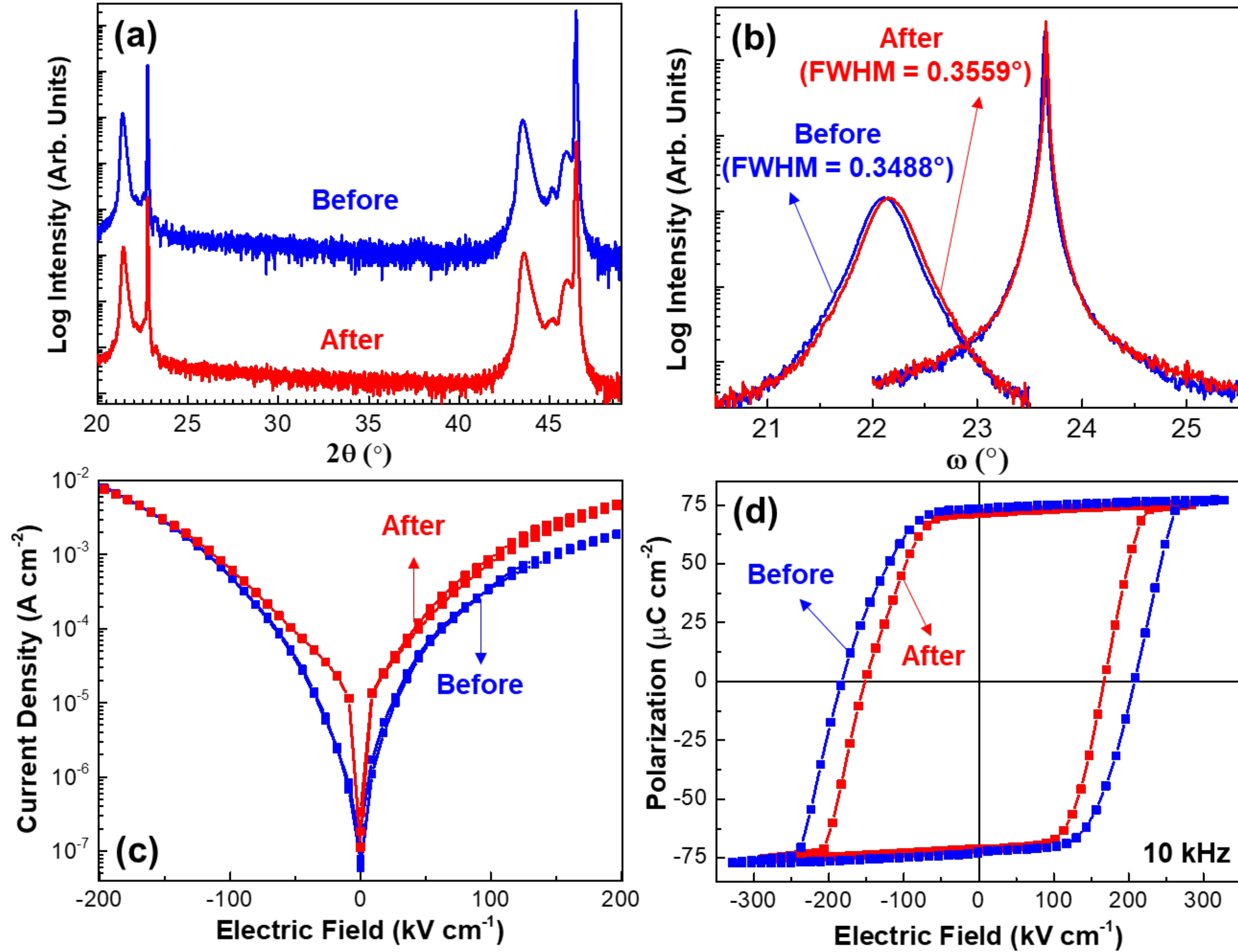

Figure 6.3. (a) $\omega - 2\theta$ X-ray diffraction scans, (b) ω-scans (rocking curves) about the 002-diffraction conditions of film and substrate, (c) current density *vs.* DC electric field, and (d) ferroelectric polarization-electric field hysteresis loops measured at 10 kHz for a low-pressure O_2 heterostructure before (in the as-grown state) and after annealing in an oxygen pressure of 760 Torr for 3 hours at 600°C.

range studied herein), and stem mainly from the overall magnitude of the growth pressure, and hence, from the difference in the kinetic energy of the incoming adatoms. As discussed in Section 4.2.2.1, as the growth pressure is decreased, the adatoms undergo less scattering events in transit to the substrate and thus arrive to the surface of the film with higher kinetic energy [143,145,178,179], resulting in knock-on damage and formation of structural defects (isolated *intrinsic* point defects, complexes, or clusters), consistent with the expanded lattice parameter and low crystalline quality, which, in turn, could be responsible for reduction of the leakage and improvement of ferroelectric properties.

6.3 *Ex Situ* Creation of Defects via High-Energy Helium-Ion Bombardment and Their Impact on Leakage Properties of $PbTiO_3$ Thin Films

In order to confirm the possible role of bombardment-induced defects in reduction of leakage and improvement of ferroelectric properties, a series of *ex situ* helium-ion bombardment experiments with varying bombardment doses (10^{14}-10^{16} ions cm^{-2}) were conducted on the high-quality,

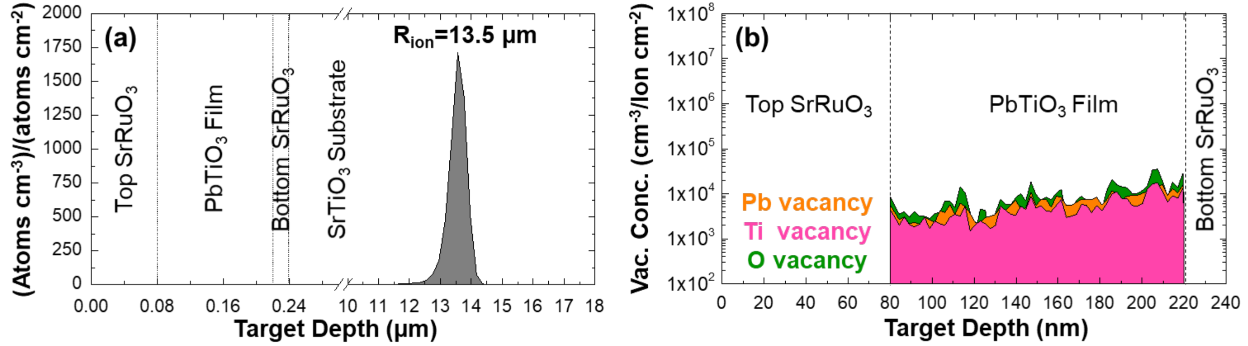

Figure 6.4. (a) SRIM simulation of He^{2+} concentration as a function of depth, suggesting that essentially no He^{2+} ions are implanted into the film, but instead the vast majority of the ions are stopped at a depth of ≈ 13.5 μm into the $SrTiO_3$ substrate, due to high incident energy of the ions (3.04 MeV). (b) SRIM simulation of induced defect concentrations as a function of depth in $PbTiO_3$ layer.

pristine high-pressure O_2 heterostructures [30]. For these experiments, a defocused He^{2+} ion beam with an energy of 3.04 MeV was made incident across the entire sample as described in Section 4.2.2.2. SRIM simulations suggest that due to the high incident ion energy used in our experiments, essentially no He^{2+} ions are implanted into the film, but instead the vast majority of He^{2+} ions are stopped at an average depth of ≈ 13.5 μm, deep into the $SrTiO_3$ substrate (Figure 6.4a). Furthermore, according to the simulations, lead, titanium, and oxygen vacancies are formed in the film as a result of bombardment, resulting in a defect concentration in the range of 10^{18}-10^{20} cm^{-3} for the dose range 10^{14}-10^{16} ions cm^{-2} (Figure 6.4b). It should also be noted that the concentration of defects generated by the ion beam is relatively uniform throughout the thickness of the ferroelectric layer. Rutherford backscattering spectrometry studies were completed before and after ion bombardment (Figure 6.5) and reveal no change in the chemistry of the heterostructures for any dose studied herein. Therefore, defects produced in this process must be occurring in a stoichiometric fashion. Increasing the bombardment dose, however, does systematically worsen the crystalline quality of the heterostructures as manifested by a gradual increase in the FWHM of

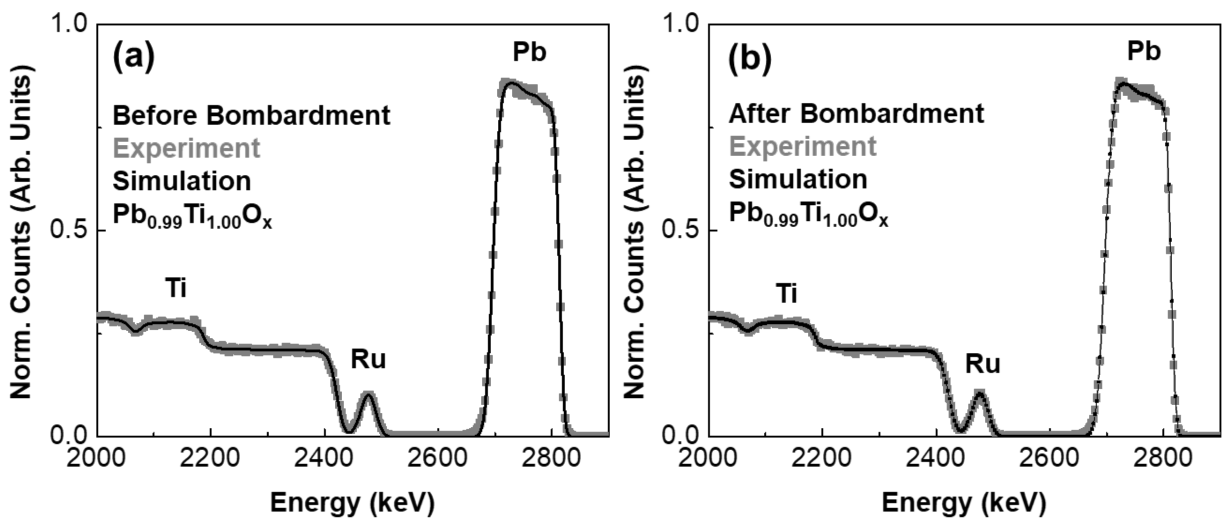

Figure 6.5. Rutherford backscattering spectrometry data for a heterostructure grown in high-pressure O_2 (a) before and (b) after He^{2+} ion bombardment with a dose of 10^{16} ions cm^{-2}. No overall change of chemistry is detected as a result of ion bombardment.

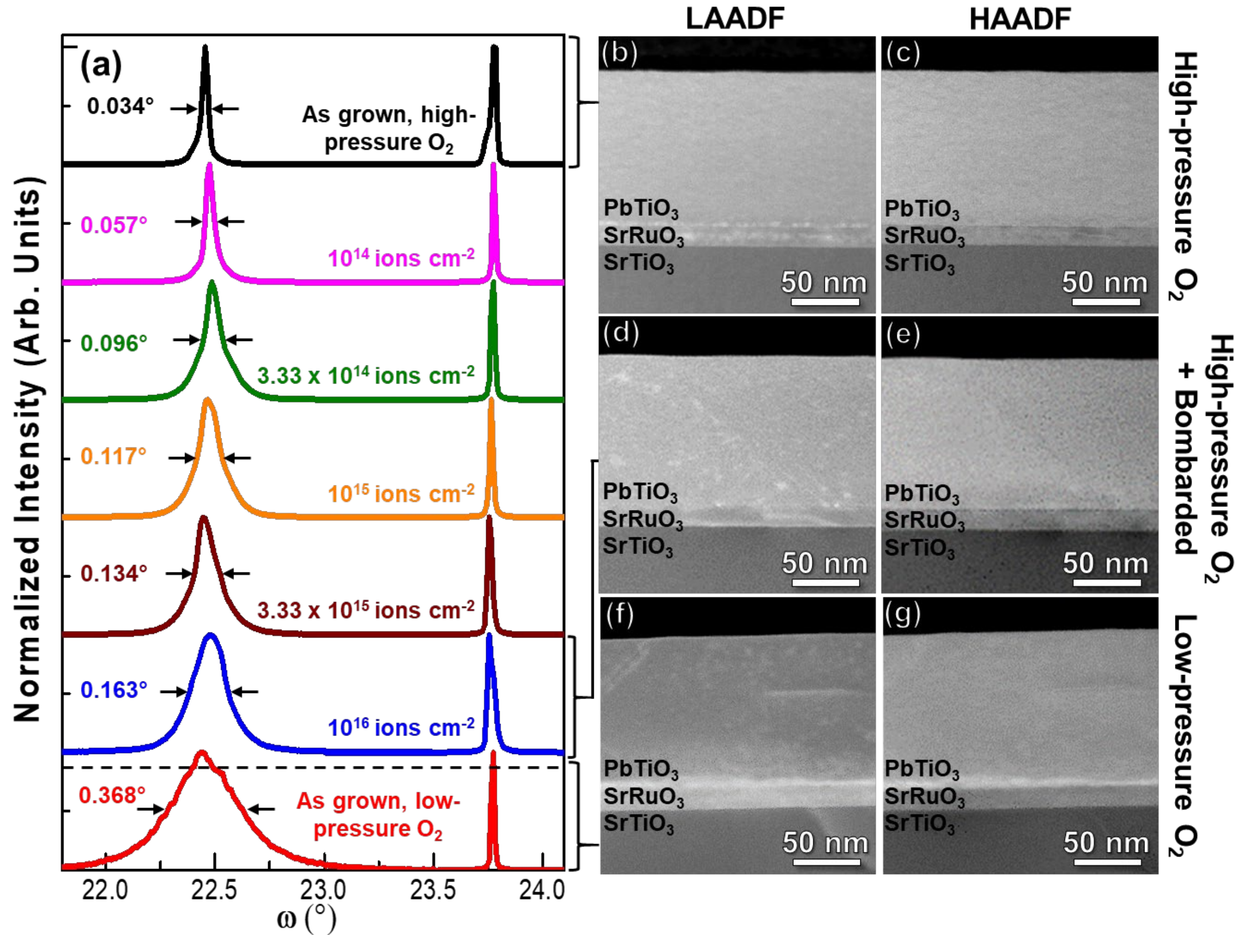

Figure 6.6. (a) Rocking curves of a high-pressure O_2 heterostructure as a function of He^{2+} bombardment dose obtained about the 002-diffraction condition; the bottom rocking curve is for a low-pressure O_2 heterostructure for comparison. LAADF-STEM and HAADF-STEM images of (b), (c) high-pressure O_2, (d), (e) He^{2+} bombarded, high-pressure O_2 (dose of 10^{16} ions cm^{-2}), and (f), (g) low-pressure O_2 heterostructures, respectively.

the rocking curves for the 002-diffraction condition of the film from 0.034° for the as-grown, high-pressure O_2 heterostructures to 0.163° after bombardment with a He^{2+} dose of 10^{16} ions cm^{-2} (Figure 6.6a). A slight expansion of out-of-plane lattice parameter is also observed upon *ex situ* bombardment of the high-pressure O_2 heterostructures similar to what is observed in the *in situ* bombarded heterostructures (Figure 6.7). It appears that the *ex situ* bombardment of a highly-crystalline, high-pressure O_2 heterostructure can be made to exhibit a similar crystallinity – or lack thereof – to the *in situ* bombarded, low-pressure O_2 heterostructures.

To further confirm the similarities between *in situ* and *ex situ* bombarded heterostructures, HAADF-STEM and LAADF-STEM studies were completed. The HAADF-STEM provides chemical information in the form of *Z*-contrast, while LAADF-STEM is additionally sensitive to structure or anything that dechannels the transiting electrons (*e.g.*, phonons or strain fields from point defects) [190,191]. Examination of the high-pressure O_2 heterostructures reveals uniform contrast in both the LAADF-STEM and HAADF-STEM images suggesting uniform structure and chemistry and minimal defect density (Figure 6.6b,c). Following the *ex situ* bombardment (dose of 10^{16} ions cm^{-2}), however, these heterostructures are found to change dramatically wherein LAADF-STEM images show the formation of a splotchy contrast likely due to the formation of

point defects and clusters (Figure 6.6d) [263], although no Z-contrast is observed in HAADF-STEM images (Figure 6.6e). Finally, the LAADF-STEM images of the low-pressure O_2 heterostructures (Figure 6.6f) exhibit similar splotchy patterns to the ion-bombarded heterostructures, again with no *Z*-contrast in HAADF-STEM images (Figure 6.6g) suggesting that the bombardment from the *in situ* high-energy adatoms and that from the *ex situ* He^{2+} bombardment produce similar defect types.

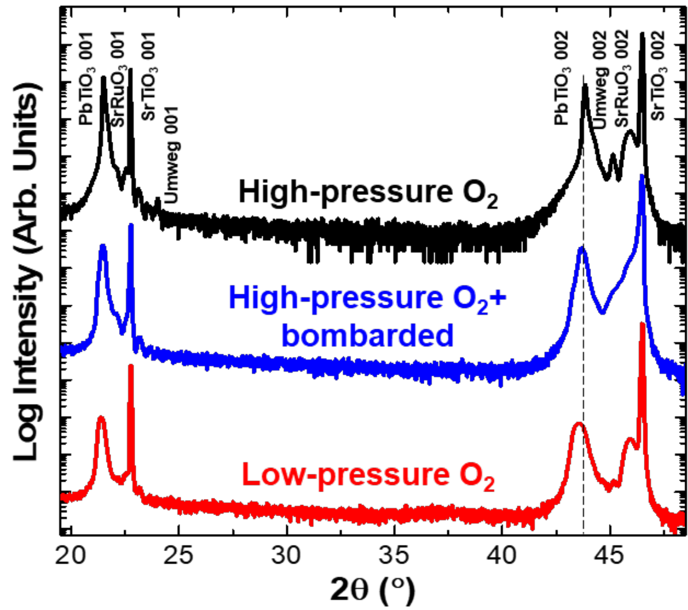

Figure 6.7. $\omega - 2\theta$ X-ray diffraction scans of high-pressure O_2, high-pressure O_2-bombarded (dose of 3.33×10^{15} ions cm^{-2}), and low-pressure O_2 heterostructures. Both *in situ* and *ex situ* bombardment of the heterostructures result in slight expansion of the out-of-plane lattice parameter.

The *ex situ* He^{2+} bombardment also has a similar effect to the *in situ* bombardment at low pressures on the transport and ferroelectric properties of the heterostructures. Increasing He^{2+} dose systematically decreases the leakage current density of the heterostructures grown at high pressures by up to ≈ 5 orders of magnitude (Figure 6.8a), concurrent with lowering the crystalline quality of the films. As a result of this reduction of leakage, fully-saturated ferroelectric loops with saturation polarization of ≈ 78 µC cm^{-2} (similar to that of the low-pressure O_2 heterostructures) are obtained in the dose range of 3.33×10^{15}-1.00×10^{16} ions cm^{-2} (Figure 6.8b). This further supports the idea that formation of knock-on-damage-related defects is responsible for lower leakage in the *in situ* and *ex situ* bombarded heterostructures as compared to the “pristine” high-pressure heterostructures.

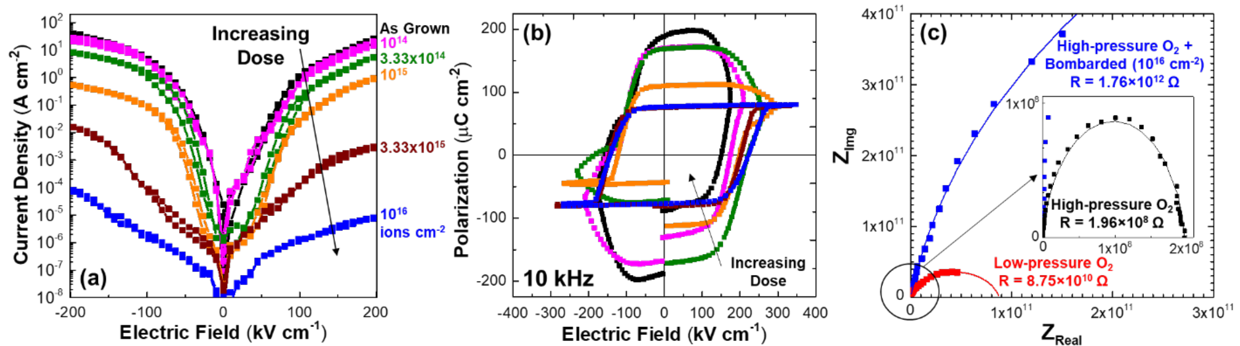

Figure 6.8. (a) Leakage current density as a function of DC electric field for a high-pressure O_2 heterostructure which is progressively He^{2+} bombarded with the noted doses. (b) Ferroelectric polarization-electric field hysteresis loops measured at 10 kHz for the same high-pressure O_2 heterostructures after various He^{2+} bombardment doses. (c) Nyquist plots of Z_{Img} *vs.* Z_{Real} for high-pressure O_2, He^{2+} bombarded, high-pressure O_2 (dose of 10^{16} ions cm^{-2}), and low-pressure O_2 heterostructures. The presence of one semicircle in all heterostructures reveals a single transport mechanism while the magnitude of resistance (extracted from the intercept of the semicircles on the real axis) varies as noted.

6.4 Characterization of Bombardment-Induced Defects in $PbTiO_3$ Thin Films

To better understand the mechanism for the dramatic changes in electrical leakage, I have leveraged an array of characterization techniques [30]. First, impedance spectroscopy provides a way to differentiate between various contributions to the overall resistive response [213,214], as discussed in Section 4.3.3.8. Impedance spectroscopy studies of the high-pressure O_2, low-

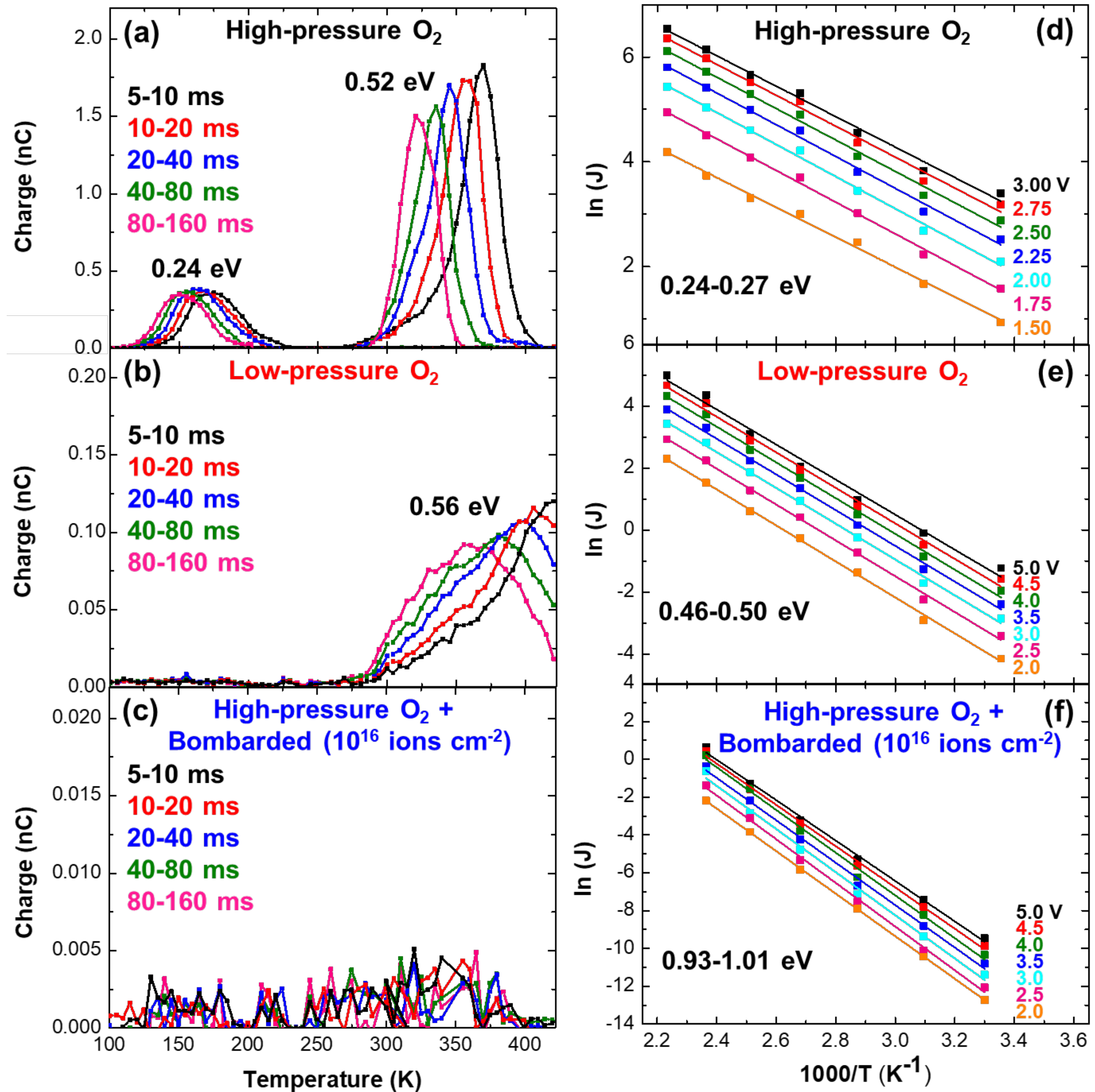

Figure 6.9. Deep-level transient spectroscopy signal measured at five different time windows for (a) high-pressure O_2, (b) low-pressure O_2, and (c) He^{2+} bombarded, high-pressure O_2 (dose of 10^{16} ions cm^{-2}) heterostructures. Arrhenius plots of $ln(J)$ *vs.* $1000/T$ at different voltages for (d) high-pressure O_2, (e) low-pressure O_2, and (f) He^{2+} bombarded, high-pressure O_2 (dose of 10^{16} ions cm^{-2}) heterostructures. The activation energies (noted) are extracted from the slope of the linear fits.

pressure O_2, and He^{2+} bombarded, high-pressure O_2 (dose of 10^{16} ions cm^{-2}) heterostructures were

undertaken (Figure 6.8c). In all cases, only a single semicircle is observed; suggesting a single transport mechanism dominated by the bulk of the film. The magnitude of the resistance (extracted from the intercept of the semicircles on the real axis), however, is found to vary largely from $1.96 \times 10^8\ \Omega$ to $8.75 \times 10^{10}\ \Omega$ to $1.76 \times 10^{12}\ \Omega$ for the high-pressure O_2, low-pressure O_2, and He^{2+} bombarded high-pressure O_2 (dose of 10^{16} ions cm^{-2}) heterostructures, respectively.

Having established that the transport remains bulk mediated, I explored the origin of the large differences in the conductivity by applying both deep-level transient spectroscopy and temperature-dependent current-voltage measurements. Deep-level transient spectroscopy measurements can be used to probe a variety of trap states present in a material [215] as described in Section 4.3.3.9, while current-voltage studies can be used to reveal the dominant trap states and conduction mechanisms, as discussed in Section 4.3.3.7. Deep-level transient spectroscopy signal was obtained for five different rate windows (in the range of 5-160 ms) at temperatures in the range of 100-425 K (Figure 6.9a-c). The activation energy of each trap state is extracted from the shift of the deep-level transient spectroscopy peaks with temperature (Figure 6.10). In the case of the high-pressure O_2 heterostructures (Figure 6.9.a), two peaks can be observed indicating the presence of two different defect states with activation energies of 0.24 eV and 0.52 eV. The difference in the intensity of the peaks indicates a higher concentration of the deeper trap state. For the low-pressure O_2 heterostructures (Figure 6.9b), only a single high-temperature peak is observed corresponding to an activation energy of 0.56 eV albeit with a much lower intensity compared to the similar peak in the high-pressure O_2 heterostructures. Moreover, this high-temperature peak in the *in situ* bombarded low-pressure O_2 heterostructures is broader and shifted in temperature compared to the same peak in the high-pressure O_2 heterostructures. Broadening of deep-level transient spectroscopy peaks is usually attributed to the formation of defect clusters which can give rise to a distribution in emission energy of the defects, while shifts of a peak can be caused by changes in the environment surrounding the defects or the defect configuration [264,265]. Finally, no deep-level transient spectroscopy signal could be measured for the *ex situ* He^{2+} bombarded, high-pressure O_2 heterostructures (Figure 6.9c) within the same temperature and time windows, likely because of the highly-insulating nature of this heterostructure. Studies at higher temperatures (in hopes of extracting high signals from the bombarded heterostructures) have been also unsuccessful.

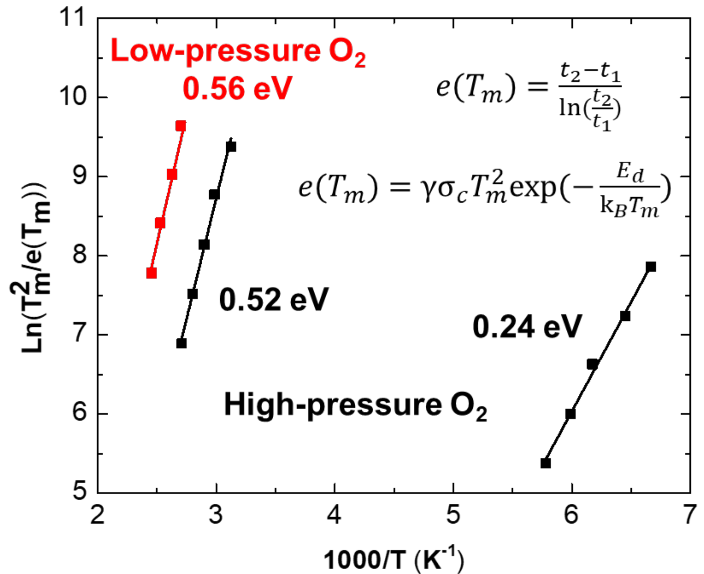

Figure 6.10. Arrhenius plot of $\ln(\frac{T_m^2}{e(T_m)})$ *vs.* $\frac{1000}{T_m}$. The activation energy of each trap state is extracted from the slope of the linear fits.

Current-voltage measurements were carried out in order to identify the dominant conduction mechanism and trap state in each heterostructure. For the high-pressure O_2, low-pressure O_2, and He^{2+} bombarded, high-pressure O_2 (dose of 10^{16} ions cm^{-2}) heterostructures, the current-voltage data fits well with both Poole-Frenkel and Schottky emission conduction

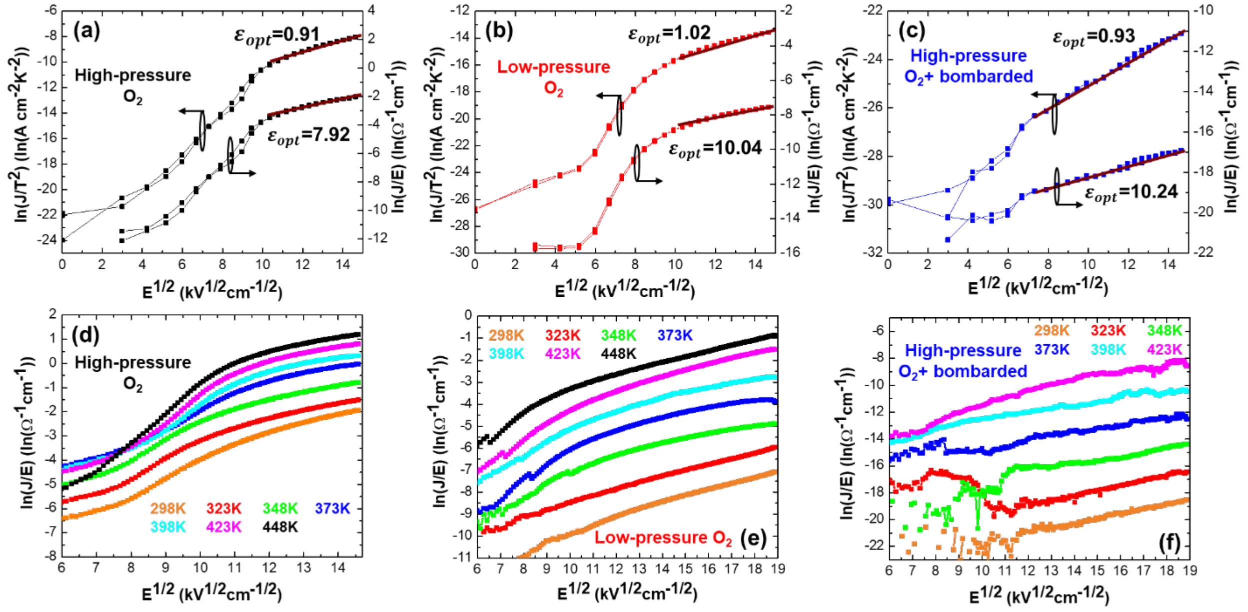

Figure 6.11. Forward bias room temperature current-voltage data represented on the standard Schottky and Poole-Frenkel plots for (a) high-pressure O_2, (b) low-pressure O_2, and (c) He^{2+} bombarded, high-pressure O_2 (dose of 10^{16} ions cm^{-2}) heterostructures. The data shows good linear fit (red lines) to both mechanisms at high electric fields, but only Poole-Frenkel fits give reasonable values of optical dielectric constant (extracted from the slope of linear fits). Temperature dependence of the current-voltage characteristics in a Poole-Frenkel plot for (d) high-pressure O_2, (e) low-pressure O_2, and (f) He^{2+} bombarded, high-pressure O_2 (dose of 10^{16} ions cm^{-2}) heterostructures.

mechanisms (Figure 6.11a-c). For all heterostructures, the values of optical dielectric constant extracted from the Poole-Frenkel fit (7.92 for as-grown high-pressure O_2, 10.04 for low-pressure O_2, and 10.24 for He^{2+} bombarded, high-pressure O_2 (dose of 10^{16} ions cm^{-2})) are closer to that reported from optically measured refractive index ($\varepsilon_{opt} = 6.25$ for $PbTiO_3$) [266]. Schottky emission is therefore ruled out since it yields unphysical values for the optical dielectric constant. The current-voltage measurement results also show little dependence on the polarity of the applied bias, which further confirms a conduction mechanism dominated by the bulk of the sample. Therefore, Poole-Frenkel emission is identified as the dominant conduction mechanism at electric fields above 100 kV cm^{-1}. Current-voltage response was obtained at different temperatures in the range of 300-470 K (Figure 6.11d-f), and the activation energies are extracted from the slope of the linear fits to the Arrhenius plots of $ln(J)$ *vs.* $1000/T$ for different applied voltages (Figure 6.9d-f). From these fits, a shallow trap state with an activation energy of 0.25-0.27 eV is extracted for the pristine, high-pressure O_2 heterostructures, while the leakage appears to be dominated by deeper levels, with activation energies of 0.47-0.50 eV for *in situ* bombarded low-pressure O_2 heterostructures, and even deeper trap states with energies of 0.93-1.01 eV for *ex situ* He^{2+} bombarded, high-pressure O_2 (dose of 10^{16} ions cm^{-2}) heterostructures.

These results can be understood by examining the nature of conduction and defects in these materials. The conduction in $PbTiO_3$ and $PbZr_xTi_{1-x}O_3$ systems is typically *p*-type and mediated by lead-site defects (hole conduction attributed to lead vacancies, Pb^{3+} centers, or impurities) [28,267-271]. In practice, it has been also shown that there is an abundance of lower valent substitutional cations (*i.e.*, acceptor impurities) such as Fe^{+3}, Al^{+3}, Mg^{+2}, Na^{+1}, *etc.* in these systems

resulting in the *p*-type behavior [28,270]. Lead vacancies can readily form in these systems due to high volatility of lead, which, in turn, induces acceptor levels [270]:

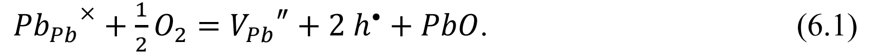

$$Pb_{Pb}^{\times} + \frac{1}{2}O_2 = V_{Pb}'' + 2\,h^{\bullet} + PbO. \quad (6.1)$$

The ionization level of lead vacancies has been calculated to be 0.56 eV from the top of valence band [270] and an acceptor level located at 0.39 eV above valance band edge has been measured in $PbZr_xTi_{1-x}O_3$ [272]. The mobile holes introduced by lead vacancies or by acceptor impurities lead to a lowering of the electrical resistivity and poor ferroelectric performance. The holes can be also trapped at lead sites, forming Pb^{3+} centers. Two Pb^{2+} ions can oxidize to Pb^{3+} for every lead site vacancy:

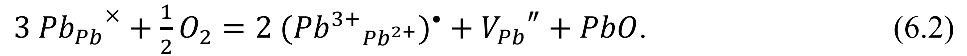

$$3\,Pb_{Pb}^{\times} + \frac{1}{2}O_2 = 2\,(Pb^{3+}{}_{Pb^{2+}})^{\bullet} + V_{Pb}'' + PbO. \quad (6.2)$$

The holes introduced to the lattice by acceptor impurities can also be trapped on the lead sites resulting in Pb^{3+} centers. Prior work has identified a shallow hole trap with an activation energy of ≈ 0.26 eV which has been attributed to Pb^{3+} centers [269,273]. Holes can also become compensated by formation of oxygen vacancies [270,274]:

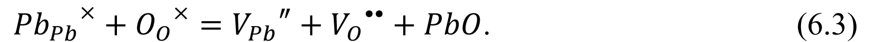

$$Pb_{Pb}^{\times} + O_O^{\times} = V_{Pb}'' + V_O^{\bullet\bullet} + PbO. \quad (6.3)$$

These oxygen vacancies are able to compensate some (or most) of the holes introduced by the lead vacancies and therefore weaken the *p*-type conduction. Oxygen-vacancy-related defects are thought to be relatively deep donors [270] limiting the potential for *n*-type conduction which is consistent with the fact that *n*-type conductivity is less frequently observed in $PbTiO_3$ systems, even at low oxygen pressures [267,268,270,274,275]. Finally, studies have indicated that Ti^{4+} ions can also be present in the Ti^{3+} state due to oxygen loss, which can act as deep electron traps located at 1 eV or more below the conduction band edge [28,267,269,270,276]:

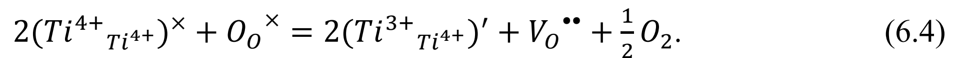

$$2(Ti^{4+}{}_{Ti^{4+}})^{\times} + O_O^{\times} = 2(Ti^{3+}{}_{Ti^{4+}})' + V_O^{\bullet\bullet} + \frac{1}{2}O_2. \quad (6.4)$$

Thus, I conclude that the transport in the high-pressure O_2 heterostructures is dominated by Pb^{3+} centers (trap energy of 0.25-0.27 eV), in the low-pressure O_2 heterostructures it is dominated by lead vacancies (trap energy of 0.46-0.50 eV), and in the He^{2+} bombarded, high-pressure O_2 heterostructures it is dominated by a much deeper state (trap energy of 0.93-1.01 eV) which is most likely associated with deep-lying defect complexes, although the energy also matches with the values reported for Ti^{3+} centers.

What all of this data comes together to reveal is that producing the "best" ferroelectric materials (in this case a ferroelectric material with high crystallinity and nearly ideal stoichiometry) does not necessarily result in the ideal properties. In particular, in $PbTiO_3$, such high-pressure O_2 heterostructures are dominated by the presence of isolated point defects, namely Pb^{3+} and lead vacancies (as detected by deep-level transient spectroscopy and current-voltage measurements), which give rise to readily activated shallow trap states and, in turn, enhanced hole conduction and poor ferroelectric performance. Upon either *in situ* or *ex situ* bombardment, the production of higher concentrations of defects results in the production of deeper trap states associated with defect complexes. In the low-pressure O_2 heterostructures, the data suggests that all trap states associated with shallow Pb^{+3} centers are quenched, but that some trap states associated with lead vacancies (which occurred in much higher concentrations even in the high-pressure O_2 heterostructures) remain. In the He^{2+} bombarded, high-pressure O_2 heterostructures, the more aggressive introduction of defects results in complete quenching of both trap states

associated with the Pb^{3+} and lead vacancies, and thus a dramatic reduction in the conductivity of the films. Besides impacting the trap states available in the material, the defects/disorder induced by the *in situ* or *ex situ* bombardment could also have the added benefit of lowering the carrier mobility (via lattice, defect, and impurity scattering) [157]. All told, the combined effects manifest themselves as a ≈ 5 order of magnitude reduction in leakage current density. I also note that earlier work on low-energy oxygen-ion bombardment of ferroelectrics [148-150] also showed the potential to control ferroelectric properties. This early work, however, did not delve into the mechanism for the improved properties and perhaps the current work begins to better explain these observations and provide a framework by which additional control of materials can be produced.

6.5 Conclusions

In conclusion, experimental observations in this work show that the growth of high-quality thin films does not necessarily lead to optimum properties. I have demonstrated in a classic ferroelectric thin film (*i.e.*, $PbTiO_3$ thin films) that the presence of even small concentrations of defects, which are hard-to-detect using conventional techniques such as X-ray diffraction and Rutherford backscattering spectrometry, can dramatically affect the properties (*e.g.*, electronic leakage and ferroelectric hysteresis response). The defects responsible for poor transport and ferroelectric properties in $PbTiO_3$ thin films are identified to be shallow isolated point defects such as Pb^{+3} centers and lead vacancies, which contribute to hole conduction. Introduction of bombardment-induced defects is shown to be an effective way to quench these trap states by turning them into deep-lying defect complexes and clusters which, in turn, leads to a dramatic reduction of leakage current by up to ≈ 5 orders of magnitude and improvement of ferroelectric device performance.

CHAPTER 7

Ex Situ Control of Bombardment-Induced Defects and Their Impact on Transport and Ferroelectric Switching Properties of $BiFeO_3$ Thin Films

This Chapter focuses on *ex situ* control of bombardment-induced defects and their impact on the electrical resistivity and ferroelectric switching properties of $BiFeO_3$ thin films. In this work, I demonstrate some of the most resistive $BiFeO_3$ thin films reported to date via *ex situ* high-energy ion bombardment. High leakage in as-grown $BiFeO_3$ thin films is shown to be due to the presence of moderately shallow isolated point defects such as oxygen vacancies, which form during the growth, dope the lattice with electrons, and contribute to *n*-type conduction. Ion bombardment is shown to be an effective way to reduce this free carrier transport (by up to $\approx$ 4 orders of magnitude) by trapping the charge carriers deep in the band gap as a result of the formation of bombardment-induced deep-lying defect complexes and clusters. Introduction of such defects, however, is also found to impact the switching behavior. The increased defect concentration, while having no evident impact on the domain structure or the switching mechanism, is shown to give rise to a systematic ion-dose-dependent increase in the coercive field, extension of the defect-related creep regime, increase in the pinning activation energy, decrease in the switching speed, and broadening of the field distribution of switching. Ultimately, the use of such defect engineering routes to enhance ferroelectric device performance requires identification of an optimum range of ion dose to achieve maximum enhancement in resistivity with minimum impact on the ferroelectric switching.

7.1 Introduction

Considerable effort in modern materials science has focused on the quest for multifunctional materials with novel or enhanced responses as a means to meet the needs of a diverse range of applications. Among complex-oxide ferroelectrics, $BiFeO_3$ has attracted considerable attention due to its multiferroic nature (*i.e.,* coexistence of a large spontaneous polarization and *G*-type antiferromagnetism), and potential for strong magnetoelectric coupling [43,67-69]. Deterministic control of this material, however, is challenging due to the complex nature of its chemistry and penchant for defects (*i.e.*, the presence of multiple cation and anion species and their corresponding point defects, complexes, and clusters). Similar to many other complex-oxide ferroelectrics, $BiFeO_3$ is known to be highly susceptible to point defect formation (which have low energy barriers of formation) and likely to create defects to maintain charge neutrality to compensate for impurities (often present in the source materials) and/or off-stoichiometry in the lattice [229,235]. The uncontrolled defect formation, in turn, can have a detrimental impact on the properties. Therefore, careful understanding of the interplay between defects and materials response, as well as establishing routes to control the type and concentration of defects, are crucial for fine-tuning and optimization of the properties of $BiFeO_3$ thin films.

For example, point defects often give rise to high leakage and losses via doping of the lattice with charge which can limit the application of $BiFeO_3$ thin films in electronic devices [29,227-231]. In turn, developing routes to enhance the resistivity of $BiFeO_3$ remains an important materials challenge. In order to reduce the electronic leakage in $BiFeO_3$, chemical doping/alloying (*i.e.*, introduction of *extrinsic* defects/dopants) has been traditionally used [221-226]. The extent to which the resistivity can be enhanced using chemical doping is, however, limited by the solid solubility, as well as by the simultaneous changes in the ferroelectric properties (*e.g.*, reduction in polarization) [11]. In Chapter 5, it was demonstrated that growth-induced control of off-stoichiometric *intrinsic* point defects can be also used as an alternative route to reduce the leakage current of $BiFeO_3$ thin films to some extent [29]. More broadly, in other systems such as group IV and III-V semiconductors, it has been shown that, controlled introduction of *intrinsic* point defects via ion bombardment can be an effective route to enhanced resistivity [157]. This technique enables the production of specific regions of high resistivity on a wafer due to the formation of mid-gap states, and isolation of neighboring active device regions (hence the name "ion bombardment for isolation") [157]. In the case of complex oxides, similar approaches have been used to locally disrupt or turn-off the material's response [150,151,154,155]. As discussed in Chapter 6, my work on $PbTiO_3$ thin films has demonstrated that, when applied appropriately, such approaches can be also used to enhance the performance of complex-oxide ferroelectric thin films by dramatically enhancing the electrical resistivity [30]. In this work, I address the leakage problem in $BiFeO_3$ thin films via *ex situ* high-energy ion bombardment [32]. The ability of this ion-bombardment technique to control the concentration of *intrinsic* point defects beyond the thermodynamic limits enables tuning of the resistivity by orders of magnitude, here demonstrated in some of the most resistive $BiFeO_3$ thin films reported to date.

More broadly, as discussed in Section 3.5, point defects can also have an impact on ferroelectric switching by controlling the local polarization stability, acting as pinning sites for domain-wall motion, and serving as nucleation sites for polarization reversal which can also place limitations on device-relevant parameters such as coercive field, energy of switching, switching speed, and more [12,58]. Despite the known relevance of defects in ferroelectric switching, limited systematic studies have been undertaken on the interplay of *intrinsic* point defects and switching

in $BiFeO_3$. In this work, I take advantage of controlled defect production via *ex situ* high-energy ion bombardment, to systematically study the relationship between bombardment-induced *intrinsic* point defects and ferroelectric polarization switching in $BiFeO_3$ thin films across many orders of magnitude of defect concentration [32].

7.2 *Ex Situ* Creation of Defects in $BiFeO_3$ Thin Films via High-Energy Helium-Ion Bombardment

This work focuses on 100 nm $BiFeO_3$/20 nm $SrRuO_3$/$DyScO_3$ (110) thin-film heterostructures [32]. $\omega - 2\theta$ X-ray diffraction studies of as-grown heterostructures (top, Figure 7.1a,b) reveal that the heterostructures are epitaxial, 00*l*-oriented, and single-phase. The chemistry of the heterostructures was studied via Rutherford backscattering spectrometry. The samples for Rutherford backscattering spectrometry were grown on $DyScO_3$ (110) substrates simultaneously with the films studied herein. Rutherford backscattering spectrometry studies on the as-grown heterostructures show that the growth conditions used in this work produce a nearly stoichiometric cation ratio ($Bi_{0.99}Fe_{1.00}O_x$), within the error of the measurement (1-2%) (top, Figure 7.2). These nominally stoichiometric thin films of $BiFeO_3$ were subsequently bombarded with varying doses

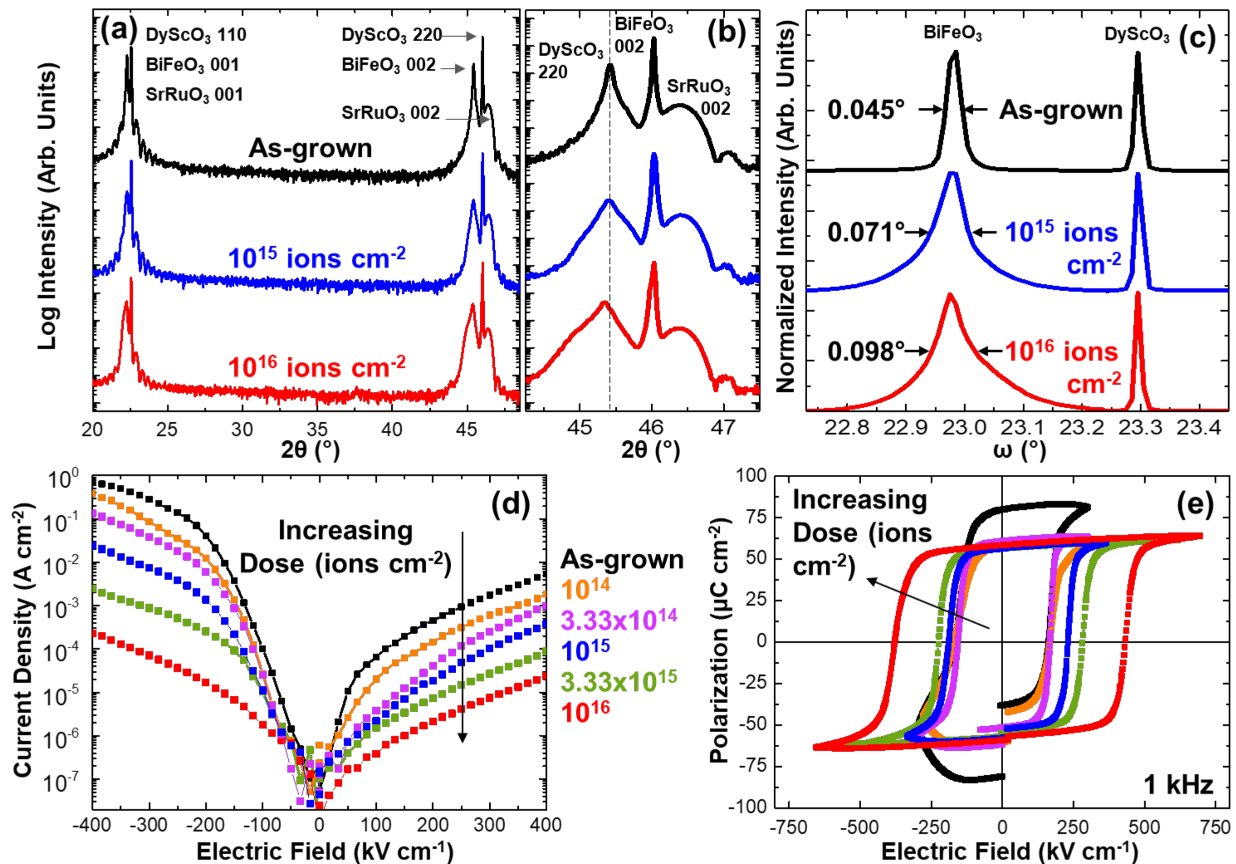

Figure 7.1. (a) Wide angle $\omega - 2\theta$ X-ray diffraction scans and (b) zoom-in about the 002- and 220-diffraction conditions for heterostructures ion bombarded with various He^{2+} doses. (c) Rocking curves for heterostructures ion bombarded with various He^{2+} doses obtained about the 002-diffraction conditions of film and substrate. (d) Leakage current density as a function of DC electric field, and (e) ferroelectric polarization-electric field hysteresis loops measured at 1 kHz after ion bombardment with various He^{2+} doses.

(10^{14}-10^{16} ions cm^{-2}) of He^{2+} ions using an energy of 3.04 MeV across the entire sample, as described in Section 4.2.2.2. Rutherford backscattering spectrometry studies completed after ion bombardment to a dose of 10^{16} ions cm^{-2} (bottom, Figure 7.2) reveal no change in the overall chemistry of the heterostructures, suggesting that the bombardment-induced defects are produced in a stoichiometric fashion for all doses studied herein.

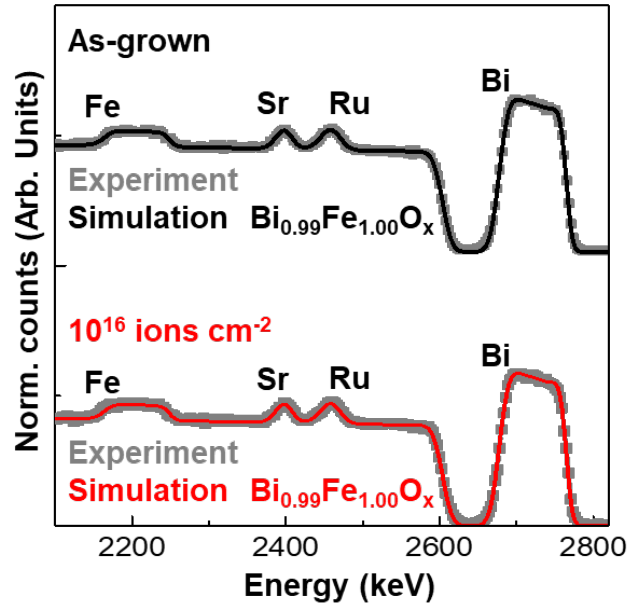

Figure 7.2. Rutherford backscattering spectrometry studies before and after He^{2+} ion bombardment with a dose of 10^{16} ions cm^{-2}. The corresponding best fit chemistries are obtained from SIMNRA.

The high energy of the ions in these experiments allow for generation of *intrinsic* point defects without ion implantation in the ferroelectric as supported by SRIM simulations. The simulations suggest that the given experimental parameters result in the He^{2+} ions being stopped deep within the $DyScO_3$ substrate (peaked at a depth of $\approx$ 15 μm), resulting in effectively zero concentration of He^{2+} ions throughout the thickness of the $BiFeO_3$ and $SrRuO_3$ layers (Figure 7.3a). Further simulations show that bismuth, iron, and oxygen vacancies are formed in the film, with a total defect concentration in the range of 10^{18}-10^{20} cm^{-3} for the dose range of 10^{14}-10^{16} ions cm^{-2} (Figure 7.3b), as a result of collision events between the high-energy He^{2+} ions and the target atoms. It should also be noted that the concentration of defects generated by the ion beam is relatively uniform throughout the thickness of the ferroelectric layer.

A signature of these ion-bombardment-induced defects can be found in the $\omega - 2\theta$ X-ray diffraction scans for the heterostructures bombarded with doses of 10^{15} ions cm^{-2} (middle, Figure 7.1a,b) and 10^{16} ions cm^{-2} (bottom, Figure 7.1a,b). Although the films remain crystalline, epitaxial, and single-phase, there is a clear broadening of the film peak (suggesting a lowering of crystalline quality), and a slight out-of-plane lattice expansion which is attributed to the formation of point

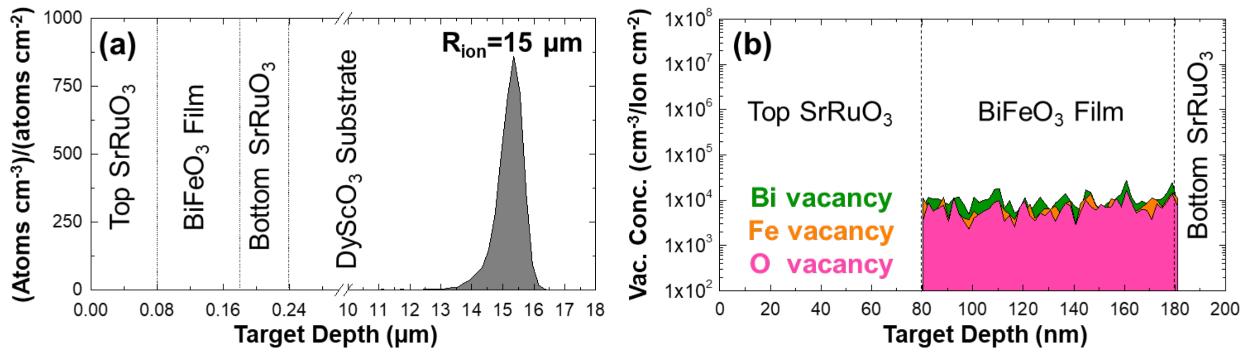

Figure 7.3. (a) SRIM simulation of He^{2+} concentration as a function of depth, suggesting that essentially no He^{2+} ions are implanted into the film, but instead the vast majority of ions are stopped at a depth of $\approx$ 15 μm into the $DyScO_3$ substrate, due to high incident energy of the ions (3.04 MeV). (b) SRIM simulation of induced defect concentrations as a function of depth in $BiFeO_3$ layer.

defects (indicated by a shift of the film peak to lower 2θ angles). The ion-dose-dependent reduction of the crystalline quality is further evidenced by a gradual increase in the FWHM of the rocking curves about the 002-diffraction conditions for the film and substrate (Figure 7.1c). The FWHM of the film peak changes from 0.045° for the as-grown heterostructures to 0.098° after bombardment with a He^{2+} dose of 10^{16} ions cm^{-2}. The substrate rocking curves are shown for comparison (FWHM varying in the range of 0.007°-0.011°).

7.3 Effect of Bombardment-Induced Defects on Transport Properties of $BiFeO_3$ Thin Films

In this Section I focus on the ion-dose-dependence of the transport properties in $BiFeO_3$ thin films [32]. The as-grown heterostructures show high leakage current density (black data, Figure 7.1d) and, as a result, the ferroelectric hysteresis loops are not fully-saturated and closed (black data, Figure 7.1e). As mentioned in Section 7.1, this high leakage current is a common feature of $BiFeO_3$

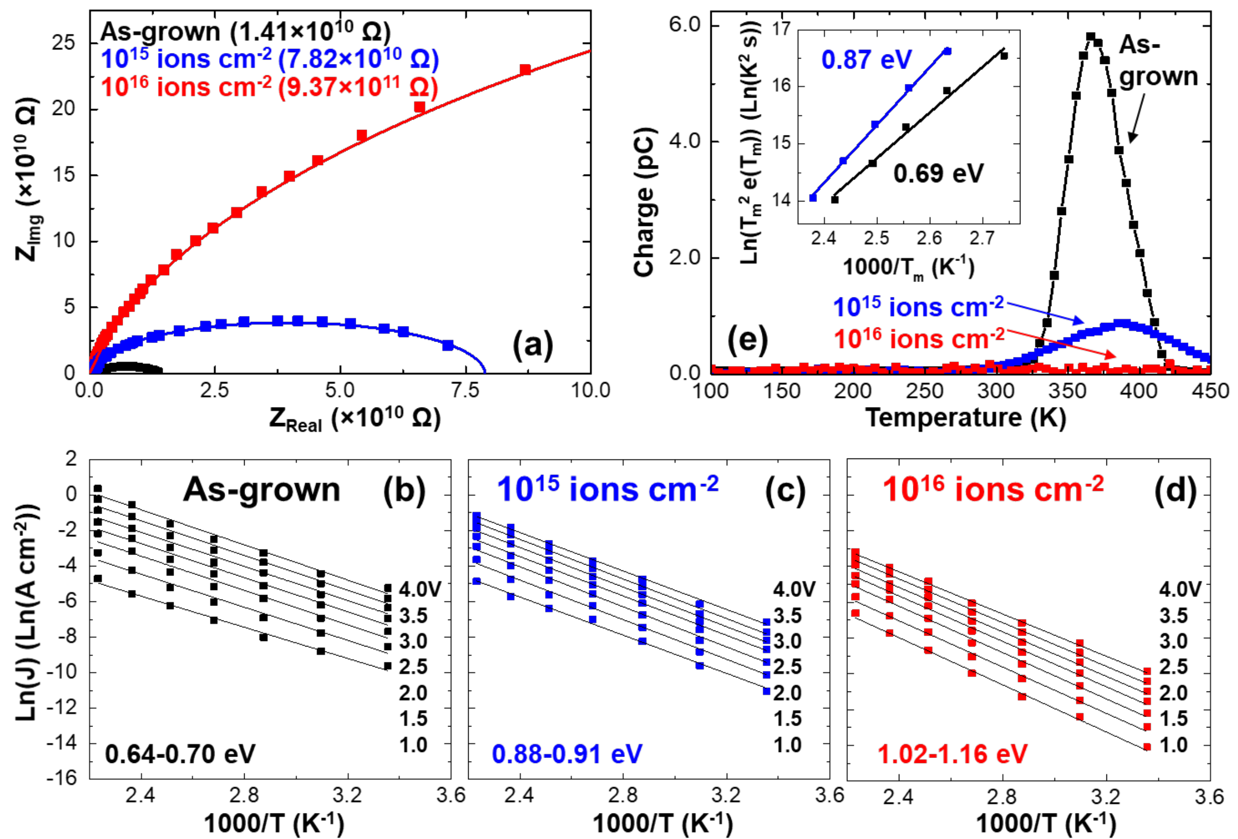

Figure 7.4. (a) Nyquist plots of Z_{Img} *vs.* Z_{Real} for heterostructures ion bombarded with various He^{2+} doses suggesting a single transport mechanism dominated by the bulk of the film with increasing resistance (extracted from the intercept of the semicircles on the real axis) with increasing dose. Arrhenius plots of $\ln(J)$ *vs.* $1000/T$ at different voltages for (b) as-grown (no bombardment), (c) 10^{15} ions cm^{-2}, and (d) 10^{16} ions cm^{-2} heterostructures. The activation energies (noted) are extracted from the slope of the linear fits. The range of activation energies corresponds to small variation in the slope of the linear fits at different voltages. (e) Deep-level transient spectroscopy signal measured at the same rate window (80-160 ms) for heterostructures bombarded with various He^{2+} doses. Inset shows the Arrhenius plot of $\ln(\frac{T_m^2}{e(T_m)})$ *vs.* $\frac{1000}{T_m}$. The activation energy of each trap state is extracted from the slope of the linear fits.

and is the result of the presence of point defects which form during the growth as well as impurities in the target materials, which in turn, dope the lattice with free charges and give rise to electronic conduction. By increasing the ion-bombardment dose, however, a systematic reduction in the leakage current density by up to ≈ 4 orders of magnitude can be achieved (Figure 7.1d). As a result of this improved resistivity, there is a clear enhancement in the ferroelectric hysteresis response (Figure 7.1e). In the dose range of 10^{15}-10^{16} ions cm^{-2}, fully-saturated and closed loops with remanent polarizations of ≈ 60 μC cm^{-2} are observed. At first glance, these observations may not be consistent with the prevailing thought that the high conductivity in $BiFeO_3$ originates from the presence of defects, and thus, increasing the concentration of *intrinsic* defects via ion bombardment should likely have a deleterious effect on properties. To understand these non-intuitive results, I have used a combination of impedance spectroscopy, deep-level transient spectroscopy, and temperature-dependent current-voltage measurements to explore the mechanisms responsible for the observed changes.

Various contributions to the overall resistive response of a material can be differentiated via impedance spectroscopy, as described in Section 4.3.3.8 [213,213]. Therefore, these studies could be particularly useful to gain information on whether the increase in the resistivity as a result of ion bombardment is induced by changes at the film-electrode interfaces or from the formation of surface layers (*e.g.*, due to the possibility of defect accumulation at the interfaces). Impedance spectroscopy measurements were carried out on heterostructures exposed to various ion-bombardment doses including as-grown (no bombardment), 10^{15} ions cm^{-2}, and 10^{16} ions cm^{-2} and show the presence of only one semicircle for all doses (Figure 7.4a). A zoom-in of the semicircle for each ion-bombardment dose is also provided (Figure 7.5). This suggests that the transport for all heterostructures is dominated by the bulk of the film. The magnitude of the resistance can be extracted from the intercept of the semicircles on the real axis. While transport remains bulk mediated, a clear and systematic increase in the resistance of the films can be observed as an increase in the radius of the semicircles with increasing ion-bombardment dose; this is in agreement with the dose-dependent reduction of the current density as a function of DC bias (Figure 7.1d). The film resistance is found to increase from 1.41×10^{10} Ω for the as-grown heterostructure, to 7.82×10^{10} Ω and 9.37×10^{11} Ω for the same heterostructure bombarded with doses of 10^{15} ions cm^{-2} and 10^{16} ions cm^{-2}, respectively.

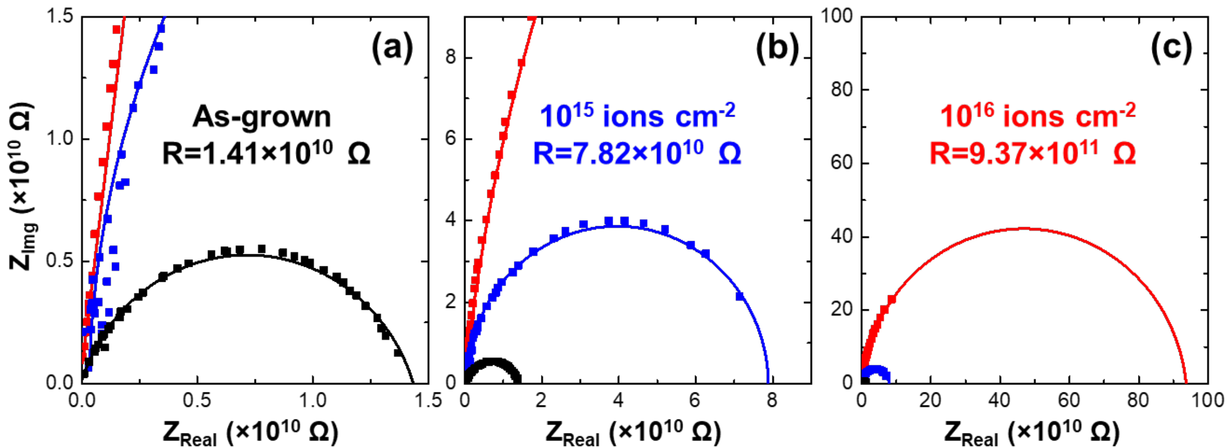

Figure 7.5. Nyquist plots of Z_{Img} *vs.* Z_{Real} for heterostructures bombarded with (a) zero (as-grown), (b) 10^{15} ions cm^{-2}, and (c) 10^{16} ions cm^{-2} He^{2+} doses. The scattered points correspond to the experimental data, and the bold lines to the fittings.

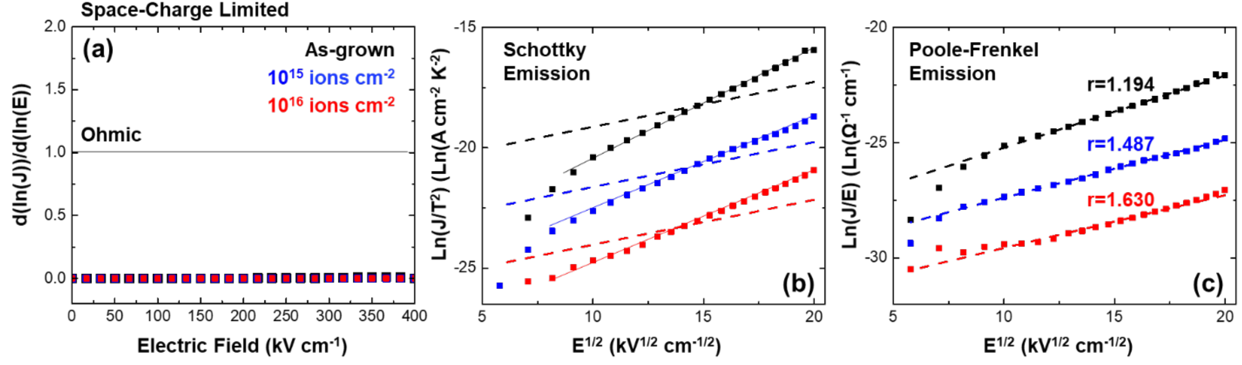

Figure 7.6. (a) Derivatives of J *vs.* E for heterostructures bombarded with various He^{2+} doses. Neither of the heterostructures exhibits ohmic conduction $(d(\ln(J))/d(\ln(E)) = 1)$ or space-charge limited conduction $(d(\ln(J))/d(\ln(E)) = 2)$. Positive bias room temperature current-voltage data represented on the standard (b) Schottky and (c) Poole-Frenkel plots for heterostructures bombarded with various He^{2+} doses. Dashed lines show the fits using the reported values of optical dielectric constant for $BiFeO_3$ ($\varepsilon_{opt} = 6.25$).

Having established that the transport remains bulk mediated, I have applied both temperature-dependent current-voltage and deep-level transient spectroscopy measurements to understand the origin of the large differences in the conductivity. Room-temperature current-voltage studies were carried out on heterostructures bombarded with various He^{2+} ion doses (including as-grown (no bombardment), 10^{15} ions cm^{-2}, and 10^{16} ions cm^{-2}) in order to determine the dominant conduction mechanism. In the analysis of current-voltage studies, a number of potential transport mechanisms can be considered, as discussed in Section 2.8.1. First, the possibility of ohmic conduction is investigated. Deviations of $d(\ln(J))/d(\ln(E))$ from 1 rule out the ohmic conduction as the dominant mechanism at any electric field or for any of the heterostructures studied herein (Figure 7.6a). The next potential mechanism considered here is the space-charge limited conduction. Deviations of $d(\ln(J))/d(\ln(E))$ from 2 also rule out the space-charge limited conduction as the dominant mechanism at any electric field or for any of the heterostructures studied herein (Figure 7.6a). Schottky emission is the next potential transport mechanism considered herein. Although the plot of $\ln(J/T^2)$ *vs.* $E^{1/2}$ is linear for all heterostructures (Figure 7.6b), the linear fits considering the previously reported values of optical dielectric constant of $BiFeO_3$ ($\varepsilon_{opt} = 6.25$) [230,256] show a poor overlap with the experimental data (dashed lines, Figure 7.6b); thus ruling out Schottky emission as the likely conduction mechanism. Finally, I have also considered Poole-Frenkel emission. A linear relation can be observed in the plots of $\ln(J/E)$ *vs.* $E^{1/2}$ for all heterostructures (Figure 7.6c). As mentioned in Section 2.8.1.3, in situations where there are large concentrations of donor and/or acceptor states, Poole-Frenkel emission can be modified by adding an exponential scaling constant r [117,118]. Considering $\varepsilon_{opt} = 6.25$ for $BiFeO_3$ and using a scaling constant $1 \leq r \leq 2$, very close linear fits to the experimental data can be achieved (dashed lines, Figure 7.6c). These analyses, therefore, show that bulk-limited modified Poole-Frenkel is likely the dominant transport process for all the heterostructures studied herein, and that the high-energy ion bombardment does not alter the conduction mechanism.

In order to identify the dominant trap states giving rise to the Pool-Frenkel conduction, temperature-dependent current-voltage measurements were carried out on the heterostructures bombarded with various He^{2+} ion doses (*i.e.*, as-grown (no bombardment), 10^{15} ions cm^{-2}, and

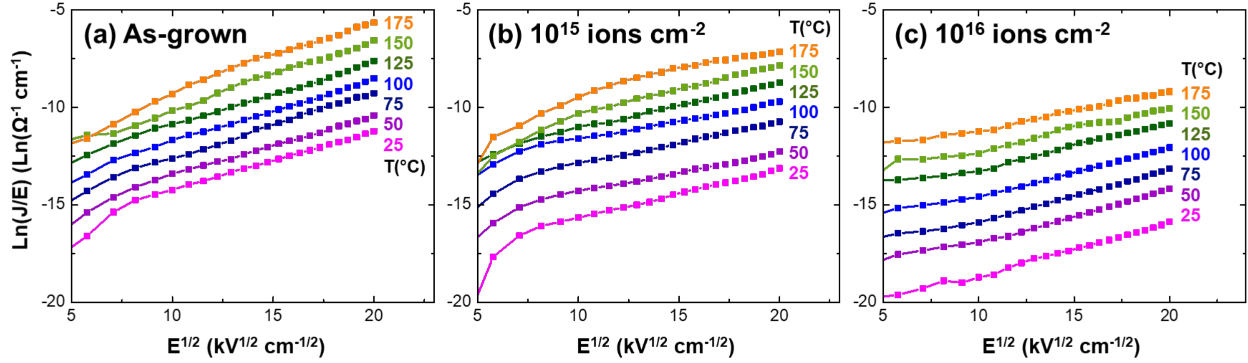

Figure 7.7. Temperature dependence of the current-voltage characteristics (in positive bias) measured in the temperature range of 25-175°C for (a) as-grow (no bombardment), (b) 10^{15} ions cm^{-2}, and c) 10^{16} ions cm^{-2} He^{2+} dose heterostructures.

10^{16} ions cm^{-2}) in temperature range of 25-175°C (Figure 7.7). The activation energies of dominant trap states are extracted from the slope of the linear fits to the Arrhenius plots of $\ln(J)$ *vs.* $1000/T$ at different electric fields considering a modified Poole-Frenkel emission (Figure 7.4b-d). While there is no change in the conduction mechanism, a systematic increase in the activation energy of the dominant trap states can be observed by increasing the ion-bombardment dose wherein it increases from 0.64-0.70 eV for the as-grown heterostructures (consistent with previous studies of $BiFeO_3$ thin films), to 0.88-0.91 eV and 1.02-1.16 eV for heterostructures ion bombarded with doses of 10^{15} ions cm^{-2} and 10^{16} ions cm^{-2}, respectively.

The main cause for high leakage currents in $BiFeO_3$ is known to be related to the presence of oxygen vacancies acting as donors, as well as to hopping of electrons from Fe^{2+} to Fe^{3+} which is expected in the presence of oxygen vacancies [221,223,226,227,230]. In turn, trap states in the range of 0.6-0.8 eV below the conduction band edge in $BiFeO_3$ have been attributed to such defects [277] and are consistent with the activation energies extracted from current-voltage measurements of the as-grown heterostructures in this work. These defects, in turn, dope the lattice with electrons and contribute to *n*-type conduction. The *n*-type nature of conduction in these as-grown $BiFeO_3$ films was confirmed in Section 5.5 [29]. The higher activation energy of 1.02-1.16 eV extracted for the dominant trap state in highly-ion-bombarded heterostructures (dose of 10^{16} ions cm^{-2}), however, implies the formation of deeper trap states. These deep-lying, ion-bombardment-induced defects (which could be related to vacancies, interstitials, and/or antisites of any of the constituent elements and their complexes and clusters) can trap charge carriers deep in the band gap, and in turn, reduce the free carrier transport. Formation of damage-related deep levels upon ion bombardment is well known in semiconductors, and it has been shown that these induced mid-gap levels are responsible for trapping of free carriers and increasing the resistivity [157].

In order to gain more insight on the type of ion-bombardment-induced defects, deep-level transient spectroscopy measurements were also carried out on the same heterostructures, as described in Section 4.3.3.9. Deep-level transient spectroscopy signals were obtained on heterostructures ion bombarded with various doses (including as-grown (no bombardment), 10^{15} ions cm^{-2}, and 10^{16} ions cm^{-2}) in the temperature range of 100-450 K for five different rate windows in the range of 5-160 ms (Figure 7.8). For more clarity in comparing the results obtained at different doses, only the signals obtained at one single rate window (80-160 ms) are shown (Figure 7.4e). A single deep-level transient spectroscopy peak is observed in the studied temperature range. The activation energies, extracted from the linear fits to the Arrhenius plots

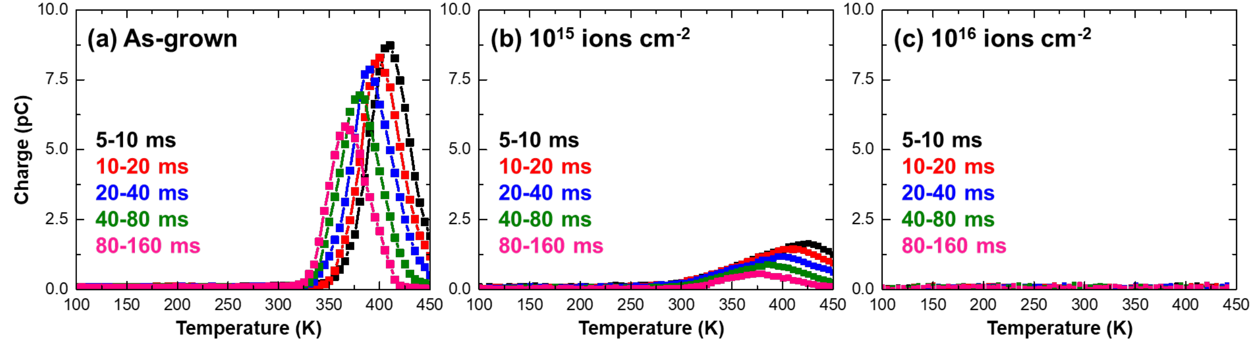

Figure 7.8. Deep-level transient spectroscopy signal measured at five different time windows, for heterostructures bombarded with He^{2+} doses of (a) zero (as-grown), (b) 10^{15} ions cm^{-2}, and (c) 10^{16} ions cm^{-2}.

(inset, Figure 7.4e), are ≈ 0.69 eV for the as-grown heterostructures, and ≈ 0.87 eV for the heterostructures ion bombarded to a dose of 10^{15} ions cm^{-2}. No deep-level transient spectroscopy peak was measured for the heterostructures ion bombarded to a dose of 10^{16} ions cm^{-2} within the same temperature and rate windows. There is a close agreement between the activation energies extracted from deep-level transient spectroscopy and current-voltage measurements for the as-grown and 10^{15} ions cm^{-2} heterostructures, suggesting that the same trap states are probed by the two techniques. Furthermore, as the ion-bombardment dose increases, the deep-level transient spectroscopy peak is found to decrease in intensity, broaden in shape, and shift to higher temperatures. Broadening of the shape and decreasing intensity of a deep-level transient spectroscopy peak are usually attributed to the formation of defect clusters which can give rise to a distribution in emission energies. Moreover, shifts of the peaks can be caused by changes in the environment surrounding the defects or the defect configuration [264,265]. These observations indicate that the shallow trap state in the as-grown heterostructures is likely related to isolated point defects as suggested by the presence of a sharp and high intensity deep-level transient spectroscopy peak. As the concentration of defects increases as a result of ion bombardment, however, it is hypothesized that these isolated defects are transformed into defect complexes and clusters (composed of cation and/or anion vacancies, and potentially interstitials or anti-sites) which would be consistent with the lowering of the intensity, broadening, and shift of the deep-level transient spectroscopy peak. Therefore, it can be concluded that in addition to giving rise to the formation of deep-lying trap states, ion bombardment also results in an increased concentration of complex defects and clusters. Therefore, high-energy ion bombardment can be an effective technique for tuning the concentration and type of *intrinsic* defects, and in turn, tuning electrical properties and enhancing the device performance.

It is important to keep in mind that the highly-resistive state will be stable only up to temperatures at which the bombardment-induced defect states anneal out. Point-defect diffusion will occur at elevated temperatures, and therefore, the highly-resistive state is likely to be stable until it is exposed to temperatures at which the bombardment-induced defect states anneal out. To demonstrate this point, an as-bombarded (10^{16} ions cm^{-2}) heterostructure was annealed at progressively higher temperatures in air, for 15 minutes at each temperature up to 600°C. After each annealing stage, the heterostructure was cooled to room temperature and its current density as a function of DC bias was measured (Figure 7.9). Note that this was a cumulative anneal so the heterostructure has seen ≈ 1.5 hours at elevated temperatures. Progressively increasing the annealing temperature (here in 100°C increments), reveals no change in the leakage characteristics

through at least 400°C. The current density begins to increase at 500°C, and becomes comparable to that of an as-grown, un-bombarded heterostructure after annealing at 600°C. This suggests stability of the bombardment induced defects up to ≈ 400°C. I also note that, due to the presence of volatile bismuth in $BiFeO_3$, high-temperature application is not widely envisioned for this system. This said, studies in semiconductor systems suggest that bombardment with heavier ions tend to produce more thermally stable defects; therefore, heavier ions could be used for the bombardment, in cases where thermal stability of the high resistivity state is of concern [157]. To better understand the potential of this technique for ferroelectric device performance optimization, however, the impact of these ion-bombardment-induced defects on the switching behavior should not be overlooked, due to the potentially prominent role of defects in ferroelectric switching.

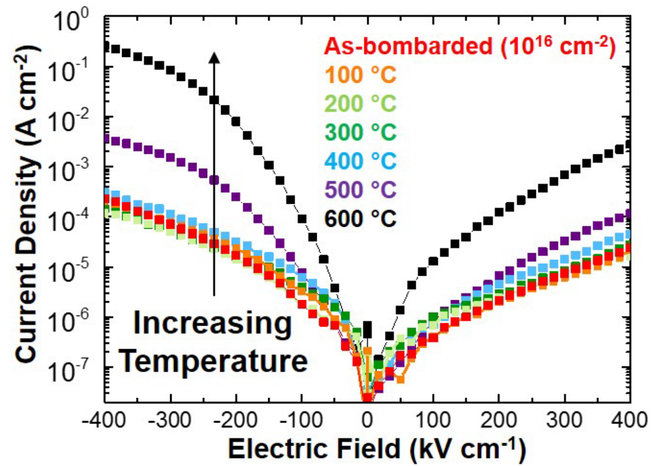

Figure 7.9. Current density *vs.* applied electric field for an as-bombarded (10^{16} ions cm^{-2}) $BiFeO_3$ heterostructure which is cumulatively annealed for 15 minutes at various progressively increasing temperatures. Conduction is seen to increase after annealing at above 400°C.

7.4 Effect of Bombardment-Induced Defects on Ferroelectric Switching Properties of $BiFeO_3$ Thin Films

In the following, I focus on the study of polarization switching in ion-bombarded versions of $BiFeO_3$ [32]. Having the ability to tune the concentration of defects by means of ion bombardment allows for a systematic study of the effect of defects on the switching behavior in terms of mechanism, rate, and energy requirements. Examination of ferroelectric hysteresis loops (obtained at 10 kHz in order to minimize the effect of high leakage in the as-grown heterostructures) reveals a clear increase in the coercive field with increasing ion-bombardment dose (Figure 7.10a). This is while no apparent change in the domain structure is detected by piezoresponse force microscopy upon ion bombardment even up to the maximum dose of 10^{16} ions cm^{-2}. This was concluded by comparison of vertical and lateral piezoresponse force microscopy images between as-grown (no bombardment) and 10^{16} ions cm^{-2} ion-bombarded heterostructures (Figure 7.11). A combination of macroscale switching kinetics and first-order reversal curve studies were used to gain more insight into the origin of the dose-dependent changes of the coercive field.

Probing the switching kinetics as a function of ion-bombardment dose, provides a pathway for better understanding the nature of domain wall motion and pinning, pinning activation energy barrier, effective growth dimensions, and characteristic switching time in the presence of varying concentrations and types of point defects. In order to study the switching kinetics, standard pulsed measurements were used as described in Section 4.3.3.3. The measurements were carried out on the heterostructures with various ion-bombardment doses (as-grown (no bombardment), 10^{15} ions cm^{-2}, and 10^{16} ions cm^{-2}) (Figure 7.12). The symbols show the measured values while the solid lines show the fitting results using the Kolmogorov-Avrami-Ishibashi model (the fitting parameters are presented in Table 7.1) [202,203]. The average value of effective geometric

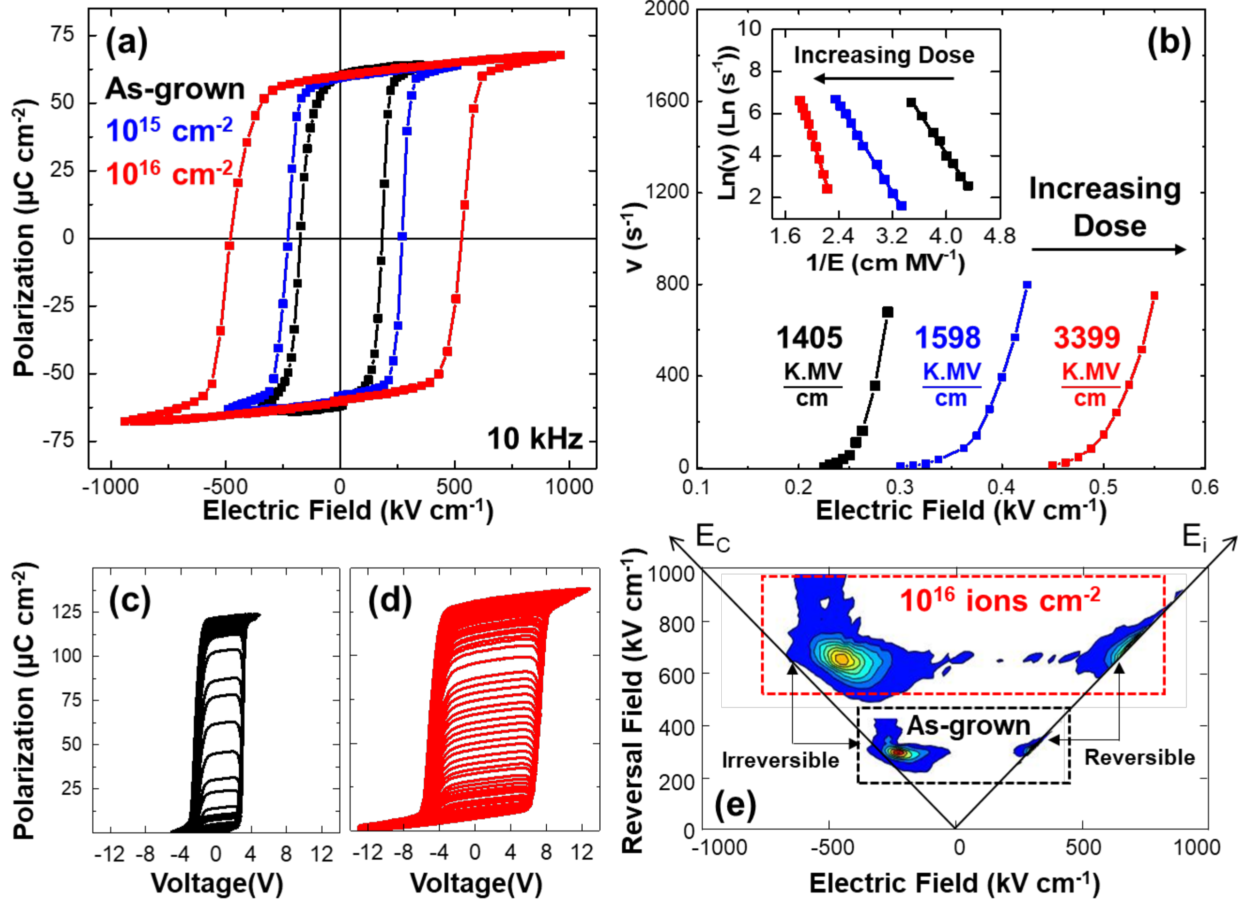

Figure 7.10. (a) Ferroelectric polarization-electric field hysteresis loops measured at 10 kHz after ion bombardment with various He^{2+} doses. (b) Switching speed as a function of electric field for heterostructures ion bombarded with various He^{2+} doses. Inset shows the plot of $\ln(\vartheta)$ *vs.* $1/E$. The activation energies are extracted from the linear fits. The minor loops measured between the negative saturation field and various reversal fields for (c) as-grown (no bombardment) and (d) 10^{16} ions cm^{-2} heterostructures. (e) The first-order reversal curve distributions for the as-grown (no bombardment) and 10^{16} ions cm^{-2} heterostructures.

dimension n_s, extracted from the fittings is $\approx 1.3 \pm 0.4$ which is in agreement with values reported for other complex-oxide ferroelectric thin films ($\approx 1.4 \pm 0.4$ for epitaxial $PbZr_xTi_{1-x}O_3$ films [204], $\approx 1.5 \pm 0.1$ for $PbZr_xTi_{1-x}O_3$-$BiFeO_3$ sol-gel films [278], and $\approx 1.5 \pm 0.1$ for epitaxial $BiFeO_3$ films [279]), suggesting the validity of the fits based on the Kolmogorov-Avrami-Ishibashi model. The values of $1/t_s$ at each field, extracted from these fittings, are assumed to be proportional to switching speed ϑ [204], and are used to find the relation between switching speed and electric field, in order to extract the characteristic switching parameters based on creep, depinning, or flow regimes.

As mentioned in Section 4.3.3.3, domain-wall velocity varies nonlinearly with electric field, and can be classified into creep, depinning, and flow regimes [204]. For the heterostructures studied herein, the plot of switching speed *vs.* electric field (Figure 7.10b) reveals that for all doses, the domain-wall motion is in the creep regime. This is due to the fact that even in the as-grown heterostructures with no ion-bombardment, there is a non-zero concentration of defects (dictated by thermodynamics and growth) which can act as pinning sites. There is a systematic extension of

the creep regime to higher electric fields, however, with increasing ion-bombardment dose. This is consistent with defect-related creep motion in ferroelectrics. The pinning activation energy can be extracted from the fits to the plot of $\ln(\vartheta)$ *vs.* $1/E$ (inset, Figure 7.10b). The linear nature of the fits suggests a long-range, random-field pinning potential for all heterostructures [204]. The activation energies at room temperature are extracted from the slope of the linear fits and show a systematic increase with increasing ion-bombardment dose, from 1405 K MV cm^{-1} for the as-grown heterostructure, to 1598 K MV cm^{-1} and 3399 K MV cm^{-1} for the heterostructures ion bombarded with doses of 10^{15} ions cm^{-2} and 10^{16} ions cm^{-2}, respectively. Therefore, increasing the concentration of defects provides more pinning sites, increases the pinning activation energy, and increases the difficulty of domain-wall motion, which in turn, gives rise to a dose-dependent increase of the coercive field.

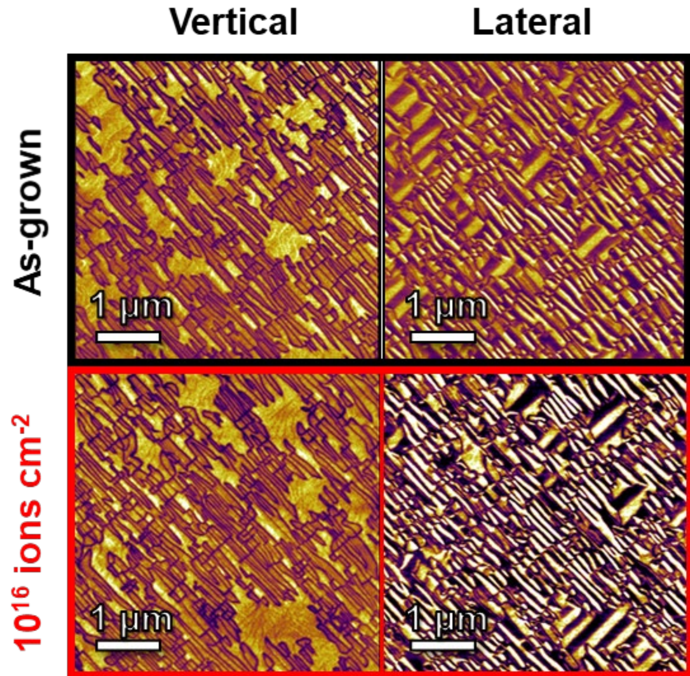

Figure 7.11. Vertical (left) and lateral (right) piezoresponse force microscopy amplitude for the heterostructures bombarded with He^{2+} doses of zero (top) and 10^{16} ions cm^{-2} (bottom).

Although switching kinetics studies provide valuable information about polarization switching dynamics at the macroscale, the switching process can vary locally due to the presence of disorder and randomness [205]. Therefore, macroscopic kinetics measurements and single major hysteresis loops measured between saturation fields are insufficient to fully describe the switching process. First-order reversal curve measurements, on the other hand, can provide additional information on the characteristic microscopic mechanisms involved in switching by offering a graphical method to probe the (in)homogeneity of the switching events, as described in

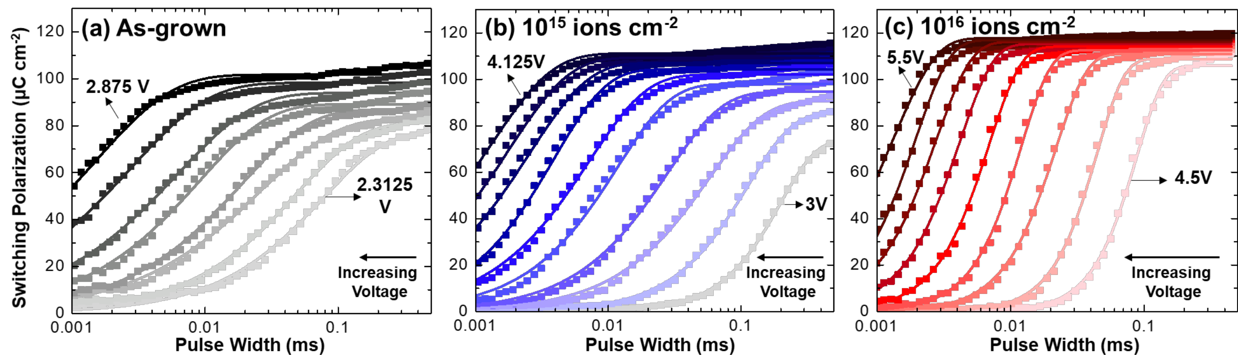

Figure 7.12. Switching polarization as a function of pulse width, under various voltages, measured at room temperature for (a) as grown heterostructures, and heterostructures bombarded with doses of (b) 10^{15} ions cm^{-2}, and (c) 10^{16} ions cm^{-2}. The solid lines show the fitting results using the Kolmogorov-Avrami-Ishibashi model (the fitting parameters are presented in Table 7.1).

Section 4.3.3.6 [208]. In our particular case, such measurements can shine light on how the introduction of ion-bombardment-induced *intrinsic* defects and disorder change the switching process and its uniformity at the microscopic scale. First-order reversal curve measurements were carried out on the as-grown (no bombardment) and 10^{16} ions cm^{-2} ion-bombarded heterostructures (Figure 7.10c,d). The distribution functions were calculated, and their contour plots are shown (Figure 7.10e). Note that, near the reversal field values, a measurable increase in polarization can be observed, even after the applied field starts to decrease (Figure 7.10c,d). In other words, there is a lag between the output (polarization) and the input (applied electric field). This effect can be attributed to the counterbalance between the applied electric field sweep rate and the switching time, and suggests a dynamic time-dependent hysteresis response, related to the kinetics of polarization switching. As discussed previously, the switching kinetics studies reveal that for all doses studied herein, the domain-wall motion is in the creep regime (Figure 7.10b), which involves a thermally-activated slow propagation of domain walls between pinning sites. As it can be seen, for all doses the characteristic switching speed is slower than the hysteresis period used for the measurement of the minor loops (10 kHz), as a result of which, the film continues to switch as the field is reduced after the reversal point. Although this lag between polarization and the applied field is less prominent for lower electric field sweep rates (not shown here), the data shown here was obtained at 10 kHz as the as-grown, un-bombarded films are rather leaky at lower frequencies. Here, the first-order reversal curve distributions were constructed using the classical Preisach model in order to qualitatively compare the effects of bombardment and defects on the distribution of the coercive fields of the elementary switchable units. I note, however, that if one desired to extract further quantitative information on the dynamics of the switching process from the first-order reversal curve measurements, so-called dynamic/moving Preisach models of hysteresis which account for the time-dependent nature of the response via introduction of single or multiple relaxation times into the classical model would be required [212].

Table 7.1. The Kolmogorov-Avrami-Ishibashi fitting parameters t_s (characteristic switching time), and n_s (effective geometric dimension) used in fitting of the switching data in Figure 7.12, as a function of electric field for heterostructures bombarded with varying He^{2+} ion doses.

Dose (Ions cm^{-2})	Voltage (V)	E Field (MV cm^{-1})	$1/t_s$ (s^{-1})	n_s
As-grown	2.3125	0.23125	12.98	0.9684
	2.375	0.2375	20.28	0.9501
	2.4375	0.24375	37.68	0.806
	2.5	0.25	53.39	0.8881
	2.5625	0.25625	110.19	0.8975
	2.625	0.2625	160.95	0.8033
	2.75	0.275	358.17	0.803
	2.875	0.2875	679.35	0.8378
10^{15}	3.0	0.3	5.03	1.624
	3.125	0.3125	8.85	1.29
	3.25	0.325	17.42	1.046
	3.375	0.3375	35.59	1.054
	3.625	0.3625	85.54	1.071
	3.75	0.375	140.33	1.061
	3.875	0.3875	255.62	1.103
	4.0	0.4	395.73	1.047
	4.125	0.4125	569.48	1.036
10^{16}	4.5	0.45	11.33	2.188
	4.625	0.4625	22.37	2.159
	4.75	0.475	45.81	1.875
	4.875	0.4875	82.92	2.00
	5.0	0.5	143.99	1.835
	5.125	0.5125	240.38	1.736
	5.25	0.525	362.06	1.636
	5.375	0.5375	515.46	1.695
	5.5	0.55	751.31	1.363

Regardless, in this representation of the first-order reversal curve data, the reversible (*i.e.*, distribution along the bias axis) and irreversible contributions to the total polarization are observed to be separated (Figure 7.10e) [208]. The overall shape of the distributions remains similar (*i.e.*, in both cases, there is a larger distribution of coercive fields with a narrower distribution of bias fields) and the ratio of the reversible to irreversible contributions remains similar upon ion bombardment. The data suggest, however, that upon ion bombardment the polarization units become dispersed and distributed in a wider range of higher coercive and bias fields. Ion bombardment clearly results in broadening and dispersion of the first-order reversal curve distribution and lowering of its maximum intensity. In the as-grown state, the distributions are, by comparison, narrower with a well-defined, high-intensity maximum, meaning that almost all the dipolar units are reversed in a limited range of fields. This suggests a reduction in the homogeneity of the ferroelectric switching upon ion bombardment, which is consistent with the fact that such high-energy ion bombardment results in an increase in the concentration of *intrinsic* point defects, formation of complexes and clusters, and hence, an increase in the disorder of the system which results in less uniform switching. The maximum intensity corresponds to the most probable fields for the largest number of switchable units which make the largest contribution to the polarization switching. This intensity maximum shifts towards higher coercive and bias fields upon ion bombardment. The increase in the coercive field, as mentioned earlier, accounts for the pinning effect of defects on the domain walls. The bias-field distribution is indicative of the nanoscale imprint characteristics of the ferroelectric as it pertains to the preferential polarization of the switching units [208]. The combined knowledge gained from the piezoresponse force microscopy, macroscale switching kinetics, and first-order reversal curve studies suggest that the *intrinsic* defects formed during the ion bombardment do not have any effect on the domain structure or the switching mechanism, but do increase the disorder of the medium (broadening the field distribution for switching) that results in a systematic dose-dependent increase in the coercive field, extension of the defect-related creep regime, increase in the pinning activation energy, and decrease in the switching speed which altogether suggest an increased resistance to switching with increasing concentration of defects.

7.5 Conclusions

In conclusion, I have shown that high-energy ion bombardment can be a valuable technique for tuning the concentration and type of *intrinsic* defects in ferroelectric thin films and provides a route to a systematic study of defect-property relations. I have also demonstrated the potential of this ion bombardment for enhancement of the properties including multiple orders of magnitude enhancement in electrical resistivity, and in turn, improvement of ferroelectric hysteresis measurements, without suppression of the polarization values. Increasing the concentration of ion-bombardment-induced defects, however, can put a limit on ferroelectric device performance in that it strongly impacts switching properties due to the presence of strong defect-polarization coupling. Introduction of deep-lying ion-bombardment-induced defect complexes and clusters are shown to be responsible for a reduction of free carrier transport, and hence, a reduction of the leakage current density, while on the other hand, they give rise to an increased resistance to switching. Therefore, the application of this technique for enhancement of ferroelectric device performance requires finding an optimum range of ion dose to achieve maximum enhancement in the resistivity with minimum impact on the ferroelectric switching.

CHAPTER 8

Local Control of Defects and Switching Properties in $PbZr_{0.2}Ti_{0.8}O_3$ Thin Films via Focused-Helium-Ion Bombardment

In this Chapter, I provide systematic experimental evidence of the role of point defects in affecting ferroelectric-polarization switching as a function of defect type and concentration in $PbZr_{0.2}Ti_{0.8}O_3$ thin films, and utilize the ability to deterministically create and spatially locate point defects via focused-helium-ion bombardment and the subsequent defect-polarization coupling as a knob for on-demand control of ferroelectric switching (*e.g.*, coercive field and imprint). At intermediate ion doses (0.22-2.2×10^{14} ions cm^{-2}), the dominant defects (isolated point defects/small clusters) show a weak interaction with domain walls (pinning potentials from 200-500 K MV cm^{-1}), resulting in small and symmetric changes in the coercive field. At high ion doses (0.22-1×10^{15} ions cm^{-2}), on the other hand, the dominant defects (larger defect complexes/clusters) strongly pin domain-wall motion (pinning potentials from 500-1600 K MV cm^{-1}), resulting in a large increase in the coercive field and imprint, and a reduction in the polarization. Furthermore, I show that such defect-induced changes can be confined to select regions defined by the ion beam and use this local control of ferroelectric switching as a route to produce novel functions, namely tunable multiple polarization states, rewritable pre-determined 180° ferroelectric domain patterns, and multiple, zero-field piezoresponse and permittivity states. Such an approach, in turn, opens up new pathways to achieve multilevel data storage and logic, nonvolatile self-sensing shape-memory devices, and nonvolatile ferroelectric field-effect transistors.

8.1 Introduction

Electric-field switching of polarization between bistable states in ferroelectrics is the building block of variety of applications including memory, logic, energy storage/conversion, sensors, actuators, *etc.* [37,109,280,281]. Next generation applications, however, are increasingly calling for the development of pathways to control ferroelectric switching beyond its bistable and degenerate nature. For example, establishing routes to access multiple polarization states can give rise to transformative changes in computation and data storage. Limited success, however, has been achieved in creating deterministically accessible and stable multi-states due to the intrinsically bistable and stochastic nature of ferroelectric switching [282-286]. In other applications, including ferroelectric field-effect transistors [287], micro-electro-mechanical systems [288], and shape-memory piezoelectric actuators [289], it is not only important to control the polarization state, but to induce asymmetry of the ferroelectric states (manifested as an electrical imprint). Imprint in ferroelectrics, however, often appears in an uncontrolled fashion, arising from a number of factors (*e.g.*, asymmetric electrodes, dead layers, trapped charges, and defects) [120,123,160] and there has been limited success in exerting on-demand control of imprint [290,291]. In the end, addressing such technological challenges requires a comprehensive understanding of the ferroelectric switching process and all the factors that affect it, as well as developing pathways for deterministic and on-demand control of such factors. Such understanding and control, however, is challenging due to the complexity of the switching process and the multitude of both intrinsic (*i.e.*, aspects of the material itself) and extrinsic (*i.e.*, related to device structure) factors at play. While there has been excellent work in developing such understanding and control of these factors, considerable work still remains to provide the kind of on-demand control that is desired.

Among all the factors affecting switching, defects are known to play a prominent role whereby they control the thermodynamic stability of ferroelectric polarization, act as nucleation sites for switching, and serve as pinning sites for domain-wall motion, as discussed in Section 3.5 [12,58]. Such defect-polarization couplings, in turn, can be used as a knob to manipulate the switching characteristics, provided there is an understanding of how specific defects affect the process and that there are approaches for the introduction of those specific defects with control over their concentration and location. Deterministic control of defects in such materials, however, has proven difficult. Complex-oxide ferroelectrics, for example, can accommodate a variety of *intrinsic* and *extrinsic* defects, which are often formed in an uncontrolled fashion. This lack of control over type, concentration, and position of defects has, in turn, hindered comprehensive, systematic, and quantitative studies of the nature of defect-polarization coupling, which ultimately limits their potential use for property control. In fact, most studies to date have been limited to the *grown-in* defects (thus lacking control over their type and concentration) or to those produced via chemical alloying (where the concentration is limited by the solid solubility and there can be simultaneous chemistry-induced changes in the ferroelectric properties which can obscure coupled effects) [29,147,161,241,283,292]. As discussed in Chapters 6 and 7, more recently there have been attempts to implement, in ferroelectrics, approaches similar to the defect-engineering routes applied in modern semiconductors [157], including the use of ion bombardment/implantation to control the concentration of defects beyond thermodynamic limits [30,32]. While such studies have relied on blanket ion bombardment, focused-ion-beam techniques provide a pathway to control the concentration and position of defects at nano/micrometer scales [156,293]. Such control over defect production, in turn, provides a new approach to the study of defect-polarization coupling in ferroelectrics. By providing pathways to both produce different types and

concentrations (across many orders of magnitude of defect concentration) of defects and to position them in a controlled way, such techniques provide a framework in which systematic and quantitative studies of the interactions between defects and ferroelectric polarization can be accomplished and, ultimately, provide guidance to the development of new functionalities [33].

8.2 *Ex Situ* Creation of Bombardment-Induced Defects via Focused-Helium-Ion Bombardment and Study of Their Impact on Ferroelectric Switching Properties of $PbZr_{0.2}Ti_{0.8}O_3$ Thin Films

This work focuses on 60 nm $PbZr_{0.2}Ti_{0.8}O_3$/20 nm $SrRuO_3$/$SrTiO_3$ (001) thin-film heterostructures [33]. $\omega - 2\theta$ X-ray diffraction studies on the as-grown heterostructures reveal that the films are fully epitaxial, 00*l*-oriented, and single-phase (Figure 8.1a) and chemical analysis via Rutherford backscattering spectrometry reveals that the films have nearly stoichiometric cation ratios ($Pb_{1.00}Zr_{0.18}Ti_{0.82}O_x$) within the error of the measurement (1-2%) (Figure 8.1b). Following growth, these heterostructures were subsequently bombarded with a He^+-ion beam of 25 keV energy, using a helium-ion microscope as described in Section 4.2.2.2. The high-spatial resolution of the focused-helium-ion beam in this microscope (nominal probe size of 0.5 nm) was used for positioning of the defects with nanometer-scale precision and to produce defects in select regions. The concentration of the induced defects was systematically controlled by varying the bombardment dose in the range of 10^{12}-10^{15} ions cm^{-2}. SRIM simulations were performed in order to gain information about the concentration profile of the bombardment-induced defects and implanted ions as a function of the film thickness. SRIM simulations suggest that lead, titanium, zirconium, and oxygen vacancies, resulting from collisions between the incoming helium ions and the target atoms, form with relatively uniform concentrations throughout the thickness of the ferroelectric layer (Figure 8.2a). The simulations suggest a total defect concentration in the range of 10^{18}-10^{21} cm^{-3} for the dose range of 10^{12}-10^{15} ions cm^{-2} used in this study. Simulations further suggest that in addition to the formation of *intrinsic* point defects, helium ions are also implanted into the heterostructure due to the low incident energies used in our experiments (Figure 8.2b). The average range of the He^+ ions is calculated to be around 240 nm. The concentration of the implanted helium ions, however, is more than three orders of magnitude smaller than the *intrinsic* point-defect concentration (Figure 8.2c),

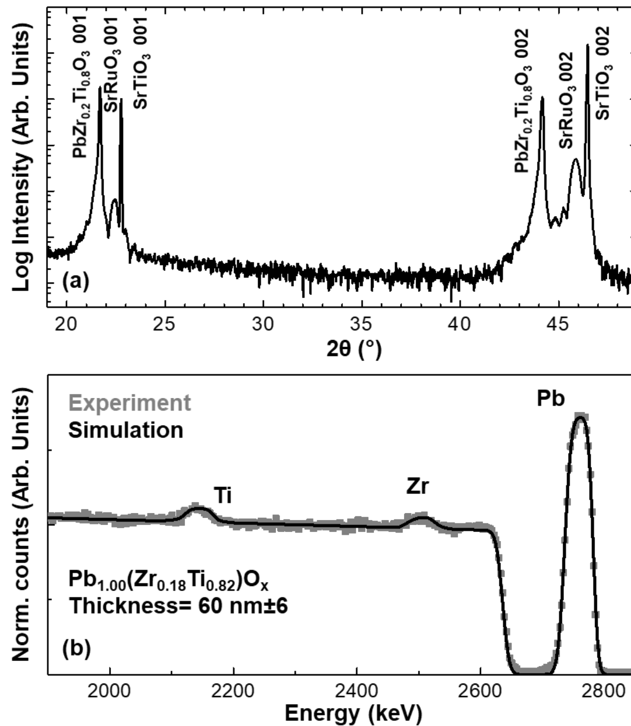

Figure 8.1. (a) Wide angle $\omega - 2\theta$ X-ray diffraction scans on as-grown heterostructures. (b) Rutherford backscattering spectrometry studies on the as-grown heterostructures. The corresponding fits are obtained from SIMNRA.

suggesting that the defect-induced effects observed in this study are predominantly related to the *intrinsic* defects. Comparison of the surface topography before and after ion bombardment to a dose of 10^{15} ions cm^{-2}, reveals no signature of formation of helium bubbles and blisters (Figure 8.3), which are known to form at higher doses [294].

In order to study the effect of the induced defects on ferroelectric switching, various ion-bombardment procedures were undertaken on the capacitor structures. First, the helium-ion beam was rastered over multiple capacitors at varying doses in order to prepare capacitors with systematically increasing defect concentrations. Ferroelectric polarization-electric field hysteresis loops were measured (at 1 kHz) before and after ion bombardment on all capacitors studied in this work. All as-grown capacitors show symmetric, well-saturated, and low-leakage hysteresis loops, with similar remanent polarization and coercive fields (≈ 70 μC cm^{-2} and ≈ 110 kV cm^{-1}, respectively) (Figure 8.4). Following ion bombardment, marked changes in the hysteresis loops are observed (Figure 8.5a). To quantify these changes, the average coercive field, imprint, and average saturation polarization are extracted as a function of ion dose (Figure 8.5b). Based on this analysis, three regimes can be identified: 1) At low doses ($0.1\text{-}2.2\times10^{13}$ ions cm^{-2}) there is effectively no change in the hysteresis loops. 2) At intermediate doses ($0.22\text{-}2.2\times10^{14}$ ions cm^{-2}) a relatively small increase in the coercive field is observed, while there is effectively no change in either the imprint or the polarization. 3) At high doses ($0.22\text{-}1\times10^{15}$ ions cm^{-2}) there are large increases in the coercive field and imprint, and a reduction in the polarization.

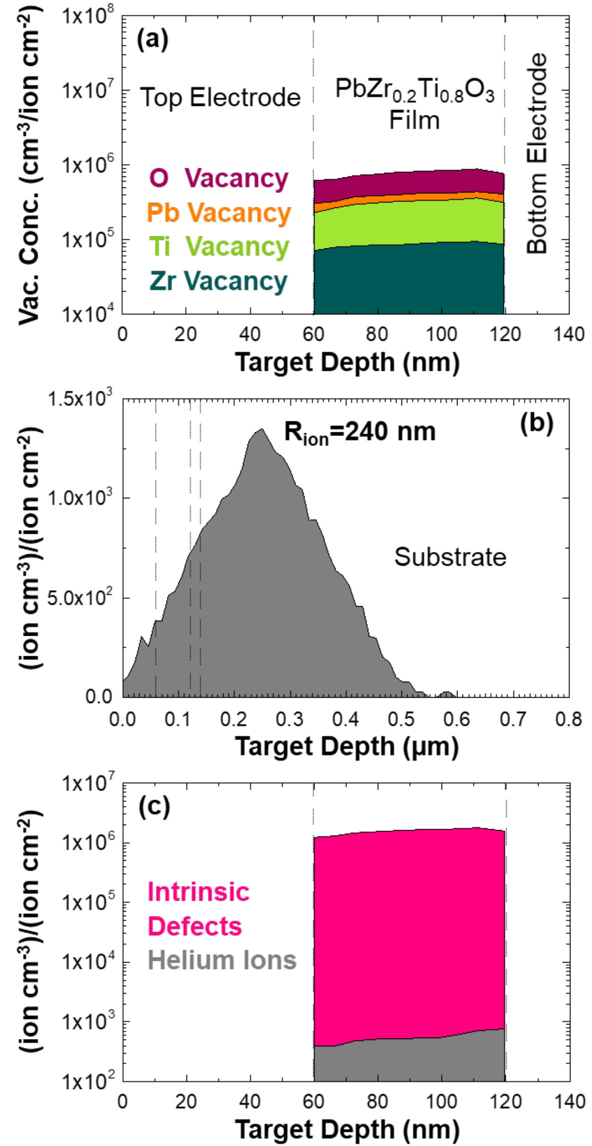

Figure 8.2. (a) SRIM simulations of the induced defect concentrations as a function of depth in the ferroelectric layer. (b) SRIM simulations of He^{+} concentration as a function of depth, suggesting that He^{+} ions are implanted into the ferroelectric layer. Range of ions is calculated to be around 240 nm. (c) SRIM simulations of the total concentration of the implanted helium ions in the ferroelectric layer in comparison to the total initial concentration of *intrinsic* point defect.

In order to understand these observations, macroscale switching-kinetics studies were performed at varying ion doses (Figure 8.6), as described in Section 4.3.3.3. The symbols show the measured $\Delta P(t)$ values while the solid lines show the fitting results using the Kolmogorov-Avrami-Ishibashi model [202,203]. The fitting parameters can be found in Table 8.1. The values of $1/t_s$ at each field, extracted from these fits, are assumed to be proportional to switching speed ϑ [204], and are used to find the relation between switching speed and electric field and to identify the characteristic switching behavior. Using this

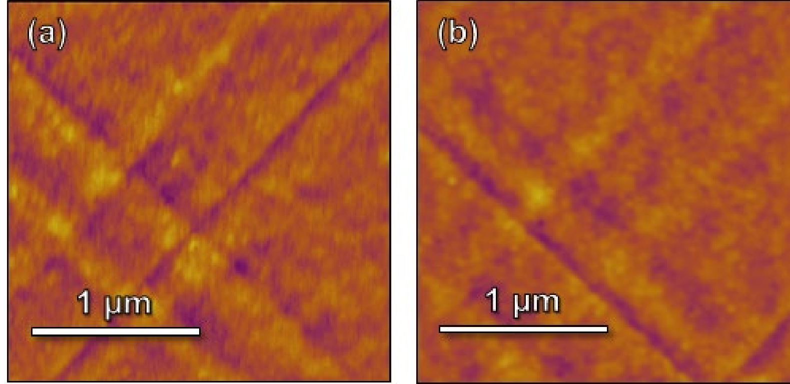

Figure 8.3. Atomic force microscopy images for (a) as-grown, and (b) bombarded (dose of 10^{15} ions cm^{-2}) regions.

approach, the domain-wall motion can be classified into creep, depinning, and flow regimes [204]. Linear variation of $\ln(\vartheta)$ with $1/E$ reveals that for all doses studied herein, the domain-wall motion is in the creep regime, considering a dynamical exponent $\mu_s = 1$ (Figure 8.5c). The average value of effective geometric dimension n_s extracted from the fits at each dose is $\approx 1.5 \pm 0.3$ which is in agreement with values reported for similar systems ($\approx 1.4 \pm 0.4$ for epitaxial $PbZr_xTi_{1-x}O_3$ films [204], $\approx 1.5 \pm 0.1$ for $PbZr_xTi_{1-x}O_3$-$BiFeO_3$ sol-gel film [278] and $\approx 1.5 \pm 0.1$ for epitaxial $BiFeO_3$ films [279]), suggesting the validity of the fits based on Kolmogorov-Avrami-Ishibashi model. The pinning energies for the creep motion, which involves thermally activated propagation of domain walls between pinning sites, are extracted from the slope of the linear fits (inset, Figure 8.5c). Different creep behavior is observed in the three dose regimes. In the low-dose regime, no change in the pinning energy is observed ($\approx$ 200 K MV cm^{-1}). In the intermediate-dose regime, the pinning energy increases up to $\approx$ 500 K MV cm^{-1}. Finally, in the high-dose regime, there is a large increase in the pining energy up to $\approx$ 1600 K MV cm^{-1}.

It is hypothesized that in the low-dose regime, the bombardment-induced defects are of the same order of magnitude as the as-grown defects, and therefore, do not give rise to marked changes in the ferroelectric switching properties. In the intermediate- and high-dose regimes, the induced defects start to interact with the domain walls. The nature and strength of this interaction, however, is different due to the difference in the dominant type of defects in these regimes. Experimental and theoretical studies of defect-domain-wall interactions suggest that point defects are more stable at the domain walls and can pin their motion, as discussed in Section 3.5 [127,131,136,161,162]. The pinning strength, however, is shown to be different for different defect types. A large difference, for example, is reported between isolated point defects and defect complexes, the latter showing at least three-times higher pinning strengths [131]. In addition, defect complexes, which can possess a dipole moment, have a strong tendency to align in the polarization direction

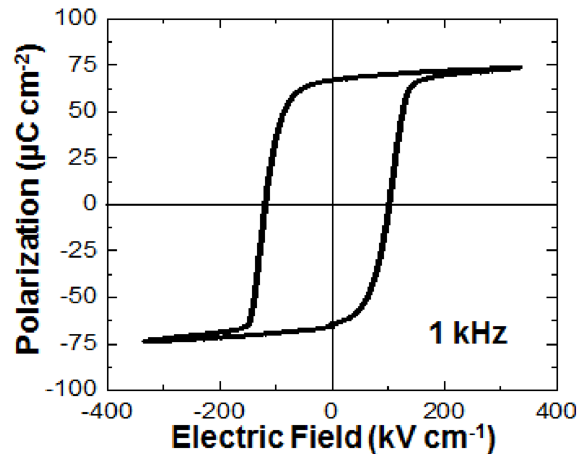

Figure 8.4. A polarization-electric field hysteresis loop measured on an as-grown capacitor.

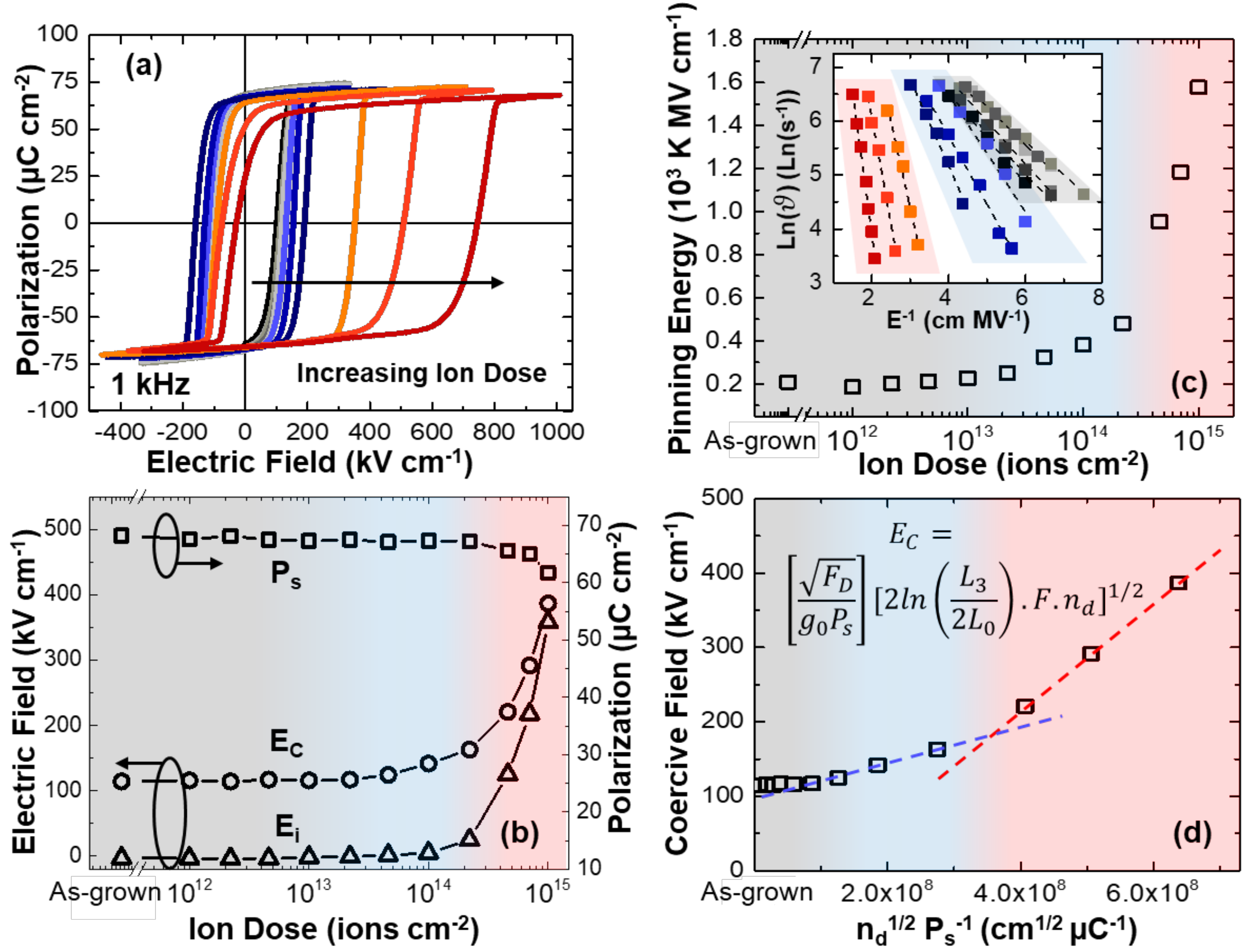

Figure 8.5. (a) Polarization-electric field hysteresis loops for capacitors exposed to bombardment doses in the range of 10^{12}-10^{15} ions cm^{-2}. (b) Evolution of the ferroelectric switching characteristics including the saturation polarization, coercive field, and imprint with ion dose. (c) Evolution of the extracted defect-pinning energy as a function of ion dose; inset shows the evolution of the switching speed as a function of inverse electric field with ion dose. The pinning energy is extracted from the slope of the linear fits. (d) Evolution of the coercive field as a function of defect concentration; inset shows mathematical relationship between defect concentration and coercive field.

and break the degeneracy of polarization states [127,131,136,161,162]. Moreover, the coercive field has been modeled in terms of the microstructure of the domain walls and the number and pinning strength of the lattice defects using the following equation [295]:

$$E_C = \left[\frac{\sqrt{F_D}}{g_0 P_s}\right]\left[2ln\left(\frac{L_3}{2L_0}\right).F.n_d\right]^{1/2} \tag{8.1}$$

where F_D is the area of the domain walls, g_0 is a geometrical factor depending on the angle between the electric field and P_s, L_3 is the average distance between the domain walls, L_0 is the average distance between the points of zero force encountered by a domain wall, and F is the pinning strength of the defects. According to this model, the coercive field is proportional to the square root of the defect concentration (${n_d}^{1/2}$), given the microstructure of the domain walls and strength of defect-domain-wall interactions are constant [295]. The concentration of the initial bombardment-induced point defects at various doses can be approximated using SRIM simulations (Figure 8.2c). In our case, the variation of coercive field is plotted as a function of ${n_d}^{1/2}{P_s}^{-1}$ (in

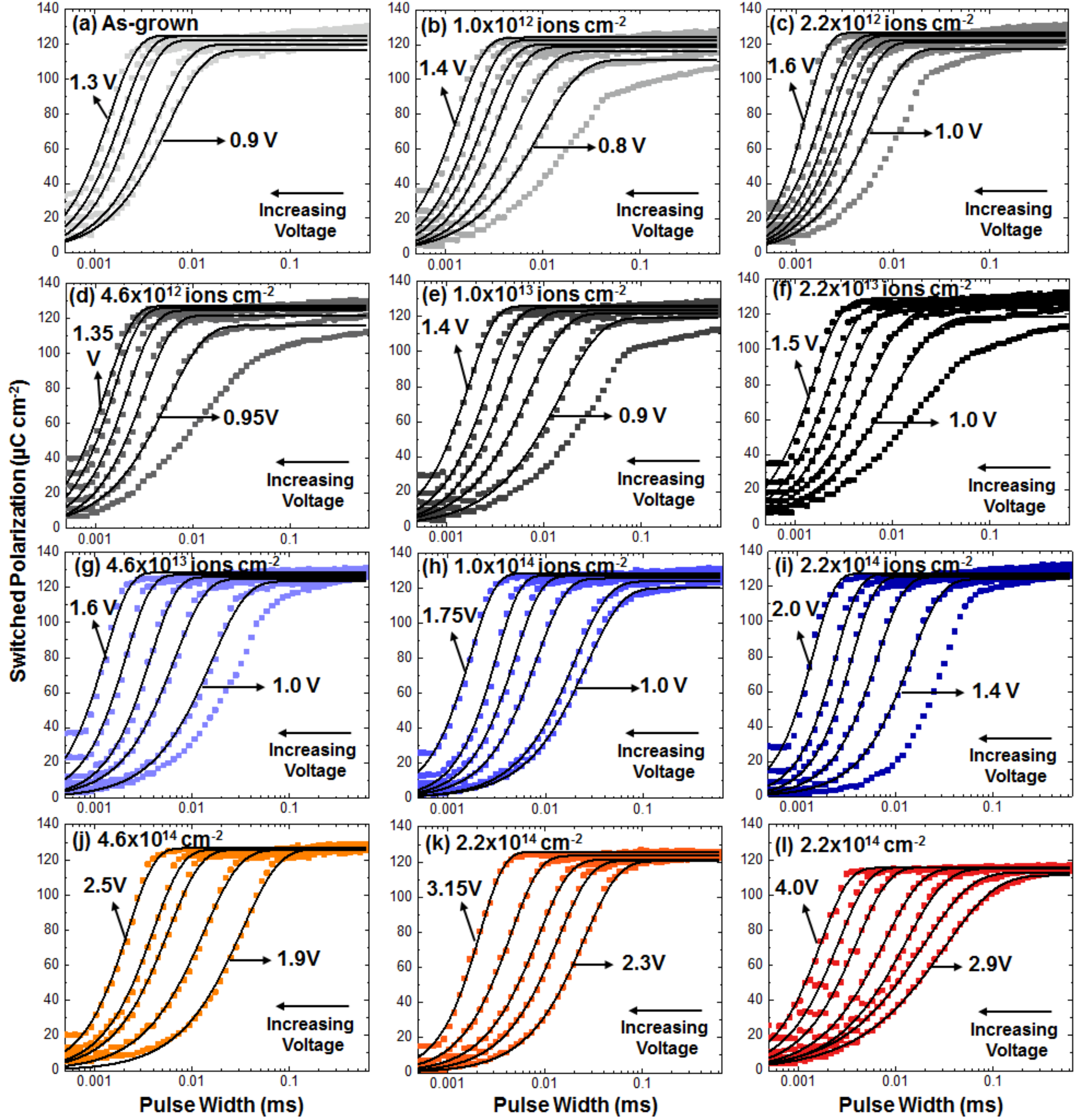

Figure 8.6. Switching polarization as a function of pulse width and under various voltages, measured at room temperature for heterostructures bombarded (a-f) in the low-dose regime (zero-2.2×10^{13} ions cm^{-2}–data in shades of gray), (g-i) in the intermediate-dose regime (2.2×10^{13}-2.2×10^{14} ions cm^{-2}–data in shades of blue), and (j-l) in the high-dose regime (2.2×10^{14}-10^{15} ions cm^{-2}–data in shades of red). The symbols show the measured values, while the solid lines show the fitting results using the Kolmogorov-Avrami-Ishibashi model (the fitting parameters can be found in Table 8.1).

order to account for variations of polarization at high doses) and shows three distinct slopes (Figure 8.5d). Again, in the low-dose regime, there is no change in the coercive field. Within the intermediate- and high-dose regimes, the coercive field varies linearly with ${n_d}^{1/2}$, but with two different slopes. This change of slope can be attributed to the difference in the pinning-strength of

Table 8.1. Kolmogorov-Avrami-Ishibashi fitting parameters t_s (characteristic switching time) and n_s (effective geometric dimension) used in fitting of the switching data in Figure 8.6, as a function of electric field for heterostructures bombarded with varying He^+ ion doses.

Voltage (V)	E Field ($MVcm^{-1}$)	$1/t_s$ (s^{-1})	n_s
As-grown			
0.9	0.150	175.04	1.179
1.0	0.167	234.36	1.286
1.1	0.183	406.01	1.521
1.2	0.200	523.29	1.517
1.3	0.217	695.89	1.558
1.0×10^{12} ions cm^{-2}			
0.8	0.133	104.015	1.04
0.9	0.150	181.917	1.245
1.0	0.167	292.569	1.427
1.1	0.183	394.945	1.453
1.2	0.2	524.659	1.565
1.4	0.233	746.826	1.551
2.2×10^{12} ions cm^{-2}			
1.0	0.167	165.975	1.252
1.1	0.183	259.875	1.447
1.2	0.2	331.126	1.515
1.3	0.217	426.621	1.599
1.4	0.233	558.034	1.578
1.6	0.267	787.402	1.942

Voltage (V)	E Field ($MVcm^{-1}$)	$1/t_s$ (s^{-1})	n_s
4.6×10^{12} ions cm^{-2}			
0.95	0.158	208.509	1.146
1.05	0.175	315.857	1.458
1.15	0.192	461.679	1.557
1.25	0.208	638.161	1.641
1.35	0.225	763.360	1.564
1.0×10^{13} ions cm^{-2}			
0.9	0.150	102.280	1.043
1.0	0.167	163.161	1.17
1.1	0.183	247.219	1.378
1.2	0.200	373.972	1.498
1.4	0.233	598.086	1.591
2.2×10^{13} ions cm^{-2}			
1.0	0.167	129.022	0.946
1.1	0.183	185.667	1.129
1.2	0.200	298.864	1.321
1.3	0.217	440.529	1.441
1.5	0.250	641.849	1.515

Voltage (V)	E Field ($MVcm^{-1}$)	$1/t_s$ (s^{-1})	n_s
4.6×10^{13} ions cm^{-2}			
1.0	0.167	62.735	1.22
1.1	0.183	150.921	1.359
1.2	0.200	266.525	1.631
1.4	0.233	474.608	1.708
1.6	0.267	776.398	1.744
1.0×10^{14} ions cm^{-2}			
1.0	0.177	38.139	1.193
1.1	0.188	50.302	1.261
1.2	0.208	123.213	1.438
1.4	0.229	205.128	1.626
1.5	0.250	317.561	1.798
1.75	0.292	584.454	1.715
2.2×10^{14} ions cm^{-2}			
1.375	0.229	87.108	1.379
1.5	0.250	189.037	1.59
1.625	0.271	322.580	1.819
1.75	0.292	458.927	1.888
2.00	0.333	787.868	1.923

Voltage (V)	E Field ($MVcm^{-1}$)	$1/t_s$ (s^{-1})	n_s
4.6×10^{14} ions cm^{-2}			
1.875	0.313	40.807	1.141
2.00	0.333	75.131	1.18
2.125	0.354	174.125	1.327
2.25	0.375	249.875	1.45
2.5	0.417	489.655	1.61
7.0×10^{14} ions cm^{-2}			
2.3	0.383	36.280	1.596
2.5	0.417	97.453	1.687
2.75	0.458	235.516	1.742
3.0	0.500	389.814	1.871
3.15	0.525	637.274	1.841
1.0×10^{15} ions cm^{-2}			
2.9	0.483	31.407	0.830
3	0.500	52.056	0.887
3.15	0.525	79.554	1.146
3.25	0.542	131.562	1.236
3.5	0.583	250.188	1.323
3.75	0.625	384.615	1.406
4	0.667	662.877	1.525

the dominant defects. This correlates with the evolution of irradiation-induced defects which need to overcome a critical size to grow. At an initial stage one increases the number of critical defects while at higher doses they cluster and grow. Therefore, I conclude that in the intermediate-dose regime the dominant defects are likely isolated point defects and small clusters with a low pinning strength which result only in a small increase in the pinning energy and coercive field. On the other hand, within the high-dose regime larger complexes and clusters are likely to form and their stronger pinning strength drives a rapid increase of the pinning energy and coercive field. In addition, the increase of imprint and reduction of polarization within the high-dose regime suggests the presence of a preferred polarization direction, further supporting the idea that defect-complexes are playing a dominant role in this dose regime. This work, therefore, provides systematic experimental evidence of the role of different defect types (*i.e.*, isolated point defects and complexes or clusters) in affecting ferroelectric-polarization switching.

8.3 Designing New Functionalities in $PbZr_{0.2}Ti_{0.8}O_3$ Thin Films via Control of the Location of Bombardment-Induced Defects

In the following, I show that the presence of strong defect-polarization coupling, and the ability to control the type, concentration, and location of defects via focused-ion beams, allows one to realize new functionalities [33]. First, I show that local control over the coercive field can provide an effective pathway for creating multi-state switching processes in intrinsically bistable ferroelectrics. To achieve this, different regions of single capacitors were bombarded with different doses. In one capacitor, the ion beam was rastered over one-third of the total area (central region) to produce an intermediate dose (2.2×10^{14} ions cm^{-2}), leaving two-thirds of the capacitor (outer region) in the as-grown state (Figure 8.7a). These regions, therefore, are expected to have different coercive fields. Under lower voltages, only the as-grown region (two-thirds of the polarization) is

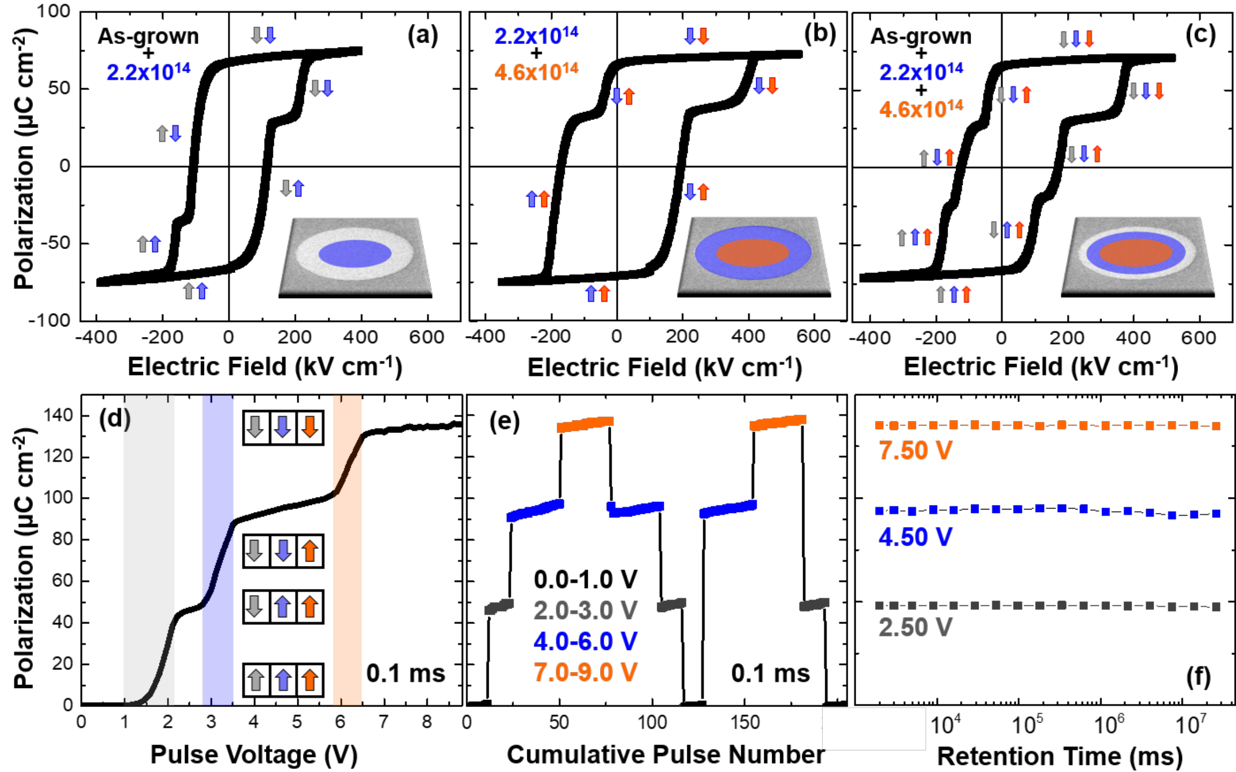

Figure 8.7. Polarization-electric field hysteresis loops for capacitors exposed to various ion-bombardment procedures including (a) as-grown (grey region) and 2.2×10^{14} ions cm^{-2} (blue region) resulting in symmetric two-step switching, (b) 2.2×10^{14} ions cm^{-2} (blue region) and 4.6×10^{14} ions cm^{-2} (red region) resulting in asymmetric two-step switching, and (c) as-grown (no bombardment, grey region), 2.2×10^{14} ions cm^{-2} (blue region), and 4.6×10^{14} ions cm^{-2} (red region) resulting in three-step switching. Focusing on the capacitors in (c), subsequent (d) PUND studies reveal the pathway to the different polarization states at a constant pulse width of 0.1 ms, (e) the ability to deterministically switch between the different polarization states, and (f) the long-term retention and stability of the multiple polarization states.

switched. The bombarded region (and the remaining one-third of the polarization) switches only once the electric field exceeds its corresponding coercive field, and consequently, a two-step switching is realized. The same process repeats itself under the opposite bias. In another capacitor, a different dose combination was used (Figure 8.7b) wherein the beam was rastered over the entire capacitor to produce an intermediate dose (2.2×10^{14} ions cm^{-2}) before being further rastered over one-third of the capacitor (central region) to produce a high dose (4.6×10^{14} ions cm^{-2}). In this case, for switching from negative to positive polarization, the intermediate-dose region switches first, followed by the high-dose region at a larger field. In the opposite direction, however, the sequence of the two-step switching is reversed, due to the induced imprint in the high-dose region. Finally, another capacitor was created wherein the beam was rastered to create three regions of equal area: 1) no ion bombardment (outer region), 2) intermediate dose (2.2×10^{14} ions cm^{-2}, middle region), and 3) high dose (4.6×10^{14} ions cm^{-2}, central region). Consequently, three-step switching processes are observed resulting in four polarization states (Figure 8.7c). Therefore, the shape of the hysteresis loops, the number of states, their polarization values, and their voltage-range stability can be engineered by choosing different dose combinations and volume ratios.

To probe the utility and robustness of this process, a capacitor exhibiting three-step switching (Figure 8.7c) was studied using PUND measurements, as described in Section 4.3.3.4.

The voltage stability range of each state was extracted (Figure 8.7d) and used to demonstrate arbitrary access to each state in an on-demand fashion (Figure 8.7e). The possible states were accessed in an ascending, descending, and random order by controlling the pulse voltage. The stability of the polarization states was probed by studying the variation of remanent polarization with time (Figure 8.7f) using a retention pulse sequence, as described in Section 4.3.3.5. Each polarization state was accessed using the appropriate pulse width and voltage and read after gradually increasing retention times. All the states were stable over time, showing no loss of polarization after ≈ 7 hours (separate studies performed weeks later also showed no loss of the written states). Therefore, nonvolatile and deterministically accessible multi-states can be produced, opening the door to multilevel data storage and logic.

In order to study the microscopic mechanisms involved in the switching process and their (in)homogeneity, first-order reversal curve studies [208,210] were performed on as-grown capacitors (Figure 8.8a) and capacitors bombarded with two doses of 4.6×10^{14} ions cm^{-2} and 7.0×10^{14} ions cm^{-2} (Figure 8.8b), as described in Section 4.3.3.6. The contour plots of the distribution functions are shown (Figure 8.8c,d). The distributions along the bias and coercive-field axes correspond to the reversible and irreversible contributions to the total polarization, respectively [208]. Focusing on the irreversible contributions, the as-grown capacitor reveals a single distribution over a small coercive field and a zero-bias field (Figure 8.8c). The same measurement on capacitors bombarded with two doses reveals two distinct distributions, showing

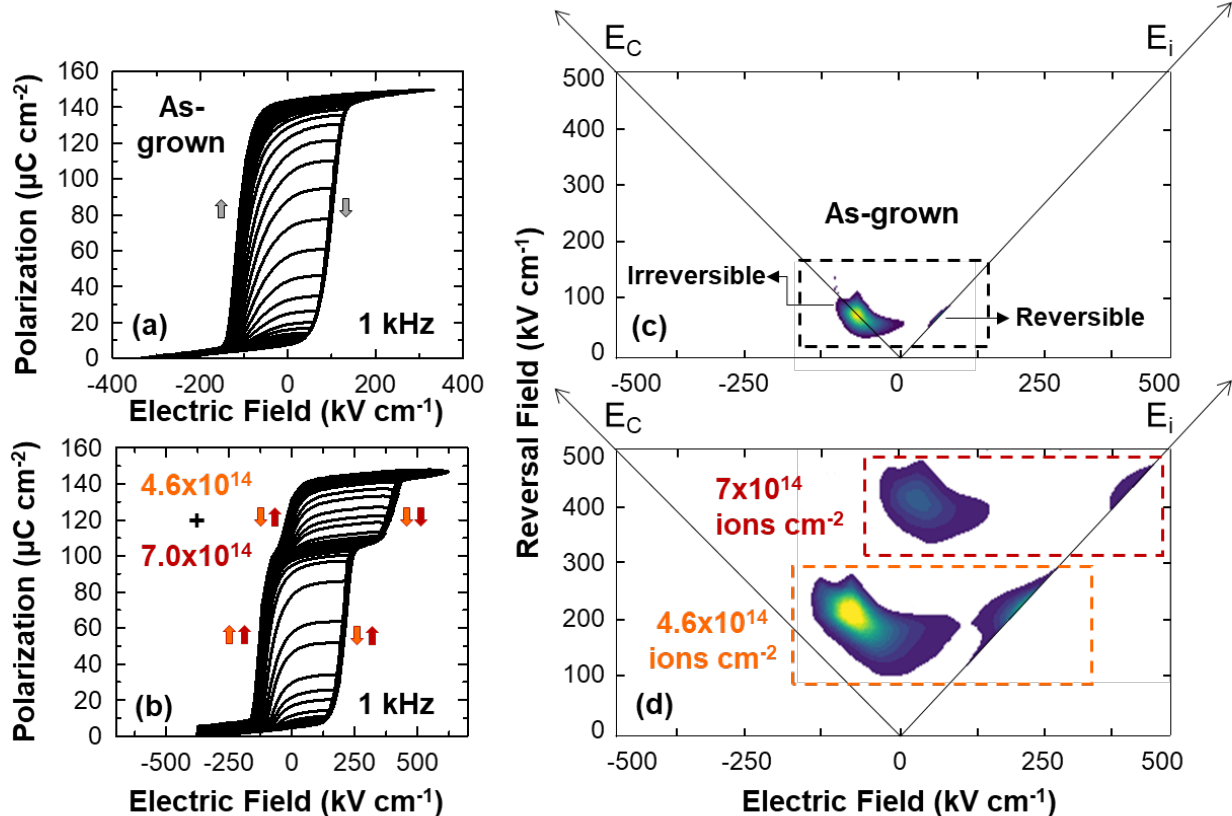

Figure 8.8. Polarization-electric field hysteresis loops taken between a negative saturation field and various positive reversal fields for (a) as-grown and (b) 4.6×10^{14} and 7.0×10^{14} ions cm^{-2} two-region ion-bombarded capacitors. Analysis of the first-order reversal curve data reveals the distribution of elementary switchable units over their coercive and bias fields for the (c) as-grown and (d) 4.6×10^{14} and 7.0×10^{14} ions cm^{-2} two-region ion-bombarded capacitors.

that increasing the dose shifts the distribution to higher coercive and bias fields, and that this shift can be confined to certain regions (Figure 8.8d).

Scanning-probe microscopy further supports my proposed mechanism for the observed multi-state switching. Band excitation piezoresponse spectroscopy measurements [198] were performed using a band-excitation waveform at remanence throughout a bipolar triangular switching waveform (Figure 8.9a), on a region bombarded with three doses of zero (as-grown), 2.2×10^{14} ions cm^{-2}, and 10^{15} ions cm^{-2}, as described in Section 4.3.2.2 and Appendix B. A movie

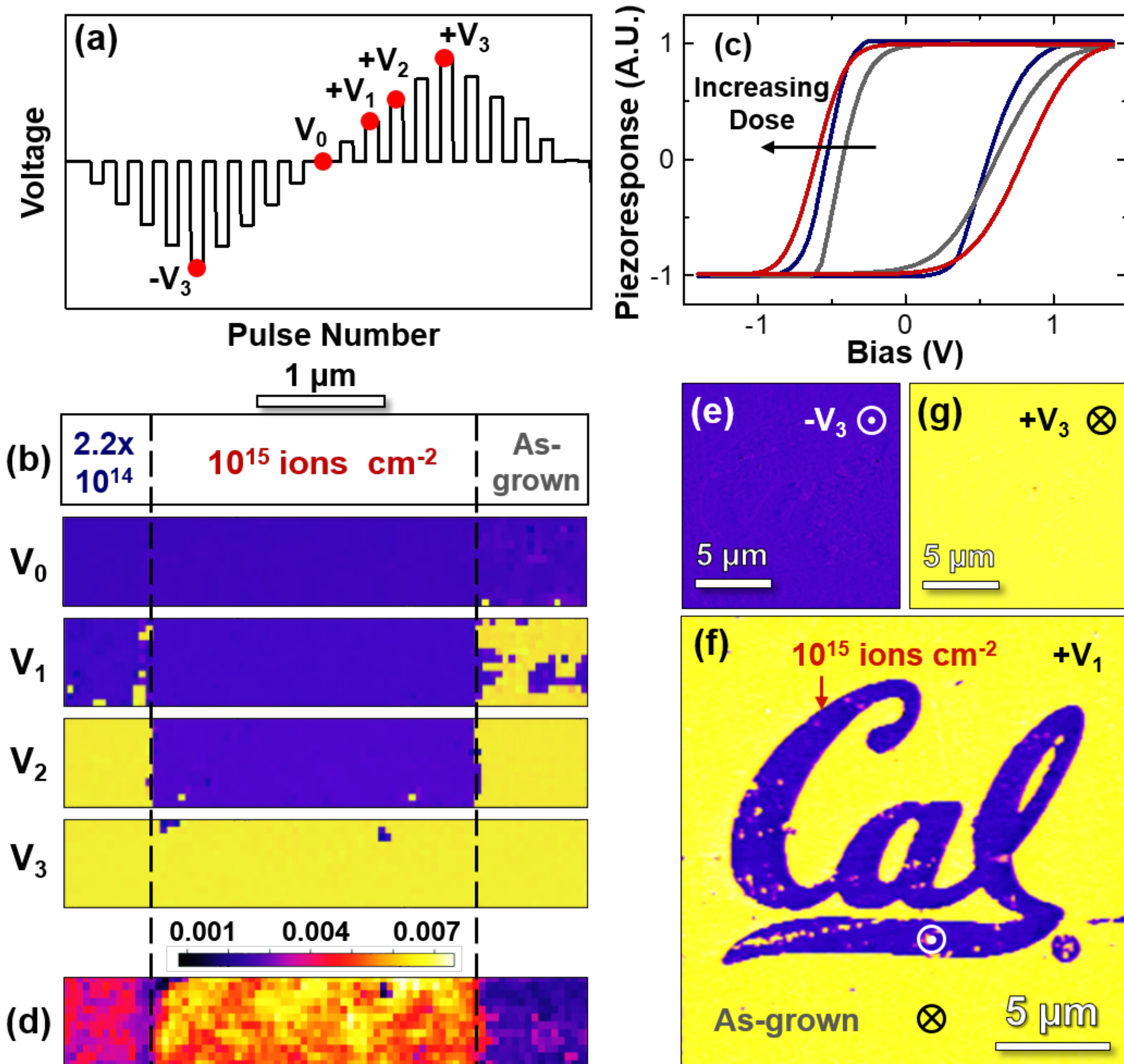

Figure 8.9. (a) Schematic of the probing waveform used for band excitation piezoresponse spectroscopy measurements. The piezoresponse was measured at remanence. (b) Schematic of the entire region studied herein (Top) including the doses used in each area, as well as the phase response at different voltages (V_0, V_1, V_2, and V_3) showing the step-by-step nature of the switching. (c) Average piezoresponse loops extracted from each region in (b). (d) The extracted work of switching (defined as the area within the piezoelectric loops) for each region. Piezoresponse force microscopy phase images of a given area in (e) as-poled ($-V_3$), (f) partially switched ($+V_1$), and (g) fully switched states showing the ability to determinisitically write defects to produce arbitrary 180° ferroelectric domain structures.

of the switching process from fully-upward to fully-downward poled directions was constructed by forming phase images at each voltage step throughout the switching waveform. A few snapshots (phase images) during the switching are provided (Figure 8.9b). At zero voltage (V_0) the entire region has an upward polarization. At voltage $+V_1$, which is larger than the coercive field of the as-grown region, but smaller than that of the bombarded regions, only the as-grown region switches. The switching proceeds by switching of the regions bombarded with doses of 2.2×10^{14} ions cm^{-2} and 10^{15} ions cm^{-2}, at voltages of $+V_2$ and $+V_3$, respectively. This shows the step-by-step nature of the switching, and that the defects and their induced effects can be confined to select regions defined by the ion beam. The amplitude and phase response were also fit to extract the piezoelectric loops. The average of the piezoelectric loops was extracted from each bombarded region to allow for a simple comparison between their response. The piezoelectric loops extracted from the points near particles and near the boundaries between regions bombarded with different ion doses were excluded from the average, in order to obtain more representative values of the film behavior. A dose-dependent increase is observed in the coercive field of the average piezoelectric loops (Figure 8.9c), and the work of switching (*i.e.*, the area within the piezoelectric loops) (Figure 8.9d), which is consistent with other experimental data in this work, showing an increase in the coercive field with increasing defect concentration, as a result of defect pinning.

Motivated by the ability to locally manipulate the coercive field, I have examined the possibility of creating arbitrary 180° ferroelectric domain patterns. Selective regions of the films were bombarded with a dose of 10^{15} ions cm^{-2} in the form of the Cal™ logo. A 15×15 μm region containing the bombarded area and its as-grown background was then poled to an upward direction

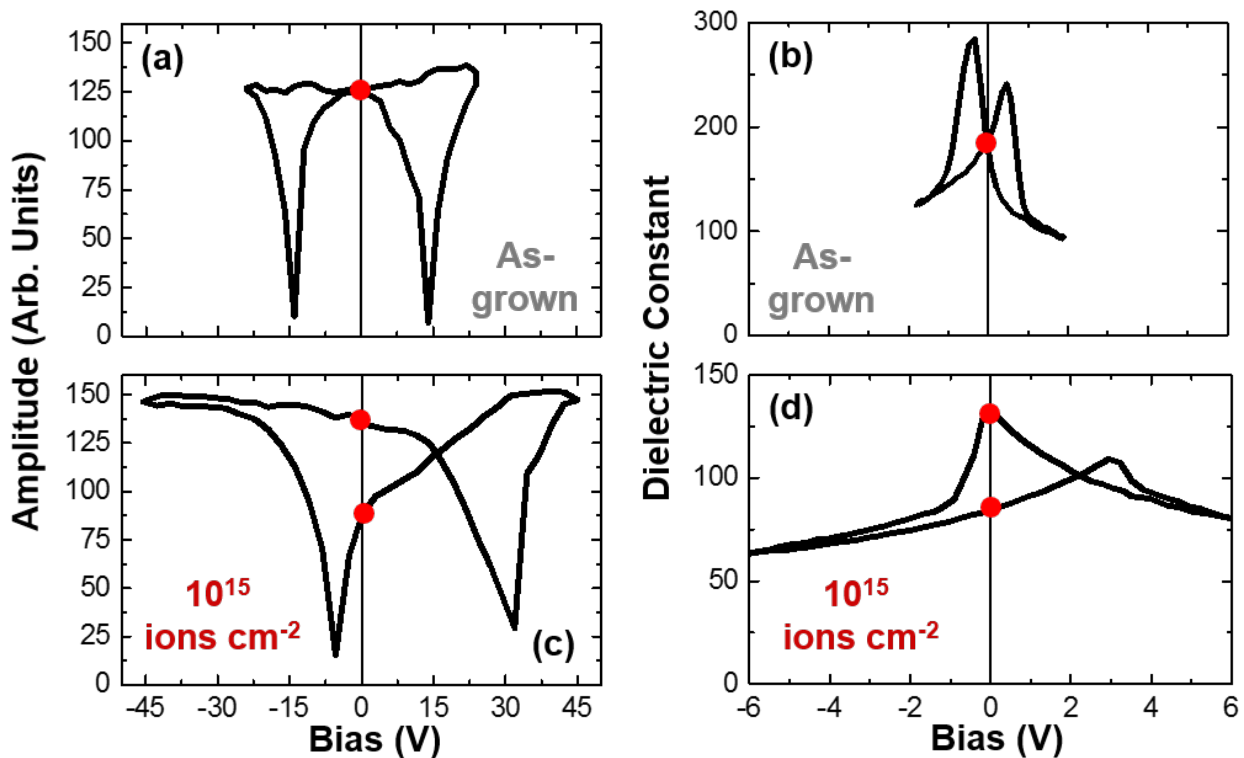

Figure 8.10. (a) Piezoresponse amplitude as extracted from piezoresponse force microscopy studies and (b) dielectric permittivity (constant) as a function of applied bias for as-grown capacitors. (c) Piezoresponse amplitude as extracted from piezoresponse force microscopy studies and (d) dielectric permittivity (constant) as a function of applied bias for 10^{15} ions cm^{-2} ion-bombarded capacitors.

using piezoresponse force microscopy (Figure 8.9e). Afterwards, a small positive voltage $+V_1$ (only sufficient to switch the as-grown region) was applied to the entire area. The logo appears (still unswitched) after this step with a 180° contrast from its background (Figure 8.9.f). Applying a positive voltage higher than the coercive field of the bombarded region ($+V_3$) switches the entire area to a down-poled polarization and the logo disappears (Figure 8.9g). Therefore, predetermined and rewritable 180° ferroelectric domain patterns can be written, with feature sizes being limited only by the size and interaction volume of the ion beam.

As mentioned in Section 8.2, the dose-dependent increase in the coercive field is accompanied by an increase of electrical imprint in the high-dose regime due to the formation of defect complexes and clusters. Here, I demonstrate that the dose-dependence of imprint can also be used to modify the function and can be useful for any application where stabilizing the ferroelectric polarization in one direction is beneficial. For example, imprint is important in ferroelectric field-effect transistors (in order to address retention issues) [287,291] and gives rise to asymmetry in strain and permittivity responses which are useful for self-sensing shape-memory piezoelectric actuators [289,290,296]. Here, I show that the imprint associated with ion bombardment can give rise to features in both the piezoresponse and permittivity, suggesting that such processing approaches can be useful for deterministically tuning devices used for the abovementioned applications. For example, in both local piezoresponse (Figure 8.10a) and dielectric permittivity measurements (Figure 8.10b), the as-grown capacitors show only one stable state at zero field. After ion bombardment (10^{15} ions cm^{-2}), the defect-induced imprint means that multiple zero-field states are realized with the reversal of polarization in both the piezoresponse (Figure 8.10c) and permittivity (Figure 8.10d). In turn, such memory effects can be used for self-sensing operations and position detection in shape-memory piezoelectrics [289,290,296].

8.4 Conclusions

In conclusion, I have shown that on-demand tuning of type, concentration, and position of defects can provide a powerful tool for the systematic and quantitative study of defect-polarization interactions and enables a deterministic control of the switching properties in ferroelectric thin films. For example, the coercive field and imprint characteristics can be tuned in select regions using focused-ion beams. I have shown that this control is the result of interactions between defects and domain walls, and that the strength of these interactions is strongly dependent on the type and concentration of the defects. While isolated-point defects and small clusters which are dominant at low defect concentrations show a weak interaction with the domain walls (pinning potentials from 200-500 K MV cm^{-1}) and give rise to a relatively small and symmetric increase in the coercive field, larger complexes and clusters which are dominant at higher defect concentrations strongly pin the domain-wall motion (pinning potentials from 500-1600 K MV cm^{-1}) and give rise to a large increase in the coercive field and a preferred polarization direction (manifested as an electrical imprint and a reduction in the polarization). Using the ability to manipulate the coercive field in select regions, I have demonstrated multiple stable states in an otherwise bistable ferroelectric, where the number of states, their polarization values, and switching voltages can be varied systematically. I have also demonstrated the potential of this technique for creating rewritable predetermined 180° ferroelectric domain patterns. Finally, I have demonstrated controllable electrical imprint which can give rise to multiple zero-field dielectric- and piezo-responses.

CHAPTER 9

Ex Situ Control of Bombardment-Induced Defects and Study of Defect-Induced (Dis)Order in Relaxor Ferroelectric Thin Films

In this Chapter, I provide systematic experimental evidence of the effect of *intrinsic* point defects on relaxor properties of $0.68PbMg_{1/3}Nb_{2/3}O_3$-$0.32PbTiO_3$ thin films across nearly two orders of magnitude of defect concentration via *ex situ* ion bombardment. A weakening of the relaxor character is observed with increasing concentration of bombardment-induced point defects which is attributed to strong interactions between defect dipoles and the polarization. Although more defects and structural disorder are introduced in the system as a result of ion bombardment, the special type of defects that are created (*i.e.,* defect dipoles) and their ordering stabilize the direction of polarization against thermal fluctuations, and in turn, weaken the relaxor behavior. This study, therefore, shows the complex effect of point defects in controlling the local (dis)order, and suggests that having the ability to carefully control both concentration and type of point defects is instrumental in controlling and understanding relaxor materials physics and engineering of relaxor materials.

9.1 Introduction

As discussed in Section 2.5.5, relaxor ferroelectrics are characterized by broad maximum in temperature-dependent dielectric permittivity, strong frequency dispersion of dielectric response below the temperature of maximum permittivity, and absence of long-range ferroelectric order at zero field [80,81]. Relaxors also exhibit high dielectric permittivity over a broad temperature range, large electromechanical response, and negligible hysteresis [80-82]. Owing to these unique properties, relaxors have been used in a wide range of applications. Common to all relaxors, and strongly influencing their properties, is the existence of some degree of disorder in their crystalline structure [81,297]. Point defects, therefore, can be a valuable tool for controlling relaxor behavior, since they can create both random electric and strain fields [297]. In complex oxides, for example, *extrinsic* substitutional defects (*i.e.*, dopants) have been extensively used to introduce compositional disorder and to manipulate relaxor behavior (*i.e.*, to induce, strengthen, or weaken the relaxor character) [297-300]. The role of *intrinsic* point defects, on the other hand, is less developed. Structural disorder induced by *intrinsic* point defects can induce relaxor character in non-relaxors as in strontium-deficient $SrTiO_3$ [301], lanthanum-substituted $PbTiO_3$ where the resulting cation vacancies can weaken the long-range order and induce relaxor character [302], and in lead scandium tantalate and lead scandium niobate wherein *intrinsic* vacancies can affect the degree of cation ordering and relaxor character [303,304]. A full understanding of how various types and concentrations of *intrinsic* point defects affect the properties of relaxor ferroelectrics, however, is lacking.

This paucity of knowledge regarding the role of *intrinsic* point defects is primarily related to difficulties in on-demand and controlled production of such defects, which are typically formed during the synthesis process with their concentration and type being dictated by the laws of thermodynamics [23]. In Chapters 6-8, however, I have shown that energetic ion beams are effective means for *ex situ* creation of *intrinsic* point defects with control over their type, concentration, and location [30,32,33]. This controlled defect production provides opportunities for systematic studies of defect-structure-property relations in relaxors [34]. Here, although the introduction of point defects is shown to increase the structural disorder, strong interactions between specific defect types (*i.e.*, defect dipoles) and polarization result in suppression of the polarization fluctuations and weakening of the relaxor behavior. Ultimately, having the ability to carefully control both concentration and type of point defects is necessary in controlling and understanding relaxor materials physics [34].

9.2 *Ex Situ* Creation of Bombardment-Induced Defects in $0.68PbMg_{1/3}Nb_{2/3}O_3$-$0.32PbTiO_3$ Thin Films via High-Energy Helium-Ion Bombardment

This work focuses on 55 nm $0.68PbMg_{1/3}Nb_{2/3}O_3$-$0.32PbTiO_3$/25 nm $Ba_{0.5}Sr_{0.5}RuO_3$/$NdScO_3$ (110) thin-film heterostructures [34]. The effect of bombardment-induced *intrinsic* point defects on the relaxor behavior is investigated across nearly two orders of magnitude of defect concentrations. A defocused 3.04 MeV helium-ion beam was used for defect production as described in Section 4.2.2.2, and the concentration of the induced defects was controlled by the ion dose (3.33×10^{14}-10^{16} ions cm^{-2}). SRIM simulations show that *intrinsic* vacancies, including lead, titanium, magnesium, niobium, and oxygen vacancies, are formed with uniform concentrations across the thickness of the $0.68PbMg_{1/3}Nb_{2/3}O_3$-$0.32PbTiO_3$ (Figure 9.1a) as a

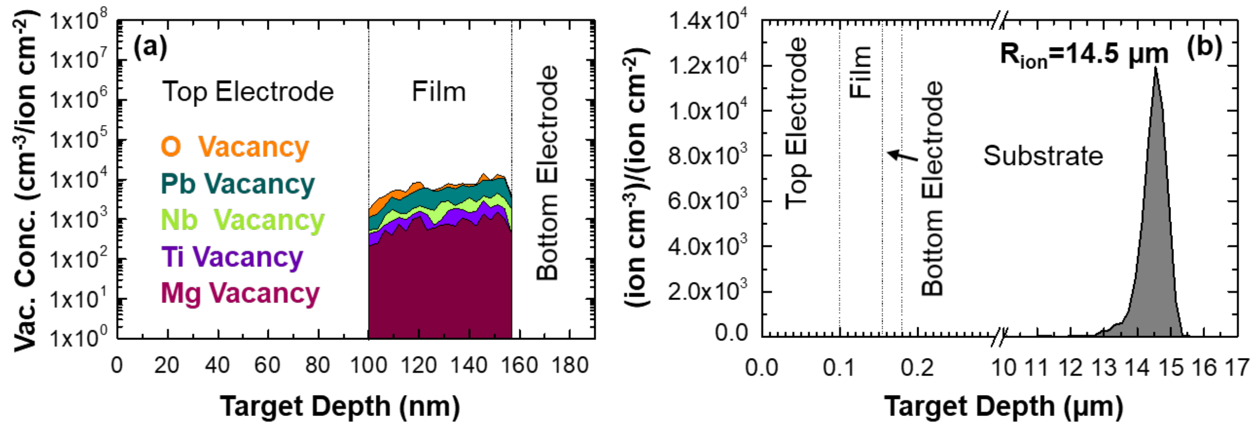

Figure 9.1. (a) SRIM simulation of induced defects concentration as a function of depth in $0.68PbMg_{1/3}Nb_{2/3}O_3$-$0.32PbTiO_3$ layer. (b) SRIM simulation of He^{2+} concentration as a function of depth, suggesting that essentially no He^{2+} ions are implanted into the film, but instead the vast majority of ions are stopped at a depth of ≈ 14.5 μm into the $NdScO_3$ substrate, due to high incident energy (3.04 MeV) of the ions.

result of collision events between the incoming helium ions and target atoms. The total initial concentration of induced defects is calculated to vary from ≈ 10^{18} to ≈ 10^{20} cm^{-3}, for the ion-dose range used. It is important to note that the helium ions are implanted at a depth of ≈ 14.5 μm within the $NdScO_3$ substrate (Figure 9.1b); therefore, the concentration of helium ions in the relaxor is effectively zero, and the observed defect-induced effects can be primarily attributed to the induced *intrinsic* defects.

Formation of structural defects in the bombarded heterostructures is confirmed by X-ray diffraction studies (Figure 9.2). $\omega - 2\theta$ X-ray diffraction studies reveal that the heterostructures are fully epitaxial and single-phase for all doses (Figure 9.2a). A zoom in of the $\omega - 2\theta$ scans about the 002- and 220-diffraction conditions, however, reveals a systematic out-of-plane lattice expansion with increasing dose (Figure 9.2b) which is attributed to the formation of point defects

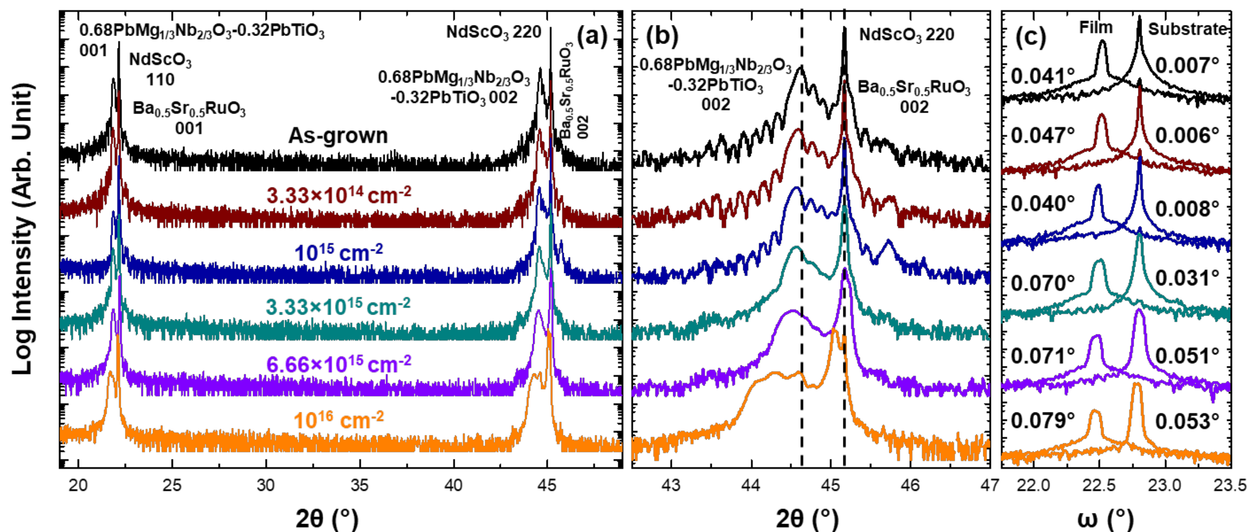

Figure 9.2. (a) Wide angle $\omega - 2\theta$ X-ray diffraction scans for heterostructures bombarded with various ion doses. (b) Zoom-in of $\omega - 2\theta$ scans about the 002- and 220-diffraction conditions. (c) Rocking curves for heterostructures bombarded with various doses obtained about the 002- and 220-diffraction conditions of film and substrate.

such as vacancies in many related complex oxides [172,242]. Moreover, although insignificant at doses below 10^{15} ion cm^{-2}, dramatic changes in the crystalline quality are observed at higher doses. This is manifested by broadening of the diffraction peaks, disappearance of the Laue fringes (Figure 9.2b) which occur only in highly crystalline and homogeneous films, and increase of the FWHM of the $0.68PbMg_{1/3}Nb_{2/3}O_3$-$0.32PbTiO_3$ rocking curves as shown in comparison to that of the substrate (Figure 9.2c). These observations point to increased structural disorder in the system with increasing ion dose as a result of the formation of bombardment-induced point defects. In turn, these materials, provide the opportunity to study the effect of point defects on the evolution of relaxor behavior across nearly two orders of magnitude of defect concentration and at varying degrees of disorder.

9.3 Effect of Bombardment-Induced Defects on Relaxor Properties of $0.68PbMg_{1/3}Nb_{2/3}O_3$-$0.32PbTiO_3$ Thin Films

To study the impact of the induced defects on the relaxor behavior, the evolution of the dielectric response as a function of ion dose was probed [34]. DC-bias dependence of capacitance (C-V sweep) and the frequency-dependence of the capacitance (C-f sweep) were carried out from room temperature up to 650 K with 10 K increments. C-f sweeps were carried out by driving the top electrode with an AC voltage of 10 mV in a frequency range of 100 Hz-1 MHz. DC-bias dependence of capacitance was measured by driving the top electrode with an AC voltage of 10 mV at a frequency of 10 kHz while sweeping the DC bias between +/-200 kV cm^{-1} in both directions. During the C-f sweeps, a background DC bias, corresponding to the average of the field

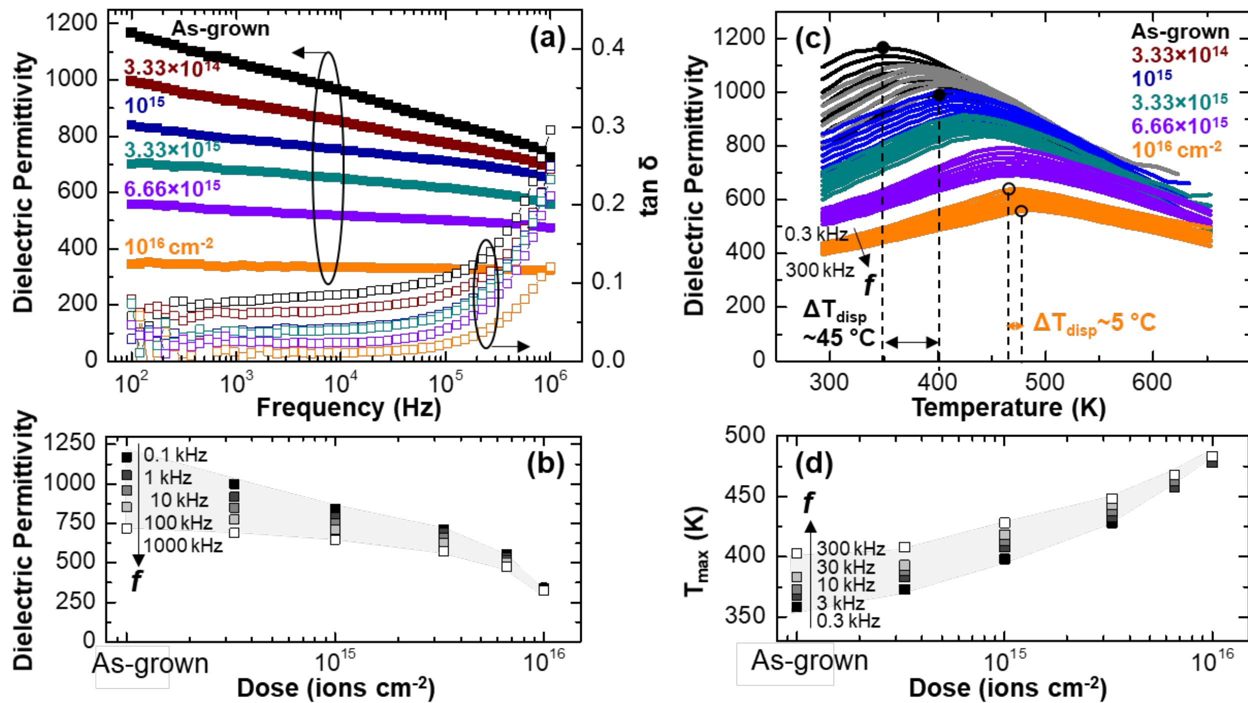

Figure 9.3. (a) Room-temperature dielectric permittivity (filled squares) and loss (open squares) as a function of frequency for heterostructures bombarded with various ion doses. (b) Dielectric permittivity as a function of ion dose extracted at various frequencies (0.1-1000 kHz). (c) Dielectric permittivity as a function of temperature and frequency (0.3-300 kHz) for heterostructures bombarded with various ion doses. (d) Extracted values of T_{max} as a function of ion dose at various frequencies (0.3-300 kHz).

at which the capacitance was maximum during sweep-up and sweep-down in C-V measurements, was applied to compensate for the imprint which is present in these heterostructures [305]. Dielectric permittivity studies as a function of frequency reveal a number of changes (Figure 9.3a). First, a dose-dependent reduction in dielectric permittivity and loss is observed; consistent with effects attributed to the presence of defects in similar systems [150,306,307]. A systematic reduction in frequency dispersion is also observed with increasing bombardment and is almost fully suppressed in highly bombarded heterostructures (Figure 9.3a,b). To better understand these changes, temperature-dependent studies were also completed (Figure 9.3c). While a frequency-dependent change in the dielectric maximum temperature:

$$\Delta T_{disp} = T_{max}^{300\,kHz} - T_{max}^{0.3\,kHz} \tag{9.1}$$

which characterizes the strength of the relaxor behavior [308], and strong frequency dispersion below T_{max} (as expected for relaxor ferroelectrics) can be observed in the as-grown heterostructures ($\Delta T_{disp} \approx 45$ K), the frequency-dependence of the response systematically weakens as the ion dose is increased (Figure 9.3d). For example, the heterostructures exposed to 10^{16} ion cm^{-2} show negligible dispersion ($\Delta T_{disp} < 5$ K). It is also important to note that, in addition to a suppression of the frequency dispersion, T_{max} shifts to higher temperatures with increasing ion dose (Figure 9.3c,d). These observations suggest a weakening of the relaxor character as a result of increasing defect concentration. Thus, it should be noted that the increased structural disorder (due to the displacement of the atoms from their ideal lattice sites) is not the only factor affecting the relaxor response.

A similar increase of T_{max} and decrease of ΔT_{disp} has been previously reported as a result of compressive strain in relaxor thin films [309-311], and has been related to changes of the correlation length and polar nanoregion morphology, and the direction of dipoles within them [94,309-312]. To examine whether defect-induced changes in the morphology of the local-polar order are responsible for the weakening of the relaxor response, a series of two-dimensional reciprocal space mapping studies were conducted (Figure 9.4a-e). Two-dimensional KL-cuts about the 002-diffraction condition of $0.68PbMg_{1/3}Nb_{2/3}O_3$-$0.32PbTiO_3$ reveal classic butterfly-shaped diffuse-scattering patterns, with diffuse rods extending along the $[011]$ and $[0\bar{1}1]$ for all doses. Although increased peak broadening and lattice expansion can be observed in both the film and substrate diffraction peaks with increasing dose, the overall shape of the diffuse-scattering patterns remain unchanged. Intensity profiles along the $[011]$ are also extracted (Figure 9.4f) and show no significant change as a function of ion dose. These observations imply that there is no change in

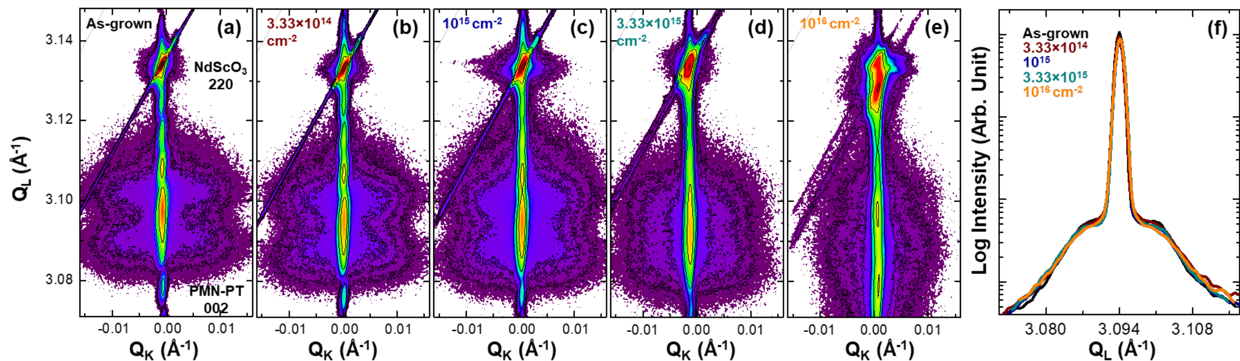

Figure 9.4. (a-e) Two-dimensional reciprocal space mapping studies and KL-cuts about the 002-diffraction conditions of $0.68PbMg_{1/3}Nb_{2/3}O_3$-$0.32PbTiO_3$ for heterostructures bombarded with various ion doses. (f) Diffuse-scattering intensity profiles extracted along [011] direction for various ion doses.

the shape or size of the polar nanoregions as a result of defect introduction, and thus, additional considerations are required to explain the dose-dependent evolution of the relaxor behavior.

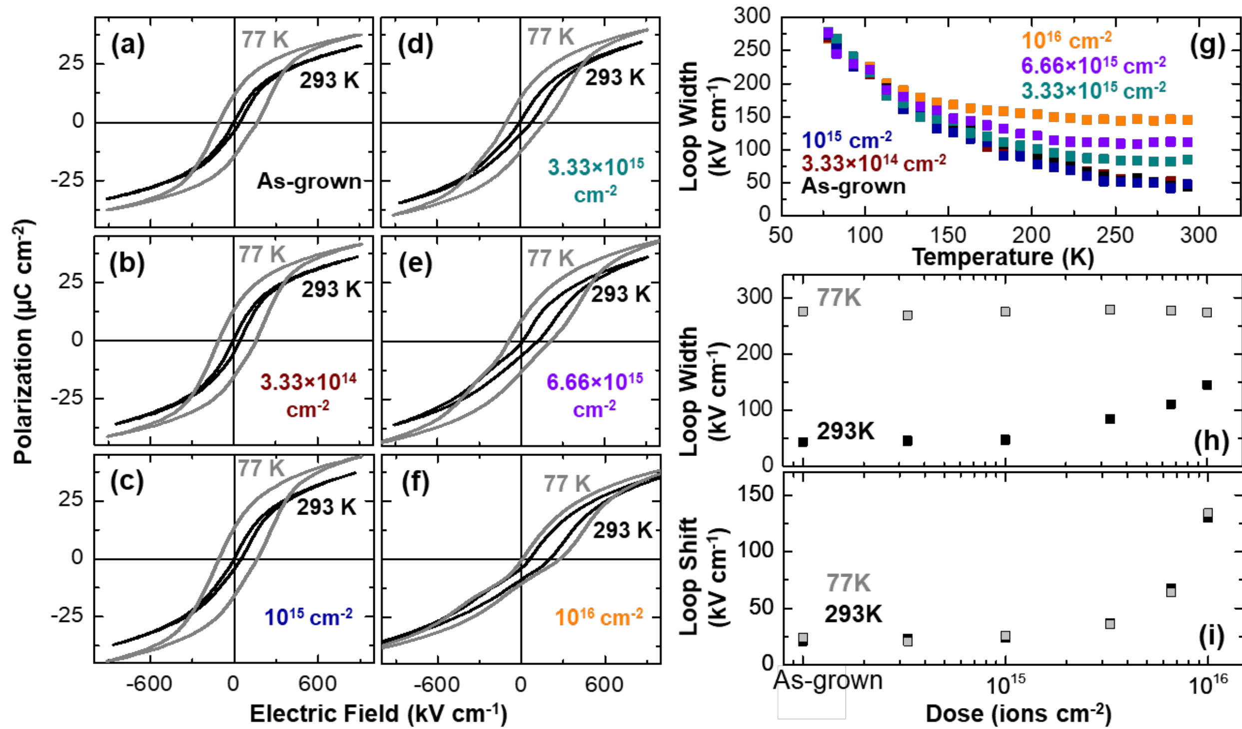

Figure 9.5. (a-f) Polarization-electric field hysteresis loops measured at a frequency of 10 kHz at 77 K and 293 K for heterostructures bombarded with various ion doses. (g) Width of the hysteresis loops extracted as a function of temperature for heterostructures bombarded with various ion doses. (h) Width of the hysteresis loops as a function of ion dose extracted at 77 K and 293 K. (i) Horizontal shift of the hysteresis loops as a function of ion dose extracted at 77 K and 293 K.

To further explore the origin of the defect-induced effects, polarization-electric field hysteresis loops were measured at a frequency of 10 kHz as a function of temperature (from room temperature down to 77 K with 10 K increments) and ion dose (Figure 9.5a-f), and the width of the hysteresis loops at zero polarization, and shift of the center of the hysteresis loops on the field axis were extracted (Figure 9.5g-i). The as-grown heterostructures show slim hysteresis loops at room temperature, typical of relaxor ferroelectrics (Figure 9.5a). Upon reducing the temperature, however, the width of the hysteresis loops increases from ≈ 40 kV cm^{-1} at room temperature to ≈ 280 kV cm^{-1} at 77 K. Neither the overall shape (Figure 9.5a-c) nor the width and shift of the hysteresis loops at both room temperature and 77 K (Figure 9.5g-i), exhibit any appreciable changes up to 10^{15} ions cm^{-2}. At higher doses, however, a number of changes are apparent. A slight pinching appears in the hysteresis loops and becomes more pronounced as the ion dose is increased (Figure 9.5d-f). Additionally, a dose-dependent increase in the width of the hysteresis loops is observed at higher temperatures (Figure 9.5g,h). At room temperature, for example, the width of the hysteresis loops increases from ≈ 40 to ≈ 160 kV cm^{-1} with increasing dose, but this is less pronounced at lower temperatures (at 77 K, for example, the width of the loops remains constant at ≈ 280 kV cm^{-1}). An increase in the shift of the hysteresis loops is also observed at all temperatures (Figure 9.5i) from ≈ 24 to ≈ 135 kV cm^{-1}, with increasing ion dose.

The pinching and horizontal shift of the hysteresis loops are signatures of the formation of defect dipoles in the relaxors, similar to effects seen in other polar systems [12,31,33,125,147,160], and consistent with the evolution of bombardment-induced defects. It is known that as the defect concentration increases, the initially formed point defects can cluster into complexes. Thus, by increasing the ion dose, the concentration of isolated point defects decreases while the concentration of defect complexes increases, causing more pronounced pinching and shifting of the hysteresis loops. Strong interactions between the electric dipole of such defect complexes and the polarization have been predicted and measured [12,125,127,131,136-138,147,160-162]. As mentioned in Section 3.5, defect dipoles typically align in the direction of the polarization and act as pinning centers for polarization switching, with pinning strengths considerably larger than that of isolated point defects [33,127,131]. This strong defect-dipole-polarization coupling explains the increase of the width of the hysteresis loops at high ion doses (>10^{15} ions cm^{-2}) where a considerable concentration of defect complexes appears to exist (as indicated by the pronounced shift and pinching of the hysteresis loops). Polarization reversal, on the other hand, is a thermally-activated process and the activation-energy barrier for switching increases as the temperature is lowered. As a result, at high temperatures, where thermal fluctuations play a significant role, the pinning effect of defects on polarization reversal is more pronounced as compared to lower temperatures, where the polarization switching is predominantly field driven. Therefore, different ion-dose and temperature regimes can be identified. In the low-dose regime (<10^{15} ions cm^{-2}), where the induced defects are predominantly isolated point defects, there is no significant change in the switching. Within the high-dose regime (>10^{15} ions cm^{-2}), where defect dipoles start to form, strong defect-polarization interaction (*i.e.*, pinching and an increase of the width and shift of the hysteresis loops) are observed. Within this regime, the effect of defect dipoles on polarization reversal is temperature dependent. At high temperatures, the process is limited by the presence of defects (*i.e.* pinning of polarization by defect dipoles), while at low temperatures it is limited by the freezing of polarization fluctuations. This is useful in explaining the evolution of the dielectric response and weakening of the relaxor behavior with increasing ion dose. Although more displacement defects (and disorder) are introduced in the system, the special type of defects that are created (*i.e.*, defect dipoles) and their ordering stabilize the direction of the polarization against thermal fluctuations, and, in turn, weaken the relaxor behavior, while the morphology and size of the local-polar order remains effectively unaltered.

To further analyze this defect-induced deviation from relaxor behavior, I have extracted the critical exponent γ (which describes the diffuseness of a phase transition) according to a modified Curie-Weiss law:

$$\frac{1}{\varepsilon} - \frac{1}{\varepsilon_{max}} = c^{-1}(T - T_{max})^{\gamma} \tag{9.2}$$

where ε_{max} corresponds to the maximum dielectric permittivity and c is a constant [313]. While the dielectric permittivity of a normal ferroelectric follows the Curie-Weiss law above the Curie temperature as discussed in Section 2.4.2, relaxors exhibit a temperature dependence of dielectric permittivity that deviates from Curie-Weiss behavior over a wide temperature range above T_{max}. This deviation can be used to characterize the strength of the relaxor behavior and is quantified by the critical exponent γ. For a normal ferroelectric (*i.e.*, sharp transition) $\gamma = 1$, while for an ideal relaxor (*i.e.*, completely diffuse phase transition) $\gamma = 2$ [313-315]. For relaxors, it is not uncommon to find $1 < \gamma < 2$ depending on the strength of the relaxor character [313]. γ was determined for the heterostructures exposed to various doses from the slope of the plot of

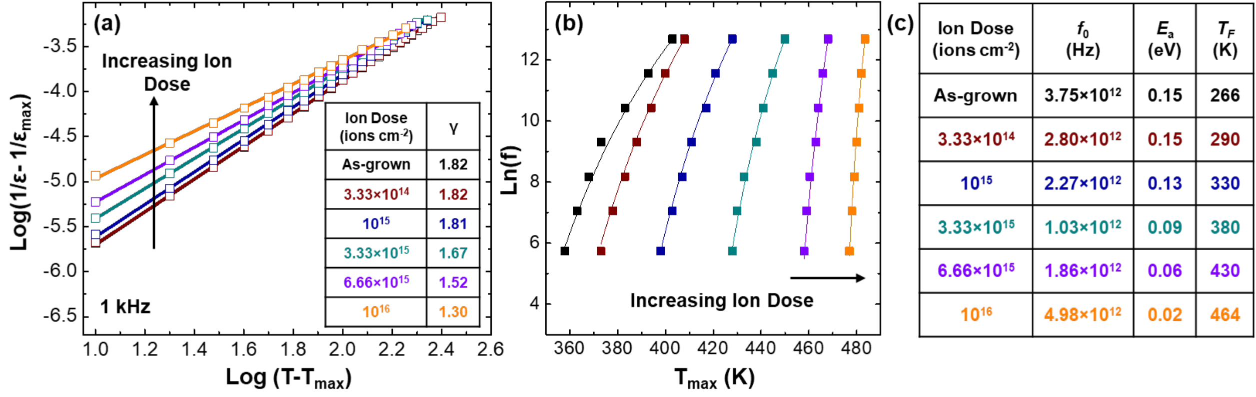

Ion Dose (ions cm^{-2})	f_0 (Hz)	E_a (eV)	T_F (K)
As-grown	3.75×10^{12}	0.15	266
3.33×10^{14}	2.80×10^{12}	0.15	290
10^{15}	2.27×10^{12}	0.13	330
3.33×10^{15}	1.03×10^{12}	0.09	380
6.66×10^{15}	1.86×10^{12}	0.06	430
10^{16}	4.98×10^{12}	0.02	464

Figure 9.6. (a) Plot of modified Curie-Weiss law ($log\left(\frac{1}{\varepsilon}-\frac{1}{\varepsilon_{max}}\right)$ *vs.* $log\,(T-T_{max})$) for heterostructures bombarded with various ion doses. The critical exponent γ is extracted from the slope of the linear fits (inset). (b) Vogel-Fulcher plot ($\ln(f)$ *vs.* T_{max}) for heterostructures bombarded with various ion doses. Solid squares and lines correspond to experimental data and fittings, respectively. (c) Vogel-Fulcher parameters extracted from fits of the experimental data for various ion doses.

$log\left(\frac{1}{\varepsilon}-\frac{1}{\varepsilon_{max}}\right)$ *vs.* $log\,(T-T_{max})$ (Figure 9.6a). For the as-grown heterostructures, $\gamma = 1.82$ which is indicative of strong relaxor character, and there is little change in γ up to 10^{15} ions cm^{-2}. At higher doses, γ systematically decreases with increasing dose and reaches $\gamma = 1.3$ for a dose of 10^{16} ions cm^{-2}. This reduction of γ above 10^{15} ions cm^{-2} correlates well with the onset of pinching and the dose-dependent increase of the width and shift of the hysteresis loops, and further supports the hypothesis that the formation and ordering of defect dipoles are responsible for suppression of polarization fluctuations, thus weakening the relaxor behavior.

In addition to deviation of the dielectric response from Curie-Weiss behavior, it is known that, due to the presence of dipolar correlations, the frequency dependence of T_{max} in relaxors deviates from the Arrhenius dependence expected for normal dielectrics [83,84]. It is generally observed that this dependence obeys an empirical Vogel-Fulcher relation which can be used to study cooperative thermal relaxation processes:

$$f = f_0\, exp^{\left(\frac{-E_a}{K_B(T_{max}-T_F)}\right)} \tag{9.3}$$

where f is the applied AC field frequency, f_0 is the limiting response frequency of the dipoles, and E_a is the activation energy [83,84]. Vogel-Fulcher fits were obtained from the temperature-dependent dielectric permittivity data (Figure 9.6b). The degree of relaxor behavior is represented by the curvature of the $\ln(f)$ *vs.* T_{max} plot, and is found to reduce with increasing ion dose as noted by the decreased T_{max} range and more linear and vertical Vogel-Fulcher curves. Values of T_F, E_a, and f_0 were extracted from the fits of the experimental data (Figure 9.6c). While f_0 values are similar and within a reasonable range for thermally-activated polarization fluctuations (10^{11}-10^{13} Hz) [83,84] at all doses, there is a systematic reduction of E_a and increase of T_F as the ion dose is increased. E_a is related to the energy required for a thermally-activated and cooperative transition between different polarization configurations and is, therefore, the product of the number of dipoles which are free to take part in the cooperative rearrangement and the chemical potential change associated with the reconfiguration [316]. The reduction of E_a with increasing defect concentration is, thus, consistent with the fact that ordering of special defect types (*i.e.*, defect dipoles) can stabilize the polarization direction, and therefore, reduce the number of lattice dipoles

that are free to fluctuate. This is also consistent with the dose-dependent increase of T_F which suggests that the suppression of polarization fluctuations occurs at higher temperatures as the ion dose increases. These observations further confirm the hypothesis that ordering of defect dipoles plays an important role in weakening the relaxor behavior.

9.4 Conclusions

This work demonstrates a weakening of the relaxor character as a result of the formation of *intrinsic* point defects in $0.68PbMg_{1/3}Nb_{2/3}O_3$-$0.32PbTiO_3$ thin films, despite a defect-induced increase of structural disorder. Formation and ordering of the defect dipoles are found to be responsible for the observed changes in macroscopic properties. Such ordered defects stabilize the direction of polarization against thermal fluctuations, and, in turn, weaken the relaxor behavior. This study, therefore, shows the complex effect of point defects in controlling the local (dis)order, and suggests that having the ability to carefully control both the concentration and type of point defects is instrumental in engineering relaxor materials.

CHAPTER 10

Summary of Findings and Suggestions for Future Work

10.1 Summary of Findings

In this Section, I summarize the main findings of the current work:

1- *Point defects are unavoidable*: Similar to any other material system, defects are unavoidable in complex-oxide ferroelectrics. This is in particular true for non-equilibrium growth processes such as pulsed-laser deposition, wherein, in addition to equilibrium defects, large concentrations of non-equilibrium defects can also be present. As discussed throughout this Thesis, formation of off-stoichiometric and/or stoichiometric displacement point defects (*i.e.*, *intrinsic* point defects) during the synthesis process is triggered by the ionic nature of these materials and requirements for charge neutrality, low formation energy of defects, presence of impurities and/or off-stoichiometry, and the presence of energetic adatom species which can displace the atoms from their lattice sites. As a result, regardless of our best efforts to minimize defect concentrations by optimizing the growth process, there are always finite concentrations of various structural and compositional defects even in the most "perfect" thin films. More importantly, I have shown that such defects are often undetectable using conventional techniques. Only focusing on the conventional techniques, all as-grown thin films studied in this work show signatures of "perfect," fully optimized ferroelectric thin films as perceived by our community (Chapters 5-9). They show nearly stoichiometric compositions (suggested by Rutherford backscattering spectrometry), and high crystalline quality (suggested by X-ray diffraction studies). This is while application of more advanced techniques such as deep-level transient spectroscopy suggests the presence of small concentrations of point defects in those nearly "ideal" thin films (Chapters 6 and 7). Add to this the large tolerance of the perovskite structure to the point defects and the difficulties in the detection of such defects become more apparent. Even in instances where chemical analysis shows large deviations from stoichiometric composition, the material is still highly crystalline with no signatures of the presence of secondary phases (Chapter 5).

2- *Materials with minimum defect concentrations are not always the best*: What is more important to note, however, is that such "ideal" thin films with a high degree of crystallinity and chemical stoichiometry often exhibit some of the least desirable properties. For example, nearly-stoichiometric highly-crystalline thin films often suffer from high electronic leakage and losses, which in turn, adversely impact their ferroelectric hysteresis response and precludes them from use in electronic devices (Chapters 5-7). This is shown to be related to the fact that these "ideal" films still contain small concentrations of *grown-in* point defects which can strongly impact the properties, while their concentration is too low to be detected using conventional techniques. In contrast, some of the highly defective thin films (containing larger concentrations of off-stoichiometric or stoichiometric displacement defects which give rise to deviations from ideal stoichiometry, lower crystalline qualities, and large lattice expansions) are shown to exhibit more desired properties such as orders of magnitude higher resistivities.

3- *Establishing routes for controlled and on-demand defect creation and defect characterization open up new avenues for the use of defects in ferroelectric materials control and design*: One

of the most important findings of this work is that defects in complex-oxide ferroelectrics (similar to most material systems) can have both positive and negative impact on the properties. Often, if defects are formed in an uncontrolled fashion during the synthesis process, they show detrimental impact on the materials properties. What turns defect into "magic" ingredients for making ferroelectric materials better and smarter is the ability to create them on-demand with control over their type, concentration, and location, and the ability to characterize the induced defects in order to understand their nature and their impact on materials response. In the present work, I have introduced various *in situ* and *ex situ* approaches for controlled defect creation. For example, I have shown that variations in laser fluence, laser-repetition rate, target composition, and growth pressure can be used to effectively control the type and concentration of *intrinsic* point defects (including off-stoichiometric and displacement defects) during the growth process (Chapters 5 and 6). I have also shown that we can implement in ferroelectric systems some of the defect-engineering approaches which are extensively used in other material systems. For example, I have introduced energetic ion bombardment (which is widely used in the semiconductor industry) as a practical technique to control the type and concentration, as well as position (through the use of focused ion beams), of point defects in complex-oxide ferroelectric thin films (Chapters 6-9). I have also introduced various characterization techniques such as advanced ferroelectric (*e.g.*, switching kinetics studies, first-order reversal curve analysis) and electrical (*e.g.*, impedance spectroscopy, deep-level transient spectroscopy) measurements, which, combined with more conventional techniques (*e.g.*, X-ray diffraction-based structural analysis, chemical analysis, scanning probe-based studies, and traditional electrical, dielectric and ferroelectric measurements) can provide a benchmark for gaining information regarding the nature of the induced defects. Use of such characterization techniques combined with the ability to control the type, concentration, and location of defects, in turn, provide valuable opportunities for systematic experimental studies of defect-structure-property relations in these complex materials.

4- *Defect-structure-property relations are strongly dependent on and can be controlled by the type and concentration of defects*: Using the established methods in this work for on-demand defect creation, I have systematically probed the impact of defects on various materials properties as a function of defect type and across many orders of magnitude of defect concentration.

Transport properties: I have shown that transport properties are sensitive to the defects. Defects can directly impact both the conduction mechanism and magnitude in these systems. In $BiFeO_3$, for example, it was shown that depending on the type and concentration of off-stoichiometric point defects the conduction mechanism can change between interface-limited Schottky emission, and bulk-limited classic and modified Poole-Frenkel emissions, with slight variations in the magnitude of leakage current (Chapter 5). On the other hand, the conduction in $BaTiO_3$ heterostructures in the presence of various types and concentrations of off-stoichiometric defects, and in nearly stoichiometric $PbTiO_3$ and $BiFeO_3$ heterostructures in the presence of various types and concentrations of bombardment-induced defects, are shown to be governed by classic or modified Poole-Frenkel emissions. Although no change in the conduction mechanism is detected, orders of magnitude reduction in the magnitude of leakage current density is achieved by increasing the defect concentration. For example, in barium titanate thin films (Chapter 5), a growth-induced change of composition from $Ba_{1.00}TiO_{3.00}$ to $Ba_{0.93}TiO_{2.87}$ is shown to reduce the leakage current density by ≈ 3 orders of magnitude through formation of compensating off-stoichiometric defects. In the case of lead titanate thin

films (Chapter 6), I have shown highly-crystalline, perfectly stoichiometric $Pb_{1.00}Ti_{1.00}O_x$ thin films which suffer from crippling leakage and losses. A reduction in leakage current density is shown, by almost ≈ 3 orders of magnitude, via introduction of growth-induced (*in situ*) displacement defects (films remain nearly stoichiometric $Pb_{1.01}Ti_{1.00}O_x$), and by up to $\approx$ 5 orders of magnitude via introduction of ion-beam-induced (*ex situ*) displacement defects (films remain nearly stoichiometric $Pb_{1.00}Ti_{1.00}O_x$). Similarly, in bismuth ferrite thin films (Chapter 7), *ex situ* ion bombardment is shown to reduce the leakage current density in nearly stoichiometric $Bi_{0.99}Fe_{1.00}O_x$ thin films by up to ≈ 4 orders of magnitude (the chemistry does not change upon ion bombardment). Such dramatic changes in the leakage current density is shown to be related to a change in the type of the dominant defects as the defect concentration is increased. At low defect concentrations (*i.e.*, in the as-grown films) the dominant defects are isolated point defects with energy levels close to the band edges (*i.e.*, shallow-trap states) which can be readily ionized at room temperature, dope the lattice with electrons/holes, and give rise to high electronic conduction. At higher defects concentrations, however, there is a higher probability for such isolated point defects to turn into complexes and clusters which often create deeper trap states in the band gap, and in turn, reduce the electronic conduction by trapping free charge carriers.

Ferroelectric switching properties: In the present work, I have shown that point defects can impact ferroelectric-switching properties, and experimentally demonstrated that the strength of such defect-polarization interactions is directly related to the type and concentration of point defects. In barium titanate thin films, for example, a change in the chemistry from $BaTiO_3$ to $Ba_{0.93}TiO_{2.87}$ is shown to give rise to emergence of large imprint (shifted loops) and hysteresis-loop pinching, which is attributed to the formation of $V_{Ba}'' - V_O^{\bullet\bullet}$ defect-dipoles in the presence of high cation and anion off-stoichiometries (Chapter 5). In bismuth ferrite thin film, the most bismuth-deficient heterostructures ($Bi_{0.90}Fe_{0.98}O_{2.49}$) are shown to exhibit the largest coercive field values compared to other chemistries, attributed to pinning of domain walls by defects in the presence of large off-stoichiometric defect concentrations (Chapter 5). On the other hand, I have demonstrated that increasing the concentration of bombardment-induced defects in nearly stoichiometric $BiFeO_3$ thin films, while having no evident impact on the domain structure or the switching mechanism (creep motion is the dominant mechanism in all cases), does give rise to a systematic increase in the coercive field of switching, extension of the defect-related creep regime to higher electric fields, an increase in the pinning activation energy, a decrease in the switching speed, and broadening of the field distribution of switching (Chapter 7). Finally, in $PbZr_{0.2}Ti_{0.8}O_3$ thin films, I have shown that interactions between defects and domain walls give rise to systematic changes in the coercive field of switching and imprint characteristics (Chapter 8). I have shown that at intermediate defect concentrations isolated-point defects and small clusters are the dominant defects. Such defects are shown to have a weak interaction with the domain walls (pinning potentials from 200-500 K MV cm^{-1}), giving rise to a relatively small and symmetric increase in the coercive field with no electrical imprint and no reduction of polarization. At higher defect concentrations, I have shown that larger complexes and clusters become dominant. Such defects are shown to strongly pin the domain-wall motion (pinning potentials from 500-1600 K MV cm^{-1}), giving rise to a large increase in the coercive field and a preferred polarization direction (manifested as an electrical imprint and a reduction in the polarization).

Relaxor properties: In addition to classical ferroelectric systems, I have also studied the impact of point defects on the properties of relaxor ferroelectric systems such as

$0.68PbMg_{1/3}Nb_{2/3}O_3$-$0.32PbTiO_3$ thin films (Chapter 9). I have shown that defects play a complex role in controlling the local (dis)order, and hence, the properties of these systems. I have demonstrated a weakening of the relaxor character (*i.e.*, a systematic increase of T_{max}, and reduction in frequency dispersion of the dielectric response below T_{max}) as a result of the formation of bombardment-induced *intrinsic* point defects. Although increasing the concentration of such defects increases the structural disorder of the system by displacing the atoms from their ideal lattice sites, special types of defects that are created (*i.e.*, defect dipoles) and their ordering are shown to be responsible for weakening of the relaxor character by stabilizing the direction of polarization against thermal fluctuations (manifested as an increase in the width and shift of the hysteresis loops and appearance of slight loop-pinching).

5- *Having the ability to control defects and understand defect-structure-property relations enables utilization of defects in our advantage to achieve improved properties and performance and/or engineer novel functions:* For example, the presence of high electronic leakage in ferroelectric thin films has been one of the long-lasting issues in the use of such materials in electronic devices. In the present work, I have demonstrated some of the most resistive versions of ferroelectric thin films via defect engineering (Chapters 5-7). I have also shown dramatic improvements in ferroelectric-hysteresis measurements without suppression of polarization values as a result of defect-induce enhancement in resistivity of the thin films. Finally, I have shown that the ability to deterministically create and spatially locate point defects through the use of focused ion beams allows for engineering new functionalities (Chapter 8). In particular, by confining the impact of bombardment-induced defects to select regions defined by the ion beam, I have demonstrated tunable multiple polarization states in a bistable ferroelectric such as $PbZr_{0.2}Ti_{0.8}O_3$, rewritable pre-determined 180° ferroelectric domain patterns, and multiple, zero-field piezoresponse and permittivity states which can opens up new pathways to achieve multilevel data storage and logic, nonvolatile self-sensing shape-memory devices, and nonvolatile ferroelectric field-effect transistors.

10.2 Suggestions for Future Work

In this Section, I suggest a few directions for future investigations as follow-up for the current Thesis:

1- *On-demand defect creation:* In the present work, I have only focused on the use of helium-ion beams with fixed energies for creation of bombardment-induced damage in complex-oxide ferroelectric thin films. Further investigation, however, is required to develop a more detailed understanding of how the type and energy of incident ions impact the nature of defects and damage profiles, thermal stability of defects, critical dose for amorphization, and defect-induced evolution of structure and properties in these complex materials.

Additionally, in this work, I have only focused on the creation of *intrinsic* bombardment-induced defects without changing the overall chemistry of the thin films. It was also shown that small deviations from stoichiometric composition and creation of small concentrations of off-stoichiometric point defects can be achieved via variations of growth parameters, while the concentration of such defects was shown to be strictly limited by the growth conditions. It is, however, possible to largely alter the chemistry of these films by carefully choosing the type and energy of the ions used for ion bombardment. In the current work I have used high ion energies to avoid ion implantation in the ferroelectric thin films. Even when a focused-ion beam with a low energy was used, the implantation resulted in small concentrations of inert helium ions. By using lower-ion energies, however, it is possible to implant various species

into the ferroelectric thin films and systematically alter their concentration with a large degree of freedom. Such ion implantations should typically be followed by annealing steps in order to move the implanted ions into the lattice sites. One interesting experiment, for example, would be to perform ion implantation procedures aimed to change the stoichiometry of the films on demand. For instance, can we use oxygen-ion implantation to "correct" the oxygen off-stoichiometry which is often present in complex-oxide ferroelectric thin films? Similarly, can we design implantation processes in order to tune the cation off-stoichiometry?

In addition to implantation with constituent elements of the ferroelectric thin films, it is also of interest to implant certain foreign elements in order to dope or alloy the system through cation substitution, and to study the induced changes in materials response. While chemical doping using ion beams is extensively used in other materials systems such as semiconductors [317], it has not been widely applied to ferroelectric systems. In addition to cation substitution, it is also of great interest to explore the possibility of anion substitution in complex-oxide ferroelectric thin films via ion implantation. Although chemical tuning of properties by cation doping is extensively studied, anion substitution has been much less investigated due to the high stability of the cation-oxygen bonds that makes the synthesis of anion-substituted perovskites less straightforward [318]. Such anion substitutions, however, can strongly alter the properties of perovskites due to different charges and differences in the ionicity of the metal-anion bonds [319]. Oxygen substitution in transition-metal oxides with nitrogen and sulfur giving rise to oxynitrides ($ABO_{3-x}N_x$) and oxysulfides ($ABO_{3-x}S_x$), for example, has gained a lot interest in recent years because of the novel properties of such materials including electronic and ionic conductivity, catalytic activity, dielectric, magneto-resistive, and optical properties, resulting from changes in the electronic structure of the material, concomitant interactions between oxygen and nitrogen ions, and difference in geometrical configuration of oxygen and nitrogen ions around cations [318-321]. The synthesis of such materials, however, is proven to be challenging and commonly achieved through treatment of mixtures of reactants or oxide precursors in ammonia gas at high temperature ($\approx$ 1000°C) [319]. Use of ion implantation for anion substitution, therefore, can be an efficient alternative method for synthesis of such materials. Moreover, there is limited work in the literature showing the potential for synthesis and realization of novel properties in oxynitrides and oxysulfides based on ferroelectric complex-oxides such as $PbTiO_3$ and $BaTiO_3$ [320,321]. Nitrogen and sulfur implantation in ferroelectric complex-oxide thin films, therefore, is of great interest.

Finally, in the current work I have only focused on single ion-bombardment processes. While a spatial control over the position of defects is demonstrated by using focused ion beams, no attempts have been made to control and design the depth profile and distribution of the ions and resultant defects. The depth distribution of implanted ions and induced defects can be carefully engineered by tuning the ion energy and type and using multiple ion-implantation/bombardment schemes as opposed to single-ion and single-energy processes. Such approaches are commonly used in semiconductor industry to engineer the depth distribution of the implants [157]. Using similar approaches in ferroelectric thin films can provide a much broader phase space for materials design. For example, using such approaches one can design defect gradients or chemical gradients across the thickness of the films. Such gradients are not limited to the concentration of defects or implanted ions, and can also include gradients in the type of defects or implanted ions, and can be used to engineer complex damage and/or chemistry profiles.

2- *Defect characterization*: As mentioned throughout this Thesis, characterization of point defects in complex-oxide ferroelectric thin films is an extremely challenging task, specifically in the presence of small defect concentrations, and due to the tolerance of perovskite structure to defect formation. The current work only began to establish routes to gain more information on the nature of point defects. The knowledge gained from this work regarding the exact nature of induced defects, however, is still limited, and calls for future studies. This work relied on using a combination of different techniques with an attempt to gather small pieces of information from each technique to build an overall image and an indirect understanding of the nature of defects. The current work mostly focused on indirect methods to characterize the defects based on their impact on macroscopic properties. The use of common electrical defect-characterization techniques such as Hall, Seebeck, and capacitance-voltage measurements, and spectroscopic techniques such as impedance spectroscopy, deep-level-transient spectroscopy, thermally-stimulated-current spectroscopy have been proven to be very challenging due to the high resistivity of these insulating materials and subsequently small electrical signals (*i.e.*, high noise-to-signal ratios) extracted from such measurements. Chemical analyses and direct imaging of point defects in these complex systems using high-resolution microscopy techniques have been also proven to be difficult and rather unsuccessful due to the often-low concentrations of point defects. Everyday advances in development of more sophisticated and advanced characterization techniques, and fast progress in developing more-precise, sensitive, and efficient instrumentations, combined with rapid improvements in processing methods with the ability to control chemistry and structure on a near-atomic scale, and improved computational tools with considerably more realistic modeling capabilities, however, will enable more careful studies of the nature of point defects in these complex systems in the near future, which is of great scientific and technological importance.

3- *Fundamental studies of defect-structure-property relations:* In the current work, I have only focused on the interactions of point defects with a few properties of complex-oxide ferroelectric thin films (mainly electronic transport and ferroelectric switching properties). In order to build a more comprehensive understanding of defect-structure-property relations and to use defects as design parameters in engineering the response of these multifunctional materials, it is important to also understand how such defects impact other relevant materials properties such as ionic transport, thermal, dielectric, elastic, pyroelectric, piezoelectric, thermoelastic, optical, magnetic, and *etc*. properties. The *in situ* and *ex situ* defect-engineering methodologies established in this work can be used as a roadmap for such studies.

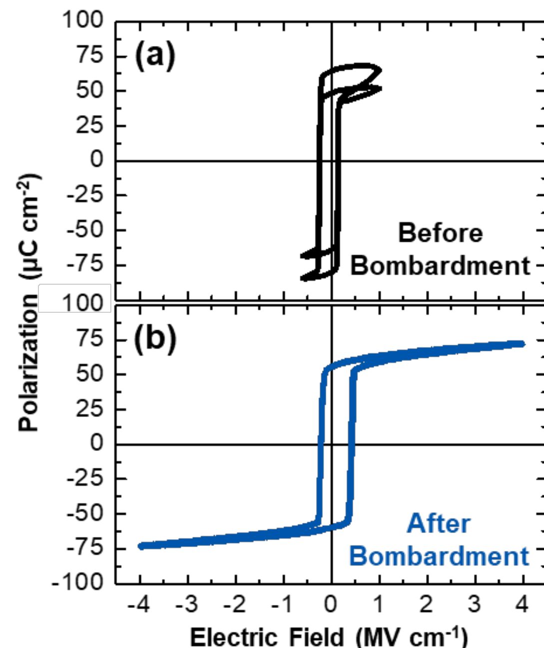

Figure 10.1. Polarization-electric field hysteresis loops obtained from a $PbZr_{0.2}Ti_{0.8}O_3$ thin film in the (a) as-grow state, and (b) after high-energy helium-ion bombardment to a dose of 3.3×10^{15} ions cm^{-2}.

4- *Engineering new functionalities*: The current work only began to use defect-property couplings and the ability to control the type,

concentration, and location of defects, in order to demonstrate the potential of defect engineering for realizing novel functions in complex-oxide ferroelectric thin films. There is still immense amount of opportunities to explore this material's design space, and to fully exploit the power of defects in engineering of ferroelectric materials. Here, I propose a few ideas among many more which can be explored in the future.

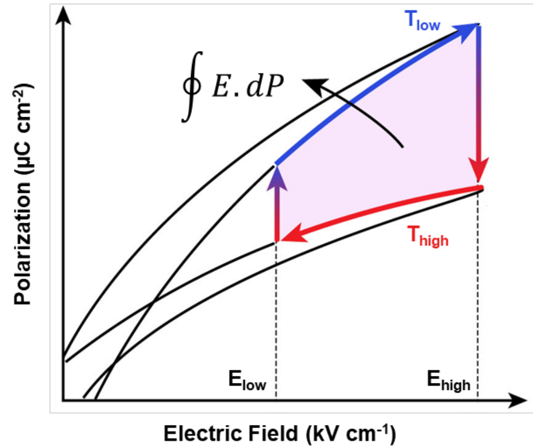

Figure 10.2. A schematic of a pyroelectric Olsen cycle showing various isothermal and isoelectric processes.

Enhancement of pyroelectric energy conversion via defect engineering: In the current work, I have shown that bombardment-induced defects can enhance the resistivity of ferroelectric thin films by orders of magnitude. My preliminary work on $PbZr_{0.2}Ti_{0.8}O_3$ thin films has shown that as a result of such enhanced resistivities, the thin films can withstand large magnitudes of external electric fields unattainable even in the most resistive non-defective as-grown ferroelectric films (Figure 10.1). The large magnitude of electric field which can be applied to the defective films can enable large enhancements in the pyroelectric energy conversion density and efficiency. Pyroelectric energy conversion is often achieved through an Olsen cycle (an adaptation of the Ericsson cycle) [322-324], which includes two isothermal and two isoelectric processes (Figure 10.2). In an Olsen cycle, the total energy density per cycle is given by the area of the closed loop (shaded region, Figure 10.2), which can be increased by increasing the upper limit of the electric field.

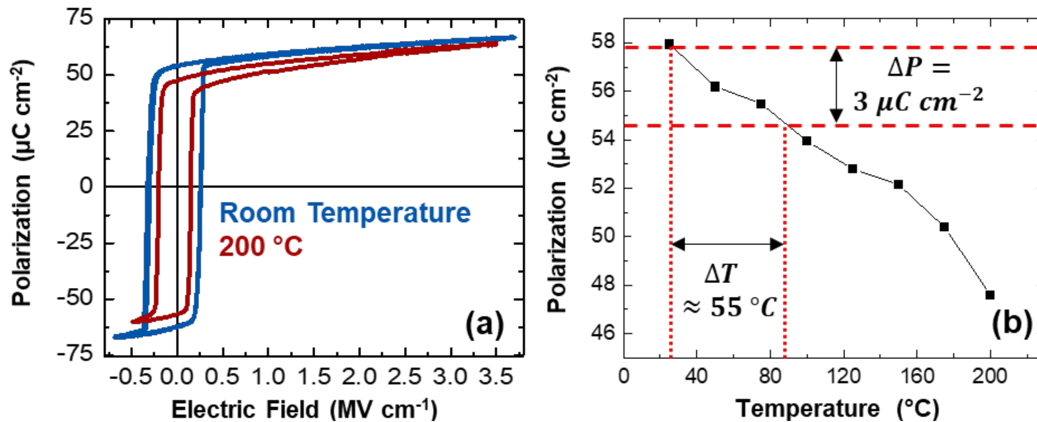

Figure 10.3. Ferroelectric polarization-electric field hysteresis loops as a function of temperatures, and (b) saturation polarization as a function of temperature for a $PbZr_{0.2}Ti_{0.8}O_3$ thin film.

My preliminary temperature-dependent measurements of ferroelectric hysteresis loops on ion-bombarded $PbZr_{0.2}Ti_{0.8}O_3$ thin films (Figure 10.3) suggest that the defect-induced high resistivity is stable up to 200°C, and that a temperature change of ≈ 55°C in such bombarded thin films gives rise to a polarization change of ≈ 3 μC cm^{-2}. Given a maximum electric field of 3.5 MV cm^{-1} which can be applied to these heterostructures, an energy density of ≈ 10 J cm^{-3} and a scaled efficiency of ≈ 30% are envisioned, which are dramatically larger than the values

reported to date [325]. To demonstrate such enhanced values, pyroelectric energy conversion measurements need to be completed on such ion-bombarded thin films.

Multi-state switching process via stress-induced movement of defects: In the current work, I have shown multi-state switching processes in bistable ferroelectrics by local control of position of point defects via application of focused-ion beams. A potential alternative route to such multistate operations would be to locally change the nature of switching by application of a local mechanical stress (using a scanning-probe tip, for example) to control the location of defects in accordance with Vegard's effect [326,327]. An equilibrium polarization and domain configuration can be achieved in the presence of a given defect concentration, and the polarization can be switched by application of an electric field. Application of a local mechanical stress, on the other hand, can drive defects to either preferentially exit or enter the regions affected by the mechanical stress. As I have shown in this work, local changes in the defect concentration (here proposed to be achieved via application of local stresses) can locally alter the energy requirement and speed of switching. As a result, a right combination of electric field and mechanical stress can result in switching to a partially-poled stable intermediate state, or complete switching followed by partial relaxation due to redistribution of the defects. A systematic study of how mechanical stress can impact the movement of defects (produced with different types and concentrations) and local polarization switching in complex-oxide ferroelectric thin films is required in order to examine the feasibility of this idea.

APPENDIX A

Pulsed-Laser Deposition of Ferroelectric Thin Film Heterostructures

All parameters involved in pulsed-laser deposition were carefully optimized for every ferroelectric material system used in this work in order to achieve desired composition, phases, and morphologies. The optimized parameters for each material system are provided in the following and summarized in Table A.1.

A.1 Growth of $BaTiO_3$ Heterostructures

100 nm $BaTiO_3$ thin films were grown on 30 nm $SrRuO_3/GdScO_3$ (110) substrates. The $SrRuO_3$ bottom electrodes were grown from a $SrRuO_3$ ceramic target at a heater temperature of 700°C in a dynamic-oxygen pressure of 100 mTorr, with a laser fluence of 1.1 J cm^{-2}, and at a laser-repetition rate of 15 Hz. The $BaTiO_3$ films were grown from a $BaTiO_3$ ceramic target at a heater temperature of 600°C in a dynamic-oxygen pressure of 40 mTorr and at a laser-repetition rate of

Table A.1. Summary of optimized growth conditions for various materials used in this work.

Substrate	$GdScO_3$ (110)		$SrTiO_3$ (001)		$SrTiO_3$ (001)		$DyScO_3$ (110) $LaAlO_3$ (001) 0.5% Nb:$SrTiO_3$ (001)		$NdScO_3$ (110)	
Bottom Electrode/ Film	$SrRuO_3$	$BaTiO_3$	$SrRuO_3$	$PbTiO_3$	$SrRuO_3$	$PbZr_{0.2}Ti_{0.8}O_3$	$SrRuO_3$	$BiFeO_3$	$Ba_{0.5}Sr_{0.5}RuO_3$	$0.68PbMg_{1/3}Nb_{2/3}O_3$ $-0.32PbTiO_3$
Thickness (nm)	30	100	20	140	20	60	30	100	25	55
Temperature (°C)	700	600	690	675	690	650	645	700	750	600
Pressure (mTorr)	100	40	100	50 200	100	200	100	100	20	200
Laser-Repetition Rate (Hz)	15	2	14	2 15	15	3	17	8-20	3	2
Laser Fluence (J cm^{-2})	1.1	1.25 1.45 1.65	1.3	1.9	1.3	1.0	1.2	1.1	1.85	1.8

2 Hz. In order to study the effect of laser fluence on the defects, chemistry, and structure of $BaTiO_3$, thin films with laser fluences of 1.25, 1.45, and 1.65 J cm^{-2} were grown. The laser fluence was varied by increasing the energy of the laser pulse while maintaining the spot size. Top $SrRuO_3$ electrodes with a thickness of 50 nm were grown using the *ex situ* technique.

A.2 Growth of $PbTiO_3$ Heterostructures

140 nm $PbTiO_3$ thin films were grown on 20 nm $SrRuO_3/SrTiO_3$ (001) substrates. The $SrRuO_3$ bottom electrodes were grown from a $SrRuO_3$ ceramic target at a heater temperature of 690°C in a dynamic oxygen pressure of 100 mTorr at a laser-repetition rate of 14 Hz and a laser fluence of 1.3 J cm^{-2}. The $PbTiO_3$ films were grown from a $Pb_{1.1}Ti_{1.0}O_3$ ceramic target. The excess lead content in the target was used to compensate for the loss of volatile lead during the high-temperature growth. The growth was done at a heater temperature of 675°C and a laser fluence of 1.9 J cm^{-2}. In order to study the effect of growth pressure on the defects and structure of $PbTiO_3$, the films were grown at dynamic oxygen pressures of 200 mTorr and 50 mTorr at a laser-repetition rate of 15 and 2 Hz, respectively, in order to maintain the cation ratio as close as possible to the stoichiometric composition. A third variant of $PbTiO_3$ films were grown at a total pressure of 200 mTorr, but with a mixture of 50 mTorr of oxygen and balance argon to explore the role of lower oxidative potential, but higher deposition pressures. All other conditions were the same as the 200 mTorr growth in pure oxygen. Top $SrRuO_3$ electrodes with a thickness of 80 nm were grown using the *ex situ* technique.

A.3 Growth of $PbZr_{0.2}Ti_{0.8}O_3$ Heterostructures

60 nm $PbZr_{0.2}Ti_{0.8}O_3$ films were grown on 20 nm $SrRuO_3/SrTiO_3$ (001) substrates. The bottom $SrRuO_3$ electrodes were grown from a $SrRuO_3$ ceramic target at a temperature of 690°C in a dynamic oxygen pressure of 100 mTorr at a laser-repetition rate of 15 Hz and a laser fluence of 1.3 J cm^{-2}. The $PbZr_{0.2}Ti_{0.8}O_3$ films were grown from a $Pb_{1.1}Zr_{0.2}Ti_{0.8}O_3$ ceramic target at a temperature of 650°C in a dynamic oxygen pressure of 200 mTorr at a laser-repetition rate of 3 Hz, and a laser fluence of 1.0 J cm^{-2}. The excess lead content in the $Pb_{1.1}Zr_{0.2}Ti_{0.8}O_3$ target was used to compensate for the loss of volatile lead during the high-temperature growth. Top $SrRuO_3$ electrodes with a thickness of 60 nm were grown using the *ex situ* technique.

A.4 Growth of $BiFeO_3$ Heterostructures

100 nm $BiFeO_3$ thin films were grown on 30 nm $SrRuO_3/DyScO_3$ (110) and $LaAlO_3$ (001) and 0.5% Nb:$SrTiO_3$ (001) substrates. The bottom $SrRuO_3$ electrodes were grown from a $SrRuO_3$ ceramic target at a heater temperature of 645°C, in a dynamic oxygen pressure of 100 mTorr, with a laser fluence of 1.2 J cm^{-2}, and a laser-repetition rate of 17 Hz. The $BiFeO_3$ films were grown at a heater temperature of 700°C, in a dynamic oxygen pressure of 100 mTorr, with a laser fluence of 1.1 J cm^{-2}. The $BiFeO_3$ films were grown as a function of laser-repetition rate ranging from 8 to 20 Hz from ceramic targets of various compositions including $Bi_{1.1}FeO_3$, $Bi_{1.2}FeO_3$, or $Bi_{1.3}FeO_3$, in order to study the effect of laser-repetition rate and target chemistry on the defects, chemistry, and structure of the $BiFeO_3$. To maintain consistency upon changing the laser-repetition rate and target chemistry, 57,600 laser pulses were used to produce all $BiFeO_3$ heterostructures studied herein with a thickness of $\approx$100 nm. The $BiFeO_3$ films grown at a laser-repetition rate of 20 Hz,

from $Bi_{1.1}Fe_{1.0}O_3$ ceramic targets were also used for subsequent *ex situ* ion bombardment experiments. Top $SrRuO_3$ electrodes with a thickness of 80 nm were grown using the *ex situ* technique.

A.5 Growth of $0.68PbMg_{1/3}Nb_{2/3}O_3$-$0.32PbTiO_3$ Heterostructures

55 nm $0.68PbMg_{1/3}Nb_{2/3}O_3$-$0.32PbTiO_3$ thin films were grown on 25 nm $Ba_{0.5}Sr_{0.5}RuO_3$/$NdScO_3$ (110) substrates. The $Ba_{0.5}Sr_{0.5}RuO_3$ bottom electrodes were grown from a $Ba_{0.5}Sr_{0.5}RuO_3$ ceramic target at a temperature of 750°C in a dynamic-oxygen pressure of 20 mTorr at a laser-repetition rate of 3 Hz, and a laser fluence of 1.85 J cm^{-2}. The $0.68PbMg_{1/3}Nb_{2/3}O_3$-$0.32PbTiO_3$ films were grown from $0.68PbMg_{1/3}Nb_{2/3}O_3$-$0.32PbTiO_3$ ceramic targets at a temperature of 600°C in a dynamic-oxygen pressure of 200 mTorr at a laser-repetition rate of 2 Hz, and a laser fluence of 1.8 J cm^{-2}. Top $Ba_{0.5}Sr_{0.5}RuO_3$ electrodes with a thickness of 100 nm were grown using the *in situ* technique.

APPENDIX B

Band Excitation Piezoresponse Spectroscopy – Loop Fitting

Piezoresponse force microscopy has historically relied on periodically applying a single frequency excitation to the cantilever at the cantilever resonance to amplify the cantilever response and probe the sample. This single-frequency approach is limited by the assumption that the cantilever behaves as a simple harmonic oscillator. When operated at a single frequency, the resonance (a function of the tip-surface spring constant), quality factor of the resonance (function of tip-surface dissipation), and amplitude of the response can become tangled in the tip-surface interactions.

In order to bypass the frequency limitations and improve the accuracy of the measured piezoresponse while unpredictable changes in cantilever dynamics occur, it becomes necessary to apply a large bandwidth signal near the cantilever resonance. Band excitation piezoresponse force microscopy achieves this large bandwidth by applying a computer-generated waveform that spans several frequencies around the cantilever resonance. The waveform electrically perturbs the material, and the cantilever response is measured with a high-speed data acquisition system. The signal is then Fourier transformed into frequency space, and with the assumption that the tip-sample interaction is small, the amplitude (A) and phase (θ) are fit to a simple harmonic oscillator model as:

$$A(\omega) = \frac{A_0\omega_0^2}{\sqrt{(\omega^2-\omega_0^2)^2+(\omega\omega_0/Q)^2}}, \tag{B.1}$$

$$\tan\big(\theta(\omega)\big) = \frac{\omega\omega_0/Q}{\omega^2-\omega_0^2} \tag{B.2}$$

where A_0 and ω_0 are the amplitude and frequency at resonance, and Q is the quality factor. Once the fitting is complete, and the error of the fitting is established, the data yields two-dimensional maps of resonance amplitude, resonance frequency, quality factor, and phase of the response. When carefully applied, band excitation piezoresponse force microscopy enables the exclusion of position-dependent changes in cantilever resonance, minimizing the tip-surface interactions.

Additionally, one is able to increase the dimensionality of band excitation measurements, further increasing insight into the material. With the addition of a DC voltage (V_{DC}) to the measurement, local piezoelectric hysteresis loops can be measured. In order to achieve this, a $n \times n$ grid is superimposed on the scanned region of interest (Figure B.1a). At each point on the grid, a full bipolar triangular switching waveform signal is applied to the cantilever and its response is measured in the off-state by superimposing a band-excitation waveform as a sense pulse (Figure B.1b-d). In this work this process is done within 5 ms. Once the data is acquired, it is fit via the simple harmonic oscillator model (Figure B.1e), providing data in the form $\{A_0,\omega_0,Q,\theta\}(x,y,V_{DC})$. The rotation angle ($\varphi$) is adjusted in order to maximize the real component of the hysteresis loop mixed signal ($A_0 cos\varphi$), thereby generating local piezoelectric hysteresis loops of the same general form as the macroscopic ferroelectric hysteresis loops (Figure B.1f).

The piezoresponse is intentionally reported in arbitrary units. This is due to measuring the cantilever deflection via the beam bounce approach. In this approach the angular displacement of the laser reflection is measured in lieu of the vertical displacement by the photodiode. The conversion from angular to vertical displacement requires assumptions to be made. While

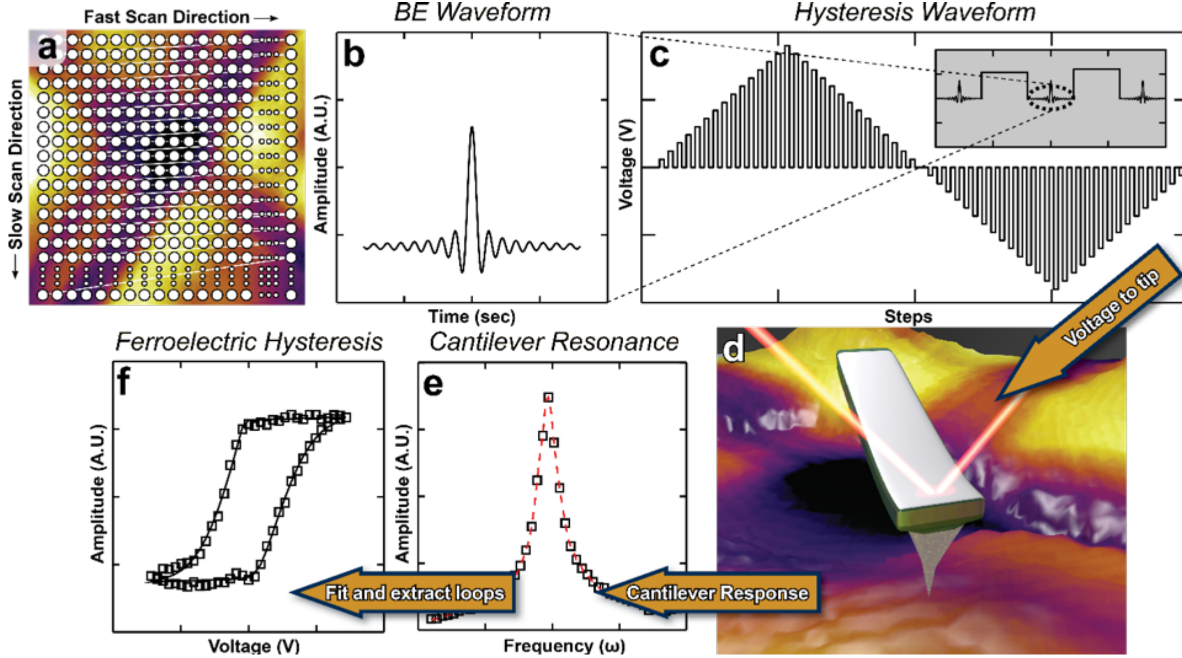

Figure B.1. Schematic illustration of work flow for band excitation piezoresponse spectroscopy. (a) Schematic of the sampling, and fast and slow scan direction used for imaging. (b) Example of band excitation chirp waveform in time domain used to excite the tip at a range of frequencies. (c) Triangular switching waveform used to locally switch the film. (d) Schematic drawing of a cantilever in contact with surface. (e) Typical cantilever resonance response shown in frequency domain. Red dashed line shows the fit, based on Equations B.1 and B.2. (f) Typical piezoelectric hysteresis loop obtained from band excitation piezoresponse spectroscopy.

relatively accurate in air, the assumptions result in significant error when the cantilever is in contact with the surface. Therefore, the measured piezoresponse can vary by orders of magnitude depending on the laser spot position and cantilever resonance.

As mentioned above, the measured input data can be used to form a local piezoelectric hysteresis loop by maximizing $Acos\varphi$, with the choice of the rotation angle. After the piezoresponse hysteresis loops are obtained, the top and bottom branches of the loop are isolated and fit using the following equations:

$$\sigma_1 = \left(\frac{b_1+b_2}{2}\right) + \left(\frac{b_2-b_1}{2}\right) \mathrm{erf}\left(\frac{V_{DC}-b_7}{b_5}\right), \tag{B.3}$$

$$\sigma_2 = \left(\frac{b_4+b_3}{2}\right) + \left(\frac{b_3-b_4}{2}\right) \mathrm{erf}\left(\frac{V_{DC}-b_8}{b_6}\right), \tag{B.4}$$

$$\Gamma_1 = \left(\frac{a_1+a_2}{2}\right) + \left(\frac{a_2-a_1}{2}\right) \mathrm{erf}\left(\frac{V_{DC}-E_C^-}{\sigma_1}\right) + a_3 V_{DC} \quad (Upper\ Branch), \tag{B.5}$$

$$\Gamma_2 = \left(\frac{a_1+a_2}{2}\right) + \left(\frac{a_2-a_1}{2}\right) \mathrm{erf}\left(\frac{V_{DC}-E_C^+}{\sigma_2}\right) + a_3 V_{DC} \quad (Lower\ Branch), \tag{B.6}$$

where b_{1-4} control the sharpness of the corners of the loops (as $b \to 0$ the angle of the corner approaches 90°), b_{5-6} control the transition rate from b_1 to b_2, and b_3 to b_4, respectively, b_{7-8} locate the midpoint of the transition from b_1 to b_2, and b_3 to b_4, a_{1-2} represent the bottom and top saturation amplitudes, and a_3 represents the linear contribution. These equations are derived due to the ability to represent the loop shape and the inclusion of empirical parameters that correlate to common loop features.

REFERENCES

[1] N. Setter, D. Damjanovic, L. Eng, G. Fox, S. Gevorgian, S. Hong, A. Kingon, H. Kohlstedt, N. Y. Park, G. B. Stephenson, I. Stolitchnov, A. K. Taganstev, D. V. Taylor, T. Yamada, S. Streiffer, *J. App. Phys*. **2006**, *100*, 051606.

[2] M. Dawber, K. M. Rabe, J. F. Scott, *Rev. Mod. Phys.* **2005**, *77*, 1083.

[3] D. G. Schlom, L. Q. Chen, C. B. Eom, K. M. Rabe, S. K. Streiffer, J. M. Triscone, *Annu. Rev. Mater. Res.* **2007**, *37*, 589.

[4] L. W. Martin, Y.-H. Chu, R. Ramesh, *Mat. Sci. Eng. R.* **2010**, *68*, 89.

[5] L. W. Martin, A. M. Rappe, *Nat. Rev. Mater.* **2016**, *2*, 16087.

[6] S. A. Chambers, *Surf. Sci. Rep.* **2000**, *39*, 105.

[7] L. W. Martin, R. Ramesh, *Acta Mater.* **2012**, *60*, 2449.

[8] D. G. Schlom, *APL Mater.* **2015**, *3*, 062403.

[9] B. Jaffe, W. R. Cook, H. Jaffe, *Piezoelectric Ceramics*, Academic Press, New York, USA **1971**.

[10] L. E. Cross, R. E. Newnham, *History of Ferroelectrics, Ceramics and Civilization, Vol. III,* The American Ceramic Society, Ohio, USA **1987**.

[11] L. E. Cross, *Ferroelectric Ceramics*, Birkhäuser, Basel, Switzerland **1993**.

[12] D. Damjanovic, *Rep. Prog. Phys.* **1998**, *61*, 1267.

[13] Y. Kobayashi, S. Endo, K. Deguchi, L. C. Ming, G. Zou, *Solid State Commun.* **2001**, *120*, 515.

[14] A. R. Damodaran, J. C. Agar, S. Pandya, Z. Chen, L. Dedon, R. Xu, B. Apgar, S. Saremi, L. W. Martin, *J. Phys. Condens. Matter* **2016**, *28*, 263001.

[15] J. C. Agar, S. Pandya, R. Xu, A. K. Yadav, Z. Liu, T. Angsten, S. Saremi, M. Asta, R. Ramesh, L. W. Martin, *MRS Commun.* **2016**, *6*, 151.

[16] Z. Syrowiak, Y. S. Nikitin, E. V. Svirdov, V. M. Mukhortov, V. P. Dudkevich, *Izv. Akad. Nauk SSSR* **1991**, *55*, 500.

[17] B.-D. Qu, W.-L. Zhong, P.-L. Zhang, *J. Phys. Condens. Matter* **1994**, *6*, 1207.

[18] M. Demartin, D. Damjanovic, *Appl. Phys. Lett.* **1996**, *68*, 3046.

[19] N. A. Pertsev, A. G. Zembilgotov, A. K. Tagantsev, *Phys. Rev. Lett.* **1998**, *80*, 1988.

[20] V. G. Koukhar, N. A. Pertsev, R. Waser, *Phys. Rev. B* **2001**, *64*, 214103.

[21] V. G. Kukhar, N. A. Pertsev, H. Kohlstedt, R. Waser, *Phys. Rev. B* **2006**, *73*, 214103.

[22] T. Ohnishi, K. Shibuya, T. Yamamoto, M. Lippmaa, *J. Appl. Phys.* **2008**, *103*,103703.

[23] S. Saremi, R. Gao, A. Dasgupta, L. W. Martin, *Am. Ceram. Soc. Bull.* **2018**, *97*, 16.

[24] S. A. Campbell, *The Science and Engineering of Microelectronic Fabrication*, Oxford University Press, New York, USA **2001**.

[25] *Handbook of Semiconductor Manufacturing Technology* (Eds: R. Doering, Y. Nishi), CRC Press, Florida, USA **2008**.

[26] E. G. Seebauer, K. W. Noh, *Mater. Sci. Eng. R* **2010**, *70*, 151.

[27] D. M. Smyth, *Annu. Rev. Mater. Sci.* **1985**, *15*, 329.

[28] D. M. Smyth, *Curr. Opin. Solid State Mater. Sci.* **1996**, *1*, 692.

[29] L. R. Dedon, S. Saremi, Z. Chen, A. R. Damodaran, B. A. Apgar, R. Gao, L. W. Martin, *Chem. Mater.* **2016**, *28*, 5952.

[30] S. Saremi, R. Xu, L. R. Dedon, J. A. Mundy, S.-L. Hsu, Z. Chen, A. R. Damodaran, S. P. Chapman, J. T. Evans, L. W. Martin, *Adv. Mater.* **2016**, *28*, 10750.

[31] A. Dasgupta, S. Saremi, R. Xu, L. R. Dedon, S. Pandya, A. R. Damodaran, L. W. Martin, *J. Mater. Chem. C* **2018**, *6*, 10751.

[32] S. Saremi, R. Xu, L. R. Dedon, R. Gao, A. Ghosh, A. Dasgupta, L. W. Martin, *Adv. Mater. Interfaces* **2018**, *5*, 1700991.

[33] S. Saremi, R. Xu, F. I. Allen, J. Maher, J. C. Agar, R. Gao, P. Hosemann, L. W. Martin, *Phys. Rev. Mater.* **2018**, *2*, 084414.

[34] S. Saremi, J. Kim, A. Ghosh, D. Meyers, L. W. Martin, *Phys. Rev. Lett.* **2019**, to be published.

[35] E. Fatuzzo, W. E. Merz, *Ferroelectricity*, North-Holland, Amsterdam, Netherlands **1967**.

[36] T. Mitsui, I. Tatsuzaki, E. Nakamura, *An Introduction to the Physics of Ferroelectrics*, Gordon & Breach, London, England **1976**.

[37] M. E. Lines, A. M. Glass, *Principles and Applications of Ferroelectrics and Related Materials*, Oxford University Press, New York, USA **1977**.

[38] K. M. Rabe, M. Dawber, C. Lichtensteiger, C. H. Ahn, J.-M. Triscone, *Physics of Ferroelectrics: A Modern Perspective*, Springer-Verlag, Berlin, Germany **2007**.

[39] B. A. Strukov, A. P. Levanyuk, *Ferroelectric Phenomena in Crystals*, Springer-Verlag, Berlin, Germany **1998**.

[40] J. F. Nye, *Physical Properties of Crystals*, Oxford University Press, New York, USA **1985**.

[41] G. H. Haertling, *J. Am. Ceram. Soc.* **1999**, *82*, 797.

[42] J. F. Scott, *Science* **2007**, *315*, 954.

[43] L. W. Martin, D. G. Schlom, *Curr. Opin. Solid State Mater. Sci.* **2012**, *16*, 199.

[44] R. F. W. Bader, *Mol. Phys.* **1960**, *3*, 137.

[45] R. E. Cohen, *Nature* **1992**, *358*, 136.

[46] P. S. Halasyamani, K. R. Poeppelmeier, *Chem. Mater.* **1998**, *10*, 2753.

[47] H. A. Jahn, E. Teller, *Proc. R. Soc. Lond. A Math. Phys. Sci.* **1937**, *161*, 220.

[48] H. A. Jahn, *Proc. R. Soc. Lond. A Math. Phys. Sci.* **1938**, *164*, 117.

[49] U. Öpik, M. H. L. Pryce, *Proc. R. Soc. Lond. A Math. Phys. Sci.* **1957**, *238*, 425.

[50] N. A. Hill, *Annu. Rev. Mater. Res.* **2002**, *32,*1.

[51] V. M. Goldschmidt, *Naturwissenschaften* **1926**, *14*, 477.

[52] W. Cochran, *Adv. Phys.* **1960**, *9*, 387.

[53] R. Waser, U. Bottger, S. Tiedke, *Polar Oxides: Properties, Characterization, and Imaging*, Wiley-VCH Verlag GmbH & Co. KGaA, Weinheim, Germany **2005**.

[54] A. K. Tagantsev, L. E. Cross, J. Fousek, *Domains in Ferroic Crystals and Thin Films*, Springer-Verlag, Berlin, Germany **2010**.

[55] V. Y. Shur, *Ferroelectric Thin Films: Synthesis and Basic Properties* (Eds: C. P. de Araujo, J. F. Scott, G. W. Taylor), Gordon and Breach, Amsterdam, Netherlands **1996**.

[56] J. Fousek, V. Janovec, *J. Appl. Phys.* **1969**, *40*, 135

[57] J. F. Scott, C. A. Paz De Araujo, *Science* **1989**, *246*, 1400.

[58] S. M. Yang, J. G. Yoon, T. W. Noh, *Curr. Appl. Phys.* **2011**, *11*, 1111.

[59] R. E. Newnham, *Properties of Materials*, Oxford University Press Inc., New York, USA **2005**.

[60] W. G. Cady, *Piezoelectricity*, McGraw-Hill & Co., New York, USA **1946**.

[61] A. K. Bain, P. Chand, *Ferroelectrics*, Wiley-VCH Verlag GmbH & Co. KGaA, Weinheim, Germany **2017**.

[62] B. Ravel, E. A. Stern, R. I. Vedrinskii, V. Kraizman, *Ferroelectrics* **1998**, *206*, 407.

[63] R. J. Nelmes, W. F. Kuhs, *Solid State Commun.* **1985**, *54*, 721.

[64] L. E. Cross, *Nucl. Med. Commun.* **2011**, *32*, 666.

[65] W. Cao, L. E. Cross, *Phys. Rev. B* **1993**, *47*, 4825.

[66] B. Noheda, D. Cox, G. Shirane, J. Gonzalo, L. Cross, S. Park, *Appl. Phys. Lett.* **1999**, *74*, 2059.

[67] W. Eerenstein, N. D. Mathur, J. F. Scott, *Nature* **2006**, *442*, 759.

[68] G. Catalan, J. F. Scott, *Adv. Mater.* **2009**, *21*, 2463.

[69] D. Sando, A. Barthélémy, M. Bibes, *J. Phys.: Condens. Matter* **2014**, *26*, 473201.

[70] J. R. Teague, R. Gerson, W. J. James, *Solid State Commun.* **1970**, *8*, 1073.

[71] P. Fischer, M. Polomska, I. Sosnowska, M. Szymanski, *J. Phys. C Solid State Phys.* **1980**, *13*, 1931.

[72] S. M. Selbach, T. Tybell, M.-A. Einarsrud, T. Grande, *Adv. Mater.* **2008**, *20*, 3692.

[73] F. Kubel, H. Schmid, *Acta Cryst. B Struct. Sci.* **1990**, *46*, 698.

[74] F. Zavaliche, S. Y. Yang, T. Zhao, Y. H. Chu, M. P. Cruz, C. B. Eom, R. Ramesh, *Phase Transit.* **2006**, *79*, 991.

[75] J. Wang, J. B. Neaton, H. Zheng, V. Nagarajan, S. B. Ogale, B. Liu, D. Viehland, V. Vaithyanathan, D. G. Schlom, U. V. Waghmare, N. A. Spaldin, K. M. Rabe, M. Wuttig, R. Ramesh, *Science* **2003**, *299*, 1719.

[76] J. B. Neaton, C. Ederer, U. V. Waghmare, N. A. Spaldin, K. M. Rabe, *Phys. Rev. B* **2005**, *71*, 014113.

[77] P. Ravindran, R. Vidya, A. Kjekshus, H. Fjellvåg, O. Eriksson, *Phys. Rev. B* **2006**, *74*, 224412.

[78] L. E. Cross, *Ferroelectrics* **1987**, *76*, 241.

[79] Z. G. Ye, *Key Engineering Materials*, Trans Tech Publications, Switzerland **1998**.

[80] T. R. Shrout, J. Fielding, *Proceedings of the IEEE Ultrasonic Symposium*, IEEE, New Jersey, USA **1990**.

[81] L. E. Cross, *Ferroelectrics* **1994**, *151*, 305.

[82] S.-E. Park, T. R. Shrout, *J. Appl. Phys.* **1997**, *82*, 1804.

[83] D. Viehland, S. J. Jang, L. E. Cross, M. Wuttig, *J. Appl. Phys.* **1990**, *68*, 2916.

[84] D. Viehland, M. Wuttig, L. E. Cross, *Ferroelectrics* **1991**, *120*, 71.

[85] T. R. Shrout, Z. P. Chang, N. Kim, S. Markgraf, *Ferroelectrics Lett.* **1990**, *12*, 63.

[86] H. Fu, R. E. Cohen, *Nature* **2000**, *403*, 281.

[87] G. Burns, F. H. Dacols, *Phys. Rev. B* **1983**, *28*, 2527.

[88] J. Hlinka, *J. Adv. Dielect.* **2012**, *2*, 1241006.

[89] A. Bosak, D. Chernyshov, S. Vakhrushev, M. Krisch, *Acta. Cryst. A* **2012**, *68*, 117.

[90] H. Takenaka, I. Grinberg, A. M. Rappe, *Phys. Rev. Lett.* **2013**, *110*, 147602.

[91] B. Hehlen, M. Al-Sabbagh, A. Al-Zein, J. Hlinka, *Phys. Rev. Lett.* **2016**, *117*, 155501.

[92] H. Takenaka, I. Grinberg, S. Liu, A. M. Rappe, *Nature* **2017**, *546*, 391.

[93] M. J. Krogstad, P. M. Gehring, S. Rosenkranz, R. Osborn, F. Ye, Y. Liu, J. P. Ruff, W. Chen, J. M. Wozniak, H. Luo, O. Chmaissem, *Nat. Mater.* **2018**, *17*, 718.

[94] J. Kim, H. Takenaka, Y. Qi, A. R. Damodaran, A. Fernandez, R. Gao, M. R. McCarter, S. Saremi, L. Chung, A. M. Rappe, L. W. Martin, *Adv. Mater.* **2019**, *31*, 1901060.

[95] K. J. Choi, M. Biegalski, Y. L. Li, A. Sharan, J. Schubert, R. Uecker, P. Reiche, Y. B. Chen, X. Q. Pan, V. Gopalan, L. Q. Chen, *Science* **2004**, *306*, 1005.

[96] J. H. Haeni, P. Irvin, W. Chang, R. Uecker, P. Reiche, Y. L. Li, S. Choudhury, W. Tian, M. E. Hawley, B. Craigo, A. K. Tagantsev, *Nature* **2004**, *430*, 758.

[97] Y.-H. Chu, M. P. Cruz, C. H. Yang, L. W. Martin, P. L. Yang, J. X. Zhang, K. Lee, P. Yu, L. Q. Chen, R. Ramesh, *Adv. Mater.* **2007**, *19*, 2662.

[98] R. J. Zeches, M. D. Rossell, J. X. Zhang, A. J. Hatt, Q. He, C-H. Yang, A. Kumar, C. H. Wang, A. Melville, C. Adamo, G. Sheng, *Science* **2009**, *326*, 977.

[99] S. W. Bailey, V. A. Frank-Kamenetskii, S. Goldsztaub, A. Kato, A. Pabst, H. Schulz, H. F. W. Taylor, M. Fleischer, A. J. C. Wilson, *Acta Cryst. A* **1977**, *33*, 681.

[100] S. L. Miller, P. J. McWhorter, *J. Appl. Phys.* **1992**, *72*, 5999.

[101] S. Mathews, R. Ramesh, T. Venkatesan, J. Benedetto, *Science* **1997**, *276*, 238.

[102] A. Chanthbouala, V. Garcia, R. O. Cherifi, K. Bouzehouane, S. Fusil, X. Moya, S. Xavier, H. Yamada, C. Deranlot, N. D. Mathur, M. Bibes, *Nat. Mater.* **2012**, *11*, 860.

[103] R. Guo, L. You, Y. Zhou, Z. S. Lim, X. Zou, L. Chen, R. Ramesh, J. Wang, *Nat. Commun.* **2013**, *4*, 1.

[104] D. Dimos, C. H. Mueller, *Annu. Rev. Mater. Sci.* **1998**, *28*, 397.

[105] P. Muralt, *J. Micromechanics Microengineering* **2000**, *10*, 136.

[106] P. Muralt, *IEEE Trans. Ultrason. Ferroelectr. Freq. Control* **2002**, *47*, 903.

[107] S. R. Anton, H. A. Sodano, *Smart Mater. Struct.* **2007**, *16*, R1.

[108] S. Trolier-McKinstry, F. Griggio, C. Yaeger, P. Jousse, D. Zhao, S. S. Bharadwaja, T. N. Jackson, S. Jesse, S. V. Kalinin, K. Wasa, *IEEE Trans. Ultrason. Ferroelectr. Freq. Control* **2011**, *58*, 1782.

[109] U. K. Bhaskar, N. Banerjee, A. Abdollahi, Z. Wang, D. G. Schlom, G. Rijnders, G. Catalan, *Nat. Nanotechnol.* **2016**, *11*, 263.

[110] G. Sebald, L. Seveyrat, D. Guyomar, L. Lebrun, B. Guiffard, S. Pruvost, *J. Appl. Phys.* **2006**, *100*, 124112.

[111] G. Sebald, E. Lefeuvre, D. Guyomar, *IEEE Trans. Ultrason. Ferroelectr. Freq. Control* **2008**, *55*, 538.

[112] Y. Yang, W. Guo, K. C. Pradel, G. Zhu, Y. Zhou, Y. Zhang, Y. Hu, L. Lin, Z. L. Wang, *Nano Lett.* **2012**, *12*, 2833.

[113] F.-C. Chiu, *Adv. Mater. Sci. Eng.* **2014**, *2014*, 1.

[114] N. F. Mott, R. W. Gurney, *Electronic Processes in Ionic Crystals*, Clarendon Press, Oxford, UK **1940**.

[115] M. A. Lampert, P. Mark, *Current Injection in Solids*, Academic Press, New York, USA **1970**.

[116] J. Frenkel, *Phys. Rev.* **1938**, *54*, 647.

[117] J. G. Simmons, *Phys. Rev.* **1967**, *155*, 657.

[118] J. R. Yeargan, H. L. Taylor, *J. Appl. Phys.* **1968**, *39*, 5600.

[119] W. Schottky, *Naturwissenschaften* **1938**, *26*, 843.

[120] W. L. Warren, B. A. Tuttle, D. Dimos, G. E. Pike, H. N. Al-Shareef, R. Ramesh, J. T. Evans, *Jpn. J. Appl. Phys.* **1996**, *35*, 1521.

[121] J. Lee, R. Ramesh, V. G. Keramidas, W. L. Warren, G. E. Pike, J. T. Evans, *Appl. Phys. Lett.* **1995**, *66*, 1337.

[122] A. K. Tagantsev, I. Stolichnov, N. Setter, J. S. Cross, *J. Appl. Phys.* **2004**, *96*, 6616.

[123] A. K. Tagantsev, G. Gerra, *J. Appl. Phys.* **2006**, *100*, 051607.

[124] J. M. Herbert, *Ceramic Dielectrics and Capacitors,* Gordon and Breach, New York, USA **1985**.

[125] K. Carl, K. H. Haerdtl, *Ferroelectrics* **1978**, *17*, 473.

[126] Y. Xu, *Ferroelectric Materials and Their Applications,* North-Holland, Amsterdam, Netherlands **1991**.

[127] U. Robels, G. Arlt, *J. Appl. Phys.* **1993**, *73*, 3454.

[128] L. A. Girifalco, *Statistical Physics of Materials*, Wiley, New York, USA **1973**.

[129] T. Suzuki, Y. Nishi, M. Fujimoto, *Philos. Mag. A* **2000**, *80*, 621.

[130] D. A. Freedman, D. Roundy, T. A. Arias, *Phys. Rev. B* **2009**, *80*, 064108.

[131] A. Chandrasekaran, D. Damjanovic, N. Setter, N. Marzari, *Physical Review B* **2013**, *88*, 214116.

[132] M. Boswarva, A. B. Lidiard, *Philos. Mag.* **1967**, *16*, 805.

[133] A. B. Lidiard, *Philos. Mag. A* **1981**, *43*, 291.

[134] N. G. Eror, U. Balachandran, *Solid State Commun.* **1982**, *44*, 1117.

[135] M. Leslie, N. J. Gillan, *J. Phys. C: Solid State Phys.* **1985**, *18*, 973.

[136] L. Zhang, E. Erdem, X. Ren, R.-A. Eichel, *Appl. Phys. Lett.* **2008**, *93*, 202901.

[137] R.-A. Eichel, P. Erhart, P. Träskelin, K. Albe, H. Kungl, M. J. Hoffmann, *Phys. Rev. Lett.* **2008**, *100*, 095504.

[138] T. Rojac, S. Drnovsek, A. Bencan, B. Malic, D. Damjanovic, *Phys. Rev. B* **2016**, *93*, 014102.

[139] F. A. Kröger, H. J. Vink, *Solid State Phys. Adv. Res. Appl.* **1956**, *3*, 307.

[140] H. L. Tuller, S. R. Bishop, *Annu. Rev. Mater. Res.* **2011**, *41*, 369.

[141] X. Luo, B. Wang, Y. Zheng, *Phys. Rev. B* **2009**, *80*, 104115.

[142] D. B. Chrisey, G. K. Hubler, *Pulsed Laser Deposition of Thin Films*, John Wiley & Sons, New York, USA **1994**.

[143] T. F. Tseng, M. H. Yeh, K. S. Liu, I. N. Lin, *J. Appl. Phys.* **1996**, *80*, 4984.

[144] K. Jagannadham, A. K. Sharma, Q. Wei, R. Kalyanraman, J. Narayan, *J. Vac. Sci. Technol. A.* **1998**, *16*, 2804.

[145] C. Wang, B. L. Cheng, S. Y. Wang, H. B. Lu, Y. L. Zhou, Z. H. Chen, G. Z. Yang, *Thin Solid Films* **2005**, *485*, 82.

[146] J.-F. Lagrange, J. Wolfman, O. Motret, *J. Appl. Phys.* **2012**, *111*, 063301.

[147] A. R. Damodaran, E. Breckenfeld, Z. Chen, S. Lee, L. W. Martin, *Adv. Mater.* **2014**, *26*, 6341.

[148] H. Hu, S. B. Krupanidhi, *Appl. Phys. Lett.* **1991**, *61*, 1246.

[149] S. B. Krupanidhi, H. Hu, V. Kumar, *J. Appl. Phys.* **1992**, *71*, 376.

[150] L. R. Zheng, P. X. Yang, L. W. Wang, C. L. Lin, S. C. Zo, *Nucl. Instrum. Methods Phys. Res. B* **1997**, *127*, 621.

[151] Y. Takamura, R. V. Chopdekar, A. Scholl, A. Doran, J. A. Liddle, B. Harteneck, Y. Suzuki, *Nano let.* **2006**, *6*, 1287.

[152] F. Chen, *J. Appl. Phys.* **2009**, *106*, 081101.

[153] S. Mathew, A. Annadi, T. K. Chan, T. C. Asmara, D. Zhan, X. R. Wang, S. Azimi, Z. Shen, A. Rusydi, M. B. Breese, T. Venkatesan, *ACS Nano* **2013**, *7*, 10572.

[154] Y. Bastani, A. Y. Cortés-Peña, A. D. Wilson, S. Gerardin, M. Bagatin, A. Paccagnella, N. Bassiri-Gharb, *Appl. Phys. Lett.* **2013**, *102*, 192906.

[155] H. Guo, S. Dong, P. D. Rack, J. D. Budai, C. Beekman, Z. Gai, W. Siemons, C. M. Gonzalez, R. Timilsina, A. T. Wong, A. Herklotz, P. C. Snijders, E. Dagotto, T. Z. Ward, *Phys. Rev.Lett.* **2015**, *114*, 256801.

[156] L. J. McGilly, C. S. Sandu, L. Feigl, D. Damjanovic, N. Setter, *Adv. Funct. Mater.* **2017**, *27*, 1605196.

[157] S. J. Pearton, *Mater. Sci. Rep.* **1990**, *4*, 313.

[158] G. H. Kinchin, R. S. Pease, *Rept. Prog. Phys.* **1955**, *18*, 1.

[159] T. Kakeshita, T. Fukuda, A. Saxena, A. Planes, *Disorder and Strain-Induced Complexity in Functional Materials*, Springer Science & Business Media, **2011**.

[160] G. Arlt, H. Neumann, *Ferroelectrics* **1988**, *87*, 109.

[161] W. L. Warren, G. E. Pike, K. Vanheusden, D. Dimos, B. A. Tuttle, J. Robertson, *J. Appl. Phys.* **1996**, *79*, 9250.

[162] X. Ren, *Nat. Mater.* **2004**, *3*, 91.

[163] M. N. R. Ashfold, F. Claeyssens, G. M. Fuge, S. J. Henley, *Chem. Soc. Rev.* **2004**, *33*, 23.

[164] R. Eason, *Pulsed Laser Deposition of Thin Films,* John Wiley & Sons, New Jersey, USA **2007**.

[165] C. B. Eom, R. B. Van Dover, J. M. Phillips, D. J. Werder, J. H. Marshall, C. H. Chen, R. J. Cava, R. M. Fleming, D. K. Fork, *Appl. Phys. Lett.* **1993**, *63*, 2570.

[166] M. Toyota, O. Hidaka, K. Yamakawa, O. Arisumi, H. Kanaya, T. Iwamoto, Y. Kumura, I. Kunishima, S. Tanaka, *Jpn. J. Appl. Phys.* **2000**, *39*, 2110.

[167] A. K. Tagantsev, I. Stolichnov, E. L. Colla, N. Setter, *J. Appl. Phys.* **2001**, *90*, 1387.

[168] B. Nagaraj, S. Aggarwal, R. Ramesh, *J. Appl. Phys.* **2001**, *90*, 375.

[169] Y. S. Kim, J. Y. Jo, D. J. Kim, Y. J. Chang, J. H. Lee, T. W. Noh, T. K. Song, J. G. Yoon, J. S. Chung, S.I. Baik, Y. W. Kim, *Appl. Phys. Lett.* **2006**, *88*, 072909.

[170] J. Karthik, A. R. Damodaran, L. W. Martin, *Adv. Mater.* **2012**, *24*, 1610.

[171] T. Ohnishi, M. Lippmaa, T. Yamamoto, S. Meguro, H. Koinuma, *Appl. Phys. Lett.* **2005**, *87*, 241919.

[172] D. J. Keeble, S. Wicklein, R. Dittmann, L. Ravelli, R. A. Mackie, W. Egger, *Phys. Rev. Lett.* **2010**, *105*, 226102.

[173] D. Kan, Y. Shimakawa, *Appl. Phys. Lett.* **2011**, *99*, 081907.

[174] E. Breckenfeld, R. Wilson, J. Karthik, A. R. Damodaran, D. G. Cahill, L. W. Martin, *Chem. Mater.* **2012**, *24*, 331.

[175] E. Breckenfeld, N. Bronn, J. Karthik, A. R. Damodaran, S. Lee, N. Mason, L. W. Martin, *Phys. Rev. Lett.* **2013**, *110*, 196804.

[176] E. Breckenfeld, R. B. Wilson, L. W. Martin, *Appl. Phys. Lett.* **2013**, *103*, 082901.

[177] E. Breckenfeld, Z. Chen, A. R. Damodaran, L. W. Martin, *ACS Appl. Mater. Interfaces* **2014**, *6*, 22436.

[178] J. Gonzalo, R. Gómez San Román, J. Perriere, C. N. Afonso, R. Pérez Casero, *Appl. Phys. A* **1998**, *66*, 487.

[179] S. Wicklein, A. Sambri, S. Amoruso X. Wang, R. Bruzzese, A. Koehl, R. Dittmann, *Appl. Phys. Lett.* **2012**, *101*, 131601.

[180] J. F. Ziegler, M. D. Ziegler, J. P. Biersack, *Nucl. Instr. Meth. Phys. Res. B* **2010**, *268*, 1818.

[181] W. H. Bragg, W. L. Bragg, *Proc. R. Soc. Lond. A* **1913**, *88*, 428.

[182] M. Birkholz, *Thin Film Analysis by X-Ray Scattering*, Wiley-VCH Verlag GmbH & Co. KGaA, Weinheim, Germany **2006**.

[183] J. R. Patel, N. Kato, *J. Appl. Phys.* **1973**, *44*, 971.

[184] K. Hirano, T. Fukamachi, M. Yoshizawa, R. Negishi, T. Kawamura, *Acta Cryst. A* **2009**, *65*, 253.

[185] J. Perrière, *Vacuum* **1987**, *37*, 429.

[186] J. R. MacDonald, J. A. Davies, T. E. Jackman, L. C. Feldman, *J. Appl. Phys.* **1983**, *54*, 1800.

[187] C. Huan-Sheng, S. Hao, T. Jiayong, Y. Fujia, *Nucl. Instrum. Methods Phys. Res. Sect. B Beam Interact. Mater. At.* **1993**, *83*, 449.

[188] A. F. Gurbich, *Nucl. Instrum. Methods Phys. Res., Sect. B* **2016**, *371*, 27.

[189] J. A. Nelder, R. Mead, *Comput. J.* **1965**, *7*, 308.

[190] D. D. Perovic, C. J. Rossow, A. Howie, *Ultramicroscopy* **1993**, *52*, 353.

[191] S. E. Hillyard, J. Silcox, *Ultramicroscopy* **1995**, *58*, 6.

[192] A. Gruverman, A. Kholkin, *Rep. Prog. Phys.* **2006**, *69*, 2443.

[193] B. J. Rodriguez, C. Callahan, S. V. Kalinin, R. Proksch, *Nanotechnol.* **2007**, *18*, 475504.

[194] S. V. Kalinin, A. Gruverman, *Scanning Probe Microscopy-Electrical and Electromechanical Phenomena at the Nanoscale Volume II*, Springer Science & Business Media, LLC, New York, USA **2007**.

[195] B. Voigtlander, *Scanning Probe Microscopy-Atomic Force Microscopy and Scanning Tunneling Microscopy*, Springer-Verlag Berlin Heidelberg, Germany **2015**.

[196] B. Cappella, G. Dietler, *Surf. Sci. Rep.* **1999**, *34*, 1.

[197] N. A. Geisse, *Mater. Today* **2009**, *12*, 40.

[198] S. Jesse, S. V. Kalinin, *J. Phys. D. Appl. Phys.* **2011**, *44*, 464006.

[199] D. Damjanovic, M. Demartin, *J. Phys. D: Appl. Phys.* **1996**, *29*, 2057.

[200] D. A. Hall, *Ferroelectrics* **1999**, *223*, 319.

[201] A. K. Tagantsev, I. Stolichnov, N. Setter, *Phys. Rev. B* **2002**, *66*, 214109.

[202] M. Avrami, *J. Chem. Phys.* **1940**, *8*, 212.

[203] Y. Ishibashi, Y. Takagi, *J. Phys. Soc. Jpn.* **1971**, *31*, 506.

[204] J. Y. Jo, S. M. Yang, T. H. Kim, H. N. Lee, J.-G. Yoon, S. Park, Y. Jo, M. H. Jung, T. W. Noh, *Phys. Rev. Lett.* **2009**, *102*, 045701.

[205] S. Zhukov, Y. A. Genenko, H. von Seggern, *J. Appl. Phys.* **2010**, *108*, 014106.

[206] I. Mayergoyz, *IEEE Trans. Magn.* **1986**, *22*, 603.

[207] A. T. Bartic, D. J. Wouters, H. E. Maes, J. T. Rickes, R. M. Waser, *J. Appl. Phys.* **2001**, *89*, 3420.

[208] A. Stancu, D. Ricinschi, L. Mitoseriu, P. Postolache, M. Okuyama, *Appl. Phys. Lett.* **2003**, *83*, 3767.

[209] F. Preisach, *Z. Phys.* **1935**, *94*, 277.

[210] C. R. Pike, A. P. Roberts, K. L. Verosub, *J. Appl. Phys.* **1999**, *85*, 6660.

[211] A. P. Roberts, C. R. Pike, K. L. Verosub, *J. Geophys. Res.: Solid Earth* **2000**, *105*, 28461.

[212] I. D. Mayergoyz, *Mathematical Models of Hysteresis*, Springer, New York, USA **1991**.

[213] A. R. West, D. C. Sinclair, N. Hirose, *J. Electroceram.* **1997**, *1*, 65.

[214] N. J. Donnelly, C. A. Randall, *Appl. Phys. Lett.* **2010**, *96*, 052906.

[215] D. V. Lang, *J. Appl. Phys.* **1974**, *45*, 3023.

[216] K. Uchino, *Piezoelectric Actuators and Ultrasonic Motors*, Springer Science & Business Media, Massachusetts, USA **1996**.

[217] S. Wada, S. Suzuki, T. Noma, T. Suzuki, M. Osada, M. Kakihana, S.-E. Park, L. E. Cross, T. R. Shrout, *Jpn. J. Appl. Phys.* **1999**, *38*, 5505.

[218] H. Kishi, Y. Mizuno, H. Chazono, *Jpn. J. Appl. Phys.* **2003**, *42*, 1.

[219] V. J. Tennery, R. L. Cook, *J. Am. Ceram. Soc.* **1961**, *44*, 187.

[220] F. D. Morrison, D. C. Sinclair, A. R. West, *J. Appl. Phys.* **1999**, *86*, 6355.

[221] W. M. Zhu, Z.-G. Ye, *Ceram. Int.* **2004**, *30*, 1435.

[222] X. Qi, J. Dho, R. Tomov, M. G. Blamire, J. L. MacManus-Driscoll, *Appl. Phys. Lett.* **2005**, *86*, 062903.

[223] J. K. Kim, S. S. Kim, W.-J. Kim, A. S. Bhalla, R. Guo, *Appl. Phys. Lett.* **2006**, *88*, 132901.

[224] Y.-H. Lee, J.-M. Wu, C.-H. Lai, *Appl. Phys. Lett.* **2006**, *88*, 042903.

[225] T. Kawae, Y. Terauchi, H. Tsuda, M. Kumeda, A. Morimoto, *Appl. Phys. Lett.* **2009**, *94*, 112904.

[226] C.-H. Yang, D. Kan, I. Takeuchi, V. Nagarajan, J. Seidel, *Phys. Chem. Chem. Phys.* **2012**, *14*, 15953.

[227] Y. P. Wang, L. Zhou, M. F. Zhang, X. Y. Chen, J.-M. Liu, Z. G. Liu, *Appl. Phys. Lett.* **2004**, *84*, 1731.

[228] C. Wang, M. Takahashi, H. Fujino, X. Zhao, E. Kume, T. Horiuchi, S. Sakai, *J. Appl. Phys.* **2006**, *99*, 054104.

[229] M. Valant, A.-K. Axelsson, N. Alford, *Chem. Mater.* **2007**, *19*, 5431.

[230] G. W. Pabst, L. W. Martin, Y.-H. Chu, R. Ramesh, *Appl. Phys. Lett.* **2007**, *90*, 072902.

[231] H. Yang, M. Jain, N. A. Suvorova, H. Zhou, H. M. Luo, D. M. Feldmann, P. C. Dowden, R. F. DePaula, S. R. Foltyn, Q. X. Jia, *Appl. Phys. Lett.* **2007**, *91*, 072911.

[232] S. R. Basu, L. W. Martin, Y. H. Chu, M. Gajek, R. Ramesh, R. C. Rai, X. Xu, J. L. Musfeldt, *Appl. Phys. Lett.* **2008**, *92*, 091905.

[233] J. F. Ihlefeld, N. J. Podraza, Z. K. Liu, R. C. Rai, X. Xu, *Appl. Phys. Lett.* **2008**, *92*, 142908.

[234] A. Kumar, R. C. Rai, N. J. Podraza, S. Denev, M. Ramirez, Y.-H. Chu, L. W. Martin, J. Ihlefeld, T. Heeg, J. Schubert, D. G. Schlom, J. Orenstein, R. Ramesh, R. W. Collins, J. L. Musfeldt, V. Gopalan, *Appl. Phys. Lett.* **2008**, *92*, 121915.

[235] A. Lahmar, K. Zhao, S. Habouti, M. Dietze, C H. Solterbeck, M. Es-Souni, *Solid State Ionics* **2011**, *202*, 1.

[236] J. Yan, M. Gomi, T. Hattori, T. Yokota, H. Song, *Thin Solid Films* **2013**, *542*, 150.

[237] X. Xie, S. Yang, F. Zhang, S. Fan, Q. Che, C. Wang, X. Guo, L. Zhang, *J. Mater. Sci.: Mater. Electron.* **2015**, *26*, 10095.

[238] S. Guillemet-Fritsch, Z. Valdez-Nava, C. Tenailleau, T. Lebey, B. Durand, J.-Y. Chane-Ching, *Adv. Mater.* **2008**, *20*, 551.

[239] H. Han, D. Ghosh, J. L. Jones, J. C. Nino, *J. Am. Ceram. Soc.* **2013**, *96*, 485.

[240] H. Han, C. Voisin, S. Guillemet-Fritsch, P. Dufour, C. Tenailleau, C. Turner, J. C. Nino, *J. Appl. Phys.* **2013**, *113*, 024102.

[241] R. Gao, S. E. Reyes-Lillo, R. Xu, A. Dasgupta, Y. Dong, L. R. Dedon, J. Kim, S. Saremi, Z. Chen, C. R. Serrao, H. Zhou, J. B. Neaton, L. W. Martin, *Chem. Mater.* **2017**, *29*, 6544.

[242] D. Marrocchelli, N. H. Perry, S. R. Bishop, *Phys. Chem. Chem. Phys.* **2015**, *17*, 10028.

[243] G. Robert, D. Damjanovic, N. Setter, *Appl. Phys. Lett.* **2000**, *77*, 4413.

[244] I. Fujii, M. Ugorek, S. Trolier-McKinstry, *J. Appl. Phys.* **2010**, *107*, 104116.

[245] S. H. Wemple, M. Didomenico, I. Camlibel, *J. Phys. Chem. Solids* **1968**, *29*, 1797.

[246] P. Erhart, K. Albe, *J. Appl. Phys.* **2007**, *102*, 084111.

[247] N.-H. Chan, D. M. Smyth, *J. Am. Ceram. Soc.* **1984**, *67*, 285.

[248] P. Erhart, K. Albe, *J. Appl. Phys.* **2008**, *104*, 044315.

[249] G. Koschek, E. Kubalek, *Phys. Status Solidi A* **1983**, *79*, 131.

[250] T.-B. Wu, J.-N. Lin, *J. Am. Ceram. Soc.* **1994**, *77*, 759.

[251] G. V. Lewis, C. R. A. Catlow, *Radiat. Eff.* **1983**, *73*, 307.

[252] G. V. Lewis, C. R. A. Catlow, *J. Phys. Chem. Solids* **1986**, *47*, 89.

[253] A. I. Kingon, J. B. Clark, *J. Am. Ceram. Soc.* **1983**, *66*, 253.

[254] Y. L. Tu, S. J. Milne, *J. Mater. Sci.* **1995**, *30*, 2507.

[255] J. F. Ihlefeld, A. Kumar, V. Gopalan, D. G. Schlom, Y. B. Chen, X. Q. Pan, T. Heeg, J. Schubert, X. Ke, P. Schiffer, J. Orenstein, L. W. Martin, Y.-H. Chu, R. Ramesh, *Appl. Phys. Lett.* **2007**, *91*, 071922.

[256] S. Iakovlev, C. H. Solterbeck, M. Kuhnke, M. Es-Souni, *J. Appl. Phys.* **2005**, *97*, 094901.

[257] P. Blom, R. Wolf, J. Cillessen, M. Krijn, *Phys. Rev. Lett.* **1994**, *73*, 2107.

[258] J. J. Lee, S. B. Desu, *Ferroelectr. Lett. Sect.* **1995**, *20*, 27.

[259] J. C. Agar, A. R. Damodaran, G. A. Velarde, S. Pandya, R. V. K. Mangalam, L. W. Martin, *ACS Nano* **2015**, *9*, 7332.

[260] V. R. Palkar, J. John, R. Pinto, *Appl. Phys. Lett.* **2002**, *80*, 1628.

[261] S. L. Morelhaoa, J. Z. Domagalab, *J. Appl. Cryst.* **2007**, *40*, 546.

[262] A. H. G. Vlooswijk, *Ph.D. Thesis*, Zernike Institute, Groningen, Netherlands **2009**.

[263] D. A. Muller, N. Nakagawa, A. Ohtomo, J. L. Grazul, H. Y. Hwang, *Nature* **2004**, *430*, 657.

[264] M. Levinson, C. A. Aemiento, S. S. P. Shah, *Mat. Res. Soc. Symp. Proc.* **1987**, *92*, 353.

[265] P. K. Giri, Y. N. Mohapatra, *Mater. Sci. Eng. B* **2000**, *71*, 327.

[266] J. Robertson, C. W. Chen, *Appl. Phys. Lett.* **1999**, *74*, 1168.

[267] R. Gerson, H. Jaffe, *J. Phys. Chem. Solids* **1963**, *24*, 979.

[268] V. V. Prisedsky, V. I. Shishkovsky, V. V. Klimov, Ferroelectrics **1977**, *17*, 465.

[269] J. Robertson, W. L. Warren, B. A. Tuttle, D. Dimos, D. M. Smyth, *Appl. Phys. Lett.* **1993**, *63*, 1519.

[270] D. J. Wouters, G. J. Willems, H. E. Maes, *Microelectron. Eng.* **1995**, *29*, 249.

[271] Z. Zhang, P. Wu, L. Lu, C. Shu, *Appl. Phys. Lett.* **2006**, *88*, 142902.

[272] T. P.-C. Juan, S.-M. Chen, J. Y.-M. Lee, *J. Appl. Phys.* **2004**, *95*, 3120.

[273] P. F. Baude, C. Ye, D. L. Polla, *Appl. Phys. Lett.* **1994**, *64*, 2670.

[274] B. A. Boukamp, M. T. N. Pham, D. H. A. Blank, H. J. M. Bouwmeester, *Solid State Ionics* **2004**, *170*, 239.

[275] R. Gerson, *J. Appl. Phys.* **1960**, *31*, 188.

[276] C. Sudhama, J. Kim, J. Lee, V. Chikarmane, W. Shepard, E. R. Meyers, *J. Vac. Sci. Technol. B* **1993**, *11*, 1301.

[277] S. J. Clark, J. Robertson, *Appl. Phys.* Lett. **2009**, *94*, 022902.

[278] B. J. Rodriguez, S. Jesse, A. P. Baddorf, S. -H. Kim, S. V. Kalinin, *Phys. Rev. Lett.* **2007**, *98*, 247603.

[279] G. Catalan, H. Bea, S. Fusil, M. Bibes, P. Paruch, A. Barthelemy, J. F. Scott, *Phys. Rev. Lett.* **2008**, *100*, 027602.

[280] J. F. Scott, *Ferroelectric Memories*, Springer, Germany **2000**.

[281] C. R. Bowen, J. Taylor, E. LeBoulbar, D. Zabek, A. Chauhan, R. Vaish, *Energy Environ. Sci.* **2014**, *7*, 3836.

[282] M. H. Park, H. J. Lee, G. H. Kim, Y. J. Kim, J. H. Kim, J. H. Lee, Ch. S. Hwang, *Adv. Funct. Mater.* **2011**, *21*, 4305.

[283] D. Lee, B. C. Jeon, S. H. Baek, S. M. Yang, Y. J. Shin, T. H. Kim, Y. S. Kim, J.-G. Yoon, Ch. B. Eom, T. W. Noh, *Adv. Mater.* **2012**, *24*, 6490.

[284] A. Ghosh, G. Koster, G. Rijnders, *Adv. Funct. Mater.* **2016**, *26*, 5748.

[285] L. Baudry, I. Lukyanchuk, V. M. Vinokur, *Sci. Rep.* **2017**, *7*, 42196.

[286] R. Xu, S. Liu, S. Saremi, R. Gao, J. J. Wang, Z. Hong, H. Lu, A. Ghosh, S. Pandya, E. Bonturim, Z. Chen, *Nat. Commun.* **2019**, *10*, 1.

[287] T. Ma, J.-P. Han, *IEEE Electron Device Lett.* **2002**, *23*, 386.

[288] S. Baek, J. Park, D. Kim, V. Aksyuk, R. Das, S. Bu, D. Felker, J. Lettieri, V. Vaithyanathan, S. Bharadwaja, *Science* **2011**, *334*, 958.

[289] T. Morita, Y. Kadota, H. Hosaka, *Appl. Phys. Lett.* **2007**, *90*, 082909.

[290] W.-H. Kim, J. Y. Son, Y.-H. Shin, H. M. Jang, *Chem. Mater.* **2014**, *26*, 6911.

[291] A. Ghosh, G. Koster, G. Rijnders, *APL Mater.* **2016**, *4*, 066103.

[292] S. Zhang, R. E. Eitel, C. A. Randall, T. R. Shrout, E. F. Alberta, *Appl. Phys. Lett.* **2005**, *86*, 262904.

[293] C. A. Volkert, A. M. Minor, *MRS Bull.* **2007**, *32*, 389.

[294] P. B. Johnson, D. J. Mazey, J. H. Evans, *Radiat. Eff.* **1983**, *78*, 147.

[295] O. Boser, *J. Appl. Phys.* **1987**, *62*, 1344.

[296] Y. Kadota, H. Hosaka, T. Morita, *Jpn. J. Appl. Phys.* **2008**, *47*, 217.

[297] F. Chu, I. M. Reaney, N. Setter, *J. Appl. Phys.* **1995**, *77*, 1671.

[298] M. P. Harmer, J. Chen, P. Peng, H. M. Chan, D. M. Smyth, *Ferroelectrics* **1989**, *97*, 263.

[299] G. A. Samara, *J. Phys. Condens. Matter* **2003**, *15*, R367.

[300] A. A. Bokov, Z.-G. Ye, *J. Mater. Sci.* **2006**, *41*, 31.

[301] H. W. Jang, A. Kumar, S. Denev, M. D. Biegalski, P. Maksymovych, C. W. Bark, C. T. Nelson, C. M. Folkman, S. H. Baek, N. Balke, C. M. Brooks, D. A. Tenne, D. G. Schlom, L. Q. Chen, X. Q. Pan, S. V. Kalinin, V. Gopalan, C. B. Eom, *Phys. Rev. Lett.* **2010**, *104*, 197601.

[302] T.-Y. Kim, H. M. Jang, *Appl. Phys. Lett.* **2000**, *77*, 3824.

[303] F. Chu, N. Setter, A. K. Tagantsev, *J. Appl. Phys.* **1993**, *74*, 5129.

[304] C. Malibert, B. Dkhil, J. M. Kiat, D. Durand, J. F. Berar, A. Spasojevic-de Bire, *J. Phys. Condens. Matter* **1997**, *9*, 7485.

[305] J. C. Frederick, T. H. Kim, W. Maeng, A. A. Brewer, J. P. Podkaminer, W. Saenrang, V. Vaithyanathan, F. Li, L. Q. Chen, D. G. Schlom, S. Trolier-McKinstry, *Appl. Phys. Lett.* **2016**, *108*, 132902.

[306] F. T. Rogers, Jr., *J. Appl. Phys.* **1956**, *27*, 1066.

[307] S. A. Yang, B. H. Kim, M. K. Lee, G. J. Lee, N.-H. Lee, S. D. Bu, *Thin Solid Films* **2014**, *562*, 185.

[308] I. Grinberg, P. Juhás, P. K. Davies, A. M. Rappe, *Phys. Rev. Lett.* **2007**, *99*, 267603.

[309] V. Nagarajan, C. S. Ganpule, B. Nagaraj, S. Aggarwal, S. P. Alpay, A. L. Roytburd, E. D. Williams, R. Ramesh, *Appl. Phys. Lett.* **1999**, *75*, 4183.

[310] V. Nagarajan, S. P. Alpay, C. S. Ganpule, B. K. Nagaraj, S. Aggarwal, E. D. Williams, A. L. Roytburd, R. Ramesh, *Appl. Phys. Lett.* **2000**, *77*, 438.

[311] P. Miao, Y. Zhao, N. Luo, D. Zhao, A. Chen, Z. Sun, M. Guo, M. Zhu, H. Zhang, Q. Li, *Sci. Rep.* **2016**, *6*, 19965.

[312] S. Prosandeev, D. Wang, L. Bellaiche, *Phys. Rev. Lett.* **2013**, *111*, 247602.

[313] K. Uchino, S. Nomura, *Ferroelectrics* **1982**, *44*, 55.

[314] H. T. Martirena, J. C. Burfoot, *Ferroelectrics* **1974**, *7*, 151.

[315] X. G. Tang, K.-H. Chew, H. L. W. Chan, *Acta Materialia* **2004**, *52*, 5177.

[316] G. Adam, J. H. Gibbs, *J. Chem. Phys.* **1965**, *43*, 139.

[317] L. A. Larson, J. M. Williams, M. I. Current, *Reviews of Accelerator Science and Technology-Volume 4: Accelerator Applications in Industry and the Environment*, World Scientific Publishing Co., New Jersey, USA **2012**.

[318] A. Fuertes, *J. Mater. Chem.* **2012**, *22*, 3293.

[319] S. G. Ebbinghaus, H.-P. Abicht, R. Dronskowski, T. Müller, A. Reller, A. Weidenkaff, *Prog. Solid State Chem.* **2009**, *37*, 173.

[320] T. Bräuniger, T. Müller, A. Pampel, H.-P. Abicht, *Chem. Mater.* **2005**, *17*, 4114.

[321] J. A. Brehm, H. Takenaka, C.-W. Lee, I. Grinberg, J. W. Bennett, M. R. Schoenberg, A. M. Rappe, *Phys. Rev. B* **2014**, *89*, 195202.

[322] R. B. Olsen, *J. Energy* **1982**, *6*, 91.

[323] R. B. Olsen, D. A. Bruno, J. M. Briscoe, *J. Appl. Phys.* **1985**, *58*, 4709.

[324] I. M. McKinley, R. Kandilian, L. Pilon, *Smart Mater. Struct.* **2012**, *21*, 035015.

[325] S. Pandya, J. Wilbur, J. Kim, R. Gao, A. Dasgupta, C. Dames, L. W. Martin, *Nat. Mater.* **2018**, *17*, 432.

[326] F. Yang, *Mater. Sci. Eng. A* **2005**, *409*, 153.

[327] A. N. Morozovska, E. A. Eliseev, A. K. Tagantsev, S. L. Bravina, L.-Q. Chen, S. V. Kalinin, *Phys. Rev. B* **2011**, *83*, 195313.